Targeted nanoparticle platforms for selective photodynamic therapy of cancer

Girgis Obaid

School of Chemistry
University of East Anglia
Norwich, UK
February 2013

Thesis submitted in partial fulfilment of the requirement for the degree of Doctor of Philosophy of the University of East Anglia.

Declaration

I declare that the work contained in this thesis submitted by me for the Degree of Doctor of Philosophy is my work, except where due reference is made to other authors, and has not previously been submitted by me for a degree at this or any other university.

Girgis Obaid

Acknowledgements

ⲧⲫⲉⲡ ϩⲱⲟⲩ ⲛⲧⲟⲧⲕ: ⲕⲁⲧⲁ ϩⲱⲃ ⲛⲓⲃⲉⲛ ⲛⲉⲱ ⲉⲃⲃⲉ ϩⲱⲃ ⲛⲓⲃⲉⲛ ⲛⲉⲱ ϫⲉⲛ ϩⲱⲃ ⲛⲓⲃⲉⲛ

'Many of the great achievements of the world were accomplished by tired and discouraged men who kept on working.'

Firstly I would like to thank my primary supervisor Professor David Russell for his continued faith in me from the start and for his consistent support throughout my Ph.D. I simply wouldn't be where I'm at now if it wasn't for his help. I would also like to thank my secondary supervisor Professor Steve Meech for his guidance. Financial support by the EPSRC is gratefully acknowledged. The invaluable technical assistance provided by Dr. Alba Warn, Dr. Colin Macdonald and Dr. Paul Thomas is hugely appreciated.

A special thanks goes to my past and present colleagues in the Russell group: Dr. Claire Schofield, Dr. Tanya Stuchinskaya, Dr. Pompi Hazarika, Dr. Maria Marin-Altaba, Lawrence Eaglen, Susan van der Heide and Smita Ramma. Thanks to Claire for introducing me to the project as an undergraduate, to Tanya for humouring my philosophical rants, to Pompi for calmly guiding me through, to Maria for being a reliable friend and scientist, to Lawrence for getting me through my first and hardest year, to Susan for her friendship and love of coffee, and to Smi for her company and moral support.

Housemates past and present always provided me with distractions from the stresses of the Ph.D. life. Balm, Lewis, Nunn, Moore, George and Minak – cheers!

Most importantly I want to thank my family for their unfailing love and for acquiring an unusual taste for nanoparticle-based complaints.

Dad, Mum, Tony and Ela (& co.), and Bav – this thesis is dedicated to you.

Abstract

Numerous studies have demonstrated the substantial improvement in the photodynamic therapy (PDT) of cancer using multifunctional nanoparticles. The tumour-selectivity of nanoparticles carrying PDT agents can be achieved through conjugation to cancer-specific biomolecules that provide the particles with an improved tumour localisation and a marked enhancement in the therapeutic outcome.

The primary aim of this thesis was to establish the therapeutic potential of lectin, a carbohydrate binding protein, targeted PDT treatment of cancer cells using zinc phthalocyanine (C11Pc)-PEG gold nanoparticles (*ca.* 4 nm). Using a number of colorimetric techniques the interactions of Concanavalin A and succinyl-Concanavalin A with MCF-7 and SK-BR-3 human breast cancer cells expressing α-mannose was explored. The targeted PDT treatment of the breast cancer cells was attempted using C11Pc-PEG gold nanoparticles conjugated to Concanavalin A. However, Concanavalin A conjugation provided no enhancement in photodynamic breast cancer cell kill, as compared to the non-conjugated C11Pc-PEG gold nanoparticles.

The lectin jacalin was also conjugated to C11Pc-PEG gold nanoparticles to target HT-29 human colon cancer cells expressing the oncofoetal Thomsen-Friedenreich (T) antigen. Using laser scanning confocal microscopy a substantial improvement in the cellular internalisation was observed with the jacalin nanoparticle conjugates, as compared to the non-conjugated particles. Similarly, the phototoxicity of the HT-29 cells incubated with the jacalin conjugates was dramatically improved following irradiation at 633 nm, as compared to treatment using the non-conjugated particles. The PDT efficacy of the lectin-photosensitising nanoparticle conjugates was competitively inhibited by methyl-α-galactopyranoside and the T antigen-expressing glycoprotein, asialofetuin. The ApoTox-Glo™ triplex assay confirmed that the jacalin targeted phototoxicity of the HT-29 cells was through necrosis, with no evidence of apoptotic induction. Overall, it was found that jacalin conjugated nanoparticles achieved a *ca*. 95-98% photodynamic cancer cell kill, whereas the non-conjugated particles were minimally phototoxic.

The targeting efficiency of jacalin was compared to that of a monoclonal anti-HER-2 antibody. C11Pc-PEG gold nanoparticles functionalised with either the lectin or the antibody were used to target SK-BR-3 breast cancer cells and HT-29 colon cancer cells. Both nanoparticle conjugates exerted a similar level of targeted phototoxicity in both the breast cancer and colon cancer cell lines. The predominant mechanism of lectin or antibody targeted phototoxicity was found to be necrosis in both the SK-BR-3 cells and the HT-29 cells. Using confocal microscopy, both conjugates were shown to partially localise in the acidic organelles, suggesting that the conjugates were uptaken by the SK-BR-3 cells and the HT-29 cells through receptor mediated endocytosis.

Finally, in an exploratory study, titanium dioxide nanoparticles coated in polyacrylic acid were investigated as potential agents for sonodynamic cancer therapy. The findings suggested that exposure of the particles to ultrasound (1 MHz, 0.5 $W.cm^{-2}$) lead to a sonocatalytic enhancement in singlet oxygen production. Preliminary *in vitro* studies using HT-29 colon cancer cells show that preincubation with the nanoparticles had no effect on sonodynamic cell death. However, extracellular sonodynamic activation of the nanoparticles may prove more effective than intracellular activation at delivering the ultrasound-induced reactive oxygen species to the cancer cells.

Contents

Chapter 1

Introduction

Photodynamic therapy is a therapeutic modality that exploits the interaction of light with photosensitising molecules to treat a number of conditions including cancer. Some photosensitisers suffer from poor aqueous solubility and limited biodistribution. Pre-clinical studies using nanoparticle technologies have been shown to dramatically improve the *in vitro* and *in vivo* efficacy of photosensitisers. Further selectivity of photosensitising nanoparticle constructs can be achieved through biofunctionalisation with cancer-targeting ligands. Studies exploring the targeted photodynamic therapy of cancer using a variety of nanoparticle formulations have demonstrated a remarkable improvement in the specificity and efficacy of the treatment. A number of tumour-associated molecules can act as potential targets for selective cancer treatment using multifunctional nanoparticle technologies.

This chapter introduces the photophysical processes within photodynamic therapy and an overview of photosensitisers with clinical applications. A number of nanoparticles shown to improve photodynamic therapy are described and attempts at targeted treatment using nanoparticles are highlighted. Finally, the potential for using lectins as carbohydrate-specific cancer targeting agents is discussed. Lectins with current and prospective therapeutic applications are also outlined in this chapter.

1.1 Photodynamic cancer therapy

1.1.1 Photosensitisation

Photodynamic therapy (PDT) is a rapidly expanding therapeutic modality for various clinical conditions that has great potential for effective cancer treatment.[1] The photodynamic process involves the synergistic interaction of light, a photoactive molecule known as a photosensitiser, and molecular oxygen to produce cytotoxic reactive oxygen species (ROS).[2] There are two mechanisms by which photosensitisers can generate ROS: type I and type II reactions.[3] The photosensitisation reaction type is governed by the oxygen partial pressure, the nature and concentration of photosensitiser used, and the

concentration of the oxidation substrates.[2] Some overlap between the two mechanisms may occur.[2,3]

The initial stage of photosensitiser excitation is observed in both mechanisms of photosensitisation. Upon irradiation with light of a wavelength that is absorbed by the photosensitiser, the molecule is excited to its singlet excited state. The photosensitiser may then undergo intersystem crossing and be converted to its triplet excited state. During type I reactions, the sensitiser in the triplet excited state undergoes electron or hydrogen atom transfer to molecular oxygen or directly to cellular substrates to initiate free radical chain reactions involving a variety of radical intermediates.[3] Radical intermediates generated through this mechanism include sensitiser radicals, sensitiser radical ions, substrate radicals, substrate radical ions and reactive oxygen intermediates.[2,3] Ultimately the radical chain reactions lead to significant oxidation of the cellular substrates inducing cell death.[2] The reactive oxygen species formed during type I reactions include hydroxyl radicals ($^{\bullet}OH$), superoxide anions ($^{\bullet}O_2^-$) and hydrogen peroxide (H_2O_2).[3]

Type II photosensitisation is typically the predominant mechanism during PDT, which leads to the production of singlet oxygen ($^1O_2$), the main cytotoxic species responsible for cellular oxidative damage.[1] The stages involved in the photosensitised generation of singlet oxygen are summarised in **equations 1.1-1.4**.[2]

$$^1PS + h\nu \rightarrow {}^1PS^* \quad \textbf{(1.1)}$$

$$^1PS^* \rightarrow {}^3PS^* \quad \textbf{(1.2)}$$

$$^3PS^* + {}^3O_2 \rightarrow {}^1PS + {}^1\mathbf{O_2} \quad \textbf{(1.3)}$$

$$^1\mathbf{O_2} + \textit{Cellular Substrates} \rightarrow \textit{Oxidative Stress} \quad \textbf{(1.4)}$$

Photoirradiation (*hν*) of the photosensitiser in its singlet ground state (^1PS) excites the photosensitiser to its singlet excited state ($^1PS^*$) (**1.1**). Intersystem crossing allows the photosensitiser to exist in its triplet excited state ($^3PS^*$) (**1.2**). The long-lived triplet excited state of the sensitiser increases the likelihood of it being quenched by triplet ground state molecular oxygen ($^3O_2$) through a spin-forbidden Dexter energy transfer process.[4] Molecular oxygen is then converted to singlet oxygen ($^1\mathbf{O_2}$) (**1.3**), which induces

cell death through oxidative stress (**1.4**).[1,2] These energy transfer processes are also summarised in the simplified Jablonski diagram shown in **Figure 1.1**.

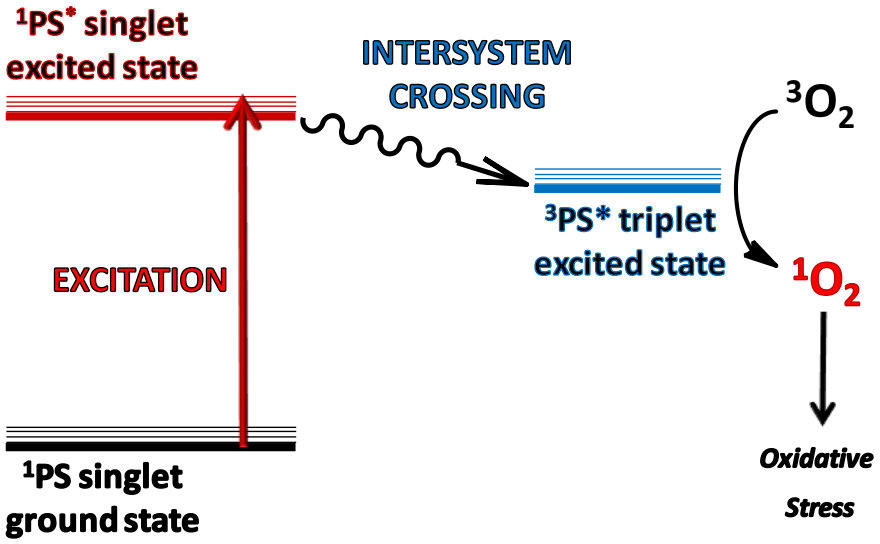

Figure 1.1 **A Jablonski diagram representing the electronic transitions that occur during type II photosensitisation that ultimately lead to singlet oxygen production and oxidative stress.**

PDT can induce direct cell death through apoptosis, necrosis or autophagy.[5,6] Cell death following PDT can be multifactorial and some overlap between the three main pathways involved can occur. The mechanisms of cell death induced by PDT are dependent on cell type, photosensitiser localisation, photosensitiser concentration and light dosage.[6] Typically, apoptosis occurs following PDT damage to the mitochondria leading to cytochrome c release, and damage to the anti-apoptotic B-cell lymphoma 2 (Bcl-2) proteins. [5-7] Cytoplasmic delivery of singlet oxygen can lead to damage of nuclear factor κ-light-chain-enhancer of activated B cells (NF-κB), an anti-apoptotic family of dimeric transcription factors.[6] Autophagy has also been observed following PDT treatment, which can be attributed to singlet oxygen generation within the endoplasmic reticulum. Bcl-2 damage in the endoplasmic reticulum results in a rise in free Beclin-1, a pro-autophagic protein. PDT within the endoplasmic reticulum leads to the activation of the mammalian target of rapamycin (mTOR), a cell growth regulator involved in the autophagic signalling pathway.[6] Cell membrane damage by PDT treatment typically induces necrosis. Cells undergoing apoptosis can also revert to necrosis if the PDT induced damage becomes

overwhelming.[6] Necrosis is typically regarded as a non-regulated, randomised mechanism of cell death. However, it has recently been suggested that PDT treatment of glioblastoma cells using 5-aminolevulinic acid (ALA) induces necrosis, which can also be programmed and regulated through the formation of necrosome complexes leading to 'necroptosis'.[8]

In addition to direct cytotoxicity of the cancer cells, PDT destroys the tumour microvasculature causing it to shut down, thus restricting the tumour's blood supply.[9] This depletes nutrients and oxygen at the site of the tumour, which can enhance the outcome of the treatment. PDT treatment also promotes localised inflammation within the vicinity of the irradiated tumour due to the release of cytokines, stress signals and arachidonic acid.[10] These signals result in leukocyte recruitment and tumour infiltration, followed by systemic immunity against tumour cell antigens.[5,10]

1.1.2 Photosensitisers in clinical PDT for cancer

The clinical outlook of PDT as an effective treatment for cancer is advancing, as many photosensitisers are clinically used for several cancers such as those of the skin, bladder, and head and neck.[5] Clinically available photosensitisers include porphyrins (*e.g.* Photofrin® and Photogem®), porphyrin precursors (*e.g.* Levulan®, Metvix® and Hexvix®), texaphyrins (*e.g.* Antrin®), chlorins (*e.g.* Foscan®, Photolon® and Photochlor) and phthalocyanines (*e.g.* Photosens® and Pc4).[5,11-14]

Porphyrin sensitisers are photoactive heterocyclic tetrapyrroles, whose photophysical properties differ with varying peripheral chemical substituents.[13] Photofrin® (**Figure 1.2**), also known as porfimer sodium, is a widely used photosensitiser for the treatment of Barrett's oesophagus,[15] oesophageal cancer,[16] endobronchial cancer[17] and lung cancer,[18] amongst other malignancies. Irradiation at 630 nm is approved for Photofrin® PDT.[18]

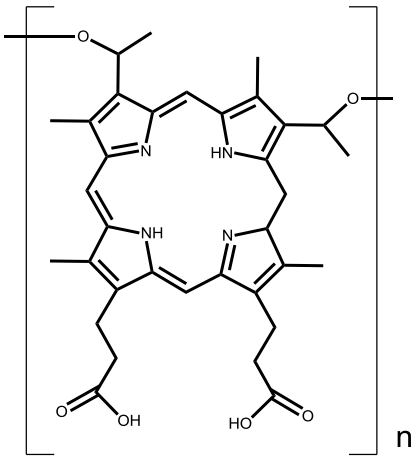

Figure 1.2 **The chemical structure of Photofrin® (porfimer sodium), adapted from Allison *et al.*[14]**

Prodrugs, such as Levulan® (5-aminolevulinic acid, ALA), exploit cellular biosynthetic pathways to synthesise porphyrin photosensitisers. ALA (**Figure 1.3** (**A**)) is the natural precursor of the intrinsic photosensitiser protoporphyrin IX (PpIX, **Figure 1.3** (**B**)), which is produced in the haem biosynthesis pathway.[19,20] Incubation with an excess of the prodrug ALA results in an intracellular accumulation of the photosensitising PpIX, and it has been shown that malignant cells exhibit higher levels of PpIX accumulation than normal cells as a result of altered enzymatic biosynthesis regulation.[21-23] ALA is commonly used for the treatment of surface malignancies,[19] precancerous (*e.g.* actinic keratosis[24]) and non-cancerous abnormalities (*e.g.* acne vulgaris[20,25]). Additionally, ALA has seen widespread use for photodynamic diagnosis, where preferential accumulation of ALA and protoporphyrin IX biosynthesis is exploited for real-time fluorescence monitoring of tumours for diagnostic and surgical applications.[20] Blue light (*ca.* 400 nm) is typically used to excite PpIX due to the spectral dominance of the Soret band.[26] However, excitation with blue wavelengths of light only allows specific imaging of thin tissue (*e.g.* lung tissue).[26] Derivatives of ALA with more hydrophobic, and cell membrane permeating, characteristics are also in use. Examples include the methyl ester (Metvix®), butyl ester, hexyl ester (Hexvix®) and octyl ester of ALA.[27] The biggest use of ALA in the PDT treatment of cancer is for dermatological malignancies. These include Bowen's disease, superficial basal cell carcinoma, superficial squamous cell carcinoma, cutaneous T-cell lymphoma, malignant melanoma and Kaposi's sarcoma.[26]

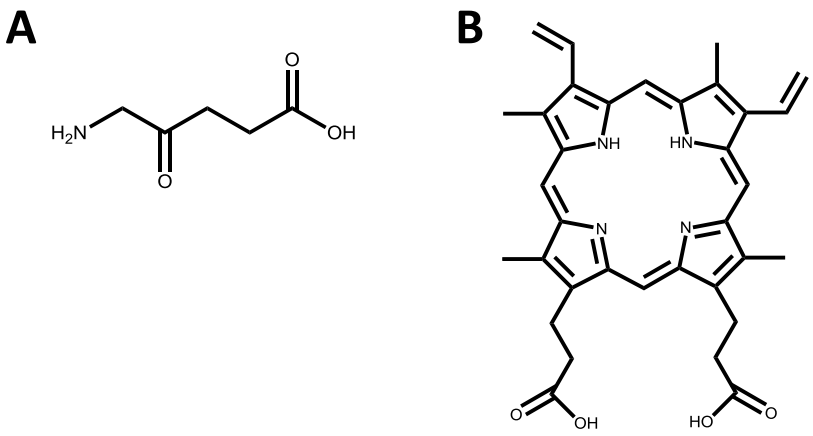

Figure 1.3 **Structures of A) 5-aminolevulinic acid (ALA, Levulan®) and B) its metabolic product protoporphyrin IX (PpIX) adapted from Bonnett.[28]**

Texaphyrins are a class of expanded lanthanide metal complexed porphyrin derivatives with relatively new applications as photosensitisers for PDT treatment and as radiosensitisers for enhanced radiotherapy.[11] The archetypal structure of a texaphyrin, a macrocyclic porphyrin derivative ring complexed to a central lanthanide ion, is shown in **Figure 1.4**. Antrin® is a water soluble lutetium (III) texaphyrin photosensitiser that has been heavily investigated for the treatment of prostate cancer[29,30] and other indications, such as breast cancer.[31,32] The sensitiser exhibits maximal absorption at 732 nm and has a unique tumour selectivity (tumour: muscle ratio of 10.55).[31] Xcytrin® is a gadolinium (III) texaphyrin with potential applications as a radiosensitiser for brain metastases, with the added advantage of also being MRI detectable allowing for *in vivo* monitoring.[11,33]

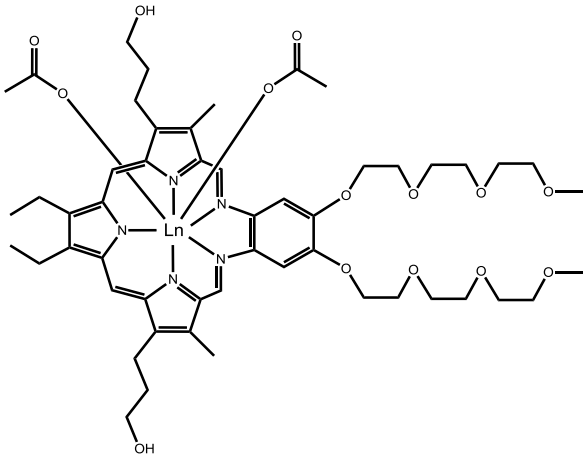

Figure 1.4 **Structure of a typical texaphyrin radio/photosensitiser adapted from Sessler and Miller.[11] The lanthanide metal ion (Ln) complexed is usually gadolinium(III) or lutetium(III).**

Like porphyrins, chlorins are aromatic macrocycles consisting of four pyrrole rings, however, one of the pyrrole rings is reduced resulting in increased absorption in the red region of the spectrum.[34] 5,10,15,20-tetra(m-hydroxyphenyl)chlorin, also known as temoporfin or Foscan®, is a chlorin photosensitiser with four hydroxyphenyl substituents (**Figure 1.5**), which is not FDA approved but has received clinical approval in the EU.[35] Indications for Foscan® use include the treatment of anal cancers, malignant brain tumours, breast cancers, malignant mesotheliomas, oesophageal cancers, skin cancers, gynaecological cancers and oral cancers.[35] The solubility and tumour localisation of Foscan® has proven to be challenging and therefore liposomal and PEG-modified formulations, namely Foslip® and Fospeg®, respectively, have been extensively studied.[35,36]

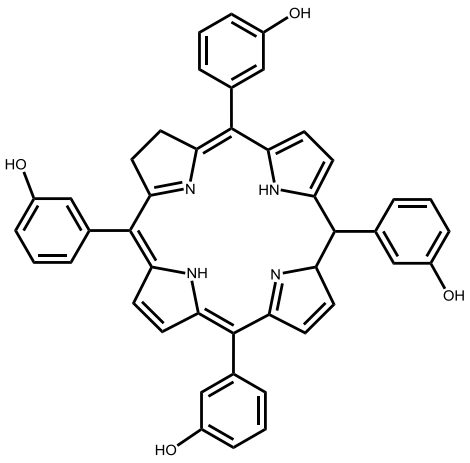

Figure 1.5 The chemical structure of Foscan® adapted from Bonnet *et al.*[34]

Phthalocyanines are azaporphyrin derivatives containing a central ion that exhibit red-shifted Q-bands, as compared to porphyrins.[28,37] The optical characteristics of phthalocyanines can be further enhanced by modifying the peripheral substituents of the macrocycle, or by introducing axial ligands to the central ion.[37,38] By using a closed d shell or diamagnetic central ion, such as Zn^{2+}, Al^{3+} and Ga^{3+}, the sensitisers exhibit longer triplet lifetimes and higher singlet oxygen quantum yields of 0.3-0.5.[28,37,39] Phthalocyanines containing central open d shell or paramagnetic ions, such as Fe^{2+}, exhibit shortened triplet lifetimes and minimal singlet oxygen production.[28,37] However, phthalocyanines are strongly hydrophobic and systemic administration is achieved through preparations of liposomes or emulsions.[28,37] Increased hydrophilicity of phthalocynanines has been commonly achieved through varying degrees of peripheral sulfonation.[40] However, studies have shown that the PDT efficacy of such sensitisers can be highly variable, as stability, biodistribution and pathways of intracellular uptake are dependent on charge, hydrophobicity and isomer purity.[40-42]

Zinc phthalocyanines have seen extensive use for *in vitro* and *in vivo* PDT studies for cancer. The delivery of these hydrophobic sensitisers to tumours following liposomal administration is known to be through association with lipoproteins.[43] Zinc phthalocyanines have been shown to be effective PDT agents for the treatment of lewis lung carcinomas,[44] fibrosarcomas,[45] mammary carcinomas,[46] and transformed fibroblasts,[47] amongst other cancers. Photosens® is a sulfonated aluminium phthalocyanine that is commercially available in Russia.[12,48] Photosens® has been used for the treatment of cancers of the oesophagus, lungs, breasts, bladder, cervix, lip, tongue,

pharynx and larynx.[12,49-51] Silicon phthalocyanine (Pc4, **Figure 1.6**) is a sensitiser that has drawn considerable attention for PDT applications due to its alkyl axial ligand that prevents sensitiser aggregation and allows isomeric purity. Pc4 has been extensively used in pre-clinical and clinical studies in patients for the treatment of cancerous, precancerous and non-malignant skin conditions. These include actinic keratosis, Bowen's disease, squamous cell carcinoma and basal cell carcinoma, amongst others.[52-54]

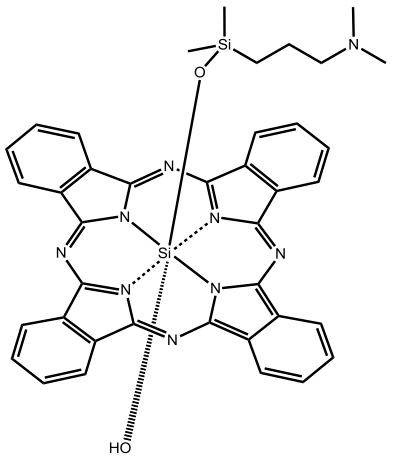

Figure 1.6 **Structure of the axially-substituted silicon phthalocyanine, Pc4, adapted from Baron *et al.*[53]**

When topically applied to early surface carcinomas, photodynamic treatment has the capacity to effectively eradicate the malignancy. Sensitisers with hydrophobic or amphiphilic characteristics have been found to penetrate the plasma membrane lipid bilayer and enter cancer cells more efficiently than hydrophilic photosensitisers.[41] However, a major drawback to the lipophilic nature of hydrophobic photosensitisers is their limited solubility in aqueous environments and their high tendency to aggregate, which can render them inactive and clinically ineffective.[1,5] A balance between photoactivity, physiological stability, effective biodistribution, and tumour localisation of photosensitisers must be obtained to maximise the PDT outcome. Nanoparticles composed of an array of materials have been shown to be an effective technology for the *in vivo* delivery of a variety of photosensitisers. Additionally, the multifunctionality of nanoparticles is proving to be increasingly valuable for the PDT treatment of cancer.

1.2 Nanoparticles for enhanced PDT

Nanoparticles, particles with diameters below 100 nm, have seen a dramatic rise in the number of applications that make use of their intriguing physical, chemical and optical properties. At the nanoscale, materials can possess characteristics that differ from their bulk state, expanding the use of such materials for various biomedical applications. Such applications include drug delivery, bioimaging and phototherapy, in addition to various other clinical, diagnostic and therapeutic applications.[55-57] Tumours develop an increasing demand for blood that is met by rapidly forming vascularisation. The newly formed vessels are of poor quality and are more 'leaky' than healthy vasculature, thus giving rise to a phenomenon referred to as the enhanced permeability and retention (EPR) effect.[56,58] Given sufficient systemic circulation time, nanoparticles extravasate into the tumour stroma and accumulate within the malignant tissue through the EPR effect, making them of particular interest for the delivery of anticancer agents.[57,59] In addition to their small size, nanoparticles can serve as multifunctional platforms for therapy allowing the combination of drug delivery and cancer specificity through the conjugation of biological targeting ligands.[56,60]

Nanoparticles have drawn particular interest in PDT for their ability to stabilise photosensitisers in aqueous environments and to preserve the photoactive monomeric form of the sensitisers. Some nanoparticles, also known as 'active' nanoparticles, possess photophysical characteristics that are directly or indirectly involved in the photogeneration of ROS.[61] In this chapter the potential uses of a variety of nanoparticles for PDT-based cancer therapy will be highlighted, including silica and polymeric nanocarriers, gold and magnetic nanoparticles for 'theranostics'[62], luminescent and non-luminescence semiconductors for diagnostics and therapy, and self-illuminating nanoparticles for PDT treatment and imaging of deeply situated tumours. The synthesis, biocompatibility, functionalisation and phototoxicity of such nanoparticle systems will be outlined and their potential for clinical use for the effective treatment of cancer will also be discussed based on *in vitro* and *in vivo* experiments.

1.2.1 Gold nanoparticles

Gold nanostructures are of particular interest in therapies such as PDT due to their biocompatibility, stability, size control and ease of surface functionality.[63] The nature of the gold-sulfur bond has been exploited in the self-assembly of thiolated photosensitiser molecules onto the surface of gold nanoparticles for PDT.[64] **Figure 1.7** shows a gold nanoparticle with a photosensitiser supported on the surface. Excitation of the photosensitiser attached to the gold nanoparticle results in the production of singlet oxygen and/or other ROS species. The gold core can be used also for plasmonic imaging or hyperthermal treatment.

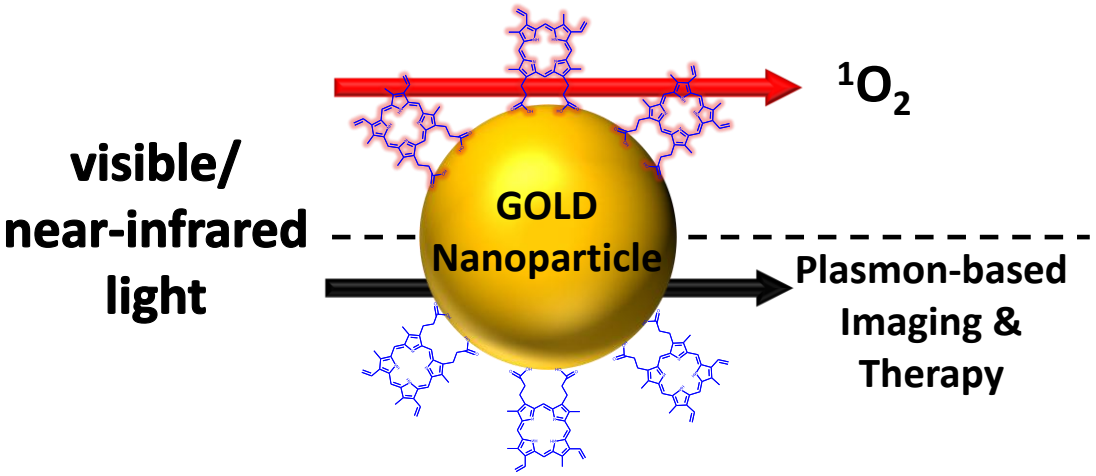

Figure 1.7 **A schematic diagram of a gold nanoparticle modified with a photosensitiser. Top: Irradiation of the photosensitiser with light induces production of singlet oxygen. Bottom: Irradiation of the gold core with light can be used for surface plasmon-based imaging and hyperthermal therapy.**

The Russell group were the first to use gold nanoparticles for supporting a zinc phthalocyanine (Pc) photosensitiser *via* a C11 mercaptoalkyl tether.[64] Reduction of gold chloride by sodium borohydride in the presence of the phase transfer reagent, tetraoctylammonium bromide (TOAB), and the thiolated Pc yielded stable nanoparticles with a diameter of 2-4 nm. The TOAB not only provided solubility for the hydrophobic system in polar solvents, but also enhanced the singlet oxygen quantum yield. The same Pc-gold nanoparticle system was shown to enhance the PDT effect on HeLa cervical adenocarcinoma cells as compared to an emulsion of the free photosensitiser.[65] *In vivo* studies further demonstrated the ability of these Pc gold nanoparticle conjugates to inhibit the growth of an implanted amelanotic melanoma following irradiation, and showed that irradiation of the nanoparticles was effective against the tumours 3 h following

intravenous administration in mice.[66] Gold nanoparticles have been synthesised carrying the same Pc photosensitiser together with polyethylene glycol (PEG).[67] PEG provided the nanoparticle system with aqueous solubility and colloidal stability, in addition to providing terminal carboxyl moieties that allowed conjugation of biomolecules. By conjugating anti-HER-2 antibodies to the gold nanoparticles through PEG, it was shown that the nanoparticles could actively target human breast cancer cells overexpressing the HER-2 receptor for enhanced cancer specific PDT. In the research reported in **Chapter 4**, the cancer-associated carbohydrate T antigen present at the surface of HT-29 human colon adenocarcinoma cells has been targeted using the lectin, jacalin, conjugated to PEG-Pc gold nanoparticles.[68] Jacalin conjugation to the gold nanoparticles induced substantial targeted phototoxicity (*ca.* 95-98%) of the HT-29 colon cancer cells.

The fate of nanoparticles of various compositions and morphologies has been the focus of much research in recent years. The *in vivo* biodistribution, pharmacokinetics and excretion of 5 nm PEG modified gold nanoparticles carrying a hydrophobic silicon phthalocyanine photosensitiser (Pc4) have been recently studied in a mouse tumour model by the Burda group.[69] The photosensitiser was non-covalently associated with the nanoparticles by association of the aminoalkyl axial ligand of Pc4 with the gold surface. The nanoparticles were found to efficiently deliver Pc4 to the cytoplasm of tumour cells by diffusion of the hydrophobic photosensitiser through the lipid membrane. It is known that PEG modification prolongs systemic nanoparticle circulation times.[59,70-72] Clearance of nanoparticles from the blood by the reticuloendothelial system (RES) limits the potential for nanoparticles to accumulate at the site of the tumour *via* the EPR effect, leading to a rapid build-up of nanoparticles in the liver and spleen, both major organs involved in the RES.[70] The PEG modified gold nanoparticles were found to have a circulation half-life of 3 h, avoiding rapid clearance by the RES system. The nanoparticles caused maximal accumulation of the photosensitiser deep within the tumour 4 h following intravenous tail vein administration. The gold nanoparticles were found to accumulate in the liver and spleen throughout the 7 days following administration. However, the nanoparticles that escaped RES clearance were observed in the kidneys at 4 h after administration and continuously declined in number over the 7 days studied.[69] These findings suggests that although the particles were eventually cleared by the RES system, some gold nanoparticles were likely to be excreted from the body through renal clearance.

Two conjugates composed of brucine and a porphyrin have been synthesised and conjugated to 3-mercaptopropionic acid decorated gold nanoparticles *ca.* 15 nm in

diameter.[73] These nanoparticle vehicles showed no evidence of enhanced *in vitro* PDT efficacy on PE/CA-PJ34 squamous cell carcinoma cells as compared to the free photosensitiser, possibly due to nanoparticle aggregation. Conversely, the nanoparticles were shown to completely eradicate subcutaneous tumours *in vivo* for up to 30 days post-PDT. This was thought to be due to the interaction of the nanoparticle conjugates with serum proteins, improving their accumulation at the site of the tumour.

The PDT efficacy of gold nanoparticles functionalised with the widely used photosensitiser haematoporphyrin (HP) has been studied *in vitro* to compare particles of 15 nm and 45 nm in diameter.[74] The citrate capped nanoparticles (15 nm and 45 nm) were stabilised with a layer of polyvinylpyrrolidone (PVP) and HP was then adsorbed within the polymer. It was found that upon irradiation, these gold-photosensitiser conjugates produced significantly more ROS than free HP, which was likely to be due to the heavy atom effect of the gold nanoparticles. The *in vitro* application of these nanoparticle conjugates on MT4 and Jurkat leukaemia cells showed that the 45 nm gold nanoparticle conjugates were the most effective at photodynamic cell destruction.

Nanoparticles possessing optimal absorption characteristics have been used in combination with photosensitisers for dual photothermal-photodynamic therapies. An aluminium phthalocyanine photosensitiser and PEG were conjugated to gold nanorods (*ca.* 34x9 nm) for *in vitro* and *in vivo* photodynamic, photothermal and combined photodynamic-photothermal therapy.[75] The fluorescence of the phthalocyanine was used to monitor both the intracellular uptake and the biodistribution of the free and bound phthalocyanine. The nanorods proved to enhance the cellular uptake of the photosensitiser and to improve the physiological delivery of the photosensitiser to the tumour. *In vivo* studies of a subcutaneously implanted SCC7 mouse tumour model indicated that dual photodynamic-photothermal therapy was significantly more effective at inhibiting tumour growth than either therapy alone. The photosensitiser hypocrellin B was also trapped within gold nanocages (*ca.* 50x50x50 nm) that exhibit a broad absorption spectrum in the near-infrared region of the spectrum.[76] Viability of HeLa cervical adenocarcinoma cells incubated with the nanocage complexes following irradiation at 790 nm was significantly reduced through synergistic photothermal-photodynamic effects.

The surface plasmon absorption characteristics of gold nanoparticles also have been used for surface enhanced Raman scattering (SERS) based detection of cancer cells in

conjunction with PDT for theranostic (combined therapy and diagnostics) applications in cancer treatment. Silica coated star shaped gold nanoparticles with a surface plasmon absorption band centred at *ca.* 900 nm have been synthesised for use in dual SERS-PDT theranostics.[77] The silica shell was co-doped with a SERS dye to enhance the Raman scattering signal and the photosensitiser methylene blue (MB) for singlet oxygen generation. The nanoparticle conjugates were shown to induce significant cell death of BT549 human breast carcinoma cells following irradiation.

Citrate capped gold nanoparticles with diameters from 5-250 nm were also found to catalytically enhance the generation of $^{\bullet}OH$ and $^{\bullet}O_2^-$ upon UV and X-ray irradiation in water, thus potentially enhancing the antitumour effect of radiotherapy.[78]

Gold has appealing physical and optical qualities that is both appropriate for chemical modification with sensitisers and effective for clinical use. Both *in vivo* and *in vitro* studies have shown the suitability of gold nanoparticles as stable delivery systems of PDT drugs. Further studies into the physiological fate of such gold nanoparticles are needed to assess the extent and duration of the nanoparticle accumulation in organs such as the liver and spleen.

1.2.2 ORMOSIL nanoparticles

Silica is a robust material with tuneable chemical properties. Its versatile polymerisation has meant that silica is frequently used for the stabilisation of photosensitisers and to functionalise various types of nanoparticles for biomedical applications.[79] A wide range of photosensitisers have been entrapped within silica nanoparticles. This method has proven to be effective in preserving the activity of hydrophobic photosensitisers in aqueous environments. Organically modified silica (ORMOSIL) based nanoparticles have seen widespread use due to their flexible hydrophobic/hydrophilic properties, which can be tuned in accordance with the degree of hydrophobicity of the photosensitiser.[79] In addition to the physical entrapment of photosensitisers within a silica nanoparticle, some photosensitising drugs have been incorporated within nanoparticles by covalent coupling to monomeric precursors of silica. Following condensation of the silica, the nanoparticles formed contain covalently integrated photosensitisers with a regulated sensitiser content.[79] **Figure 1.8** shows a schematic representation of silica nanoparticles doped with a photosensitiser.

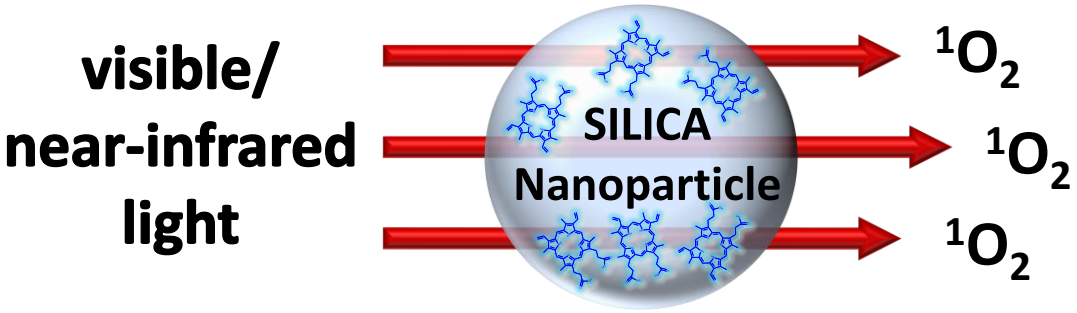

Figure 1.8 **A schematic diagram of silica nanoparticles with a photosensitiser encapsulated within the core. Irradiation of the photosensitiser with light produces singlet oxygen.**

The Prasad group were the first to encapsulate a photosensitiser in silica nanoparticles to yield stable nanoparticulates dispersed in an aqueous medium.[80] The ORMOSIL nanoparticles were synthesised by loading the photosensitiser 2-devinyl-2-(1-hexyloxyethyl)pyropheophorbide (HPPH) into the hydrophobic core of micelles along with the silica precursor, triethoxyvinylsilane, and the aminoalkyl silica precursor, 3-aminopropyltriethoxysilane (APTES). Complete condensation of the silica precursors yielded 30 nm nanoparticles with a hydrophobic core entrapping HPPH, and a hydrophilic amine functionalised surface provided by APTES condensation. These HPPH encapsulated nanoparticles were capable of producing singlet oxygen at levels identical to those generated by an aqueous emulsion of free HPPH. Importantly, these ORMOSIL particles caused substantial cytotoxicity at a HPPH equivalent concentration of 20 μM in both HeLa cervical adenocarcinoma cells and UCI-107 ovarian carcinoma cells. The Prasad group went on to synthesise 20 nm ORMOSIL nanoparticles by the coprecipitation of the photosensitiser iodobenzylpyropheophorbide (IP) covalently coupled to the silica precursors 4-(triethoxysilyl)-aniline and vinyltriethoxysilane.[81] Three different types of ORMOSIL nanoparticles were synthesised by varying the ratio of the two silica precursors. All of the nanoparticles covalently incorporated the IP photosensitiser, and preserved both the fluorescence properties of the sensitiser and its capacity to produce singlet oxygen. Fluorescence imaging confirmed that all three types of nanoparticles were readily internalised by Colon-26 mouse adenocarcinoma cells at an IP equivalent concentration of 2 μM. Phototoxicity was effectively induced with an IP equivalent concentration of 0.5 μM in a light dose dependent manner by irradiation at 665 nm. The same group also demonstrated the enhanced *in vitro* PDT efficacy of 30 nm ORMOSIL nanoparticles entrapping HPPH through iodination of the particles.[82] By using an iodinated silica

precursor, the efficiency of singlet oxygen production by the nanoparticle complex was potentiated through the heavy-atom effect.

ORMOSIL nanoparticles have been synthesised from the silica precursor, APTES, covalently bound to the photosensitiser protoporphyrin IX (PpIX).[83] Singlet oxygen production of the PpIX derivatised, amino functionalised silica nanoparticles (*ca.* 70 nm) was verified by the characteristic phosphorescence of singlet oxygen at 1270 nm and also by singlet oxygen induced photobleaching of 1,3-diphenylisobenzofuran (DPBF) upon illumination with 532 nm light. These authors observed that the efficiency of singlet oxygen delivery of the PpIX-nanoparticle system was higher than that of free PpIX, further suggesting that by preserving photosensitisers in their monomeric form, nanoparticles can enhance singlet oxygen production.[84] The same enhancement in singlet oxygen production has been reported with haematoporphyrin entrapped in silica nanoparticles (37 nm and 57 nm).[85] Additionally, the nanoparticles were co-doped with fluorescein isothiocyanate for simultaneous bioimaging and PDT, whilst maintaining their superior photosensitising capacity.

The PDT agent meso-tetraphenylporphyrin (TPP) was co-encapsulated in ORMOSIL nanoparticles with the pH indicator bromothymol blue (BTB) for selective PDT within the acidic tumour interstitium.[86] In basic pH conditions, spectral overlap between BTB and the photosensitisers resulted in competitive light absorption and insufficient TPP activation. However, a spectral shift in the pH indicator upon acidification resulted in effective sensitiser activation, thus demonstrating their potential as tumour sensitiser delivery systems.

PpIX was also encapsulated in silica nanoparticles *ca.* 10, 25 and 60 nm in diameter.[87] The silica precursor, triethoxyvinylsilane, was condensed in the presence of PpIX and dioctadecyl tetramethyl indodicarbocyanine chlorobenzene (DID), a fluorophore used for bioimaging experiments. Initial studies with all three nanoparticle sizes incubated with HCT 116 human adenocarcinoma cells showed no difference in internalisation rate or cytotoxicity following irradiation. Phototoxicity of the PpIX doped nanoparticles (25 nm) was investigated in human colon, breast, epidermoid and lymphoblastoid cancer cell lines. The nanoparticles were most effective on HCT-116 colon cancer cells with a half maximal effective concentration (EC_{50}) of 0.44 ± 0.05 μM.

Mannose functionalised silica nanoparticles carrying a covalently bound photosensitiser have been used to target mannose-binding lectins at the surface of MDA-MB-231 breast

cancer cells, and have demonstrated the potency of carbohydrates as selective cytoadhesive molecules.[88] A further study has looked into the functionalisation of silica nanoparticles with mannose residues to enhance bioadhesion and cellular uptake.[89] The nanoparticles contained a covalently bound porphyrin derivative photosensitiser, which was activated by multiphoton excitation using 760 nm laser light. *In vitro* PDT studies on MCF-7 and MDA-MB-231 human breast adenocarcinoma cells, and on HCT-116 human colon adenocarcinoma cells concluded that the nanoparticles exhibited no significant dark toxicity. However, significant phototoxicity of the conjugates upon multiphoton excitation reduced cell viability to *ca.* 44%, 33% and 27%, respectively. The authors showed that multiphoton irradiation of the silica nanoparticle conjugates intravenously administered to a HCT-116 tumour-bearing mouse model also exhibited significant *in vivo* PDT efficacy by reducing the tumour mass by *ca.* 70%. The silicon content in urine of mice treated with the silica nanoparticles was monitored using inductively coupled plasma mass spectrometry (ICP-MS) over the first 14 days post-PDT. It was found that the amount of silicon in urine reached a maximum around 6-8 days following PDT, and then decreased gradually till 14 days post-treatment. These findings suggest that the silica nanoparticles could be readily excreted from the body through the renal clearance pathway within two weeks of intravenous administration.

Calcium phosphosilicate nanoparticles carrying the photosensitiser indocyanine green have been conjugated to anti-CD117 or anti-CD96 antibodies for targeted PDT.[90] This study has shown that leukaemia cells overexpressing CD117 or CD96 cell-surface receptors can be selectively targeted for cancer cell-specific PDT.

Multifunctional silica nanoparticles *ca.* 100 nm in diameter entrapping the near-infrared dye ATTO 647N and the photosensitiser palladium tetraphenylporphyrin (PdTPP) have been synthesised for dual diagnostics and PDT.[91] Furthermore, the nanoparticles were functionalised with an arginine-glycine-aspartate (RGD) peptide to target U87-MG glioblastoma cells overexpressing $\alpha_v\beta_3$ integrins enabling selective binding and phototoxicity by the nanoparticles.

The Prasad group also investigated the *in vivo* biodistribution and clearance of 20 nm ORMOSIL nanoparticles loaded with a near-infrared fluorescent dye or radiolabeled with Iodine-124.[92] They found that almost all of the nanoparticles were cleared from the body of a mouse *via* the hepatobiliary system 6 days following intravenous administration. Examination of the liver, spleen, kidney, lungs and skin 15 days post administration

showed no residual nanoparticles (as determined by the lack of fluorescence of the loaded dye) and showed no cell or tissue damage.

There have been a number of reports indicating that silica nanoparticles can interfere with cellular function and viability *in vitro,* and can induce systemic toxicity and organ damage *in vivo*. The effects of different sized silica particles (40 nm to 5 μm) on human and rat epithelial cell lines have been investigated.[93] The authors found that 40-70 nm nanoparticles were able to enter the cell nucleus, whereas larger particles (0.2-5 μm) were confined to the cytoplasm. Once inside the nucleoplasm, silica nanoparticles (40-70 nm) induced aberrant aggregates of topoisomerase I, an enzyme crucial for processes including DNA replication. Subsequently, these silica nanoparticles inhibited DNA replication, transcription and cell proliferation, none of which were observed when the cells were incubated with 0.2-5 μm particles.[93] An *in vivo* study found that intravenous administration of non-porous silica nanoparticles (70 nm) at a dose of 30 $mg.kg^{-1}$ was lethal to mice, although a higher dose (100 $mg.kg^{-1}$) of 0.3 μm and 1 μm silica particles had no effect.[94] Repeated administration of a sub-lethal dose of 70 nm silica nanoparticles resulted in hepatic fibrosis, an indication of chronic liver injury.[94]

Silica nanoparticles are highly versatile and robust nanoparticles useful for PDT studies. The feasibility of co-doping the nanoparticles with photosensitisers and imaging agents has suggested their potential as theranostic nanoplatforms. Both *in vitro* and *in vivo* experiments have highlighted the powerful PDT efficacy of photosensitisers entrapped within silica nanoparticles. Additionally, evidence of renal clearance of silica nanoparticles and clearance through the hepatobiliary system make them worthy of further investigation for clinical PDT. However, the reports suggesting the potential for silica nanoparticles to impair cellular function and viability, and induce systemic toxicity and organ damage raise concerns over *in vivo* use for theranostic applications, and, therefore, further toxicological studies should be performed.

1.2.3 Polymeric nanocarriers

Synthetic organic polymers have been routinely used for the solubilisation, stabilisation and encapsulation of many nanoparticles in aqueous environments. Their capacity to be readily loaded with photosensitisers whilst providing a platform for further functionalisation with biomolecules has suggested their use as nanoparticle systems for cancer cell-specific PDT.[61] Nanoparticle size and sensitiser loading efficiency can be

precisely modulated by controlling polymer composition, reaction conditions and the chemical characteristics of the photosensitiser.[61] Some sensitisers have also been covalently tethered to monomers prior to polymerisation and formation of nanoparticles to prevent leaching of physisorbed PDT drugs before reaching the target site.[95] Conversely, weakly entrapped photosensitisers within polymeric nanoparticles have been exploited for the controlled release of PDT agents. For example, pH responsive polymer nanoparticles, such as glycol-chitosan nanoparticles, have been shown to selectively release photosensitisers within the acidic tumour interstitium (pH 6.84) as opposed to healthy tissue (pH 7.40).[96,97]

Many polymers used for PDT treatment, such as polylactic-co-glycolic acid (PLGA), have the added advantage of being biodegradable. As a result, polymeric nanoparticle delivery systems can be enzymatically degraded and excreted from the body, thus minimising risks of long term accumulation.[61] Although polymer encapsulation techniques have been described for a wide variety of PDT drugs, the resultant particles are typically micrometre sized with diameters ranging from *ca.* 117 nm to *ca.* 988 nm. **Figure 1.9** demonstrates the PDT action of polymeric nanoparticles loaded with photosensitiser molecules, irradiated with a specific wavelength of visible or near-infrared light to produce cytotoxic singlet oxygen.

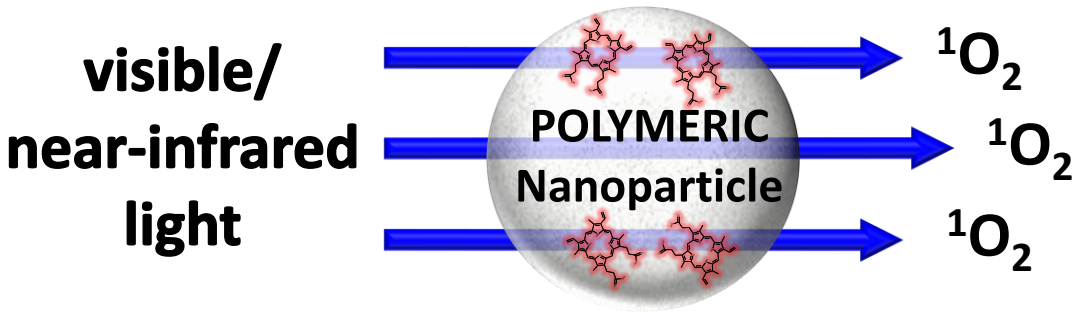

Figure 1.9 **A schematic representation of polymeric nanoparticles with a photosensitiser entrapped within the core. Irradiation of the photosensitiser with light generates cytotoxic singlet oxygen.**

Early studies of polymeric nanoparticles as PDT drug carriers showed that sulfonated zinc phthalocyanine and naphthalocyanine could be efficiently incorporated into polyisobutylcyanoacrylate and polyethyl-2-butylcyanoacrylate nanoparticles with diameters ranging from 10 to 380 nm.[98] The size of the nanoparticles, which were formed

by polymerisation in the presence of the sensitisers, was strongly dependent on pH as smaller nanoparticles were produced at alkaline pH conditions.

The *in vitro* and *in vivo* effects of PLGA nanoparticles have been investigated for the encapsulation of the lipophilic chlorin photosensitiser meso-tetraphenylporpholactol.[99] The nanoparticles had a hydrodynamic diameter of *ca.* 98 nm and a meso-tetraphenylporpholactol loading efficiency of 12%. Nanoparticles (10 μM) were incubated with 9L glioblastoma cells for 16 h followed by irradiation at 650 nm, which caused *ca.* 95% cell cytotoxicity. Intravenous administration of the nanoparticle formulation in mice implanted with a prostate carcinoma tumour caused significant tumour shrinkage following irradiation, and tumour regrowth was not observed up to 27 days post-PDT. It was found, however, that encapsulation reduced the efficiency of singlet oxygen production as a result of photosensitiser aggregation within the nanoparticle. Also, 20% of the photosensitiser leached out of the nanoparticles when they were kept in a 0.5% lipid solution for 360 min, outlining the limited stability of polymer nanoparticles for photosensitisers.

Aerosol OT™ surfactant-alginate polymer hybrid nanoparticles were used to simultaneously encapsulate the photosensitiser methylene blue and the chemotherapeutic agent, doxorubicin.[100] Mice bearing JC mammary adenocarcinoma tumours were used to compare the biodistribution and tumour delivery of the free drugs and the polymeric nanoparticle carriers. It was found that the nanoparticles significantly increased the tumour localisation of the two drugs, and enhanced their ability to reduce viability and induce apoptosis. Thus, the versatility of such polymeric systems outlines their potential to enhance the delivery of multiple drugs to tumours for synergistic combination therapies. Similarly, zinc phthalocyanine was co-encapsulated with docetaxal into poly ε-caprolactone and polyethylene oxide nanoparticles.[101] Nanoparticles loaded with both agents exhibited an enhanced cytotoxic effect on HeLa human cervical adenocarcinoma cells and on an *in vivo* orthotopic amelanotic melanoma model following irradiation, as compared to nanoparticles loaded with only docetaxal.

Methylene blue was used to compare three different PDT delivery systems: polyacrylamide nanoparticles (20-30 nm), sol-gel silica particles (190 nm) and ORMOSIL particles (160 nm).[102] The singlet oxygen molecular probe anthracene-9, 10-dipropionic acid (ADPA) was used to compare the delivery of singlet oxygen from the entrapped photosensitiser. It was found that the delivery of singlet oxygen was the highest using the

polyacrylamide nanoparticles. However, the loading of methylene blue was 3.5 times higher in the sol-gel silica particles than in the polyacrylamide nanoparticles. The Kopelman group recently reported the synthesis of two variants of polyacrylamide nanoparticles covalently conjugated to two methylene blue (MB) derivatives to enhance the loading of the photosensitiser and to prevent leaching from the nanoparticles.[95] The nanoparticles had an average diameter of 74.4 nm and 38.4 nm, depending on the MB derivative. Both types of nanoparticles were either modified with PEG or conjugated to an F3 peptide, a molecule specific for the commonly overexpressed receptor nucleolin. The PDT efficacy of the nanoparticles was assessed using MDA-MB-435 human breast adenocarcinoma cells *in vitro*. A dual live/dead cell stain using Calcein-AM/propidium iodide (PI), respectively, revealed that both types of nanoparticles exhibited no phototoxic behaviour, however cytotoxicity was observed when the nanoparticles were targeted to the cells using the F3 peptide.

The Hamblin group recently reported the use of hyperbranched polyether-ester nanoparticles composed of hybrids of chlorin e6 (Ce6) and hyperbranched ether-ester monomers for the enhanced PDT of Cal-27 human tongue carcinoma cells.[103] The water soluble nanoparticles had an average diameter of *ca*. 50 nm. Confocal fluorescence imaging confirmed the intracellular localisation of the polymeric nanoparticles. The conjugates exhibited a 3-4-fold higher PDT efficacy of Cal-27 cell kill as compared to the free sensitiser.

The Hasan group prepared PEG-PLGA block co-polymer nanoparticles entrapping the sensitiser benzoporphyrin derivative monoacid, which were enveloped in a liposomal formulation along with the anti-angiogenic agent, Avastin®.[104] The 'nanocell' liposomal formulation was delivered intracellularly in AsPC-1 human pancreatic adenocarcinoma cells *in vitro* and *in vivo* in a pancreatic cancer tumour model. The nanocells enhanced the PDT therapeutic outcome through the synergistic blocking of intracellular vascular endothelial growth factor (VEGF) signalling by Avasitn®.

The Boyle group studied the effects of two different polyacrylamide nanoparticles *in vitro*: nanoparticles (*ca.* 45 nm) entrapping polylysine modified aluminium phthalocyanine tetrasulfonate, and nanoparticles (*ca.* 95 nm) entrapping the same sensitiser with another surface bound porphyrin photosensitiser, 5,10,15,20-tetrakis(4-N-methylpyridyl)porphyrin.[105] The uptake of the nanoparticles in HT-29 human colon adenocarcinoma cells was investigated using flow cytometry and was found to be dose

dependent, reaching a maximum at 18 h. It was found that the polyacrylamide nanoparticles containing the two photosensitisers exhibited higher levels of phototoxicity. Cells irradiated in the presence of the nanoparticles without prior incubation were effectively killed even more than those incubated for 25 h before PDT. These results suggested that the use of two photosensitisers with different absorption profiles within one nanoparticle system can be more effective than using a single photosensitiser. It was also shown that nanoparticles in close proximity to the cells were sufficient to deliver cytotoxic levels of singlet oxygen.

Experiments using non-toxic and biodegradable nanoparticles for delivering photosensitisers to cancer cells have proven to be effective. However, photosensitiser aggregation within the polymeric matrix has been reported in several instances and leaching of the PDT drugs from the nanoparticle may also prove to be problematic as it can decrease the efficiency of photosensitiser delivery to tumours.

1.2.4 Multimodal magnetic nanosystems

Magnetic nanoparticles have drawn considerable attention due to the intrinsic properties that enable multiple functions to be performed, including enhancement of Magnetic Resonance Imaging (MRI), magnetically guided treatment and magnetic hyperthermal therapy.[106] In several studies, the intrinsic characteristics of magnetic nanoparticles have been combined with the potent cytotoxicity of photosensitisers to yield multifunctional nanoparticles for combined cancer therapy and diagnostics. Colloidal suspensions of magnetic nanoparticles composed of iron oxide and manganese oxide have been utilised as theranostic agents, which act as efficient nanocarriers of photosensitising agents for improved PDT, in addition to enhancing MRI-based tumour imaging and diagnosis. **Figure 1.10** is a schematic representation of a multifunctional magnetic nanoparticle modified with a photosensitiser.

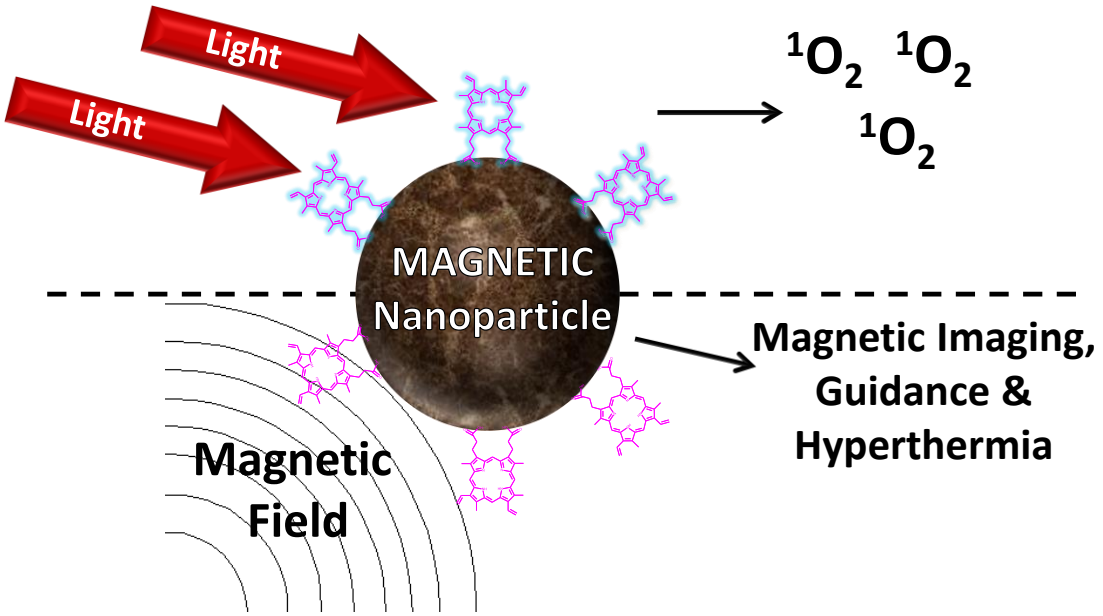

Figure 1.10 **A schematic of a multifunctional magnetic nanoparticle based PDT system. Top: Irradiation of the immobilised photosensitiser with visible or near-infrared light producing singlet oxygen. Bottom: Magnetic properties of the nanoparticle core allow for imaging, magnetic guidance and hyperthermal treatment with an externally applied magnetic field.**

The synthesis of biocompatible magnetic nanoparticles functionalised with a PDT agent was reported by the Tedesco group who used magnetite (Fe_3O_4) nanoparticles coated with the photosensitiser zinc phthalocyanine.[107] Spectroscopic characterisation confirmed that the phthalocyanine maintained its optical characteristics, following immobilisation onto the magnetic nanoparticles, and therefore retained its photosensitising capacity. In this instance, the system was proposed to be a potential bimodal PDT-hyperthermia agent for cancer treatment. Similarly, the same group reported the successful modification of magnetic particles with the photosensitiser pheophorbide on magnetite (Fe_3O_4) particles[108] and chlorin e6 on maghemite (Fe_2O_3) particles,[109] yielding photoactive magnetic nanosystems.

The hyperthermal effects of a magnetic PDT system composed of 10 nm magnetite nanoparticles functionalised with either haematoporphyrin or ALA have been investigated.[110] The authors report the successful thermalisation of the nanoparticle conjugates upon exposure to an alternating current magnetic field at 50 Hz. The degree of thermalisation of the nanoparticle conjugates was dependent on magnetic field exposure

time, and the nanoparticles remained stable up to 88-98 °C, depending on the sensitiser conjugated.

The first report of the *in vivo* use of nanoparticles for PDT combined with MR imaging used polyacrylamide nanoparticles co-doped with the photosensitiser Photofrin® and an MRI contrast agent.[111] The group showed that *in vivo* tumour growth was arrested following PDT using the nanoparticles which had been targeted to tumour vessels overexpressing $\alpha_v\beta_3$ and $\alpha_v\beta_5$ integrins using an RGD peptide bound to the surface. The entrapped MRI contrast agent enabled *in vivo* monitoring of the destruction of the tumour.

Magnetite nanoparticles have been synthesised and modified with a porphyrin photosensitiser.[112] Intracellular uptake of the iron oxide conjugates in HeLa cervical adenocarcinoma cells was observed by exploiting the fluorescence of the photosensitiser. Irradiation of the cells incubated with the nanoparticle conjugates with light ranging from 540-580 nm directly induced cytotoxicity of the HeLa cells. Although no attempt at hyperthermal treatment was made, their potential for dual PDT-hyperthermal treatment was proposed.

The Prasad group prepared magnetite nanoparticles encapsulated within a PEG-coated lipid micelle containing the photosensitiser Photochlor (HPPH) to treat HeLa cervical adenocarcinoma cells, with the potential for magnetic guidance and enhanced delivery to cancer cells.[113] Cellular uptake of the nanoparticle conjugates was confirmed by utilising the fluorescence of the photosensitiser and the ability of the system to induce cell death was demonstrated by the MTT viability assay.[113]

The *in vivo* PDT efficiency of MRI guided magnetite nanoparticles coated with chitosan, which encapsulated the porphyrin-based photosensitiser, 2,7,12,18-tetramethyl-3,8-di-(1-propoxyethyl)-13,17-bis-(3-hydroxypropyl) porphyrin (PHPP) has been investigated.[114] PDT treatment of SW480 colorectal adenocarcinoma cells with the *ca.* 20 nm magnetic nanoparticle conjugates was demonstrated using an MTT viability assay. Importantly, the nanoparticles were successfully guided to a mouse tumour using an external magnetic field, and PDT was monitored *in vivo* using quantitative MRI-based imaging. An investigation into the biodistribution of these nanoparticles concluded that the nanoparticles accumulated at the tumour more than in the liver and skin.

Similarly, iron oxide nanoparticles have been covalently modified with the photosensitiser chlorin e6 (Ce6).[115] Using a MGC803 gastric carcinoma mouse model, the nanoparticle

conjugates enabled fluorescence and MRI visualisation of the tumour within 6 h of administration. As the nanoparticles accumulated in the tumour with the assistance of external magnetic guidance, the fluorescence intensity of the Ce6 bound nanoparticles increased, and the MRI contrast image darkened. Following PDT treatment, inhibition of tumour growth was the most significant for up to 28 days when the conjugates had been magnetically guided to the tumour.

An alternative material that has seen significant interest in PDT-based theranostics due to its paramagnetic behaviour is manganese oxide. Hydrophobic monodisperse manganese oxide nanoparticles (*ca*. 14 nm in diameter) have been coated in a PEG shell with the photosensitiser PpIX covalently attached to the polymer.[116] The study highlighted the potential use of this nanoparticle platform as an alternative to iron oxide for combined fluorescence and MRI based imaging of cancer cells by exploiting the luminescence of the photosensitiser and the paramagnetism of the nanoparticle core, respectively. Moreover, following conjugation to the nanoparticle, the photosensitiser retained its ability to generate singlet oxygen as confirmed by its cytotoxic effects on Caki-1 human renal carcinoma cells.

Recently, the synthesis of paramagnetic core-shell nanoparticles consisting of terbium oxide (Tb_2O_3) and gadolinium oxide (Gd_2O_3) coated in a silica shell has been reported.[117] The shell covalently incorporated the photosensitiser 5-(4-carboxyphenyl)-10,15,20-triphenyl-chlorin (TPC) for dual MRI imaging and PDT applications. It was found that the fluorescence and singlet oxygen production of the TPC within the nanoparticles was quenched with increasing intraparticle concentrations of the sensitiser through long-range FRET and self-quenching processes.

These studies outline the significant potential of such magnetic nanoparticles for the improvement of PDT for cancer treatment. Such magnetic nanoparticles provide an additional dimension to *in vivo* theranostics using an external magnetic field for MRI tumour detection, nanoparticle guidance and hyperthermal treatment using these versatile, multifunctional composite nanosystems.

1.2.5 Metal oxide semiconductors

Some metal oxide nanoparticles are inherently photosensitising and can produce various forms of ROS that are usually associated with type I reactions. Examples of these are titanium dioxide (TiO_2) and zinc oxide (ZnO) nanoparticles, which are semiconductor nanocrystals that catalytically generate ROS upon photoexcitation.[118] Following irradiation with photons of energies greater than or equal to their band-gap, these metal oxide nanoparticles undergo a charge separation in their crystal lattice where electrons in the valance band move to the conduction band leaving behind a positive hole. The electron in the conduction band becomes trapped and recombination of this electron-hole pair (exciton) is delayed. This results in a long-lived charge separation, thus increasing the photocatalytic efficiency of ROS production at the surface of the nanoparticles. The positive hole can oxidise water molecules to produce $^{\bullet}OH$, and the electrons in the conduction band can reduce molecular oxygen to produce $^{\bullet}O_2^-$ and H_2O_2; all of these species can be cytotoxic oxidising species.[118] **Figure 1.11** demonstrates the photoinduced charge separation within these nanoparticles and the subsequent ROS species produced.

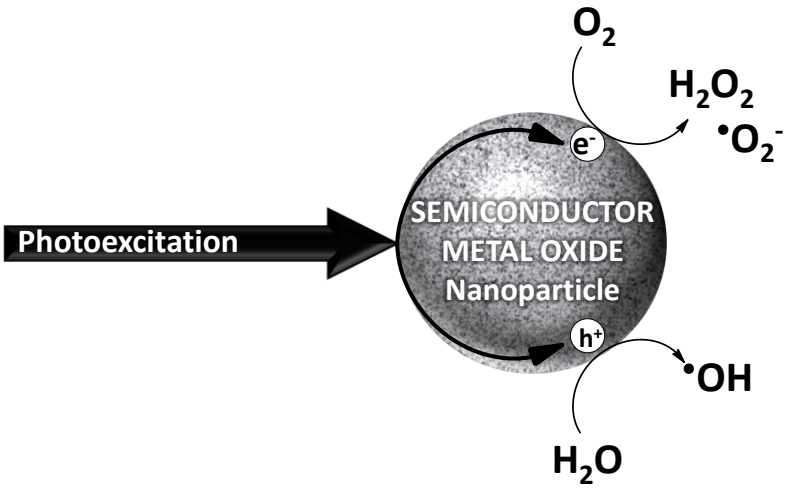

Figure 1.11 **A schematic representation of the photoinduced charge separation of semiconductor metal oxide nanoparticles resulting in the generation of a free electron (e^-) and a positive hole (h^+).**

As a result of their high rates of photocatalysis, metallic oxide nanoparticles, in particular TiO_2 nanoparticles, have been intensely investigated for their potential in the photodynamic therapy of cancer. The earliest report of using TiO_2 nanoparticles for UV induced phototoxicity for the treatment of cancer showed that 30 nm TiO_2 nanoparticles effectively destroyed HeLa human cervical adenocarcinoma cells *in vitro* when exposed to

UV light, and also inhibited tumour growth *in vivo* when administered in mice.[119] Tumour inhibition was most significant when the tumour received a second cycle of PDT treatment 13 days following the initial cycle.

It has been demonstrated that TiO_2 nanoparticles doped with platinum exhibited greatly improved phototoxicity against HeLa cervical adenocarcinoma cells.[120] Platinum-doped TiO_2 nanoparticles caused a *ca.* 85% reduction in cancer cell viability compared to a *ca.* 35% reduction in viability induced by non-doped TiO_2 nanoparticles following UV irradiation.

The *in vivo* antitumour potential of TiO_2 nanoparticles was further demonstrated using intravenously administered nanoparticles with UV irradiation, which prolonged the life of U87 glioblastoma tumour bearing mice by *ca.* 14 days.[121] However, to effectively excite the administered TiO_2 nanoparticles, the tumour was exposed to UV light following incision and temporary removal of the covering skin. This highlights the limitation of using UV light for the photosensitisation of deeply situated tumours treated with such nanoparticles.

Near-infrared light (1200 nm) has been used to indirectly activate 30 nm TiO_2 nanoparticles doped with 10 nm gold nanoparticles to overcome the limitation of short-wavelength excitation.[122] Multiphoton surface plasmon absorption of the nanogold-doped semiconductors resulted in a rapid injection of electrons within the TiO_2 conduction band, allowing the potential for ROS generation in the absence of UV irradiation. TiO_2 nanoparticles doped with 5% gadolinium, 1% erbium and 1% europium were also used as radiosensitisers to enhance the antitumour effect of X-ray irradiation, thus enabling activation with deeply penetrating radiation.[123]

The synthesis of 19.3 nm hybrid TiO_2 nanoparticles doped with cadmium sulfide semiconductor nanoparticles has been reported, and the enhanced visible light activation of the hybrid TiO_2 particles has been demonstrated.[124] Excitation of the cadmium sulfide particle dopants with visible light results in charge separation of the semiconductor. The photoinduced electron is then injected into the TiO_2 conduction band, thus initiating TiO_2 photochemistry. As compared to TiO_2 nanoparticles, irradiation of the TiO_2-CdS particles with a 390-425 nm LED showed a higher efficiency of radical-induced methyl orange degradation and an enhanced PDT efficacy on HL60 human promyelocytic leukaemia cells.

TiO_2 nanoparticles (25 nm) have also been functionalised with antibodies specific for carcinoembryonic antigen to target LoVo human colon adenocarcinoma cells overexpressing the cell surface antigen.[125] The targeted nanoparticle conjugates destroyed 100% of the cancer cells following 90 min UV irradiation at 254 nm, which was preceded by electroporation to maximise the cellular uptake of the particles. Glioblastoma multiforme (GBM) cells overexpressing the interleukin-13α2 receptor (IL-13α2R) have also been targeted with 5 nm TiO_2 nanoparticles functionalised with monoclonal anti-IL-13α2R antibodies through the 3,4-dihydroxyphenylacetic acid surface linker.[126] By acting as an electron donor to the TiO_2 conduction band, 3,4-dihydroxyphenylacetic acid reduced the band-gap of the TiO_2 nanoparticles from 3.2 eV to 1.6 eV, causing a large red shift in the nanoparticle absorption band. A172 GBM cells expressing high levels of IL-13α2R and U87 GBM cells expressing low levels of IL-13α2R were incubated with the targeted nanoparticle conjugates and irradiated with visible light (λ>400 nm) for 5 min. Phototoxicity of A172 GBM cells was significantly higher than that of the U87 GBM cells, highlighting the efficacy of selective PDT using biofunctionalised TiO_2 nanoparticles.

There have been several reports on the use of ZnO nanoparticles for PDT. For example, the different photoinduced toxicities of 20, 60 and 100 nm ZnO nanoparticles coated with aminopolysiloxane has been explored using SMMC-7721 hepatocellular carcinoma cells.[127] Significant reduction in SMMC-7721 cell activity (*ca*. 80%) was observed with the 20 nm nanoparticles at the lowest concentration of 2.5 $\mu g.ml^{-1}$ upon 245 nm UV irradiation for 180 seconds. At the highest concentration of 10 $\mu g.ml^{-1}$, all three sizes of nanoparticles reduced cell activity by *ca.* 100% although varying degrees of dark toxicity were observed. These findings clearly highlight the size and dose dependence of ZnO nanoparticles on their photodynamic activity, showing that smaller (20 nm) ZnO nanoparticles exhibit higher phototoxicity at lower concentrations; however they also appear to exhibit higher dark toxicity at larger concentrations.

ZnO nanoparticles have also been used as photoactive delivery agents for a porphyrin photosensitiser bound to the ZnO surface through an L-cysteine linker.[128] The ZnO nanoparticles have an excitation band at 300 nm and two fluorescence emission bands, one of which is centred at 445 nm. The emission band at 445 nm was used to excite the attached photosensitiser through fluorescence resonance energy transfer (FRET), which was found to be 83% efficient. By incubating NIH:OVCAR-3 human ovarian adenocarcinoma cells with the nanoparticle conjugates and irradiating them for 30 min with 365 nm UV light, cell viability was reduced to *ca.* 10% whereas in the dark, viability

remained at *ca.* 98%. Non-conjugated ZnO nanoparticles alone, however, did not induce a photodynamic response under the conditions of the experiment, highlighting possible limitations of the photosensitising capacity of ZnO.

Overall, photocatalytic metal oxide semiconductor nanoparticles provide opportunities for effective PDT, especially TiO_2 nanoparticles, which exhibit exceptional photocatalytic efficiency. However, short wavelength excitation is a significant limitation. Furthermore, there are many conflicting reports regarding the genotoxicity, photogenotoxicity and carcinogenicity of ZnO and TiO_2 nanoparticles, which must be addressed before these nanoparticles can be used *in vivo.*[129]

1.2.6 Quantum dots

Quantum dots (QDs) are semiconductor nanocrystals that have drawn considerable attention for luminescence-based applications including bioimaging, bioanalytics and diagnostics as a result of their intrinsic photophysical characteristics. Compared to organic fluorophores, QDs exhibit remarkable photostability, higher fluorescence quantum yields, significantly longer fluorescence lifetimes and broader absorption bands.[130] QDs typically exhibit quantum size effects with finely tuned absorption and emission profiles: the band gap of the QD widens with decreasing size causing a blue-shift in absorption and photoluminescence.[130] In addition, optical properties of QDs can be controlled by composition and surface functionality.[130] A noticeable drawback of QDs is the acute toxicity of cadmium (Cd), a common integral component of these semiconductor nanocrystals. To overcome this limitation, efforts to graft the QDs within various non-porous polymers or shells including zinc sulfide (ZnS) have been investigated, and attempts to use non-toxic photoluminescent QDs, such ZnS, silicon and carbon QDs are ongoing.[131] For example, Cd-free core-shell indium phosphide (InP)-ZnS QDs have been synthesised and the photosensitiser chlorin e6 (Ce6) has been encapsulated in a thin silica shell coating the nanoparticle.[132] These authors found that the rate determining step of singlet oxygen production by Ce6 activated by the QD emission was the distance-dependent energy transfer between the nanoparticle and the sensitiser.

QDs undergo charge separation upon excitation with light of an appropriate wavelength; however, radiative exciton recombination readily occurs resulting in strong fluorescence emission and weak ROS production. It has been reported that QDs can induce significant cytotoxicity upon UV excitation although this is attributed to surface oxidation, crystal

deterioration and subsequent Cd^{2+} release, rather than ROS production.[131] However, in contrast, results with cadmium telluride (CdTe) QDs have shown production of ROS in quantities sufficient for cancer cell kill (*ca.* 80% cytotoxicity); the photosensitisation process was proposed to be type I, as the singlet oxygen quantum yield of these quantum dots was found to be only 1%.[133] As a result of their unique photoluminescent properties, QDs have been exploited for non-radiative energy transfer to photosensitisers supported onto their surface. **Figure 1.12** shows an example of this energy transfer process that causes activation of a photosensitiser associated with the QDs.

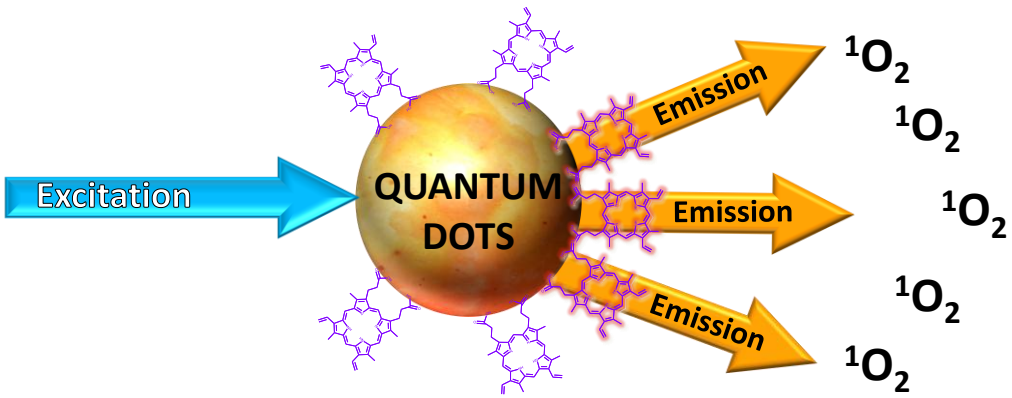

Figure 1.12 **Schematic diagram of the indirect FRET-based activation of a photosensitiser bound to the surface of QDs following direct photoexcitation of the nanoparticles. Visible light emitted from the photoexcited QDs is absorbed by the photosensitiser which subsequently generates singlet oxygen.**

The Burda group were the first to successfully functionalise the surface of 5 nm cadmium-selenide (CdSe) QDs with a phthalocyanine (Pc4) photosensitiser.[134] They showed that non-conjugated QDs produced singlet oxygen upon excitation in toluene, but found that the singlet oxygen quantum yield was only *ca.* 0.05. By conjugating Pc4 to the QDs, a FRET efficiency of 77% was observed following direct excitation with 488 nm light, which ultimately resulted in fluorescence emission of the sensitiser at 680 nm.

CdTe QDs have also been functionalised with the photosensitiser meso-tetra(4-sulfonatophenyl)porphine dihydrochloride (TSPP).[135] By irradiating the QD-TSPP

conjugates in D_2O at 355 nm, a singlet oxygen quantum yield of 0.43 was determined. No singlet oxygen production was observed following the excitation of the non-conjugated QDs. However, the singlet oxygen quantum yield of these TSPP-CdTe QD conjugates has been found to be lower than that reported for free TSPP (0.64).[136]

Another study has shown that CdTe QDs can produce singlet oxygen but with a singlet oxygen quantum yield of only 0.010-0.012 when irradiated at 532 nm in D_2O.[137] Singlet oxygen was quantified using the phosphorescence at 1270 nm and singlet oxygen-mediated photobleaching of anthracene-9,10-diyl-bismethylmalonate (ADMA). However, the CdTe QDs conjugated to a sulfonated aluminium phthalocyanine had an elevated singlet oxygen quantum yield of 0.15. Once again, the free sensitiser had a higher quantum yield (0.36) than that of the QD-photosensitiser conjugate.

The intrinsic photosensitising capacity of QDs was further investigated using core-shell CdSe-ZnS QDs and core-shell indium gallium phosphide (InGaP)-ZnS QDs.[138] The authors observed no singlet oxygen production following excitation of these QDs, as determined by the lack of photooxidation of 9,10-dimethylanthracene (DMA) and the Singlet Oxygen Sensor Green (SOSG). Conversely, generation of nitric oxides, such as peroxynitrite, was detected by the photooxidation of dihydrorhodamine 123 (DHR). Peroxynitrite is the reaction product of nitric oxide (NO) and $\cdot O_2^-$.

Non-peripherally tetra-triethyleneoxythia substituted aluminium, gallium and indium phthalocyanines were synthesised and their photophysical properties were investigated in the absence and presence of thioglycolic acid-capped CdTe QDs.[139] Singlet oxygen quantum yields were measured in DMSO using the singlet oxygen probe 1,3-diphenylisobenzofuran (DPBF). It was found that the singlet oxygen quantum yield of all the sensitisers synthesised was elevated in the presence of the QDs upon direct irradiation of the sensitisers. This trend was attributed to the heavy atom effect induced by the presence of cadmium. However, the singlet oxygen quantum yield following indirect FRET activation of the sensitisers in the presence of the QDs was not measured.

Green and red-emitting core-shell CdSe/CdS QDs coated with ZnS have been synthesised and modified with rose bengal and chlorin e6 (Ce6), respectively.[140] Singlet oxygen production of the conjugates was confirmed by photoluminescence centred at 1270 nm and also by the photobleaching of anthracene-9, 10-dipropionic acid (ADPA). It was found that both QD systems could act as efficient FRET donors and/or photosensitiser carriers for bioimaging and PDT.

Multiphoton excitation has also been employed for photoactivation of QD-based PDT systems. CdSe/ZnS core-shell QDs (*ca.* 5.4 nm) have been synthesised and modified with mercaptopropionic acid.[141] These nanoparticles had an absorption band maximum at 515 nm and an emission band centred at 535 nm. Irradiation of these QDs with 400 nm light in the presence of 1,3-diphenylisobenzofuran (DPBF) indicated that singlet oxygen was not produced by the QDs. An amine modified rose bengal derivative with an absorption band maximum centred at 565 nm was covalently conjugated to the QDs, which enhanced the aqueous solubility of the sensitiser. *In vitro* cell viability was assessed using the MTT assay upon single photon excitation of the QD-rose bengal conjugates with 365 nm light. HeLa human cervical adenocarcinoma cells were incubated with 0, 1, 10 and 100 μM QDs with no significant dark toxicity. However following irradiation at 365 nm, a *ca.* 33% decrease in cell viability was observed with 100 μM QDs. In addition, multiphoton excitation of the intracellular QD conjugates at 800 nm resulted in generation of singlet oxygen as determined by the oxidation of 2',7'-dichlorodihydrofluorescein diacetate (DHFA), a fluorescence based singlet oxygen probe.

Bioluminescence has recently been utilised as a source of photoexcitation of QDs, which enables bioimaging and phototherapy without the need for an external light source. These self-illuminating QD conjugates have been found to indirectly excite the photosensitiser Foscan® through a process referred to as bioluminescence resonance energy transfer (BRET).[142] Commercially available carboxyl functionalised QDs with a fluorescence emission band at *ca.* 600-710 nm were used for the study. The QDs with a diameter of *ca.* 19-25 nm were covalently conjugated to luciferase through EDC/NHS amide bond formation. Incubation of the luciferase-QD conjugates with the luciferase substrate, coelenterazine, resulted in a broad bioluminescence emission (390-600 nm). The bioluminescence subsequently excited the QDs as confirmed by the fluorescence emission profile of the conjugates. HeLa human cervical adenocarcinoma cells were incubated with the nanoparticle conjugates for 3 h, then incubated with Foscan® containing micelles for a further 3 h. PDT treatment was initiated by the addition of coelenterazine which triggered BRET activation of the QD and subsequent excitation of Foscan®. PDT efficacy was assessed using the MTT cell viability assay 24 h following initiation of the self-illuminating PDT. Cell viability was effectively reduced by *ca.* 40%, demonstrating the potential of a BRET-based QD system for PDT of cancer.

CdTe QDs conjugated to folic acid have also been used for targeted PDT of KB human head and neck carcinoma cells overexpressing the folate receptor-α.[143] Phototoxicity of the QDs

towards KB cells was found to be significantly higher than that of the HT-29 cells, which do not express the folate receptor-α.

Due to the remarkably low photobleaching of QDs and their highly tuneable photoluminescence emission, the various potential applications of QDs for photodiagnostic and phototherapeutic applications are broad. Although the excitation of QDs is usually limited to shorter wavelengths of light, it has been shown that BRET or multiphoton excitation is sufficient for PDT treatment. Additionally, evidence suggests that QDs below 5.5 nm are readily removed from the body of rodents through renal clearance.[144] Nevertheless, the majority of the QD-based PDT systems investigated to date are somewhat limited by the toxicity of the Cd based nanocrystals.

1.2.7 Scintillation nanocrystals

Light penetration through tissue has proven to be a significant barrier in activation of PDT systems present within solid tumours. To address this deficiency in clinical PDT, scintillation nanoparticles have been investigated.[145,146] These self-lighting nanoparticles absorb ionising radiation, such as X-rays and γ-rays, that can penetrate into human tissue deeper than light of UV or visible wavelengths. Following absorption, the nanoparticles become excited and radiative recombination of the electron-hole pair results in an emission of visible light, *i.e.*, scintillation.[145] Some scintillation nanoparticles, also known as persistent luminescence nanoparticles, exhibit a sustained afterglow of visible light lasting for up to several hours as a result of the prolonged decay lifetime of the phosphors.[145,147]

The scintillation nanoparticles can be utilised as FRET donors by photosensitisers supported on the surface, assuming that sufficient spectral overlap between the scintillation and sensitiser absorption exists. This scintillation phenomenon has opened up an array of materials that can be excited by high energy radiation for simultaneous photodynamic and radiation therapy for cancer, as well as *in vivo* imaging of solid tumours.[146,148] Semiconducting materials, such as TiO_2, ZnO, ZnS, cerium fluoride (CeF_3), CdSe and CdTe have been proposed as potential scintillation nanoparticles for PDT.[145] Additionally, a number of doped materials have been suggested to be promising potential candidates for PDT using scintillation. These materials include: cerium doped lanthanum fluoride ($LaF_3:Ce^{3+}$); cerium doped lutetium fluoride ($LuF_3:Ce^{3+}$); manganese doped calcium fluoride ($CaF_2:Mn^{2+}$); europium doped calcium fluoride ($CaF_2:Eu^{2+}$); europium

doped barium fluoride bromide ($BaFBr:Eu^{2+}$); manganese doped barium fluoride bromide ($BaFBr:Mn^{2+}$); and manganese doped calcium phosphate $CaPO_4:Mn^{2+}$, all of which are promising potential candidates for PDT using scintillation.[145] **Figure 1.13** is a schematic representation of a model multifunctional scintillation nanoparticle modified with photosensitiser molecules.

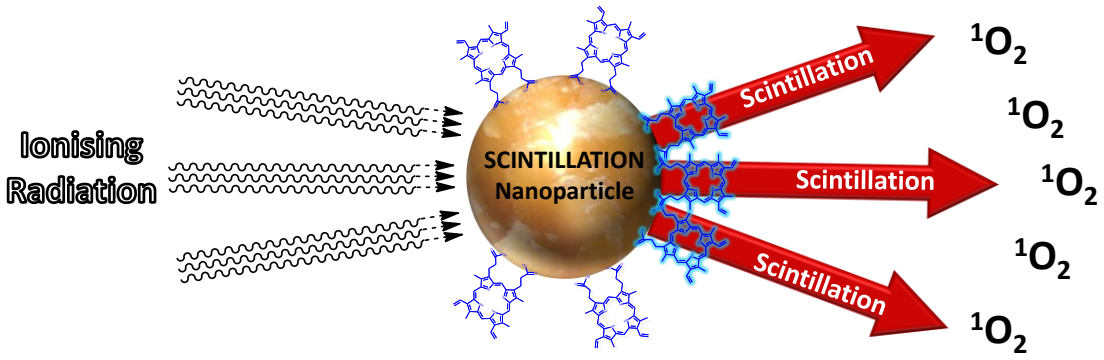

Figure 1.13 **A schematic representation of a scintillation nanoparticle with a photosensitiser coating the surface. Irradiation of the nanoparticles with ionising radiation induces scintillation, thereby emitting visible light, which can activate the photosensitiser through FRET.**

Scintillating lanthanum fluoride nanoparticles doped with terbium ions ($LaF_3:Tb^{3+}$) have been synthesised and functionalised with the photosensitiser meso-tetra(4-carboxyphenyl) porphine (MTCP).[149] Excitation of the $LaF_3:Tb^{3+}$nanoparticles (*ca.* 15 nm) with 260 nm UV light resulted in multiple luminescence emission bands, centred at 489, 542, 584 and 621 nm, which exhibited significant spectral overlap with the MTCP excitation spectrum. For the emission bands at 542, 584 and 621 nm a FRET efficiency of 68%, 52% and 50%, respectively, was determined. The production of singlet oxygen following X-ray irradiation of the MTCP coated $LaF_3:Tb^{3+}$ nanoparticles was then measured as a function of the decrease in anthracene-9, 10-dipropionic acid (ADPA) fluorescence emission. It was found that both free MTCP and MTCP conjugated $LaF_3:Tb^{3+}$ nanoparticles produced singlet oxygen in a time dependent manner during X-ray irradiation, although the scintillation nanoparticle conjugates were significantly more efficient.

Amine functionalised QDs have also been used as nanoscale scintillators which emit light at 520 nm upon X-ray excitation.[150] The nanoparticles were modified with the

photosensitiser Photofrin®. By applying 6 MV of X-ray radiation, FRET at 520 nm occurred from the scintillation of the QD to the conjugated Photofrin® molecules. It was shown that X-ray irradiation of these QD conjugates generated singlet oxygen in a dose dependent manner from 6 Gy to 30 Gy. H460 human lung carcinoma cells were then incubated with 48 nM of Photofrin®-conjugated QDs for 24 h, and were then exposed to a total X-ray dose of 6 Gy. Apoptosis was confirmed as the primary mechanism of PDT cytotoxicity by positive TUNEL staining.

Preliminary studies of scintillation nanoparticles have so far been mostly promising, indicating that radiotherapy of tumours could be enhanced using nanoparticles that readily absorb ionising radiation and scintillate to activate a PDT drug. If *in vivo* studies prove successful, scintillation nanoparticles could aid radiotherapy by reducing the dosage of high energy rays required for tumour eradication, thereby minimising unnecessary secondary effects of the treatment.

1.2.8 Upconverters

An alternative route to overcome the limitation of light penetration through tissue is to utilise upconversion. Upconversion is a phenomenon by which light is absorbed by a material at one wavelength, but the photons emitted following excitation are of a shorter wavelength than that used for excitation.[151] This photophysical process has been explored for possible use in PDT, where upconverting nanocrystals are excited by near-infrared light (**Figure 1.14**). These nanoparticles, which are doped with rare earth metal ions, typically lanthanide ions, emit light in the visible region of the spectrum. The visible light is then used to excite the photosensitiser supported onto the upconverter surface. This process activates the photosensitiser with a wavelength of light that favours tissue penetration.[151] Upconverting nanoparticles can also exhibit multiple tuneable emission peaks, which can be exploited for bimodal diagnostic and photodynamic purposes.

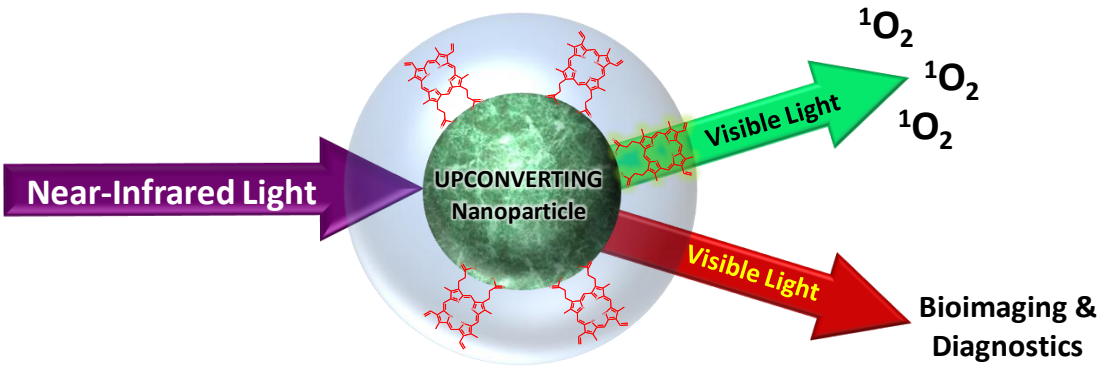

Figure 1.14 **An upconverting nanoparticle coated in a silica shell encapsulating photosensitiser molecules. Following irradiation of the nanoparticle with near-infrared light, the upconverter emits visible light, which can be used for bioimaging or diagnostics and used to activate the photosensitiser.**

The PDT potential of sodium yttrium fluoride ($NaYF_4$) nanoparticles co-doped with ytterbium (Yb^{3+}) and erbium ions (Er^{3+}) has been reported.[152] The $NaYF_4$:Yb^{3+},Er^{3+} upconverting nanoparticles (*ca.* 60-120 nm) exhibit sharp emission bands centred at 537 nm and 635 nm following excitation with 974 nm near-infrared light. The upconverters were embedded in a silica shell doped with the photosensitiser Merocyanine 540. Following modification, the upconverting nanoparticles retained their photoluminescence properties. The nanoparticles were found to generate singlet oxygen upon near-infrared irradiation in a buffered solution. To aid cancer cell-specific uptake, the upconverting nanoparticles were further functionalised with an anti-MUC1 antibody targeted to MUC1 receptors overexpressed by MCF-7/AZ human breast adenocarcinoma cells. The cells incubated with the nanoparticle conjugates were irradiated with a 974 nm laser. Following 36 min of irradiation, cell morphology was altered, which was indicative of cytotoxicity.

In vitro and *in vivo* studies have been reported highlighting the potential of using upconverting nanoparticles for PDT of cancer.[153] These authors synthesised polyethyleneimine (PEI) coated $NaYF_4$:Yb^{3+},Er^{3+} nanoparticles (*ca.* 50 nm). The nanoparticles were further modified by covalently conjugating a cancer cell targeting molecule, folic acid. A zinc phthalocyanine (ZnPc) photosensitiser was physisorbed onto the surface of the nanoparticles to enable PDT action of the conjugates. The PDT action of these conjugates was investigated *in vitro* using HT-29 human colon adenocarcinoma cells and the MTT assay. HT-29 cells incubated with the upconverting nanoparticle conjugates

for 24 h were irradiated for 30 min with a 980 nm laser. Cell viability was significantly reduced by *ca.* 80-90% following PDT, indicating that the singlet oxygen production of these upconverting nanoparticle-photosensitiser conjugates upon near-infrared excitation is sufficient for effective cancer cell kill.

In vitro and *in vivo* PDT treatment has been attempted using *ca.* 30 nm PEG coated $NaYF_4$ upconverting nanoparticles doped with 20% Yb and 2% Er, modified with chlorin e6 (Ce6).[154] The Ce6 was loaded onto the nanoparticles through hydrophobic interactions with oleic acid present at the surface. In addition to singlet oxygen measurement and *in vitro* MTT viability assays, *in vivo* studies of tumour volume, mouse survival and pharmacokinetic behaviour of the upconverting nanoparticles were conducted. 4T1 mouse breast cancer cells were incubated with 5 μM Ce6 equivalent of Ce6-modified upconverting nanoparticles for 2 h then irradiated for 10 min with a 980 nm near-infrared laser. Significant reduction of cell viability was observed in a dose dependent fashion when the cells were incubated with the Ce6-nanoparticle conjugates and irradiated. As expected, unmodified nanoparticles and free Ce6 did not exhibit significant phototoxicity. When Ce6-nanoparticle conjugates were directly injected into the tumour of a 4T1 mouse model and irradiated with the 980 nm laser, substantial tumour reduction was observed. Of the mice treated with the nanoparticle conjugates and irradiated, *ca.* 70% survived up to 60 days, whereas no mice in the control groups survived longer than 23 days.

Core-shell $NaYF_4:Yb^{3+},Er^{3+}$-$NaGdF_4$ upconverting nanoparticles conjugated to chlorin e6 (Ce6) were explored as a theranostic multimodal PDT system, a luminescent bioimaging platform and an MRI contrast agent.[155] Upon excitation at 980 nm, emission of the upconverters at 540 nm was used for *in vivo* tumour imaging and emission at 660 nm excited the Ce6 sensitiser. Additionally, the gadolinium-containing shell provided MRI contrast enhancement of tumours *in vivo.* Tail vein administration of the upconverting conjugates into mice bearing U87-MG glioblastoma tumours, followed by irradiation at 980 nm, resulted in complete tumour growth inhibition for 14 days post-treatment.

A recent report describes the preparation, *in vitro* and *in vivo* efficacy of $NaYF_4:Yb^{3+},Er^{3+}$ nanoparticles coated in a mesoporous silica shell loaded with either Merocyanine 540, zinc phthalocyanine, or co-loaded with both photosensitisers.[156] The nanoparticles exhibit two main emission bands centred at 540 nm and 660 nm, at which Merocyanine 540 and zinc phthalocyanine maximally absorb light, respectively. Following irradiation at 980 nm, the nanoparticle conjugates co-loaded with both sensitisers were more effective at

producing singlet oxygen and reducing the viability of B16-F0 mouse melanoma cells than the particles loaded with an individual photosensitiser. Irradiation of a mouse tumour consisting of B16-F0 cells pre-incubated with co-loaded upconverters resulted in substantial tumour growth inhibition, as compared to irradiation alone or incubation with particles alone. Yttrium quantification in four organs was performed in mice that were intratumourally injected with the upconverters; however, the fate of systemically administered nanoparticles was not investigated. Co-loaded upconverters were further modified with PEG and folic acid, and were injected into the tail of a melanoma bearing mouse. Irradiation of the tumours resulted in a statistically significant enhancement in antitumour efficacy when treated with folic acid targeted nanoparticles.

Selective targeted therapy using folic acid conjugated upconverting nanoparticles has also been demonstrated on JAR human placenta choriocarcinoma cells overexpressing the folate receptor.[157] $NaYF_4$:Yb^{3+},Er^{3+} upconverting nanoparticles, further modified with rose bengal and folic acid, exhibited a dose dependent phototoxicity of the JAR cells, whereas no significant toxicity was observed with NIH/3T3 mouse embryonic fibroblast cells that do not express the folate receptor.

$\alpha_v\beta_3$ integrin-overexpressing U87-MG glioblastoma cells have also been effectively targeted with RGD peptide conjugated $NaYF_4$:Yb,Er upconverting nanoparticles (*ca.* 53 nm).[158] The nanoparticles were coated with chitosan and modified with the sensitiser pyropheophorbide a and the RGD peptide sequence. The particles demonstrated selective phototoxicity of U87-MG cells, whereas no significant toxicity was observed with MCF-7 cells that express low levels of the $\alpha_v\beta_3$ integrin.

A thorough *in vitro* and *in vivo* study into PDT using NaYF4:Yb,Er upconverting nanoparticles has shown promising results.[159] The particles were coated with chitosan and modified with a zinc phthalocyanine photosensitiser. In addition to demonstrating an effective dose-dependent reduction in MCF-7 human breast adenocarcinoma cell viability following irradiation at 980 nm, the nanoparticles significantly inhibited tumour growth and prolonged the survival of tumour bearing mice. Intratumoural administration of chitosan coated upconverting nanoparticles functionalised with the near-infrared fluorescent dye, indocyanine green, revealed that the particles were not carried out of the tumour to the heart, kidneys, spleen, liver, lungs or intestines for up to 14 days. Although tumour localisation of these particles is an obvious advantage, no signs of physiological

clearance were apparent, which could raise concerns regarding prolonged nanoparticle accumulation within the body.

Upconverting nanoparticles have only relatively recently been considered for PDT, although substantial preliminary *in vitro* and *in vivo* studies show huge potential. However, long term stability and toxicity of these lanthanide-doped nanocrystals in various physiological environments must be systematically studied if they are to be used for clinical PDT.

1.2.9 Future prospects for nanoparticles in photodynamic cancer therapy

An increasing number of studies have highlighted the exciting potential of the use of nanoparticles for PDT. Nanoparticles exhibit multifunctionality which can dramatically improve current PDT modalities. The vast array of nanoparticles and their respective activities show promise to significantly enhance cancer therapy by increasing the delivery of hydrophobic photosensitisers; by radically improving photosensitiser accumulation in tumours through biofunctionality and targeted therapy; and by potentially maximising the antitumour effect of radiotherapy. However, the majority of studies with nanoparticles for PDT have so far not exceeded initial stages of *in vitro* and *in vivo* experimentation. Although many of the nanoparticles reported to date demonstrate no immediate acute toxicity, and there is some evidence to suggest that some nanoparticles are cleared by the urinary and hepatobiliary systems, significant further studies are required to establish their long term physiological effects before translation into clinical practice. However, it is clear that the future for nanoparticle technology within PDT is exceptionally promising.

1.3 Targeted PDT using lectins

1.3.1 Aberrant glycosylation pathways in cancer development and progression

A vast number of treatments for cancer have proven to be highly effective at reducing the mass of tumours and prolonging the survival rates of patients. However, the majority of these therapeutic modalities are accompanied by severe side effects, as healthy tissue can also be susceptible to damage by the treatment. The lack of specificity of cancer treatments can result in considerable discomfort and a decline in the quality of life of patients. Thus, targeted therapies that selectively destroy diseased tissue, whilst leaving

healthy tissue unharmed are hugely appealing. Targeted treatments that discriminate between cancerous and healthy tissue promise to lower the overall dosage of administered drugs, whilst enhancing their antitumour efficacy.

Lectins are carbohydrate binding proteins of non-immune, non-enzymatic origin. Their affinity for carbohydrate moieties is highly specific. The word lectin originates from the Latin word 'legere' meaning 'to select'.[160] The discovery that lectins could selectively agglutinate cancer cells gave a preliminary indication of the presence of certain differences between surface expressed carbohydrates in healthy and cancerous cells.[161,162] Many carbohydrates and carbohydrate patterns have been associated with the cancerous phenotype. Some include the over or underexpression of naturally occurring glycans, whilst others include the novel expression of glycans usually found in foetuses, providing potential targets for selective cancer therapies.[163]

Cell surface glycoproteins consist of three main types: *N*-linked glycans that are attached to asparagine residues, *O*-linked glycans that are attached to serine or threonine residues, and glycosaminoglycans (GAGs) that are linked to serine residues. *O*-linked glycans were initially discovered in mucin, a protein found in mucous, and were therefore termed mucin-type glycans.[160] Many cancer-associated carbohydrates are known to be mucin-type glycans, but the major disadvantage of these glycans is their terminal heterogeneity. For this reason, many *O*-glycans are termed by their core sequence.[160] Carbohydrate abbreviations are shown in **Table 1.1**.

Table 1.1 Common carbohydrates and their abbreviations.

Carbohydrate	Abbreviation
galactose	Gal
glucose	Glc
N-acetylgalactosamine	GalNAc
N-acetylglucosamine	GlcNAc
fucose	Fuc
mannose	Man
sialic acid/neuraminic acid	Neu

DNA mutations can lead to the overexpression, underexpression, or deletion of many genes resulting in a direct observed effect on the gene products, which can subsequently be overexpressed, underexpressed or missing, respectively.[164] Altered levels of enzymes responsible for post-transcriptional glycosylation can be attributed to many of the glycan changes associated with cancer. A common characteristic change in surface carbohydrates of cancer cells is increased branching of *N*-glycans, which can be a result of increased activity of the enzyme *N*-acetylglucosaminyltransferase V (GlcNAc-TV). This enzyme causes branching of β1-6GlcNAc, which are additional sites for the attachment of terminal sialic acid residues. Overactivity of sialyltransferases causes an overall increase in sialylation of *N*-linked glycans, a common process in core carbohydrate structures at the surface of cancer cells.[163,165,166] Early studies have demonstrated the relationship between excessive sialylation and increased metastasis.[165]

The overexpression of glycosyltransferases has also been linked to malignancy, as the downstream effect of the activity of these enzymes leads to the overexpression of terminal glycan epitopes. These include the Thomsen-Friedenreich (T) antigen, the Tn antigen, sialyl-Tn, polysialic acid (PSA), Sialyl Lewis A (sLe^a), Lewis Y (Le^Y) and Sialyl Lewis X (sLe^X), which have been implicated in a large variety of cancers.[163] **Figure 1.15** shows the structures of common cancer-associated carbohydrate antigens.

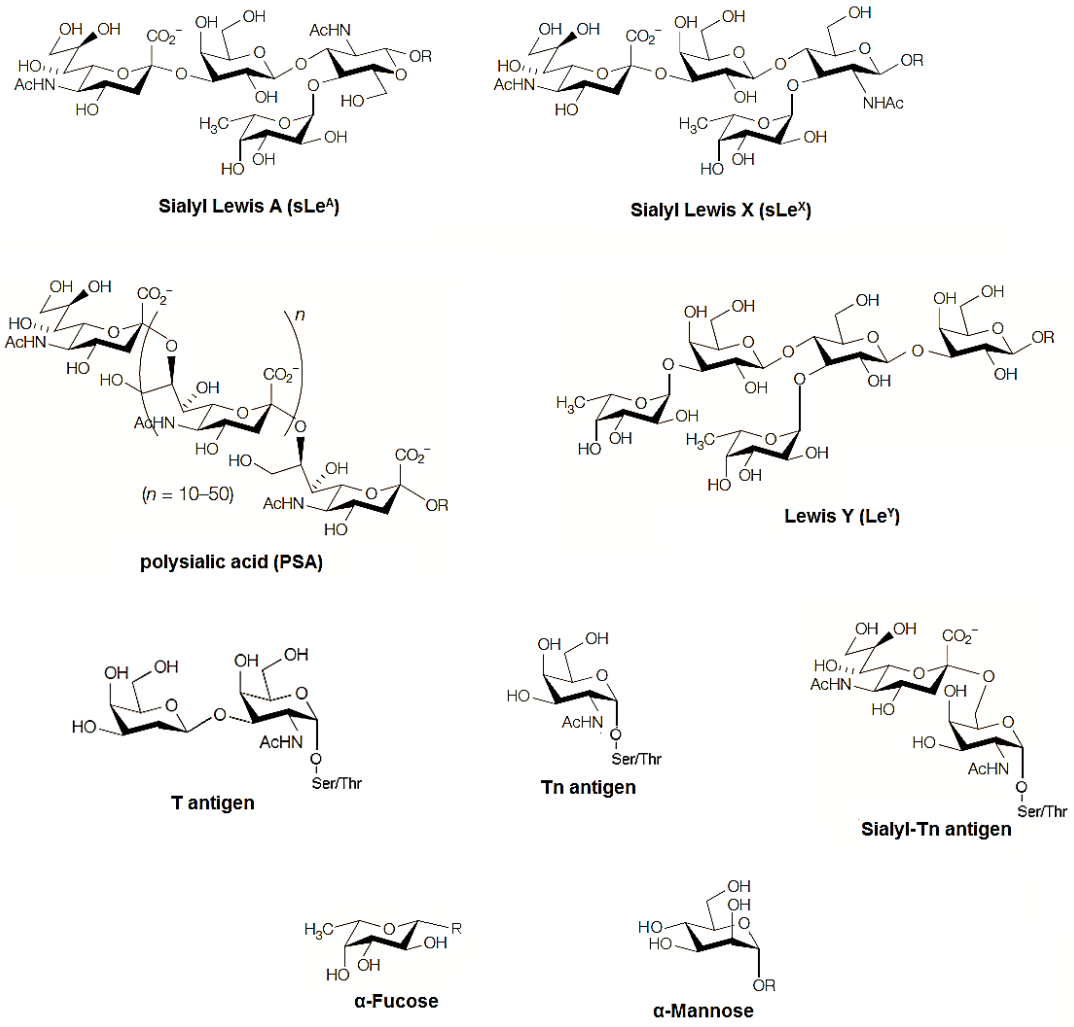

Figure 1.15 **Structures of common cancer-associated carbohydrate antigens. The 'R' group refers to conjugated glycan sequences. Figure adapted from Dube *et al.*[163]**

The Thomsen-Friedenreich antigen (also known as the TF antigen, T antigen, Core 1 and CD 176) is a mucin-type glycan found to be overexpressed in 90% of all primary human carcinomas including those of the lungs, pancreas, breast, bladder, colon, oesophagus, ovaries and prostate.[163,167] The antigen is a disaccharide consisting of Galβ1-3GalNAc-*O*- α-linked to a serine or threonine residue (Galβ1-3GalNAc-*O*-α-ser/thr) on a cell surface glycoprotein. The T antigen is a truncated *O*-glycan that is usually cryptic in healthy cells as it is concealed by further branched glycosylation, sialic acid residues, or sulfate molecules.[168] It is only exposed in cancer, inflammatory diseases such as ulcerative colitis, and in embryonic or developmental cells, hence it is referred to as being

oncofoetal.[163,166,168,169] The exposure of the T antigen in colonic cancers can be attributed to a combination of several possible defects in the glycosylation mechanisms responsible for further maturation of the T antigen as is usually observed in healthy cells. These include the decreased expression of carbohydrate sulfotransferases responsible for concealing the T antigen with *O*-sulfate esters; an increased expression of the Uridine Diphosphate-galactose (UDP-Gal) transporter, increasing its bioavailability and therefore increasing the synthesis of the T antigen; and an increased pH level inside the Golgi Apparatus favouring T antigen synthesis.[168] The fact that the T antigen is well-defined and is highly expressed in a wide range of cancers, makes it an attractive molecular target for cancer therapies such as PDT. The function of the T antigen has been previously studied and it was found that it mediates cancer cell adhesion to galectin-3 of the vascular endothelium, and assists in the metastasis of the cells.[170]

The Tn antigen is also an *O*-linked glycan, whose overexpression is correlated with the cancerous phenotype. It is the biosynthetic precursor of the T antigen and structurally consists of a monosaccharide, GalNAc-*O*-, α-linked to a serine or threonine residue.[166] The sialylated form of the Tn antigen, sialyl-Tn, is much more specific to cancer cells and arises as a result of the truncation of *O*-linked glycans.[166] The expression of Tn and sialyl-Tn is also usually correlated with poor prognosis of the disease.[171] The Tn antigen has been found to be expressed in 72% of colonic carcinoma cells and only in 14% of normal colonic cells, making it a potential target for lectin mediated therapeutic selectivity.[171]

Other mucin like glycoproteins that have certain glycosylation alterations are expressed on cancer cell surfaces and can then be shed. These act as cancer markers that can be detected in the serum and aid in the diagnosis of cancer. Glycoprotein cancer markers include the carcinoembryonic antigen and the prostate specific antigen.

1.3.2 Lectins - from discovery to biomedicine

Monosaccharides, oligosaccharides and glycoconjugates can reversibly bind to lectins with varying affinities. For example, the *Canavalia ensoformis* (Jack Bean) lectin, Concanavalin A, binds to methyl-α-Man with a dissociation constant (K_d) of 15.9 μM,[172-174] whereas the *Agaricus bisporus* (domestic mushroom) lectin binds to the T antigen with a K_d of 3.4 μM.[175] Lectins are usually multidomain, multimeric proteins containing carbohydrate recognition domains where glycan moieties specifically bind. Many lectins, like enzymes, require one or more metal ions to associate with their carbohydrate recognition domains in order for their target molecules to effectively bind.[176] For example, at each carbohydrate recognition domain in Concanavalin A, the presence of a manganese cation and a calcium cation is crucial for the ability of the lectin to bind to its respective carbohydrate moiety.[177] Concanavalin A will be discussed in greater detail in **Chapter 3**.

Lectins play integral roles in many processes that are dependent on the selective binding of glycans. For example, plants use lectins to attach to nitrogen-fixing bacteria, and to protect themselves from plant pathogens.[178] Lectins mediate cell migration and cytoadhesion, in addition to regulating uptake and translocation of glycoproteins.[178] Microorganisms, such as bacteria and parasites, use lectins to bind to host cells in addition to a number of other processes.[178]

Unlike enzymes, lectins do not have intrinsic enzymatic activity associated with their carbohydrate recognition domains, although some lectins have catalytic activity and non-carbohydrate recognition at different loci on the protein. Leczymes are a type of lectins that have dual carbohydrate recognition and mutually exclusive RNAse activity.[179] An example of these is the sialic acid-binding lectin from *Rana japonica* oocytes (jSBP) which contains a conserved pyrimidine base-specific RNAse domain as well as a sialic acid binding domain.[160,180]

Most lectins are multivalent, which is crucial for their ability to cross-link carbohydrates on different glycoconjugates.[160] These glycoconjugates could be a component of the cellular membrane glycans, which would result in the lectin cross-linking and agglutinating several cells.[160,181] Stillmark first discovered in 1888 that a lectin extracted from *Ricinus communis* (castor beans) agglutinates and precipitates all types of human erythrocytes.[182] Many interactions between lectins and mammalian erythrocytes have been discovered since, and due to the extent of this interaction, lectins have been termed agglutinins, haemagglutinins, or phytohaemagglutinins (plant lectins).[160] Erythrocytes are

a highly glycosylated cell type and express a broad diversity of saccharides with potential for highly specific lectin interactions.[181] The specific interaction of phytohaemagglutinins with erythrocytes has been routinely utilised in the determination of blood types since their discovery.

Many cancers have been associated with specific glycosylation patterns, alterations, and aberrations which have been implemented in cancer survival, metastasis, and evasion of immunosurveillance.[163] In the past these specific glycoconjugates have been intensely studied and monitored in tumour progression, and many have been sequenced, purified, and synthesised for histochemical, diagnostic and immunotherapeutic purposes.[163] Previous studies have shown a relationship between cellular affinity to certain lectins and tumourigenicity, and the study of the specificity of lectins to tumours and cancer cells is being extensively investigated showing great potential for future targeted therapies.

1.3.3 Targeting tumour cells with lectins

Several reports have demonstrated the potential of lectins as tumour targeting proteins, bioactive therapeutic agents and adjuvants for existing cancer treatments. Mistletoe (*Viscum album*) extracts have seen extensive use in pre-clinical and clinical studies for the treatment of a large number of cancers.[183] The main active component of mistletoe extracts is the mistletoe lectin-1 (ML-1). Mistletoe extracts under clinical investigations include Iscador®, Eurixor®, Helixor®, Lektinol®, Isorel®, Abnoba-viscum and recombinant ML-1. Phase I and II clinical trials have explored the efficacy of mistletoe extracts in the treatment of colorectal carcinoma, ovarian cancer, renal cell carcinoma, breast cancer, prostate cancer, lung cancer, stomach cancer, bladder cancer and melanoma.[183] Findings have reported an increased quality of life, prolonged survival and lowering side effects of conventional treatment.[183,184] The lectin consists of two chains; a cytotoxic ribosome-inactivating enzymatic A chain and a sialic acid-binding B chain.[185] The ML-1 exhibits unique specificity for gangliosides and glycoproteins expressing terminal Neu5Acα2-6Gal1-4GlcNAc-, the overexpression of which has been associated with carcinomas.[186-188] The therapeutic effect of ML-1 is a result of both its direct cytotoxic effects and indirect immunomodulatory effects. The A chain is responsible for inducing apoptosis at low concentrations (fM-pM) in a death receptor-independent mechanism.[189] ML-1 can also activate immune cells, such as natural-killer (NK) cells, and potentiate their cytotoxicity.[190] Although ML-1 has been found to agglutinate types A, B and O human erythrocytes at a

concentration of 1 μg.ml^{-1}, intravenous administration at lower concentrations is routinely used for therapy.[191]

The lectin extracted from the seeds of the *Maackia amurensis* tree is known to target terminal α2,3-sialylated *O*-linked glycans.[192] The *Maackia amurensis* lectin has been used to effectively target melanoma cells expressing the mucin receptor podoplanin, which is modified with α2,3-Neu residues. Binding of the lectin to podoplanin has been shown to inhibit the receptor's interaction with its natural ligand, and thus effectively hinder B16 melanoma cell growth and metastasis.[192]

The African legume lectin, *Griffonia simplicifolia* lectin II (GSL-II) is the only one of three *Griffonia simplicifolia* lectins that does not agglutinate human erythrocytes.[193] GSL-II has a specificity for α- or β-linked GlcNAc residues on the non-reducing terminal of oligosaccharides, also known as the TK cancer-associated antigen.[194] The lectin has been shown to bind selectively to colonic carcinoma and hyperplastic colonic tissue, but has no reactivity towards normal colonic tissue.[194]

The Gorse seed lectin, *Ulex europeaus* agglutinin I (UEA-I) specifically binds to α1,2-Fuc residues, also known as the H antigen, in addition to the carcinoembryonic antigen.[195,196] Like GSL-II, UEA-I does not bind to normal rectal mucosa but binds with high affinity to hyperplastic polyps and to carcinomatous tissue.[194] Furthermore, UEA-I was shown to bind to 12 out of 18 rectal adenomas analysed.[196] However, the lectin was found to agglutinate type O human erythrocytes, and to a lesser extent types A and B.[197]

The hexavalent *Helix pomatia* agglutinin (HPA) extracted from the Roman snail exhibits specificity towards terminal GalNAc residues and, to a lesser extent, terminal GlcNAc residues.[198] HPA is also known to bind to the T antigen, the Tn antigen and the carcinoembryonic antigen.[195,199,200] The lectin has been shown to specifically bind to MCF-7 and MDA-MB-231 human breast adenocarcinoma cells, in addition to HT-29, Caco-2 and HTC-116 human colon adenocarcinoma cells.[201-204] However, HPA was found to have no reactivity towards sub-normal, non-tumourigenic MCF-10A breast cells or to IEC-6 non-transformed rat small intestine epithelial cells.[204,205] The lectin specifically recognises human malignant melanoma cells, and lectin reactivity has been shown to be a prognostic indication of the metastatic potential of a tumour.[206] Furthermore, HPA was only found to agglutinate type A human erythrocytes.[198]

Seeds from the Hairy Vetch contain the *Vicia villosa* lectin (VVL), which is specific for α- or β-linked GalNAc, although its specificity is higher for GalNAc-α- residues (Tn antigen).[207] VVL binds to 98% of Caco-2 human colorectal adenocarcinoma cells in monolayer.[208] Histological analysis revealed that VVL is reactive towards 72% of cancerous colonic tissue, 100% of adenomatous and hyperplastic polyps, but only 14% of normal mucosa.[171] This lectin also agglutinates all types of human erythrocytes.[209]

The flowering Coral Tree contains a heterodimeric lectin, *Erythrina cristagalli* lectin (ECL) with a molecular mass of 57 kDa.[210] The carbohydrate specificity of ECL is for the Galβ-1,4GlcNAc- disaccharide. This carbohydrate structure is a precursor for many blood group antigens including those of type A, B, H and Lewis blood groups.[210,211] Therefore ECL can agglutinate all types of human erythrocytes.[210,211] This disaccharide is also known as the Type II oligosaccharide antigen, and its expression in gastrointestinal tissue is related to malignancy.[211] A study found that Galβ-1,4GlcNAc- was overexpressed in colorectal carcinomas, and this finding was highly correlated with ECL reactivity.[211] In a study including various cancerous and healthy tissue, ECL was found to bind very weakly to the healthy colorectal epithelium, but showed significant binding to colorectal carcinomatous tissue.[211] ECL binding patterns to colorectal carcinomas and their respective liver metastases was also found to be similar.[211] Additionally, the lectin was found to react to 50% of colonic adenomatous tissue analysed. In a cellular study using Caco-2 human colon adenocarcinoma cells, ECL bound to all of the cells grown in monolayer.[208]

Peanut agglutinin (PNA) is a T antigen-binding lectin that does not recognise the sialylated form of the antigen.[212] PNA only agglutinates human erythrocytes upon neuraminidase treatment.[213] The lectin has been shown to bind to MCF-7 and MDA-MB231 breast cancer cells with varying affinities.[214] PNA also binds to the sub-normal, non-tumourigenic breast cell line MCF-10A, although it's affinity is 10-fold lower towards the non-immortalised variant cell line MCF-10M.[215] The lectin has also been found to selectively target a variety of colon cancer cell lines, although a major drawback of using PNA is its ability to stimulate the proliferation of some cells, such as HT-29, SW837, HCT-15 and LoVo colon carcinoma cells.[216-218]

The lectin Amaranthin derived from the *Amaranthus caudatus* flower is another T-specific lectin that binds to both the sialylated and non-sialylated forms of the antigen.[219] The lectin binds strongly to HT-29 colon adenocarcinoma cells with an equilibrium dissociation constant (K_d) of *ca.* 16 nM and reaches maximum binding within 120 min.

However, the lectin does exert a pro-proliferative effect on the HT-29 cells.[219] Additionally, Amaranthin agglutinates all types of human erythrocytes.[220]

The edible mushroom contains a T-specific lectin, the *Agaricus bisporus* lectin (ABL).[216] ABL binds to the T antigen with a dissociation constant of (K_d) of 3.4 μM.[175] The lectin also binds to the sialylated form of the T antigen.[216] Recent studies have determined the presence of an additional carbohydrate binding site within ABL, that has a specificity for GlcNAc-exposed *N*-linked glycans.[175] ABL has been shown to reversibly inhibit the proliferation of HT-29 colon cancer cells, MCF-7 breast cancer cells and Caco-2 colon cancer cells in a dose-dependent manner.[216] The lectin has also been found to agglutinate all types of human erythrocytes.[221]

The lectin extracted from *Artocarpus integrifolia* (jackfruit), jacalin, is also a T antigen-specific lectin, which will be discussed in greater detail in **Chapter 4**. **Table 1.2** summarises the lectins with potential for targeted cancer treatment. The biomodulatory effects exerted by the lectins and their haemagglutinating characteristics are outlined.

Table 1.2 A summary of lectins with potential clinical applications for cancer treatment.

Lectin	Species	Carbohydrate Specificity	Tumour Antigen	Biomodulatory Effects	Agglutinates Human Erythrocytes?	Tumour Reactivity	Cancer Cell Reactivity
Concanavalin A (Con A)	*Canavalia ensiformis* (Jack bean)	α-Man[222]	-	Mitogenic to T-lymphocytes,[223] pro-apoptotic,[224] pro-autophagic[225]	Yes all types (weakly)[226]	Breast cancer biopsies[227]	MCF-7, BT-20, MDA-MB 157, ALAB-496, SK-BR-3 breast cancer cells[228]
Mistletoe lectin 1 (ML-1)	*Viscum album* (Mistletoe)	terminal Neu5Acα2-6Gal1-4GlcNAc- [186]	-	Toxic A chain,[185] activates natural-killer cells[190]	Yes all types[191]	Clinically effective for a number of cancer[183]	-
Maackia amurensis lectin (MAL)	*Maackia amurensis* (Amur maackia tree)	terminal α2,3-Neu-*O*-ser/thr[192]	-	Inhibition of cell growth and metastasis[192]	Yes all types (weakly)[229]	-	B16 melanoma cells,[192] BW5147 lymphoma cells,[229] Ehrlich ascites tumour cells[229]
Griffonia simplicifolia lectin II (GSL-II)	*Griffonia simplicifolia* (African legume)	α-/β-GlcNAc[194]	TK antigen[194]	-	No[193]	Colon carcinoma resections[194]	-
Ulex europeaus agglutinin I (UEA-I)	*Ulex europeaus* (Gorse seed)	α1,2-Fuc[194]	H antigen[194]	-	Yes type O[197]	Colon carcinoma resections[196]	-
Helix pomatia agglutinin (HPA)	*Helix pomatia* (Roman snail)	terminal GalNAc-[198]	(T antigen, Tn antigen)[199,200]	-	Yes, type A[198]	Malignant melanoma[206]	MCF-7, MDA-MB-231 breast cancer cells; HT-29, Caco-2, HTC-116 colon cancer cells[201-204]

Lectin	Species	Carbohydrate Specificity	Tumour Antigen	Biomodulatory Effects	Agglutinates Human Erythrocytes?	Tumour Reactivity	Cancer Cell Reactivity
Vicia villosa lectin (VVL)	*Vicia villosa* (Hairy Vetch)	GalNAc-α-*O*-ser/thr[207]	Tn antigen[207]	-	Yes all types[209]	Colon carcinoma resections[171]	Caco-2 colon cancer cells[208]
Erythrina cristagalli lectin (ECL)	*Erythrina cristagalli* (Flowering Coral tree)	Galβ-1,4GlcNAc-[210]	Type II antigen[210]	-	Yes all types[210,211]	Colon carcinoma resections[211]	Caco-2 colon cancer cells[208]
Peanut agglutinin (PNA)	*Arachis hypogaea* (Peanuts)	Galβ-1,3GalNAc-α-*O*-ser/thr[212]	T antigen[212]	Stimulates proliferation[216-218]	No[213]	*In vivo* colorectal tumour model[230]	MCF-7, MDA-MB-231 breast cancer cells; HT-29, SW837, HCT-15 and LoVo colon cancer cells[216-218]
Amaranthin	*Amaranthus caudatus* (Flower)	Galβ-1,3GalNAc-α-*O*-ser/thr, sialyl-Galβ-1,3GalNAc-α-*O*-ser/thr[219]	T antigen, sialyl-T antigen[219]	Stimulates proliferation[219]	Yes all types[220]	-	HT-29 colon cancer cells[219]
Jacalin	*Artocrapus integrifolia* (Jackfruit)	Galβ-1,3GalNAc-α-*O*-ser/thr[231]	T antigen[231]	Inhibits proliferation[219]	Yes type B>type A[232]	Cancerous and precancerous colonic carcinoma resections[233]	Caco-2 and HT-29 colon cancer cells[208,219]
Agaricus bisporus lectin (ABL)	*Agaricus bisporus* (Edible Mushroom)	Galβ-1,3GalNAc-α-*O*-ser/thr, sialyl-Galβ-1,3GalNAc-α-*O*-ser/thr[216]	T antigen, sialyl-T antigen[216]	Inhibits proliferation[216]	Yes all types[221]	-	Caco-2 and HT-29 colon cancer cells; MCF-7 breast cancer cells[216]

A number of nanoparticles have been used as potential oral drug delivery agents when functionalised with lectins such as wheat germ agglutinin (WGA)[234] and tomato lectin,[235] which target them to intestinal tissue to enhance drug uptake.[236,237] WGA has also been used to target liposomes carrying Foscan® for antimicrobial PDT.[238] Some lectin-functionalised nanoparticles have been used to target drugs to the brain[239] and lungs,[240] while other lectin-nanoparticle systems, such as gold nanoparticle conjugates[241] and quantum dot conjugates,[242] have been used for a variety of imaging techniques.[242-244] Lectins have also been used to monitor carbohydrate expression at the surface of live cells when conjugated to carbon nanotube electrochemical sensors.[245] Fluorescently labelled nanospheres functionalised with PNA have also been used to detect orthotopically implanted colorectal tumours expressing the T antigen.[230]

Owing to their exquisite specificity for a variety of cancer-associated carbohydrate antigens, the lectins described herein are suggested to be powerful prospective cancer targeting ligands. Although some lectins exhibit haemagglutinating activity above specific concentrations, topical application or intraperitoneal administration[246,247] of these lectins conjugated to drugs may still prove to be of therapeutic value. The specificity of lectins towards cancer cells, in addition to the remarkable biological effects that lectins can exert, such as apoptosis induction, inhibition of proliferation and immunomodulation, make lectins attractive multifunctional candidates for the targeted therapy of cancer.

1.4 Thesis outline

This thesis contains a number of experiments that demonstrate the efficacy of using a lectin, such as jacalin, for the targeted delivery of phthalocyanine-gold nanoparticles to cancer cells expressing tumour-associated glycans for enhanced PDT treatment. Titanium dioxide nanoparticles are also explored as potential platforms for sonodynamic therapy, which can increase ROS production upon exposure to ultrasound.

A detailed description of the materials, reagents, instrumentation and experimental procedures performed throughout the thesis is included in **Chapter 2**. In **Chapter 3**, the lectin Concanavalin A (Con A) and its dimeric succinylated derivative are explored as potential targeting ligands for PDT. Initially, the interactions between Con A and succinyl-Con A gold nanoparticle conjugates with SK-BR-3 and MCF-7 breast cancer cells are investigated using optical microscopy. The adhesion of MCF-7 breast cancer cells to Con A

and succinyl-Con A is also assessed using a colorimetric bioassay. Con A is then used to attempt the targeted PDT treatment of MCF-7 cells with Con A functionalised gold nanoparticles carrying a zinc phthalocyanine photosensitiser.

An alternative synthetic procedure for preparing zinc phthalocyanine gold nanoparticles with a higher sensitiser loading efficiency is described in **Chapter 4**. Jacalin is then used to functionalise the nanoparticles and the targeted PDT treatment of HT-29 colon cancer cells expressing the T antigen is attempted. Laser scanning confocal microscopy is used to explore the intracellular uptake of the jacalin nanoparticle conjugates. Investigations into the carbohydrate dependence of jacalin targeted PDT are also performed. Furthermore, the mechanism of jacalin targeted phototoxicity of the HT-29 cells is determined.

A comparative study into the efficacy of jacalin and anti-HER-2 antibody targeted PDT is detailed in **Chapter 5**. The enhanced phototoxicity of the nanoparticle conjugates in SK-BR-3 breast cancer cells and in HT-29 colon cancer cells is investigated. Using both types of nanoparticle conjugates, the mechanisms of the targeted phototoxicity in both cell lines are explored. Finally, the intracellular fate of the targeted nanoparticle conjugates is examined using laser scanning confocal microscopy and lysosomal colocalisation analysis.

In **Chapter 6**, the potential of using titanium dioxide nanoparticles capped with polyacrylic acid for sonodynamic therapy of HT-29 colon cancer cells is discussed. The synthesis and characterisation of stable titanium dioxide nanoparticles is described. A number of experiments are performed to probe the sonocatalytic enhancement of ROS generation by the nanoparticles. *In vitro* sonodynamic therapy of HT-29 cells using the titanium dioxide nanoparticles is attempted and the outcome of the treatment is discussed.

Conclusions of the findings for all the experiments within the thesis are provided in **Chapter 7** together with detailed suggestions for future experiments.

1.5 References

1. Dougherty, T. J.; Gomer, C. J.; Henderson, B. W.; Jori, G.; Kessel, D.; Korbelik, M.; Moan, J.; Peng, Q. *J. Natl. Cancer Inst.* **1998**, *90*, 889-905.
2. Buchardt, O. *Photochemistry of heterocyclic compounds*; John Wiley & Sons Inc., **1976**.
3. Ochsner, M. *J. Photochem. Photobiol., B* **1997**, *39*, 1-18.
4. Dexter, D. L. *J. Chem. Phys.* **1953**, *21*, 836-850.
5. Agostinis, P.; Berg, K.; Cengel, K. A.; Foster, T. H.; Girotti, A. W.; Gollnick, S. O.; Hahn, S. M.; Hamblin, M. R.; Juzeniene, A.; Kessel, D.; Korbelik, M.; Moan, J.; Mroz, P.; Nowis, D.; Piette, J.; Wilson, B. C.; Golab, J. *CA-Cancer J. Clin.* **2011**, *61*, 250-281.
6. Mroz, P.; Yaroslavsky, A.; Kharkwal, G. B.; Hamblin, M. R. *Cancers* **2011**, *3*, 2516-2539.
7. Kessel, D.; Luo, Y. *J. Photochem. Photobiol., B* **1998**, *42*, 89-95.
8. Coupienne, I.; Fettweis, G.; Rubio, N.; Agostinis, P.; Piette, J. *Photochem. Photobiol. Sci.* **2011**, *10*, 1868-1878.
9. Nelson, J. S.; Liaw, L. H.; Orenstein, A.; Roberts, W. G.; Berns, M. W. *J. Natl. Cancer Inst.* **1988**, *80*, 1599-1605.
10. Mroz, P.; Hashmi, J. T.; Huang, Y. Y.; Lange, N.; Hamblin, M. R. *Expert Rev. Clin. Immunol.* **2011**, *7*, 75-91.
11. Sessler, J. L.; Miller, R. A. *Biochem. Pharmacol.* **2000**, *59*, 733-739.
12. Allison, R. R.; Sibata, C. H. *Photodiagn. Photodyn. Ther.* **2010**, *7*, 61-75.
13. MacDonald, I. J.; Dougherty, T. J. *J. Porphyrins Phthalocyanines* **2001**, *5*, 105-129.
14. Allison, R. R.; Downie, G. H.; Cuenca, R.; Hu, X. H.; Childs, C. J. H.; Sibata, C. H. *Photodiagn. Photodyn. Ther.* **2004**, *1*, 27-42.
15. Overholt, B. F.; Lightdale, C. J.; Wang, K. K.; Canto, M. I.; Burdick, S.; Haggitt, R. C.; Bronner, M. P.; Taylor, S. L.; Grace, M. G. A.; Depot, M. *Gastrointest. Endosc.* **2005**, *62*, 488-498.
16. Lightdale, C. J.; Heier, S. K.; Marcon, N. E.; Mccaughan, J. S.; Gerdes, H.; Overholt, B. F.; Sivak, M. V.; Stiegmann, G. V.; Nava, H. R. *Gastrointest. Endosc.* **1995**, *42*, 507-512.
17. Loewen, G. M.; Pandey, R.; Bellnier, D.; Henderson, B.; Dougherty, T. *Lasers Surg. Med.* **2006**, *38*, 364-370.
18. Allison, R.; Moghissi, K.; Downie, G.; Dixon, K. *Photodiagn. Photodyn. Ther.* **2011**, *8*, 231-239.

19. Wachowska, M.; Muchowicz, A.; Firczuk, M.; Gabrysiak, M.; Winiarska, M.; Wańczyk, M.; Bojarczuk, K.; Golab, J. *Molecules* **2011**, *16*, 4140-4164.
20. Kelty, C. J.; Brown, N. J.; Reed, M. W. R.; Ackroyd, R. *Photochem. Photobiol. Sci.* **2002**, *1*, 158-168.
21. Otake, M.; Nishiwaki, M.; Kobayashi, Y.; Baba, S.; Kohno, E.; Kawasaki, T.; Fujise, Y.; Nakamura, H. *Br. J. Cancer* **2003**, *89*, 730-736.
22. Abels, C.; Heil, P.; Dellian, M.; Kuhnle, G. E.; Baumgartner, R.; Goetz, A. E. *Br. J. Cancer* **1994**, *70*, 826-833.
23. Millon, S. R.; Ostrander, J. H.; Yazdanfar, S.; Brown, J. Q.; Bender, J. E.; Rajeha, A.; Ramanujam, N. *J. Biomed. Opt.* **2010**, *15*, 018002.
24. Kurwa, H. A.; Yong-Gee, S. A.; Seed, P. T.; Markey, A. C.; Barlow, R. J. *J. Am. Acad. Dermatol.* **1999**, *41*, 414-418.
25. Gold, M. H. *Lasers Med. Sci.* **2007**, *22*, 67-72.
26. Gold, M. H. *Photodynamic Therapy in Dermatology*; Springer New York, 2011.
27. Donnelly, R. F.; McCarron, P. A.; Woolfson, A. D. *Perspect. Med. Chem.* **2008**, *1*, 49-63.
28. Bonnett, R. *Chem. Soc. Rev.* **1995**, *24*, 19-33.
29. Zhu, T. C.; Finlay, J. C.; Hahn, S. M. *J. Photochem. Photobiol., B* **2005**, *79*, 231-241.
30. Patel, H.; Mick, R.; Finlay, J.; Zhu, T. C.; Rickter, E.; Cengel, K. A.; Malkowicz, S. B.; Hahn, S. M.; Busch, T. M. *Clin. Cancer Res.* **2008**, *14*, 4869-4876.
31. Young, S. W.; Woodburn, K. W.; Wright, M.; Mody, T. D.; Fan, Q.; Sessler, J. L.; Dow, W. C.; Miller, R. A. *Photochem. Photobiol.* **1996**, *63*, 892-897.
32. Dimofte, A.; Zhu, T. C.; Hahn, S. M.; Lustig, R. A. *Lasers Surg. Med.* **2002**, *31*, 305-312.
33. Thomas, S. R.; Khuntia, D. *Int. J. Nanomed.* **2007**, *2*, 79-87.
34. Bonnett, R.; White, R. D.; Winfield, U. J.; Berenbaum, M. C. *Biochem. J.* **1989**, *261*, 277-280.
35. Senge, M. O.; Brandt, J. C. *Photochem. Photobiol.* **2011**, *87*, 1240-1296.
36. Senge, M. O. *Photodiagn. Photodyn. Ther.* **2012**, *9*, 170-179.
37. Allen, C. M.; Sharman, W. M.; Van Lier, J. E. *J. Porphyrins Phthalocyanines* **2001**, *5*, 161-169.
38. Boyle, R. W.; Leznoff, C. C.; Van Lier, J. E. *Br. J. Cancer* **1993**, *67*, 1177-1181.
39. Wagner, J. R.; Ali, H.; Langlois, R.; Brasseur, N.; Van Lier, J. E. *Photochem. Photobiol.* **1987**, *45*, 587-594.
40. Berg, K.; Bommer, J. C.; Moan, J. *Photochem. Photobiol.* **1989**, *49*, 587-594.

41. Boyle, R. W.; Dolphin, D. *Photochem. Photobiol.* **1996**, *64*, 469-485.
42. Peng, Q.; Moan, J.; Nesland, J. M.; Rimington, C. *Int. J. Cancer* **1990**, *46*, 719-726.
43. Ginevra, F.; Biffanti, S.; Pagnan, A.; Biolo, R.; Reddi, E.; Jori, G. *Cancer Lett.* **1990**, *49*, 59-65.
44. Shopova, M.; Stoichkov, N.; Milev, A.; Peev, M.; Georgiev, K.; Gizbreht, A.; Jori, G.; Ricchelli, F. *Lasers Med. Sci* **1995**, *10*, 43-46.
45. Fabris, C.; Ometto, C.; Milanesi, C.; Jori, G.; Cook, M. J.; Russell, D. A. *J. Photochem. Photobiol., B* **1997**, *39*, 279-284.
46. Allemann, E.; Brasseur, N.; Kudrevich, S. V.; La Madeleine, C.; Van Lier, J. E. *Int. J. Cancer* **1997**, *72*, 289-294.
47. Polo, L.; Valduga, G.; Jori, G.; Reddi, E. *Int. J. Biochem. Cell. Biol.* **2002**, *34*, 10-23.
48. Sokolov, V. V.; Chissov, V. I.; Filonenko, E. V.; Yakubovskaya, R. I.; Sukhin, D. G.; Galpern, M. G.; Vorozhtsov, G. N.; Gulin, A. V.; Zhitkova, M. B.; Zharkova, N. N.; Kozlov, D. N.; Smirnov, V. V. *Proc. SPIE* **1995**, *2325*, 364-366.
49. Filonenko, E. V.; Sokolov, V. V.; Chissov, V. I.; Lukyanets, E. A.; Vorozhtsov, G. N. *Photodiagn. Photodyn. Ther.* **2008**, *5*, 187-190.
50. Trushina, O. I.; Novikova, E. G.; Sokolov, V. V.; Filonenko, E. V.; Chissov, V. I.; Vorozhtsov, G. N. *Photodiagn. Photodyn. Ther.* **2008**, *5*, 256-259.
51. Sokolov, V. V.; Chissov, V. I.; Yakubovskya, R. I.; Aristarkhova, E. I.; Filonenko, E. V.; Belous, T. A.; Vorozhtsov, G. N.; Zharkova, N. N.; Smirnov, V. V.; Zhitkova, M. B. *Proc. SPIE* **1996**, *2625*, 281-287.
52. Baron, E. D.; Hanneman, K.; Scull, H. M.; Hsia, A.; McCormick, T.; Oleinick, N. L.; Kenney, M.; Cooper, K. D. *J. Invest. Dermatol.* **2005**, *125*, A7-A7.
53. Baron, E. D.; Malbasa, C. L.; Santo-Domingo, D.; Fu, P. F.; Miller, J. D.; Hanneman, K. K.; Hsia, A. H.; Oleinick, N. L.; Colussi, V. C.; Cooper, K. D. *Lasers Surg. Med.* **2010**, *42*, 728-735.
54. Miller, J. D.; Nancy, O.; Scull, H. M.; Hsia, A.; Cooper, K. D.; Baron, E. D. *J. Invest. Dermatol.* **2006**, *126*, 46-46.
55. Burda, C.; Chen, X. B.; Narayanan, R.; El-Sayed, M. A. *Chem. Rev.* **2005**, *105*, 1025-1102.
56. Davis, M. E.; Chen, Z. G.; Shin, D. M. *Nat. Rev. Drug Discovery* **2008**, *7*, 771-782.
57. Brigger, I.; Dubernet, C.; Couvreur, P. *Adv. Drug Delivery Rev.* **2002**, *54*, 631-651.
58. Maeda, H.; Fang, J.; Inutsuka, T.; Kitamoto, Y. *Int. Immunopharmacol.* **2003**, *3*, 319-328.
59. Paciotti, G. F.; Kingston, D. G. I.; Tamarkin, L. *Drug Dev. Res.* **2006**, *67*, 47-54.

60. Sinha, R.; Kim, G. J.; Nie, S.; Shin, D. M. *Mol. Cancer Ther.* **2006**, *5*, 1909-1917.
61. Bechet, D.; Couleaud, P.; Frochot, C.; Viriot, M. L.; Guillemin, F.; Barberi-Heyob, M. *Trends Biotechnol.* **2008**, *26*, 612-621.
62. Kelkar, S. S.; Reineke, T. M. *Bioconjugate Chem.* **2011**, *22*, 1879-1903.
63. Daniel, M. C.; Astruc, D. *Chem. Rev.* **2004**, *104*, 293-346.
64. Hone, D. C.; Walker, P. I.; Evans-Gowing, R.; FitzGerald, S.; Beeby, A.; Chambrier, I.; Cook, M. J.; Russell, D. A. *Langmuir* **2002**, *18*, 2985-2987.
65. Wieder, M. E.; Hone, D. C.; Cook, M. J.; Handsley, M. M.; Gavrilovic, J.; Russell, D. A. *Photochem. Photobiol. Sci.* **2006**, *5*, 727-734.
66. Camerin, M.; Magaraggia, M.; Soncin, M.; Jori, G.; Moreno, M.; Chambrier, I.; Cook, M. J.; Russell, D. A. *Eur. J. Cancer* **2010**, *46*, 1910-1918.
67. Stuchinskaya, T.; Moreno, M.; Cook, M. J.; Edwards, D. R.; Russell, D. A. *Photochem. Photobiol. Sci.* **2011**, *10*, 822-831.
68. Obaid, G.; Chambrier, I.; Cook, M. J.; Russell, D. A. *Angew. Chem. Int. Ed.* **2012**, *51*, 6158-6162.
69. Cheng, Y.; Meyers, J. D.; Broome, A. M.; Kenney, M. E.; Basilion, J. P.; Burda, C. *J. Am. Chem. Soc.* **2011**, *133*, 2583-2591.
70. Jokerst, J. V.; Lobovkina, T.; Zare, R. N.; Gambhir, S. S. *Nanomedicine* **2011**, *6*, 715-728.
71. Prencipe, G.; Tabakman, S. M.; Welsher, K.; Liu, Z.; Goodwin, A. P.; Zhang, L.; Henry, J.; Dai, H. *J. Am. Chem. Soc.* **2009**, *131*, 4783-4787.
72. Yang, S. T.; Fernando, K. A.; Liu, J. H.; Wang, J.; Sun, H. F.; Liu, Y.; Chen, M.; Huang, Y.; Wang, X.; Wang, H.; Sun, Y. P. *Small* **2008**, *4*, 940-944.
73. Záruba, K.; Králová, J.; Řezanka, P.; Poučková, P.; Veverková, L.; Král, V. *Org. Biomol. Chem.* **2010**, *8*, 3202-3206.
74. Gamaleia, N. F.; Shishko, E. D.; Dolinsky, G. A.; Shcherbakov, A. B.; Usatenko, A. V.; Kholin, V. V. *Exp. Oncol.* **2010**, *32*, 44-47.
75. Jang, B.; Park, J. Y.; Tung, C. H.; Kim, I. H.; Choi, Y. *ACS Nano* **2011**, *5*, 1086-1094.
76. Gao, L.; Fei, J.; Zhao, J.; Li, H.; Cui, Y.; Li, J. *ACS Nano* **2012**, *6*, 8030-8040.
77. Fales, A. M.; Yuan, H.; Vo-Dinh, T. *Langmuir* **2011**, *27*, 12186-12190.
78. Misawa, M.; Takahashi, J. *Nanomedicine* **2011**, *7*, 604-614.
79. Couleaud, P.; Morosini, V.; Frochot, C.; Richeter, S.; Raehm, L.; Durand, J. O. *Nanoscale* **2010**, *2*, 1083-1095.
80. Roy, I.; Ohulchanskyy, T. Y.; Pudavar, H. E.; Bergey, E. J.; Oseroff, A. R.; Morgan, J.; Dougherty, T. J.; Prasad, P. N. *J. Am. Chem. Soc.* **2003**, *125*, 7860-7865.

81. Ohulchanskyy, T. Y.; Roy, I.; Goswami, L. N.; Chen, Y.; Bergey, E. J.; Pandey, R. K.; Oseroff, A. R.; Prasad, P. N. *Nano Lett.* **2007**, *7*, 2835-2842.
82. Kim, S.; Ohulchanskyy, T. Y.; Bharali, D.; Chen, Y.; Pandey, R. K.; Prasad, P. N. *J. Phys. Chem. C* **2009**, *113*, 12641-12644.
83. Rossi, L. M.; Silva, P. R.; Vono, L. L.; Fernandes, A. U.; Tada, D. B.; Baptista, M. S. *Langmuir* **2008**, *24*, 12534-12538.
84. Zhang, R.; Wu, C.; Tong, L.; Tang, B.; Xu, Q.-H. *Langmuir* **2009**, *25*, 10153-10158.
85. Zhang, R.; Wu, C.; Tong, L.; Tang, B.; Xu, Q.-H. *Langmuir* **2009**, *25*, 10153-10158.
86. Li, Z.; Wang, J.; Chen, J.; Lei, W.; Wang, X.; Zhang, B. *Nanotechnology* **2010**, *21*, 115102.
87. Simon, V.; Devaux, C.; Darmon, A.; Donnet, T.; Thienot, E.; Germain, M.; Honnorat, J.; Duval, A.; Pottier, A.; Borghi, E.; Levy, L.; Marill, J. *Photochem. Photobiol.* **2010**, *86*, 213-222.
88. Brevet, D.; Gary-Bobo, M.; Raehm, L.; Richeter, S.; Hocine, O.; Amro, K.; Loock, B.; Couleaud, P.; Frochot, C.; Morére, A.; Maillard, P.; Garcia, M.; Durand, J.-O. *Chem. Commun.* **2009**, 1475-1477.
89. Gary-Bobo, M.; Mir, Y.; Rouxel, C.; Brevet, D.; Basile, I.; Maynadier, M.; Vaillant, O.; Mongin, O.; Blanchard-Desce, M.; Morère, A.; Garcia, M.; Durand, J.-O.; Raehm, L. *Angew. Chem. Int. Ed.* **2011**, *50*, 11425-11429.
90. Barth, B. M.; Altinoğlu, E. I.; Shanmugavelandy, S. S.; Kaiser, J. M.; Crespo-Gonzalez, D.; DiVittore, N. A.; McGovern, C.; Goff, T. M.; Keasey, N. R.; Adair, J. H.; Loughran, T. P.; Claxton, D. F.; Kester, M. *ACS Nano* **2011**, *5*, 5325-5337.
91. Cheng, S. H.; Lee, C. H.; Chen, M. C.; Souris, J. S.; Tseng, F. G.; Yang, C. S.; Mou, C. Y.; Chen, C. T.; Lo, L. W. *J. Mater. Chem.* **2010**, *20*, 6149-6157.
92. Kumar, R.; Roy, I.; Ohulchanskky, T. Y.; Vathy, L. A.; Bergey, E. J.; Sajjad, M.; Prasad, P. N. *ACS Nano* **2010**, *4*, 699-708.
93. Chen, M.; von Mikecz, A. *Exp. Cell Res.* **2005**, *305*, 51-62.
94. Nishimori, H.; Kondoh, M.; Isoda, K.; Tsunoda, S.; Tsutsumi, Y.; Yagi, K. *Eur. J. Pharm. Biopharm.* **2009**, *72*, 496-501.
95. Qin, M.; Hah, H. J.; Kim, G.; Nie, G.; Lee, Y. E.; Kopelman, R. *Photochem. Photobiol. Sci.* **2011**, *10*, 832-841.
96. Bae, B. C.; Na, K. *Int. J. Photoenergy* **2012**, *2012*.
97. Tian, L.; Bae, Y. H. *Colloids Surf., B* **2012**, *99*, 116-126.
98. Labib, A.; Lenaerts, V.; Chouinard, F.; Leroux, J. C.; Ouellet, R.; Van Lier, J. E. *Pharm. Res.* **1991**, *8*, 1027-1031.

99. McCarthy, J. R.; Perez, J. M.; Bruckner, C.; Weissleder, R. *Nano Lett.* **2005**, *5*, 2552-2556.
100. Khdair, A.; Handa, H.; Mao, G.; Panyam, J. *Eur. J. Pharm. Biopharm.* **2010**, *71*, 214-222.
101. Conte, C.; Ungaro, F.; Maglio, G.; Tirino, P.; Siracusano, G.; Sciortino, M. T.; Leone, N.; Palma, G.; Barbieri, A.; Arra, C.; Mazzaglia, A.; Quaglia, F. *J. Controlled Release* **2013**, http://dx.doi.org/10.1016/j.jconrel.2012.1012.1026.
102. Tang, W.; Xu, H.; Kopelman, R.; Philbert, M. A. *Photochem. Photobiol.* **2005**, *81*, 242-249.
103. Li, P.; Zhou, G.; Zhu, X.; Li, G.; Yan, P.; Shen, L.; Xu, Q.; Hamblin, M. R. *Photochem. Photobiol. Sci.* **2012**, *9*, 76-82.
104. Rai, P.; Chang, S. K.; Mai, Z.; Neuman, D.; Hasan, T. *Proc. SPIE* **2009**, 73800W.
105. Kuruppuarachchi, M.; Savoie, H.; Lowry, A.; Alonso, C.; Boyle, R. W. *Mol. Pharm.* **2011**, *8*, 920-931.
106. Shubayev, V. I.; Pisanic Ii, T. R.; Jin, S. *Adv. Drug Delivery Rev.* **2009**, *61*, 467-477.
107. Oliveira, D. M.; Macaroff, P. P.; Ribeiro, K. F.; Lacava, Z. G. M.; Azevedo, R. B.; Lima, E. C. D.; Morais, P. C.; Tedesco, A. C. *J. Magn. Magn. Mater.* **2005**, *289*, 476-479.
108. MacAroff, P. P.; Oliveira, D. M.; Lacava, Z. G. M.; Lima, E. C. D.; Morais, P. C.; Tedesco, A. C. *J. Appl. Phys.* **2005**, *97*.
109. Macaroff, P. P.; Oliveira, D. M.; Ribeiro, K. F.; Lacava, Z. G. M.; Lima, E. C. D.; Morals, P. C.; Tedesco, A. C. *IEEE Trans. Magn.* **2005**, *41*, 4105-4107.
110. Park, S. I.; Hwang, Y. H.; Lim, J. H.; Kim, J. H.; Yun, H. I.; Kim, C. O. *J. Magn. Magn. Mater.* **2006**, *304*, e403-e405.
111. Kopelman, R.; Koo, Y.-E. L.; Philbert, M.; Moffat, B. A.; Reddy, G. R.; McConville, P.; Hall, D. E.; Chenevert, T. L.; Bhojani, M. S.; Buck, S. M.; Rehemtulla, A.; Ross, B. D. *J. Magn. Magn. Mater.* **2005**, *293*, 404-410.
112. Gu, H.; Xu, K.; Yang, Z.; Chang, C. K.; Xu, B. *Chem. Commun.* **2005**, , 4270-4272.
113. Cinteza, L. O.; Ohulchanskyy, T. Y.; Sahoo, Y.; Bergey, E. J.; Pandey, R. K.; Prasad, P. N. *Mol. Pharm.* **2006**, *3*, 415-423.
114. Sun, Y.; Chen, Z.-l.; Yang, X.-x.; Huang, P.; Zhou, X.-p.; Du, X.-x. *Nanotechnology* **2009**, *20*, 135102.
115. Huang, P.; Li, Z.; Lin, J.; Yang, D.; Gao, G.; Xu, C.; Bao, L.; Zhang, C.; Wang, K.; Song, H.; Hu, H.; Cui, D. *Biomaterials* **2011**, *32*, 3447-3458.

116. Schladt, T. D.; Schneider, K.; Shukoor, M. I.; Natalio, F.; Bauer, H.; Tahir, M. N.; Weber, S.; Schreiber, L. M.; Schroder, H. C.; Muller, W. E. G.; Tremel, W. *J. Mater. Chem.* **2010**, *20*, 8297-8304.
117. Sevè, A.; Couleaud, P.; Lux, F.; Tillement, O.; Arnoux, P.; Andre, J. C.; Frochot, C. *Photochem. Photobiol. Sci.* **2012**.
118. Chen, X.; Mao, S. S. *Chem. Rev.* **2007**, *107*, 2891-2959.
119. Cai, R.; Kubota, Y.; Shuin, T.; Sakai, H.; Hashimoto, K.; Fujishima, A. *Cancer Res.* **1992**, *52*, 2346-2348.
120. Liu, L.; Miao, P.; Xu, Y.; Tian, Z.; Zou, Z.; Li, G. *J. Photochem. Photobiol., B* **2010**, *98*, 207-210.
121. Wang, C.; Cao, S.; Tie, X.; Qiu, B.; Wu, A.; Zheng, Z. *Mol. Biol. Rep.* **2011**, *38*, 523-530.
122. Du, L.; Furube, A.; Hara, K.; Katoh, R.; Tachiya, M. *Thin Solid Films* **2009**, *518*, 861-864.
123. Townley, H. E.; Kim, J.; Dobson, P. J. *Nanoscale* **2012**, *4*, 5043-5050.
124. Huang, K. Q.; Chen, L.; Deng, J. G.; Xiong, J. W. *J. Nanomater.* **2012**.
125. Xu, J.; Sun, Y.; Huang, J.; Chen, C.; Liu, G.; Jiang, Y.; Zhao, Y.; Jiang, Z. *Bioelectrochemistry* **2007**, *71*, 217-222.
126. Rozhkova, E. A.; Ulasov, I.; Lai, B.; Dimitrijevic, N. M.; Lesniak, M. S.; Rajh, T. *Nano Lett.* **2009**, *9*, 3337-3342.
127. Li, J.; Guo, D.; Wang, X.; Wang, H.; Jiang, H.; Chen, B. *Nanoscale Res. Lett.* **2010**, *5*, 1063-1071.
128. Liu, Y.; Zhang, Y.; Wang, S.; Pope, C.; Chen, W. *Appl. Phys. Lett.* **2008**, *92*, 143901-143903.
129. Schilling, K.; Bradford, B.; Castelli, D.; Dufour, E.; Nash, J. F.; Pape, W.; Schulte, S.; Tooley, I.; van den Bosch, J.; Schellauf, F. *Photochem. Photobiol. Sci.* **2010**, *9*, 495-509.
130. Alivisatos, A. P. *Science* **1996**, *271*, 933-937.
131. Derfus, A. M.; Chan, W. C. W.; Bhatia, S. N. *Nano Lett.* **2004**, *4*, 11-18.
132. Charron, G.; Stuchinskaya, T.; Edwards, D. R.; Russell, D. A.; Nann, T. *J. Phys. Chem. C* **2012**, *116*, 9334-9342.
133. Chen, J. Y.; Lee, Y. M.; Zhao, D.; Mak, N. K.; Wong, R. N.; Chan, W. H.; Cheung, N. H. *Photochem. Photobiol.* **2010**, *86*, 431-437.
134. Samia, A. C.; Chen, X.; Burda, C. *J. Am. Chem. Soc.* **2003**, *125*, 15736-15737.
135. Shi, L.; Hernandez, B.; Selke, M. *J. Am. Chem. Soc.* **2006**, *128*, 6278-6279.
136. Davila, J.; Harriman, A. *Photochem. Photobiol.* **1990**, *51*, 9-19.

137. Ma, J.; Chen, J. Y.; Idowu, M.; Nyokong, T. *J. Phys. Chem. B* **2008**, *112*, 4465-4469.
138. Juzenas, P.; Generalov, R.; Juzeniene, A.; Moan, J. *J. Biomed. Nanotechnol.* **2008**, *4*, 450-456.
139. Tekdas, D. A.; Durmus, M.; Yanik, H.; Ahsen, V. *Spectrochim. Acta, Part A* **2012**, *93*, 313-320.
140. Tsay, J. M.; Trzoss, M.; Shi, L.; Kong, X.; Selke, M.; Jung, M. E.; Weiss, S. *J. Am. Chem. Soc.* **2007**, *129*, 6865-6871.
141. Fowley, C.; Nomikou, N.; McHale, A. P.; McCarron, P. A.; McCaughan, B.; Callan, J. F. *J. Mater. Chem.* **2012**, *22*, 6456-6462.
142. Hsu, C.-Y.; Chen, C.-W.; Yu, H.-P.; Lin, Y.-F.; Lai, P.-S. *Biomaterials* **2013**, *34*, 1204-1212.
143. Morosini, V.; Bastogne, T.; Frochot, C.; Schneider, R.; Francois, A.; Guillemin, F.; Barberi-Heyob, M. *Photochem. Photobiol. Sci.* **2011**, *10*, 842-851.
144. Choi, H. S.; Liu, W.; Misra, P.; Tanaka, E.; Zimmer, J. P.; Itty Ipe, B.; Bawendi, M. G.; Frangioni, J. V. *Nat. Biotechnol.* **2007**, *25*, 1165-1170.
145. Chen, W.; Zhang, J. *J. Nanosci. Nanotechnol.* **2006**, *6*, 1159-1166.
146. Morgan, N. Y.; Kramer-Marek, G.; Smith, P. D.; Camphausen, K.; Capala, J. *Radiat. Res.* **2009**, *171*, 236-244.
147. Wang, X. X.; Zhang, Z. T.; Tang, Z. L.; Lin, Y. H. *Mater. Chem. Phys.* **2003**, *80*, 1-5.
148. Takahashi, J.; Misawa, M. *Nanobiotechnology* **2007**, *3*, 116-126.
149. Liu, Y.; Chen, W.; Wang, S.; Joly, A. G. *Appl. Phys. Lett.* **2008**, *92*, 43901-43903.
150. Wang, L.; Yang, W.; Read, P.; Larner, J.; Sheng, K. *Nanotechnology* **2010**, *21*, 475103.
151. Wang, C.; Cheng, L.; Liu, Z. *Ther. Delivery* **2011**, *2*, 1235-1239.
152. Zhang, P.; Steelant, W.; Kumar, M.; Scholfield, M. *J. Am. Chem. Soc.* **2007**, *129*, 4526-4527.
153. Chatterjee, D. K.; Yong, Z. *Nanomedicine* **2008**, *3*, 73-82.
154. Wang, C.; Tao, H. Q.; Cheng, L.; Liu, Z. *Biomaterials* **2011**, *32*, 6145-6154.
155. Park, Y. I.; Kim, H. M.; Kim, J. H.; Moon, K. C.; Yoo, B.; Lee, K. T.; Lee, N.; Choi, Y.; Park, W.; Ling, D.; Na, K.; Moon, W. K.; Choi, S. H.; Park, H. S.; Yoon, S. Y.; Suh, Y. D.; Lee, S. H.; Hyeon, T. *Adv Mater* **2012**, *24*, 5755-5761.
156. Idris, N. M.; Gnanasammandhan, M. K.; Zhang, J.; Ho, P. C.; Mahendran, R.; Zhang, Y. *Nat. Med.* **2012**, *18*, 1580-1585.
157. Liu, K.; Liu, X. M.; Zeng, Q. H.; Zhang, Y. L.; Tu, L. P.; Liu, T.; Kong, X. G.; Wang, Y. H.; Cao, F.; Lambrechts, S. A. G.; Aalders, M. C. G.; Zhang, H. *ACS Nano* **2012**, *6*, 4054-4062.

158. Zhou, A. G.; Wei, Y. C.; Wu, B. Y.; Chen, Q.; Xing, D. *Mol. Pharm.* **2012**, *9*, 1580-1589.
159. Cui, S. S.; Chen, H. Y.; Zhu, H. Y.; Tian, J. M.; Chi, X. M.; Qian, Z. Y.; Achilefu, S.; Gu, Y. Q. *J. Mater. Chem.* **2012**, *22*, 4861-4873.
160. Lindhorst, T. K. *Essentials of Carbohydrate Chemistry and Biochemistry*; 3rd ed.; Wiley-VCH, **2007**.
161. Aub, J. C.; Tieslau, C.; Lankester, A. *Proc. Natl. Acad. Sci. U. S. A.* **1963**, *50*, 613-619.
162. Aub, J. C.; Sanford, B. H.; Wang, L. H. *Proc. Natl. Acad. Sci. U. S. A.* **1965**, *54*, 400-402.
163. Dube, D. H.; Bertozzi, C. R. *Nat. Rev. Drug Discovery* **2005**, *4*, 477-488.
164. Alberts, B.; Johnson, A.; Lewis, J.; Raff, M.; Roberts, K.; Walter, P. *Molecular Biology of the Cell*; 4th ed.; Garland Science, **2002**.
165. Dennis, J. W.; Laferte, S.; Waghorne, C.; Breitman, M. L.; Kerbel, R. S. *Science* **1987**, *236*, 582-585.
166. Kim, Y. J.; Varki, A. *Glycoconjugate J.* **1997**, *14*, 569-576.
167. Springer, G. F. *Science* **1984**, *224*, 1198-1206.
168. Yu, L.-G. *Glycoconjugate J.* **2007**, *24*, 411-420.
169. Hounsell, E. F.; Lawson, A. M.; Feeney, J.; Gooi, H. C.; Pickering, N. J.; Stoll, M. S.; Lui, S. C.; Feizi, T. *Eur. J. Biochem.* **1985**, *148*, 367-377.
170. Glinsky, V. V.; Glinsky, G. V.; Rittenhouse-Olson, K.; Huflejt, M. E.; Glinskii, O. V.; Deutscher, S. L.; Quinn, T. P. *Cancer Res.* **2001**, *61*, 4851-4857.
171. Itzkowitz, S. H.; Yuan, M.; Montgomery, C. K.; Kjeldsen, T.; Takahashi, H. K.; Bigbee, W. L.; Kim, Y. S. *Cancer Res.* **1989**, *49*, 197-204.
172. Scott, J. K.; Loganathan, D.; Easley, R. B.; Gong, X.; Goldstein, I. J. *Proc. Natl. Acad. Sci. U. S. A.* **1992**, *89*, 5398-5402.
173. Goldstein, I. J.; Hollerman, C. E.; Smith, E. E. *Biochemistry* **1965**, *4*, 876-883.
174. Shimura, K.; Kasai, K. *Anal. Biochem.* **1995**, *227*, 186-194.
175. Nakamura-Tsuruta, S.; Kominami, J.; Kuno, A.; Hirabayashi, J. *Biochem. Biophys. Res. Commun.* **2006**, *347*, 215-220.
176. Sharon, N.; Lis, H. *Lectins*; 2nd ed.; Springer, **2003**.
177. Magnuson, J. A.; Alter, G. M.; Appel, D. M.; Christie, D. J.; Munske, G. R.; Pandolfino, E. R. *J. Biosci.* **1983**, *5*, 9-17.
178. Lis, H.; Sharon, N. *Annu. Rev. Biochem.* **1986**, *55*, 35-67.
179. Nitta, K. *Methods Enzymol.* **2001**, *341*, 368-374.
180. Nitta, K.; Ozaki, K.; Ishikawa, M.; Furusawa, S.; Hosono, M.; Kawauchi, H.; Sasaki, K.; Takayanagi, Y.; Tsuiki, S.; Hakomori, S. *Cancer Res.* **1994**, *54*, 920-927.

181. Loewus, F. A.; Ryan, C. A. *The Phytochemistry of Cell Recognition and Cell Surface Interactions*; Illustrated ed.; Plenum Press, **1981**.
182. Sharon, N.; Lis, H. *Glycobiology* **2004**, *14*, 53R-62R.
183. Zwierzina, H.; Bergmann, L.; Fiebig, H.; Aamdal, S.; Schoffski, P.; Witthohn, K.; Lentzen, H. *Eur. J. Cancer* **2011**, *47*, 1450-1457.
184. Kienle, G. S.; Kiene, H. *Integr. Cancer Ther.* **2010**, *9*, 142-157.
185. Franz, H. *Oncology* **1986**, *43*, 23-34.
186. Müthing, J.; Meisen, I.; Bulau, P.; Langer, M.; Witthohn, K.; Lentzen, H.; Neumann, U.; Peter-Katalinic, J. *Biochemistry* **2004**, *43*, 2996-3007.
187. Taki, T.; Yamamoto, K.; Takamatsu, M.; Ishii, K.; Myoga, A.; Sekiguchi, K.; Ikeda, I.; Kurata, K.; Nakayama, J.; Handa, S.; Matsumoto, M. *Cancer Res.* **1990**, *50*, 1284-1290.
188. Müthing, J.; Burg, M.; Mockel, B.; Langer, M.; Metelmann-Strupat, W.; Werner, A.; Neumann, U.; Peter-Katalinic, J.; Eck, J. *Glycobiology* **2002**, *12*, 485-497.
189. Bantel, H.; Engels, I. H.; Voelter, W.; Schulze-Osthoff, K.; Wesselborg, S. *Cancer Res.* **1999**, *59*, 2083-2090.
190. Hajto, T.; Hostanska, K.; Weber, K.; Zinke, H.; Fischer, J.; Mengs, U.; Lentzen, H.; Saller, R. *Nat. Immunol.* **1998**, *16*, 34-46.
191. Lyu, S. Y.; Park, W. B. *J. Biochem. Mol. Biol.* **2006**, *39*, 662-670.
192. Ochoa-Alvarez, J. A.; Krishnan, H.; Shen, Y.; Acharya, N. K.; Han, M.; McNulty, D. E.; Hasegawa, H.; Hyodo, T.; Senga, T.; Geng, J.-G.; Kosciuk, M.; Shin, S. S.; Goydos, J. S.; Temiakov, D.; Nagele, R. G.; Goldberg, G. S. *PLoS ONE* **2012**, *7*, e41845.
193. Goldstein, I. J.; Hayes, C. E.; Tipson, R. S.; Derek, H. *Adv. Carbohydr. Chem. Biochem.* **1978**, *Volume 35*, 127-340.
194. Rhodes, J. M.; Black, R. R.; Savage, A. *J. Clin. Pathol.* **1986**, *39*, 1331-1334.
195. Wintzer, G.; Uhlenbruck, G.; Steinhausen, G.; Carmann, H. *Experientia* **1978**, *34*, 255-256.
196. Yonezawa, S.; Nakamura, T.; Tanaka, S.; Sato, E. *J. Natl. Cancer Inst.* **1982**, *69*, 777-785.
197. Sudakevitz, D.; Imberty, A.; Gilboa-Garber, N. *J. Biochem.* **2002**, *132*, 353-358.
198. Hammarstrom, S. *Scand. J. Immunol.* **1973**, *2*, 53-66.
199. Sellei, J. *J. Immunogenet.* **1981**, *8*, 263-269.
200. Sanchez, J. F.; Lescar, J.; Chazalet, V.; Audfray, A.; Gagnon, J.; Alvarez, R.; Breton, C.; Imberty, A.; Mitchell, E. P. *J. Biol. Chem.* **2006**, *281*, 20171-20180.

201. Dwek, M. V.; Ross, H. A.; Streets, A. J.; Brooks, S. A.; Adam, E.; Titcomb, A.; Woodside, J. V.; Schumacher, U.; Leathem, A. J. *Int. J. Cancer* **2001**, *95*, 79-85.
202. Valentiner, U.; Hall, D. M.; Brooks, S. A.; Schumacher, U. *Cancer Lett.* **2005**, *219*, 233-242.
203. Schumacher, U.; Adam, E.; Flavell, D. J.; Boehm, D.; Brooks, S. A.; Leathem, A. J. *Clin. Exp. Metastasis* **1994**, *12*, 398-404.
204. de Albuquerque Garcia Redondo, P.; Nakamura, C. V.; de Souza, W.; Morgado-Diaz, J. A. *J. Histochem. Cytochem.* **2004**, *52*, 629-640.
205. Chen, S.; Zheng, T.; Shortreed, M. R.; Alexander, C.; Smith, L. M. *Anal. Chem.* **2007**, *79*, 5698-5702.
206. Thies, A.; Moll, I.; Berger, J.; Schumacher, U. *Br. J. Cancer* **2001**, *84*, 819-823.
207. Tollefsen, S. E.; Kornfeld, R. *J. Biol. Chem.* **1983**, *258*, 5172-5176.
208. Giannasca, K. T.; Giannasca, P. J.; Neutra, M. R. *Infect. Immun.* **1996**, *64*, 135-145.
209. Kaladas, P. M.; Kabat, E. A.; Kimura, A.; Ersson, B. *Mol. Immunol.* **1981**, *18*, 969-977.
210. Iglesias, J. L.; Lis, H.; Sharon, N. *Eur. J. Biochem.* **1982**, *123*, 247-252.
211. Baldus, S. E. *Int. J. Oncol.* **1996**, *9*, 43-48.
212. Campbell, B. J.; Finnie, I. A.; Hounsell, E. F.; Rhodes, J. M. *J. Clin. Invest.* **1995**, *95*, 571-576.
213. Lotan, R.; Skutelsky, E.; Danon, D.; Sharon, N. *J. Biol. Chem.* **1975**, *250*, 8518-8523.
214. Konska, G.; Vissac, C.; Zagla, K.; Chezet, F.; Vasson, M. P.; Bernard-Gallon, D.; Guillot, J. *Int. J. Oncol.* **2002**, *21*, 1009-1014.
215. Rak, J. W.; Basolo, F.; Elliott, J. W.; Russo, J.; Miller, F. R. *Cancer Lett.* **1991**, *57*, 27-36.
216. Yu, L.-G.; Fernig, D. G.; Smith, J. A.; Milton, J. D.; Rhodes, J. M. *Cancer Res.* **1993**, *53*, 4627-4632.
217. Kiss, R.; Camby, I.; Duckworth, C.; De Decker, R.; Salmon, I.; Pasteels, J. L.; Danguy, A.; Yeaton, P. *Gut* **1997**, *40*, 253-261.
218. Ryder, S. D.; Smith, J. A.; Rhodes, J. M. *J. Natl. Cancer Inst.* **1992**, *84*, 1410-1416.
219. Yu, L.-G.; Milton, J. D.; Fernig, D. G.; Rhodes, J. M. *J. Cell. Physiol.* **2001**, *186*, 282-287.
220. Rinderle, S. J.; Goldstein, I. J.; Matta, K. L.; Ratcliffe, R. M. *J. Biol. Chem.* **1989**, *264*, 16123-16131.
221. Presant, C. A.; Kornfeld, S. *J. Biol. Chem.* **1972**, *247*, 6937-6945.
222. Kussrow, A.; Kaltgrad, E.; Wolfenden, M. L.; Cloninger, M. J.; Finn, M. G.; Bornhop, D. J. *Anal. Chem.* **2009**, *81*, 4889-4897.

223. Liener, I. E.; Sharon, N.; Goldstein, I. J. *The Lectins: properties, functions, and applications in biology and medicine*; Academic Press, **1986**.
224. Liu, B.; Li, C. Y.; Bian, H. J.; Min, M. W.; Chen, L. F.; Bao, J. K. *Arch. Biochem. Biophys.* **2009**, *482*, 1-6.
225. Lei, H. Y.; Chang, C. P. *J. Biomed. Sci.* **2009**, *16*, 10.
226. Schnebli, H. P.; Roeder, C.; Tarcsay, L. *Exp. Cell Res.* **1976**, *98*, 273-276.
227. Furmanski, P.; Kirkland, W. L.; Gargala, T.; Rich, M. A. *Cancer Res.* **1981**, *41*, 4087-4092.
228. Voyles, B. A.; Kirkland, W. L.; Furmanski, P.; McGrath, C. M. *Cancer Res.* **1978**, *38*, 1578-1583.
229. Knibbs, R. N.; Goldstein, I. J.; Ratcliffe, R. M.; Shibuya, N. *J. Biol. Chem.* **1991**, *266*, 83-88.
230. Sakuma, S.; Yano, T.; Masaoka, Y.; Kataoka, M.; Hiwatari, K.; Tachikawa, H.; Shoji, Y.; Kimura, R.; Ma, H.; Yang, Z.; Tang, L.; Hoffman, R. M.; Yamashita, S. *Eur. J. Pharm. Biopharm.* **2010**, *74*, 451-460.
231. Sastry, M. V.; Banarjee, P.; Patanjali, S. R.; Swamy, M. J.; Swarnalatha, G. V.; Surolia, A. *J. Biol. Chem.* **1986**, *261*, 11726-11733.
232. Kabir, S. *Int. J. Biochem. Cell. Biol.* **1995**, *27*, 147-156.
233. Said, I. T.; Shamsuddin, A. M.; Sherief, M. A.; Taleb, S. G.; Aref, W. F.; Kumar, D. *Histol. Histopathol.* **1999**, *14*, 351-357.
234. Wang, C.; Ho, P. C.; Lim, L. Y. *Int. J. Pharm.* **2010**, *400*, 201-210.
235. Hussain, N.; Jani, P. U.; Florence, A. T. *Pharm. Res.* **1997**, *14*, 613-618.
236. Chowdary, K. P.; Rao, Y. S. *Biol. Pharm. Bull.* **2004**, *27*, 1717-1724.
237. Bies, C.; Lehr, C. M.; Woodley, J. F. *Adv. Drug Delivery Rev.* **2004**, *56*, 425-435.
238. Yang, K.; Gitter, B.; Rüger, R.; Albrecht, V.; Wieland, G. D.; Fahr, A. *Photochem. Photobiol.* **2011**, *88*, 548-556.
239. Liu, Q.; Shao, X.; Chen, J.; Shen, Y.; Feng, C.; Gao, X.; Zhao, Y.; Li, J.; Zhang, Q.; Jiang, X. *Toxicol. Appl. Pharmacol.* **2011**, *251*, 79-84.
240. Sharma, A.; Sharma, S.; Khuller, G. K. *J. Antimicrob. Chemother.* **2004**, *54*, 761-766.
241. Wang, J.; Liu, D.; Wang, Z. *Anal. Methods* **2011**, *3*, 1745-1751.
242. Gao, X.; Wang, T.; Wu, B.; Chen, J.; Yue, Y.; Dai, N.; Chen, H.; Jiang, X. *Biochem. Biophys. Res. Commun.* **2008**, *377*, 35-40.
243. Wang, J.; Duan, T.; Sun, L.; Liu, D.; Wang, Z. *Anal. Biochem.* **2009**, *392*, 77-82.
244. Madrid, J. F.; Leis, O.; Díaz-Flores, L.; Sáez, F. J.; Hernández, F. *J. Histochem. Cytochem.* **1998**, *46*, 1311-1320.

245. Xue, Y.; Bao, L.; Xiao, X.; Ding, L.; Lei, J.; Ju, H. *Anal. Biochem.* **2011**, *410*, 92-97.

246. Li, Y. R.; Liu, Q. H.; Wang, H. X.; Ng, T. B. *Biochim. Biophys. Acta, Gen. Subj.* **2008**, *1780*, 51-57.

247. Zhang, G.; Sun, J.; Wang, H.; Ng, T. B. *Phytomedicine* **2010**, *17*, 775-781.

Chapter 2

Materials and Methods

This chapter gives details of the materials, reagents, instrumentation and procedures used for the experiments described throughout the thesis.

2.1 Concanavalin A conjugated phthalocyanine-PEG gold nanoparticles for targeted PDT of MCF-7 and SK-BR-3 human breast adenocarcinoma cells

2.1.1 Synthesis of citrate capped gold nanoparticles

Aqueous solutions of trisodium citrate (50 ml, 1.3 mM, 258.06 $g.mol^{-1}$; Sigma-Aldrich) and gold (III) chloride trihydrate ($HAuCl_4$, 100 ml, 0.2 mM, 393.83 $g.mol^{-1}$; Sigma-Aldrich) were prepared. The solutions were heated to 60 °C, combined upon rigorous stirring and heated to 85 °C for 2.5 h. Once cooled to room temperature, the nanoparticle solution was filtered using sterile syringe driven filter units (0.22 μm polyethersulfone (PES), Millipore; Millex™) to remove aggregates and stored at 4 °C.

2.1.2 Conjugation of Concanavalin A and succinyl-Concanavalin A to gold nanoparticles through SPDP

3-(2-pyridyldithio)propionic acid *N*-hydroxysuccinimide ester (SPDP, 312.36 $g.mol^{-1}$; Thermo Scientific) was used to modify the lectins Concanavalin A (Con A, 104 kDa;[1] Sigma-Aldrich) and succinyl-Concanavalin A (S-Con A, 52 kDa; Vector Laboratories) with a disulfide group to allow self-assembly onto the surface of the gold nanoparticles. Conjugation of SPDP to the lectins was performed according to the protocol provided by Thermo Scientific (http://www.piercenet.com/instructions/2160279.pdf). Solutions of Con A and S-Con A (0.5 ml, 2 $mg.ml^{-1}$) were prepared in salt-free D-Hank's buffer (0.37 mM Na_2HPO_4 (Fisher Scientific), 0.44 mM KH_2PO_4 (Sigma-Aldrich), 4.20 mM $NaHCO_3$ (Fisher Scientific), pH 7.4).[2] A solution of SPDP (20 mM) in dimethyl sulfoxide (DMSO; Fisher Scientific) was prepared and 12.5 μl was added to the Con A and S-Con A solutions. The

mixtures were incubated at room temperature for 45 min. Unbound SPDP was removed from the mixture containing the SPDP-activated lectin solutions by ultrafiltration in Vivaspin™ 20 tubes (30 kDa molecular weight cut-off (MWCO), PES; Sartorius Stedim Biotech) using an Avanti™ J-25 centrifuge (3,659 xg, 4 °C, 5 min). Salt-free D-Hank's buffer was then added to replace the filtrate and the wash step was repeated a further two times. SPDP-activated Con A and S-Con A were added to 5 ml solutions of citrate capped gold nanoparticles at a molar ratio of 1:100 of gold nanoparticles to lectins.[2] The SPDP-lectin nanoparticle mixtures were left stirring for 24 h at room temperature to allow complete binding of the SPDP-lectins onto the nanoparticles. To remove unbound Con A and S-Con A, 1 ml aliquots of Con A and S-Con A conjugated gold nanoparticles were centrifuged in 'NoStick' Microcentrifuge tubes (2.0 ml, Alpha Laboratories) at 5,488 xg at 2 °C for 40 min in an Allegra X-22R centrifuge. The supernatant was then removed and the red soft pellet containing nanoparticles was resuspended in 0.3 ml D-Hank's salt balanced buffer (137.00 mM NaCl (Fisher Scientific), 5.40 mM KCl (Sigma-Aldrich), 0.37 mM Na_2HPO_4, 0.44 mM KH_2PO_4, 4.20 mM $NaHCO_3$, pH 7.4).[2] The conjugates were then stored at 4 °C.

2.1.3 Approximation of lectin coverage on gold nanoparticles – electrolyte induced aggregation assay

To determine the approximate number of Con A and S-Con A molecules bound to each gold nanoparticle, solutions of citrate capped gold nanoparticles were reacted with SPDP activated lectins (2 $mg.ml^{-1}$) at varying molar ratios of nanoparticles to lectins for 24 h at room temperature according to the volumes shown in **Table 2.1** and **Table 2.2**.

Table 2.1 **Volumes of SPDP activated Con (SPDP-Con A) and citrate capped gold nanoparticles mixed to obtain molar ratios of nanoparticles to Con A of 1:0-1:200.**

Molar ratio of nanoparticles:Con A	Volume of citrate capped nanoparticles (ml)	Volume of salt-free D-Hank's buffer (µl)	Volume of SPDP-Con A (µl, 2 mg.ml^{-1})
1:0	5.0	250.0	0.0
1:5	5.0	244.7	5.3
1:10	5.0	239.5	10.5
1:15	5.0	234.2	15.8
1:20	5.0	228.9	21.1
1:25	5.0	223.7	26.3
1:200	5.0	39.4	210.6

Table 2.2 **Volumes of SPDP activated S-Con A (SPDP-S-Con A) and citrate capped gold nanoparticles mixed to obtain molar ratios of nanoparticles to S-Con A of 1:0-1:50.**

Molar ratio of nanoparticles:S-Con A	Volume of citrate capped nanoparticles (ml)	Volume of salt-free D-Hank's buffer (µl)	Volume of SPDP-S-Con A (µl, 2 mg.ml^{-1})
1:0	2.0	50.0	0.0
1:20	2.0	46.4	3.6
1:30	2.0	44.6	5.4
1:40	2.0	42.8	7.2
1:50	2.0	41.0	9.0

To each solution of nanoparticle conjugates (1 ml), aqueous NaCl (0.5 ml, 1.5 M) was added and the UV-visible absorption spectrum was immediately measured. The surface plasmon absorption band of the citrate capped gold nanoparticles centred at 520 nm broadens and red-shifts upon particle aggregation, and the absorbance intensity of the sample at 685 nm increases. Therefore, the extent of nanoparticle aggregation can be monitored as a decrease in absorbance intensity at *ca.* 520 nm and an increase in absorbance intensity at 685 nm.[3]

2.1.4 Colorimetric labelling of breast cancer cells with lectin conjugated gold nanoparticles

Con A or S-Con A conjugated gold nanoparticles (8.46 nM) used for the treatment of MCF-7 and SK-BR-3 breast cancer cells were synthesised according to the procedure described in **section 2.1.2**. MCF-7 human breast adenocarcinoma cells (LGC Standards) were cultured in NUNC Nunclon™ Δ Surface culture flasks (Thermo Fisher Scientific) using Minimum Essential Medium (MEM) + GlutaMAX™-I (Invitrogen) supplemented with 1x non-essential amino acids (NEAA; Invitrogen), 1 mM sodium pyruvate (NaPyr, Sigma-Aldrich) and 10% Foetal Bovine Serum (FBS; Thermo Fisher Scientific). SK-BR-3 human breast adenocarcinoma cells (LGC Standards) were cultured in Dulbecco's Modified Eagle's Medium (DMEM; Invitrogen) supplemented with 1 mM L-glutamine (L-Gln, Invitrogen) and 10% FBS. All cells were incubated in a humidified incubator at 37 °C in a 5% CO_2 atmosphere.

Phosphate buffered saline (PBS) solutions used for all cell-based experiments were prepared by dissolving 10 PBS tablets (Oxoid) in water (1 L) followed by 10 min of autoclaving at 110 °C. The as-prepared PBS solutions contained 8 mM Na_2HPO_4, 1 mM KH_2PO_4, 160 mM NaCl, and 3 mM KCl; and had a pH value of 7.3.

When the MCF-7 and SK-BR-3 cells reached *ca.* 70% confluency, the cells were trypsinised by aspirating the growth medium, washing the cells with PBS (5 ml) followed by 0.25% Trypsin-EDTA (1 ml; Invitrogen), then incubating for 3 min at 37 °C in a 5% CO_2 atmosphere. Following incubation, the detached cells were suspended in 10 ml of their respective growth medium and counted using a Neubauer haemocytometer. The cells were diluted appropriately and seeded onto NUNC Nunclon™ Δ Surface 48 well multidishes (Thermo Fisher Scientific) in 0.5 ml aliquots ($3.75x10^4$ cells per well) 24 h prior to incubation with the nanoparticle conjugates. The well contents were then removed and the cells were washed 3 times in D-Hank's salt balanced buffer (150 µl). MCF-7 cells and SK-BR-3 cells were incubated with the Con A or S-Con A conjugated gold nanoparticles (8.46 nM, 150 µl) for 0, 1 or 2 h.

Prior to imaging the cells were washed 3 times with D-Hank's salt balanced buffer (150 µl). Finally D-Hank's salt balanced buffer (150 µl) was added to each well and the cells were imaged using a ZEISS Axiovert 40CFL inverted optical microscope equipped with a ZEISS AxioCam MRC camera.

SK-BR-3 cells incubated with Con A conjugated gold nanoparticles (8.46 nM) for 1 h were incubated with propidium iodide (0.5 µl, 1 $mg.ml^{-1}$ in PBS; Sigma-Aldrich) for 5 min in the dark. The cells were imaged using widefield fluorescence microscopy using a ZEISS Axiovert 40CFL Optical Microscope equipped with an EXFO X-Cite® SERIES 120Q fluorescence illumination system. Propidium iodide fluorescence was visualised using a ZEISS Filter Set 45, with excitation at 560 ± 20 nm and emission at 630 ± 37.5 nm.

2.1.5 Concentration and time dependence of lectin conjugated gold nanoparticle aggregation

Con A, *Erythrina crystagalli* lectin (ECL, 58 kDa; Vector Laboratories) and sheep serum albumin (SSA, 66 kDa; Sigma-Aldrich) were conjugated to gold nanoparticles using SPDP according to the procedure described in **section 2.1.2**. The nanoparticle conjugates were kept in serum-free MEM + GlutaMAX™-I medium, supplemented with 1x NEAA and 1 mM NaPyr.

MCF-7 cells were then seeded in 96 well multidishes, as described in **section 2.1.4**, and incubated at 37 °C in a 5% CO_2 atmosphere with varying concentrations of the Con A, ECL or SSA conjugated gold nanoparticles (200 µl; 0.25, 0.50 or 1.00 nM). The cells were imaged following 1 h incubation with the nanoparticles using optical microscopy, as described in **section 2.1.4**. No aggregation was observed, so the nanoparticle conjugates were incubated for a further 23 h and imaged once again.

2.1.6 Synthesis and characterisation of PEG modified gold nanoparticles functionalised with Con A, ECL and SSA

α-thio-ω-carboxy polyethylene glycol (PEG, 32.7 mg ,1 mM, 3,274 Da; Iris Biotech GmbH) was self-assembled for 15 h onto citrate capped gold nanoparticles (10 ml, *ca.* 3 nM). Following self-assembly, unbound PEG was removed from the sample by 3 repeated ultrafiltrations in Vivaspin™ 20 tubes (30 kDa MWCO, PES) by centrifuging at 7,741 xg at 4 °C for 10 min. Following every centrifugation, the PEG modified gold nanoparticles were redispersed in an equal volume of 2-(*N*-morpholino)ethanesulfonic acid buffer (MES, 50 mM, pH 5.5; Sigma-Aldrich). The PEG modified gold nanoparticles were then characterised using UV-visible absorption spectroscopy and transmission electron microscopy (TEM) imaging.

For TEM imaging, an aliquot of PEG modified gold nanoparticles (500 µl) was centrifuged in a Vivaspin™ 500 (100 kDa MWCO, PES) tube at 14,300 xg at 4 °C for 30 min. The concentrated sample (10 µl) was then spotted onto Holey Carbon Film 300 Mesh Cu (50) TEM grid (Agar Scientific) on top of adsorbent filter paper. The nanoparticle sample was imaged using a JEOL 2000EX TEM operating at 200 kV accelerating voltage.[4] The assistance of Dr Colin MacDonald (School of Chemistry, University of East Anglia) during the TEM imaging is gratefully acknowledged.

Con A, ECL and SSA were then covalently conjugated to the PEG on the gold nanoparticles by amide coupling of the primary amine groups at the protein lysine residues to the terminal carboxyl groups of the PEG. Amide coupling was achieved by using *N*-(3-Dimethylaminopropyl)-*N'*-ethylcarbodiimide (EDC; Sigma-Aldrich) and sulfo-*N*-hydroxysuccinimide (sulfo-NHS; Fisher Scientific). EDC (1.31 µl, 2 mM, from 0.877 $g.l^{-1}$ stock) and sulfo-NHS (2.9 mg, 5 mM) were added to PEG modified gold nanoparticles in MES buffer (5 ml; 50 mM, pH 5.5) and were stirred for 30 min. The reaction of EDC/sulfo-NHS with PEG carboxyl groups forms amine reactive sulfo-*N*-hydroxysuccinimidyl ester terminated PEG chains on the nanoparticles. Excess EDC and sulfo-NHS were removed by ultrafiltration in Vivaspin™ 20 tubes (30 kDa MWCO, PES) by centrifuging at 7,741 xg at 4 °C for 10 min. The activated sulfo-NHS ester functionalised gold nanoparticles were then redispersed in D-Hank's salt balanced buffer (5 ml, pH 7.4). Aliquots of the nanoparticles (1.5 ml each) were mixed with Con A, ECL and SSA (1 $mg.ml^{-1}$ in D-Hank's salt balanced buffer) to obtain a final protein concentration which was 100x the nanoparticle concentration. The mixtures were stirred for 2.5 h and orbital shaken at 700 RPM for 15 h at room temperature. Following conjugation, the Con A, ECL and SSA functionalised, PEG modified gold nanoparticles were pelleted in 1.5 ml aliquots by centrifugation at 7,168 xg at 4 °C for 40 min. The supernatants containing unbound proteins were then replaced with fresh D-Hank's salt balanced buffer (1.5 ml). The nanoparticle conjugates were characterised using UV-visible absorption spectrophotometry, diluted to 3 nM using D-Hank's salt balanced buffer and stored at 4 °C.

2.1.7 Physiological stability assessment of lectin conjugated, PEG modified gold nanoparticles

MCF-7 cells were trypsinised as described in **section 2.1.4** and seeded onto NUNC Nunclon™ Δ surface transparent 96 well plates (Thermo Fisher) for 24 h in 200 µl ($2x10^4$ cells per well). The cells were incubated with the Con A, ECL or SSA conjugated, PEG modified gold nanoparticles (200 µl; 0.25, 0.50 or 1.00 nM in serum-free MEM + GlutaMAX™-I medium supplemented with 1x NEAA and 1 mM NaPyr) and imaged at 1 h and 24 h following incubation, as described in **section 2.1.4**.

2.1.8 Colorimetric formazan-based lectin cytoadhesion assay

To determine the optimal lectin concentration for adsorption onto 96 well plates and the optimal cell density for the highest interaction between the cells and lectins, a cross-calibration assay using 3-(4,5-dimethyl-2-thiazolyl)-2,5-diphenyl-2H-tetrazolium bromide (MTT; Sigma-Aldrich) reagent was performed. Con A (100 µl; 0, 0.1, 0.5 or 1 $mg.ml^{-1}$ in D-Hank's salt balanced buffer) was placed in NUNC Nunclon™ Δ surface transparent 96 well multidishes and left to adsorb onto the wells for 1 h at room temperature. Unbound Con A was then removed by washing the wells once with D-Hank's buffer (100 µl). To obtain a suspension of MCF-7 breast cancer cells without the use of trypsin, *ca.* 70% confluent cells were washed twice in PBS (5 ml) then once in a PBS solution containing ethylenediaminetetraacetic acid (EDTA, 7.5 mM; Sigma-Aldrich) and ethylene glycol tetraacetic acid (EGTA, 7.5 mM; Sigma-Aldrich). The cells were then kept in the PBS EDTA:EGTA solution (5 ml) and incubated for 15 min at 37 °C and in a 5% CO_2 atmosphere with mild agitation every 5 min. The cell suspension was centrifuged in an Eppendorf 5810R Centrifuge at 181 xg at room temperature for 5 min. The supernatant was discarded and the pelleted cells were redispersed in serum-free MEM + GlutaMAX™-I medium supplemented with 1x NEAA and 1 mM NaPyr (5 ml). The MCF-7 cells were counted and placed in the Con A pre-treated wells at densities of $0.2x10^4$, $0.5x10^4$, $1.0x10^4$ or $2.0x10^4$ cells per well and incubated for 1 h at 37 °C in a 5% CO_2 atmosphere. The well contents were then removed and each well was gently washed once using serum-free MEM + GlutaMAX™-I medium supplemented with 1x NEAA and 1 mM NaPyr (200 µl). The cells were finally kept in serum-free MEM + GlutaMAX™-I medium (200 µl). MTT (12.5 µl, 5 $mg.ml^{-1}$ in PBS) was added to each well and incubated for 3 h at 37 °C in a 5% CO_2 atmosphere. The well contents were then removed and each well was washed twice gently with D-Hank's buffer (200 µl). Finally, the formazan crystals produced by the cells were

dissolved in DMSO (200 µl) and the formazan absorbance at 550 nm was measured using a MRX-Dynatech plate reader. All assays were performed in triplicate.

Con A, S-Con A and SSA (100 µl, 0.5 mg.ml^{-1}) were each adsorbed onto transparent 96 well multidishes, as described previously for the Con A. MCF-7 cells were detached from the flasks, centrifuged and redispersed in serum-free MEM + GlutaMAX™-I medium, as described earlier in this section. The cells were added to the pre-treated wells at a density of 2.0x10^{4} cells per well (200 µl), incubated for 1 h and analysed using MTT, as described earlier in this section. All assays were performed in triplicate. The assay was repeated once more for each of the three lectins Con A , S-Con A and ECL.

2.1.9 Synthesis of zinc phthalocyanine-polyethylene glycol gold nanoparticles

The phthalocyanine photosensitiser (1,1',4,4',8,8',15,15',18,18',22,22'-tetradecakisdecyl-25,25'-(11,11'dithiodiundecyl) diphthalocyanine zinc; C11Pc) was kindly provided by Dr Isabelle Chambrier (School of Chemistry, University of East Anglia).[5] Gold nanoparticles (*ca.* 4 nm in diameter) were synthesised in tetrahydrofuran (THF; Fisher Scientific) and stabilised with a mixed monolayer of the C11Pc (2,564 g.mol^{-1}) photosensitiser and PEG.[6,7] The C11Pc photosensitiser (2 mg) was dissolved in THF (1 ml). The PEG (7.5 mg) was dissolved in THF (2 ml) and then stirred with the C11Pc solution for 5 min. $HAuCl_4$ (1.2 mg) was dissolved in THF (1.2 ml) and combined with the C11Pc and PEG solution and stirred for a further 5 min. A fresh aqueous solution of sodium borohydride ($NaBH_4$, 1.5 mg in 1.2 ml water, 37.83 g.mol^{-1}; Fisher Scientific) was prepared and rapidly added to the solution of $HAuCl_4$, C11Pc and PEG under vigorous stirring. The reaction was stirred for 15 h at room temperature. The C11Pc-PEG gold nanoparticles remained stable in the THF while any gold nanoparticles not functionalised with the C11Pc precipitated. The solution containing the C11Pc-PEG gold nanoparticles was collected and the THF/water mixture was removed from the sample by rotary evaporation under reduced pressure at 60 °C. The C11Pc-PEG gold nanoparticles were dissolved in MES buffer (5.4 ml; 50 mM, 0.05% Tween 20, pH 5.5) and centrifuged at 21,913 xg at 4 °C for 30 min to remove any unbound C11Pc and those C11Pc gold nanoparticles not functionalised with PEG, both of which are insoluble in buffer. The supernatant containing purified C11Pc-PEG gold nanoparticles was removed and stored at 4 °C.

2.1.10 Con A conjugation to C11Pc-PEG gold nanoparticles

Con A was conjugated to the C11Pc-PEG gold nanoparticles using EDC/sulfo-NHS coupling. 2 mM EDC (0.8 µl, 0.877 g.ml^{-1}) and 5 mM sulfo-NHS (2.17 mg, 115.08 g.mol^{-1}) were added to the C11Pc-PEG gold nanoparticles (*ca.* 2 µM C11Pc equivalent) in MES buffer (2 ml; 50 mM, 0.05% Tween 20, pH 5.5) and stirred for 30 min at room temperature. Excess EDC and sulfo-NHS was removed by filtering the sulfo-NHS-ester functionalised C11Pc-PEG gold nanoparticles in 500 µl aliquots in Vivaspin™ 500 (100 kDa MWCO, PES; Sartorius Stedim Biotech) by centrifuging at 14,300 xg at 4 °C for 30 min. The filtrate containing excess EDC and sulfo-NHS was discarded and the sulfo-NHS-ester functionalised C11Pc-PEG gold nanoparticles were then redispersed in a PBS solution (500 µl; 10 mM phosphate buffer, 100 mM NaCl, 100 µM $CaCl_2.2H_2O$ (Sigma-Aldrich), 100 µM $MnCl_2.4H_2O$ (Lancaster Synthesis), pH 7.4).

The 10 mM phosphate buffer solution was obtained by diluting a 100 mM stock solution of phosphate buffer by 10-fold. The 100 mM stock solution was prepared by combining 19 ml of a monobasic solution of NaH_2PO_4 (200 mM; Fisher Scientific) with 81 ml of a dibasic solution of Na_2HPO_4 (200 mM; Fisher Scientific).

Con A (50 µl, 1 mg.ml^{-1} in PBS (10 mM phosphate buffer, 100 mM NaCl, 100 µM $CaCl_2.2H_2O$, 100 µM $MnCl_2.4H_2O$, pH 7.4)) was then added to the C11Pc-PEG gold nanoparticles (2 ml) to obtain a final Con A concentration of 0.24 µM, and was stirred for 15 h at room temperature. The unbound Con A was removed from the nanoparticle solution by six repeated ultrafiltrations of the samples in 500 µl aliquots in Vivaspin™ 500 tubes (100 kDa MWCO, PES) by centrifuging at 14,300 xg at 4 °C for 30 min. After each centrifugation, the Con A conjugated C11Pc-PEG gold nanoparticles were redispersed in PBS (500 µl; 10 mM phosphate buffer, 100 mM NaCl, 100 µM $CaCl_2.2H_2O$, 100 µM $MnCl_2.4H_2O$, pH 7.4). After the fifth centrifugation the Con A conjugated C11Pc-PEG gold nanoparticles were redispersed in serum free, phenol red-free Leibovitz's L15 medium (Invitrogen) supplemented with 1x NEAA, 1 mM NaPyr, 100 µM $CaCl_2.2H_2O$ and 100 µM $MnCl_2.4H_2O$. The nanoparticle samples were characterised using a Hitachi U-3010 UV-visible absorption spectrophotometer. The concentration of the C11Pc photosensitiser assembled on the nanoparticle surface was determined using an extinction coefficient of 2.23x10^5 M^{-1}.cm^{-1} at 696 nm.[8] All nanoparticle conjugates prepared were appropriately diluted as required for each experiment, filtered using sterile syringe driven filter units (0.22 µm PES) and stored at 4 °C prior to use. C11Pc-PEG gold nanoparticles without conjugation to Con A were synthesised and used as a control.

2.1.11 TEM characterisation and singlet oxygen measurement of the non-conjugated and Con A conjugated C11Pc-PEG gold nanoparticles

The non-conjugated and Con A conjugated C11Pc-PEG gold nanoparticles in PBS (10 mM phosphate buffer, 100 mM NaCl, 100 µM $CaCl_2.2H_2O$, 100 µM $MnCl_2.4H_2O$, pH 7.4) were characterised using TEM imaging, as described in **section 2.1.6**.

Singlet oxygen production was measured using the singlet oxygen molecule probe, anthracene-9,10-dipropionic acid disodium salt[9] (ADPA, 366.32 $g.mol^{-1}$; Molecular Probes). Non-conjugated and Con A conjugated C11Pc-PEG gold nanoparticles in PBS (900 µl; 10 mM phosphate buffer, 100 mM NaCl, 100 µM $CaCl_2.2H_2O$, 100 µM $MnCl_2.4H_2O$, pH 7.4) were placed in a 1.5 ml stoppered quartz cuvette with ADPA (100 µl, 1.7 mM in methanol (Fisher Scientific)) and a magnetic stirrer bar. The sample was then irradiated at 633 nm for 30 min using a 10 mW Helium-Neon (HeNe) Laser (JDS Uniphase) with continuous mixing and the absorbance of the ADPA was monitored at 400 nm every 5 min. C11Pc-free PEG gold nanoparticles were prepared as described in **section 2.1.9** without the addition of C11Pc and used as a control.

2.1.12 MTT viability assay of MCF-7 breast cancer cells following Con A targeted PDT treatment

MCF-7 cells were trypsinised as described in **section 2.1.4** and seeded onto two separate white opaque NUNC Nunclon™ Δ surface 96 well multidishes ($2x10^4$ cells per well) 24 h prior to incubation with the nanoparticles. The cells were washed once in PBS (100 µl), then kept in serum-free, phenol red-free Leibovitz's L15 medium supplemented with 1x NEAA and 1 mM NaPyr (50 µl) containing 0.0, 0.1, 0.2, 0.3, 0.4 or 0.5 µM C11Pc equivalent of Con A conjugated or non-conjugated C11Pc-PEG gold nanoparticles. The cells were incubated with the nanoparticles for 3 h at 37 °C in a 5% CO_2 atmosphere. The nanoparticles not specifically bound or internalised by the MCF-7 cells were removed by washing the cells 3 times in PBS (100 µl). Finally, the cells were kept in phenol red-free Leibovitz's L15 medium (200 µl) supplemented with 1x NEAA, 1 mM NaPyr and 10% FBS. Staurosporine (20 µM; LC Labs) was used as a positive control for cytotoxicity.[10] One of the 96 well multidishes was kept in the dark, while the other multidish was irradiated for 5 min per well using a 10 mW 633 nm HeNe laser giving a fluency rate of 34 $mW.cm^{-2}$ and a total light dose of 10.5 $J.cm^{-2}$. The laser was positioned 15 cm above the cells being irradiated. Laser light intensity was measured using a Power Max *500AD* Molectron Power

Meter. Following irradiation, the cells were incubated at 37 °C in a 5% CO_2 atmosphere for 48 h. MTT reagent (10 µl, 5 $mg.ml^{-1}$ in PBS) was added to each well and the cells were incubated at 37 °C in a 5% CO_2 atmosphere for 4 h. The well contents were then removed and the formazan was dissolved in DMSO (200 µl). The well contents were transferred to transparent 96 well multidishes and the absorbance at 550 nm was measured using a MRX-Dynatech plate reader. Background absorbance at 550 nm of Leibovitz's L15 medium alone incubated with MTT reagent was subtracted from all measurements. Cell viability was calculated as a percentage of absorbance at 550 nm of untreated, non-irradiated MCF-7 cells. All assays were performed in triplicate.

To separate the C11Pc-PEG gold nanoparticles from the particles not functionalised with C11Pc, nanoparticle synthesis was repeated as described in **section 2.1.9**; however, a further nanoparticle purification stage was introduced. Following 15 h of stirring, the C11Pc-PEG gold nanoparticles were centrifuged at 200 xg at room temperature for 2 min to remove remaining nanoparticles not functionalised with C11Pc, which are unstable in excess THF. These C11Pc-PEG gold nanoparticles were further conjugated with Con A and the targeted PDT treatment of the MCF-7 cells was repeated, as described earlier in this section.

The MTT viability assay following the Con A targeted PDT treatment of MCF-7 cells was repeated once again using a higher concentration range of C11Pc-PEG gold nanoparticle conjugates and increased irradiation times. To enhance the formazan production of the MCF-7 cells, the experiment was performed following a prolonged cell seeding time of 48 h. The MCF-7 cells were incubated for 24 h in serum-free, phenol red-free Leibovitz's L15 medium supplemented with 1x NEAA and 1 mM NaPyr containing 0.00, 0.10, 0.20, 0.50, 1.00 or 1.44 µM C11Pc equivalent of Con A conjugated or non-conjugated C11Pc-PEG gold nanoparticles (50 µl). This was followed by irradiation of 10 min per well using a 10 mW 633 nm HeNe laser giving a fluency rate of 38.4 $mW.cm^{-2}$ and a total light dose of 23.13 $J.cm^{-2}$. The cells were also incubated in the MEM + GlutaMAX™-I culture medium supplemented with 1x NEAA, 1 mM NaPyr and 10% FBS (200 µl) following incubation of the nanoparticle conjugates in Leibovitz's L15 medium to maximise the metabolic activity of the cells.

2.1.13 CellTiter-Blue™ viability assay of SK-BR-3 breast cancer cells following Con A targeted PDT treatment

The targeted PDT treatment of SK-BR-3 cells using Con A conjugated C11Pc-PEG gold nanoparticles was attempted and cell viability was assessed using the fluorescence based cell viability assay, CellTiter-Blue™ (Promega).[11] SK-BR-3 cells were cultured and trypsinised according to the procedure described in **section 2.1.4**. The cells were then seeded at a density of $2x10^4$ cells per well in white opaque 96 well multidishes in DMEM medium supplemented with 1 mM L-Gln and 10% FBS, 48 h prior to nanoparticle incubation. The cells were washed once in PBS (100 µl), then incubated for 24 h in serum-free, phenol red-free Leibovitz's L15 medium supplemented with 1x NEAA and 1 mM NaPyr containing 0.00, 0.10, 0.20, 0.50, 1.00 or 1.44 µM (C11Pc equivalent) Con A conjugated or non-conjugated C11Pc-PEG gold nanoparticles (50 µl). Staurosporine (20 µM) was used as a positive control for cytotoxicity.[10] Following incubation with the nanoparticles, the cells were washed 3 times in PBS (100 µl). Finally the cells were kept in DMEM medium supplemented with 1 mM L-Gln and 10% FBS (200 µl) and irradiated for 10 min per well, as described in **section 2.1.12**. Following irradiation, the cells were incubated at 37 °C in a 5% CO_2 atmosphere for 48 h. CellTiter-Blue™ reagent (20 µl per well) was added to the cells and incubated for 4 h at 37 °C in a 5% CO_2 atmosphere. Fluorescence emission at 590 nm (excitation at 560 nm) was measured using an EnVision™ (Wallac) 2103 Multilabel Reader (Perkin Elmer) equipped with an EnVision™ work station. Background fluorescence emission at 590 nm of DMEM medium alone incubated with CellTiter-Blue™ reagent was subtracted from all measurements. Cell viability was calculated as a percentage of fluorescence emission at 590 nm of untreated, non-irradiated SK-BR-3 cells. All assays were performed in triplicate.

2.2 Targeting the oncofoetal T antigen disaccharide with jacalin functionalised phthalocyanine-PEG gold nanoparticles for selective PDT of HT-29 colon adenocarcinoma cells

2.2.1 Jacalin conjugation to C11Pc-PEG gold nanoparticles

C11Pc-PEG gold nanoparticles were synthesised in THF, as described in **section 2.1.9**. Jacalin (66 kDa[12]; Vector Laboratories) was covalently attached to the PEG on the gold nanoparticles, as described for Con A in **section 2.1.10**, with the exception that the sulfo-NHS-ester functionalised C11Pc-PEG gold nanoparticles were redispersed in a 4-(2-hydroxyethyl)-1-piperazineethanesulfonic acid (HEPES; Sigma-Aldrich) buffered saline solution (2 ml; 10 mM HEPES, 150 mM NaCl, 100 μM $CaCl_2.2H_2O$, pH 7.4). Jacalin (31.74 μl, 1 $mg.ml^{-1}$ in HEPES buffered saline) was then added to the sulfo-NHS-ester functionalised C11Pc-PEG gold nanoparticles to obtain a final jacalin concentration of 0.24 μM and was stirred for 15 h at room temperature. The unbound jacalin was removed from the nanoparticle solution using ultrafiltration in Vivaspin™ 500 tubes, as described in **section 2.1.10**, and redispersed in HEPES buffered saline (500 μl; 10 mM HEPES, 150 mM NaCl, 100 μM $CaCl_2.2H_2O$, pH 7.4). When the nanoparticles were prepared for *in vitro* experiments, the nanoparticle conjugates were redispersed in serum-free Roswell Park Memorial Institute (RPMI) 1640 cell culture medium (Invitrogen) supplemented with 1.5 mM L-Gln after the fifth centrifugation. The samples were characterised using UV-visible absorption spectrophotometry, appropriately diluted and stored at 4 °C. The method for jacalin conjugation to C11Pc-PEG gold nanoparticles has now been reported.[13]

2.2.2 Singlet oxygen production by the irradiation of non-conjugated and jacalin conjugated C11Pc-PEG gold nanoparticles

To confirm that singlet oxygen produced by the irradiation of the C11Pc-PEG gold nanoparticles was responsible for the photobleaching of ADPA, the particles were irradiated in the absence and presence of oxygen. From this point onwards, 450 μl of nanoparticle solutions and 50 μl of ADPA (1.7 mM in methanol) were used to maximise the volume of air within the cuvette. A HEPES buffered saline solution of non-conjugated C11Pc-PEG gold nanoparticles (10 mM HEPES, 150 mM NaCl, 100 μM $CaCl_2.2H_2O$, pH 7.4) containing ADPA was prepared, as described in **section 2.1.11**. The mixture was deoxygenated by bubbling argon through the sample for 20 min. The sample was then irradiated at 633 nm using a HeNe laser for 30 min with continuous stirring. UV-visible

absorption spectra were recorded at 5 min intervals. The solution was then reoxygenated by bubbling air through the sample for a further 10 min, and then irradiated for an additional 30 min with UV-visible absorption spectra recorded at 5 min intervals.

C11Pc-PEG gold nanoparticles in HEPES buffered saline (450 µl; 10 mM HEPES, 150 mM NaCl, 100 µM $CaCl_2.2H_2O$, pH 7.4) with and without jacalin conjugation were placed in a 1.5 ml stoppered quartz UV-visible absorbance cuvette with 50 µl of ADPA (1.7 mM in methanol). The samples were irradiated at 633 nm using a HeNe laser for 30 min with continuous stirring and the UV-visible absorption spectra were recorded at 5 min intervals.

2.2.3 *In vitro* PDT of HT-29 cells using jacalin conjugated nanoparticles

HT-29 human colon adenocarcinoma cells (LGC Standards) were cultured in RPMI 1640 medium supplemented with 1.5 mM L-Gln and 10% FBS. All cells were incubated in a humidified incubator at 37 °C in a 5% CO_2 atmosphere. HT-29 cells were trypsinised according to the procedure described in **section 2.1.4** and seeded onto clear 96 well multidishes ($2x10^4$ cells per well) 24 h prior to incubation with nanoparticle conjugates. The PDT efficacy of jacalin conjugated C11Pc-PEG gold nanoparticles on HT-29 cells was investigated using the MTT viability assay, as described in **section 2.1.12**. However, the HT-29 cells were incubated with 0.00, 0.10, 0.20, 0.50, 1.00 or 1.15 µM (C11Pc equivalent) jacalin conjugated or non-conjugated C11Pc-PEG gold nanoparticles (50 µl) for 3 h. The cells were then washed 3 times in PBS and irradiated for 5 min per well, as described in **section 2.1.12**. The MTT assay was performed in RPMI 1640 medium supplemented with 10% FBS and 1.5 mM L-Gln 48 h following irradiation.

2.2.4 Synthesis of high yield C11Pc-PEG gold nanoparticles in DMF

In an attempt to increase the C11Pc loading efficiency and yield of C11Pc-PEG gold nanoparticles, alternative solvents were explored for the synthetic procedure to improve the solubility and stability of the PEG gold nanoparticles during synthesis.

The solubility of PEG gold nanoparticles (*ca.* 4 nm, C11Pc-free) during synthesis was investigated by introducing *N,N*-dimethylformamide (DMF; Sigma-Aldrich) to the synthetic procedure. DMF (logP = -0.83) was used to incrementally replace THF (logP = 0.53) in the procedure described in **section 2.1.9**, in order to vary the ratio of DMF:THF during the reaction. The volumes of THF and DMF used are shown in **Table 2.3**.

Table 2.3 **The volumes of DMF, THF and water used for the synthesis of PEG gold nanoparticles (C11Pc-free) to assess the stability of the particles in DMF.**

Sample	Volume and solvent used for PEG (3.75 mg)	Volume and solvent used for $HAuCl_4$ (0.6 mg)	Volume of water used for $NaBH_4$ (0.75 mg)	Ratio of DMF:THF
A	1.5 ml THF	0.60 ml THF	0.6 ml	0:2.1
B	1.5 ml THF	0.15 ml DMF; 0.45 ml THF	0.6 ml	0.15:1.95
C	1.5 ml THF	0.30 ml DMF; 0.30 ml THF	0.6 ml	0.3:1.8
D	1.5 ml THF	0.45 ml DMF; 0.15 ml THF	0.6 ml	0.45:1.65
E	1.5 ml THF	0.60 ml DMF	0.6 ml	0.6:1.5
F	1.0 ml DMF; 0.5 ml THF	0.60 ml DMF	0.6 ml	1.6:0.5

After mixing the reactants in their respective solvents (reactions A through F) according to the details in **Table 2.3**, the mixtures were stirred vigorously for 15 h. The nanoparticle solutions formed were visually assessed for the degree of stabilisation the DMF provided.

Using the conditions for sample F, C11Pc-PEG gold nanoparticles were synthesised by dissolving the PEG (3.75 mg) in DMF (1 ml) and the C11Pc (0.5 mg) in THF (0.5 ml). The remaining experimental conditions for sample F were maintained. Synthesis of the nanoparticles was repeated once more using the conditions for sample F; however, methanol (logP = -0.69) was used instead of DMF as the main solvent for the reaction.

Following the synthesis of C11Pc-PEG gold nanoparticle in DMF or methanol, the solvents were removed from each sample using rotary evaporation at 70 °C under reduced pressure. The particles were then redissolved in MES buffer (2.7 ml; 50 mM, pH 5.5, 0.05% Tween 20). The nanoparticle solutions were centrifuged at 21,913 xg at 4 °C for 30 min to remove any unbound C11Pc and those C11Pc gold nanoparticles not functionalised with PEG, both of which are insoluble in the buffer. The samples were characterised using UV-visible absorption spectrophotometry.

To establish whether the C11Pc present in the MES buffered nanoparticle solutions was associated with the gold surface, unbound C11Pc was separated from the particles synthesised in DMF or in methanol using thin layer chromatography (TLC). Nanoparticle samples synthesised in DMF or methanol (8 µl) were spotted onto TLC silica gel 60 F254 aluminium sheets (Merck). A THF solution of C11Pc was used as a control. Toluene (Fisher Scientific) : methanol (95:5) was used as the mobile phase to separate the free, mobile C11Pc from the immobile C11Pc-PEG gold nanoparticles.

In order to confirm that the high yield of C11Pc present in the nanoparticle solutions synthesised in DMF was due to the binding of the sensitiser to the water soluble PEG gold nanoparticles, the synthesis was repeated using the original (0.564 mM) or half (0.282 mM) concentrations of $HAuCl_4$. The MES buffered solutions (50 mM, 0.05% Tween 20, pH 5.5) of the C11Pc-PEG gold nanoparticles synthesised in DMF using 0.564 mM or 0.282 mM $HAuCl_4$ were characterised using UV-visible absorption spectrophotometry.

The photoactivity of the C11Pc-PEG gold nanoparticles synthesised in DMF (1.94 μM C11Pc equivalent) was then investigated using the singlet oxygen probe, ADPA, as described in **section 2.1.11**.

The effect of water within the synthetic procedure of the C11Pc-PEG gold nanoparticles (2.7 ml) was explored by using either an aqueous or DMF solution of $NaBH_4$ (0.75 mg in 0.6 ml). The two reactions were stirred for 15 h, as described earlier in this section, and the solvent mixtures were removed using rotary evaporation at 70 °C under reduced pressure. C11Pc-PEG gold nanoparticles and C11Pc were removed from the dry nanoparticle residues using THF (2.7 ml). The solvent was removed from the THF-soluble nanoparticle samples (referred to as the THF extracts) and the C11Pc-PEG gold nanoparticles were dissolved in MES buffer (2.7 ml; 50 mM, 0.05% Tween 20, pH 5.5). Unbound C11Pc and those C11Pc gold nanoparticles not functionalised with PEG were removed from the nanoparticle solution by centrifugation at 21,913 xg at 4 °C for 30 min. The nanoparticles not soluble in THF were dissolved in water (2.7 ml) and were referred to as the water extracts.

The THF extracts and water extracts of the C11Pc-PEG gold nanoparticles synthesised using an aqueous or DMF solution of $NaBH_4$ were characterised using UV-visible absorption spectrophotometry. The THF extracts contained the highest yield of C11Pc-PEG gold nanoparticles synthesised using an aqueous or DMF solution of $NaBH_4$ (4.35 μM and 5.90 μM C11Pc equivalent, respectively). TLC separation of the free C11Pc from the C11Pc-PEG gold nanoparticles in both THF extracts was then performed as described earlier in this section.

The THF extract of the C11Pc-PEG gold nanoparticles synthesised using a DMF solution of $NaBH_4$ contained the highest yield of C11Pc-PEG gold nanoparticles (5.90 μM C11Pc equivalent) and was therefore selected for further investigations. The singlet oxygen production by the irradiation of a MES buffered solution of this THF extract was measured

as described in **section 2.1.11**. The nanoparticles in this THF extract were also characterised using TEM imaging, as described in **section 2.1.6**.

The procedure for synthesising C11Pc-PEG gold nanoparticles in DMF using a DMF solution of $NaBH_4$ was used for the remainder of the thesis.

2.2.5 ICP-OES elemental analysis of the C11Pc-PEG gold nanoparticles

C11Pc-PEG gold nanoparticles were synthesised as described in **section 2.2.4**, dissolved in deionised water and centrifuged at 21,913 xg at 4 °C for 30 min to remove any unbound C11Pc and the C11Pc gold nanoparticles not functionalised with PEG. The gold nanoparticles were then destroyed in *aqua regia* and analysed using inductively coupled plasma-optical emission spectroscopy (ICP-OES) using a Varian Vista-PRO™ ICP-OES spectrometer. The quantification of gold (Au^{3+}) and zinc (Zn^{2+}) ions present was used to obtain a ratio of gold nanoparticles to zinc phthalocyanine molecules. Claritas PPT® Grade Multi-Element Solution 2 and Claritas PPT® Grade Multi-Element Solution 3 (SPEX CertiPrep®) were used as the zinc and gold standards, respectively. The assistance of Dr Graham Chilvers (School of Environmental Sciences, University of East Anglia) who performed the ICP-OES elemental analysis is gratefully acknowledged.

2.2.6 Conjugation of jacalin to C11Pc-PEG gold nanoparticles synthesised in DMF

Jacalin was covalently attached to the PEG on the C11Pc-PEG gold nanoparticles synthesised in DMF using EDC/NHS chemistry, as described in **section 2.2.1**, although 5 mM NHS (1.2 mg, 115.08 $g.mol^{-1}$; Sigma-Aldrich) was used rather than sulfo-NHS. The remaining experimental procedures described in **section 2.2.1** were maintained.

2.2.7 Characterisation and singlet oxygen measurement of the jacalin conjugated C11Pc-PEG gold nanoparticles synthesised in DMF

The jacalin conjugated C11Pc-PEG gold nanoparticles in HEPES buffered saline (500 µl; 10 mM HEPES, 150 mM NaCl, 100 µM $CaCl_2.2H_2O$, pH 7.4) were characterised using TEM imaging and singlet oxygen production was assessed, as described in **section 2.1.6** and **section 2.1.11**, respectively. The excitation and emission spectra of the non-conjugated and jacalin conjugated C11Pc-PEG gold nanoparticles were recorded using a Horiba Jobin Yvon FluoroLog® 3 fluorimeter.

2.2.8 Optical microscopy of HT-29 cells following jacalin targeted PDT

HT-29 cells were seeded onto transparent 96 well multidishes, as described in **section 2.2.3**, 24 h prior to incubation with the nanoparticles. The cells were then incubated with jacalin conjugated or non-conjugated C11Pc-PEG gold nanoparticles (0.00-1.15 μM C11Pc equivalent) synthesised in DMF and irradiated for 5 min per well according to the procedure outlined in **section 2.2.3**. 48 h following irradiation, changes in cell morphology following targeted PDT treatment were investigated using a ZEISS Axiovert 40CFL Optical Microscope equipped with a ZEISS AxioCam MRC camera.

2.2.9 Laser scanning confocal microscopy of HT-29 cells incubated with jacalin conjugated and non-conjugated C11Pc-PEG gold nanoparticles

HT-29 cells were cultured and trypsinised according to the procedure described in **section 2.2.3**. The HT-29 cells were then seeded ($2x10^4$ cells per well) onto 18 mm round glass coverslips (Jencons VWR) in transparent 6 well multidishes (Thermo Fisher Scientific) for 48 h in RPMI 1640 medium supplemented with 10% FBS and 1.5 mM L-Gln. The cells were then washed once in PBS (1 ml) and incubated for 3 h at 37 °C in a 5% CO_2 atmosphere in serum-free RPMI 1640 medium supplemented with 1.5 mM L-Gln (1 ml) containing jacalin conjugated or non-conjugated C11Pc-PEG gold nanoparticles (1 μM or 2 μM C11Pc equivalent). The cells were then washed 3 times in PBS (1 ml) and kept in RPMI 1640 medium supplemented with 1.5 mM L-Gln and 10% FBS (2 ml). The cells were irradiated for 6 min per coverslip using a 10 mW 633 nm HeNe laser and incubated for 15 h at 37 °C in a 5% CO_2 atmosphere. The coverslips were fitted on a heated stage (37 °C) and 1 ml imaging medium (120 mM NaCl, 5 mM KCl, 2 mM $CaCl_2.2H_2O$, 1 mM $MgCl_2.4H_2O$, 1 mM NaH_2PO_4, 1 mM $NaHCO_3$, 25 mM HEPES, 11 mM D-glucose (Sigma-Aldrich), and 1 $mg.ml^{-1}$ BSA (Sigma-Aldrich)) was added to each coverslip. The cells were imaged using a Zeiss LSM510 META laser scanning confocal microscope with a plan-apochromat 63x/1.4 oil immersion objective. Differential interference contrast (DIC) images were obtained using transmitted light from a 543 nm HeNe laser. DIC images were merged with fluorescence images of the jacalin conjugated or non-conjugated C11Pc-PEG gold nanoparticles excited using a 633 nm HeNe laser. The fluorescence emission of the C11Pc-PEG gold nanoparticles was collected using a 650 nm long pass filter.

Propidium iodide (5 μl, 1 $mg.ml^{-1}$ in PBS) was added to each coverslip containing 1 ml imaging medium and was incubated in the dark for 10 min at 37 °C. Nuclei of dead cells

with significant membrane damage stained positive for propidium iodide, which was excited with a 543 nm HeNe laser. The fluorescence emission of the propidium iodide was collected using a 560-615 nm band pass filter. For all fluorescence microscope images, settings were used which caused minimal autofluorescence of cell components.

2.2.10 *In vitro* PDT treatment of HT-29 cells using jacalin conjugated C11Pc-PEG gold nanoparticles synthesised in DMF – MTT viability assay

HT-29 cells were seeded into two separate white opaque 96 well multidishes ($2x10^4$ cells per well) for 24 h. The cells were washed once in PBS (100 µl), then kept in serum-free RPMI 1640 medium (50 µl) supplemented with 1.5 mM L-Gln containing 0.00, 0.10, 0.20, 0.50, 1.00 or 1.15 µM (C11Pc equivalent) jacalin conjugated or non-conjugated C11Pc-PEG gold nanoparticles. The cells were incubated with the nanoparticles for 3 h at 37 °C and in a 5% CO_2 atmosphere. The well contents were then removed and any nanoparticles not specifically bound or uptaken by the HT-29 cells were removed by washing the cells 3 times in PBS (100 µl). Finally, the cells were kept in RPMI 1640 medium (200 µl) supplemented with 10% FBS and 1.5 mM L-Gln. Staurosporine (20 µM) was used as a positive control for cytotoxicity.[10] One of the 96 well multidishes was kept in the dark, while the other was irradiated for 6 min per well using a 10 mW 633 nm HeNe laser fitted with a biconvex diverging lens, giving a fluency rate of 29 $mW.cm^{-2}$ and a total light dose of 10.5 $J.cm^{-2}$. Light intensity was measured using a Power Max *500AD* Molectron Power Meter. The laser was positioned 50 cm above the cells. Following irradiation, the cells were incubated at 37 °C in a 5% CO_2 atmosphere for 48 h.

MTT reagent (10 µl, 5 $mg.ml^{-1}$ in PBS) was added to each well and the cells were incubated at 37 °C in a 5% CO_2 atmosphere for 4 h. The cell medium containing MTT reagent was then removed and the formazan was dissolved in DMSO (200 µl). The well contents were transferred to transparent 96 well multidishes and the absorbance of the formazan at 550 nm was measured using a MRX-Dynatech plate reader. Background absorbance at 550 nm of RPMI 1640 medium alone incubated with MTT reagent was subtracted from all measurements. Cell viability was calculated as a percentage of absorbance at 550 nm of untreated, non-irradiated HT-29 cells. All assays were performed in triplicate.

2.2.11 Competitive inhibition of jacalin targeted phototoxicity using methyl-α-galactopyranoside and asialofetuin

Methyl-α-D-galactopyranoside and asialofetuin (a glycoprotein expressing T antigens on its surface)[14] were used as competitive inhibitors of jacalin binding to HT-29 cells. The jacalin conjugated C11Pc-PEG gold nanoparticles in serum-free RPMI 1640 medium containing 1.5 mM L-Gln (500 µl, 0.5 µM C11Pc equivalent) were supplement with either 1 µM or 2 µM asialofetuin (40 kDa; Sigma-Aldrich), or with 50 mM or 100 mM methyl-α-D-galactopyranoside monohydrate (212.20 $g.mol^{-1}$; Alfa Aesar), and stored at 4 °C for 48 h. An MTT viability assay was performed, as described in **section 2.2.10**, 48 h following irradiation of the HT-29 cells incubated with jacalin conjugated C11Pc-PEG gold nanoparticles (0.5 µM C11Pc equivalent) in the presence of asialofetuin or methyl-α-D-galactopyranoside. Cell viability was calculated as a percentage of untreated HT-29 cells in RPMI 1640 medium supplemented with 1.5 mM L-Gln and 10% FBS alone, or in the presence of asialofetuin or methyl-α-D-galactopyranoside monohydrate. All assays were performed in triplicate.

2.2.12 ApoTox-Glo™ triplex assay following jacalin targeted PDT treatment of HT-29 cells

To establish the mechanism of jacalin mediated phototoxicity of the HT-29 cells, the ApoTox-Glo™ triplex assay (Promega) was performed on the cells incubated with jacalin conjugated C11Pc-PEG gold nanoparticles 48 h following irradiation. HT-29 cells were seeded onto two white opaque 96 well multidishes ($2x10^4$ cells per well) for 24 h. The cells were washed once in PBS (100 µl) and kept in serum-free RPMI 1640 medium supplemented with 1.5 mM L-Gln (50 µl), containing either jacalin conjugated or non-conjugated C11Pc-PEG gold nanoparticles (1 µM C11Pc equivalent). The cells were incubated for 3 h with the nanoparticle conjugates and washed 3 times in PBS (100 µl). Finally, RPMI 1640 medium supplemented with 10% FBS and 1.5 mM L-Gln (100 µl) was added to the cells. Staurosporine (20 µM) was used as a positive control for cell death predominantly *via* apoptosis.[10] One of the 96 well multidishes was kept in the dark, while the other was irradiated for 6 min per well using a 633 nm HeNe laser. The cells were then incubated at 37 °C in a 5% CO_2 atmosphere for 48 h.

A viability/cytotoxicity reagent was prepared using the ApoTox-Glo™ triplex assay kit by adding 10 µl of the viability substrate, glycylphenylalanyl-aminofluorocoumarin (GF-AFC),

and 10 µl of the cytotoxicity substrate, bis-alanylalanyl-phenylalanyl-rhodamine 110 (bis-AAF-R110) to 2 ml of Assay Buffer provided in the kit. The mixture was vortexed until both reagents were completely solubilised in the Assay Buffer. The viability/cytotoxicity reagent was then added to the cells (20 µl per well) and the multidishes were orbital shaken for 30 s at 500 RPM. The cells were then incubated at 37 °C in a 5% CO_2 atmosphere for 1 h. The products of the viability/cytotoxicity reagent were measured by fluorescence using an EnVision™ (Wallac) 2103 Multilabel Reader (Perkin Elmer). The fluorescence emission of the product of the GF-AFC viability substrate (aminofluorocoumarin) was measured using a 405 nm excitation filter and a 492 nm emission filter. The fluorescence emission of the product of the bis-AAF-R110 cytotoxicity substrate (rhodamine 110) was measured using a 492 nm excitation filter and a 530 nm emission filter. Background fluorescence of the viability/cytotoxicity reagent with RPMI 1640 medium alone was subtracted from all measurements. The reconstituted Caspase-Glo® 3/7 reagent and the cells were equilibrated to room temperature. Caspase-Glo® 3/7 reagent (100 µl) was then added to each well and the multidishes were orbital shaken for 30 s at 500 RPM. The cells were then incubated with the Caspase-Glo® 3/7 reagent for 30 min at room temperature. Active caspase 3/7 enzymes in apoptotic cells result in bioluminescence following the reaction between UltraGlo™ luciferase and aminoluciferin. Bioluminescence emission centred at 576 nm[15] was measured using an EnVision™ (Wallac) 2103 Multilabel Reader. Background bioluminescence of Caspase-Glo® 3/7 reagent with RPMI 1640 medium alone was subtracted from all measurements. All of the ApoTox-Glo™ triplex assays were performed in triplicate. The ApoTox-Glo™ triplex assay was then repeated a further time 6 h following irradiation of the HT-29 cells incubated with jacalin conjugated or non-conjugated C11Pc-PEG gold nanoparticles.

2.3 A comparative study of targeted phototoxicity of HT-29 colon and SK-BR-3 breast adenocarcinoma cells using jacalin or anti-HER-2 antibodies

2.3.1 Synthesis of jacalin and anti-HER-2 antibody conjugated C11Pc-PEG gold nanoparticles

Monoclonal rat IgG anti-HER-2 antibodies (77 kDa; Abcam) were conjugated to C11Pc-PEG gold nanoparticles synthesised in DMF using EDC/NHS chemistry, as described for jacalin in **section 2.2.6**. However, 37.04 µl anti-HER-2 antibodies (1 $mg.ml^{-1}$) was added to NHS ester-functionalised C11Pc-PEG gold nanoparticles (2 ml, in PBS (10 mM phosphate buffer, 150 mM NaCl, 100 µM $CaCl_2.2H_2O$, pH 7.4)) to obtain a final antibody concentration of 0.24 µM. Following 15 h of stirring, unbound antibodies were removed from the anti-HER-2 antibody conjugated C11Pc-PEG gold nanoparticles by six repeated ultrafiltrations in Vivaspin™ 500 tubes (100 kDa MWCO, PES) by centrifuging at 14,300 xg at 4 °C for 30 min. After each centrifugation, the nanoparticle conjugates were redispersed in PBS (500 µl; 10 mM phosphate buffer, 150 mM NaCl, 100 µM $CaCl_2.2H_2O$, pH 7.4). Jacalin conjugated C11Pc-PEG gold nanoparticles were also synthesised as described in **section 2.2.6**. The jacalin or anti-HER-2 antibody conjugated C11Pc-PEG gold nanoparticles prepared for incubation with HT-29 cells were redispersed in serum-free RPMI 1640 medium supplemented with 1.5 mM L-Gln after the fifth centrifugation. The conjugates prepared for incubation with SK-BR-3 cells were redispersed in serum-free DMEM medium supplemented with 1 mM L-Gln after the fifth centrifugation. All nanoparticle samples were appropriately diluted following removal of unbound jacalin or anti-HER-2 antibodies and stored at 4 °C.

2.3.2 Singlet oxygen measurements of the conjugated and non-conjugated C11Pc-PEG gold nanoparticles

The production of singlet oxygen by the irradiation of the jacalin conjugated, anti-HER-2 antibody conjugated or non-conjugated C11Pc-PEG gold nanoparticles was measured, as described in **section 2.2.2**. All singlet oxygen measurements were performed in PBS (10 mM phosphate buffer, 150 mM NaCl, 100 µM $CaCl_2.2H_2O$, pH 7.4).

2.3.3 Comparative targeted PDT of HT-29 cells – MTT Assay

An MTT viability assay was performed on HT-29 cells according to the procedure described in **section 2.2.3**. The cells were incubated for 3 h with 0.00-1.15 μM C11Pc equivalent of non-conjugated, jacalin conjugated or anti-HER-2 antibody conjugated C11Pc-PEG gold nanoparticles, then irradiated for 6 min per well. The MTT assay was performed 48 h following irradiation.

2.3.4 Comparative targeted PDT of SK-BR-3 cells – CellTiter-Blue™ Assay

A CellTiter-Blue™ viability assay was performed on SK-BR-3 cells according to the procedure outlined in **section 2.1.13**. The cells were incubated for 3 h with 0.00-1.15 μM C11Pc equivalent of non-conjugated, jacalin conjugated or anti-HER-2 antibody conjugated C11Pc-PEG gold nanoparticles, then irradiated for 6 min per well. The viability assay was performed 48 h following PDT treatment.

2.3.5 ApoTox-Glo™ triplex assay following targeted PDT treatment

Jacalin and anti-HER-2 antibody conjugated C11Pc-PEG gold nanoparticles were prepared, as described in **section 2.3.1**. In addition, SSA conjugated C11Pc-PEG gold nanoparticles were prepared according to the same procedure. SSA (31.74 μl, 1 $mg.ml^{-1}$) was added to NHS-ester functionalised C11Pc-PEG gold nanoparticles in PBS (2 ml; 10 mM phosphate buffer, 150 mM NaCl, 100 μM $CaCl_2.2H_2O$, pH 7.4) to obtain a final protein concentration of 0.24 μM. The mixture was stirred for 15 h and unbound SSA was removed from the nanoparticle conjugates by six repeated ultrafiltrations in Vivaspin™ 500 tubes, as described in **section 2.2.1**.

SK-BR-3 and HT-29 cells were trypsinised and seeded onto white opaque 96 well multidishes ($2x10^4$ cells per well) 24 h prior to incubation with the nanoparticle conjugates. The cells were then incubated for 3 h with jacalin conjugated, anti-HER-2 antibody conjugated or SSA conjugated C11Pc-PEG gold nanoparticles (0.1 μM or 1 μM C11Pc equivalent). Following incubation, the cells were irradiated for 6 min per well and the ApoTox-Glo™ triplex assay was performed 6 h after irradiation, as described in **section 2.2.12**. Cells not incubated with nanoparticles without irradiation were used as a control and staurosporine (20 μM) was used as a positive control for cytotoxicity primarily through the apoptotic pathway.[10]

2.3.6 Lysosomal colocalisation of targeted nanoparticle conjugates

HT-29 cells and SK-BR-3 cells were seeded onto 18 mm round glass coverslips 48 h prior to nanoparticle incubation, as described in **section 2.2.9**. The cells were then washed once in PBS (1 ml) and incubated for 3 h with serum-free RPMI 1640 medium (HT-29 cells) or serum-free DMEM medium (SK-BR-3 cells) containing jacalin or anti-HER-2 antibody conjugated C11Pc-PEG gold nanoparticles (1 μM C11Pc equivalent, 1 ml). Following incubation with the nanoparticles, the cells were washed 3 times in PBS (1 ml) and finally kept in their respective media containing 10% FBS (2 ml). The cells were incubated for 15 h at 37 °C in a 5% CO_2 atmosphere. Prior to imaging, the cells were incubated for 1 h with LysoSensor™ Green DND-189 (1 μM from 1 mM stock in DMSO; Invitrogen). The coverslips were mounted on a heated stage (37 °C) and 1 ml imaging medium (120 mM NaCl, 5 mM KCl, 2 mM $CaCl_2.2H_2O$, 1 mM $MgCl_2.4H_2O$, 1 mM NaH_2PO_4, 1 mM $NaHCO_3$, 25 mM HEPES, 11 mM glucose, and 1 $mg.ml^{-1}$ BSA) was added to each coverslip. The cells were visualised with DIC imaging using transmitted light from a 458 nm Argon laser. The fluorescence of the C11Pc-PEG gold nanoparticles was visualised using excitation from a 633 nm HeNe laser and the red emission was collected using a 650 nm long pass filter. The fluorescence of the LysoSensor™ Green DND-189 was visualised using excitation from a 458 nm Argon laser and the green emission was collected using a 475-525 nm band pass filter. Colocalisation of the C11Pc-PEG gold nanoparticles with the LysoSensor™ Green DND-189 was assessed by the yellow coloration of the merged red and green fluorescence images overlaid with the DIC images.

2.4 Sonodynamic therapy (SDT) of HT-29 colon adenocarcinoma cells using titanium dioxide nanoparticles

2.4.1 Synthesis of tetramethylammonium hydroxide capped titanium dioxide nanoparticles

Synthesis of titanium dioxide (TiO_2) nanoparticles capped with tetramethylammonium hydroxide (TiO_2NP.TMAOH) was achieved according to a previously reported protocol.[16] Tetramethylammonium hydroxide pentahydrate (TMAOH, 0.2572 mg, 181.15 $g.mol^{-1}$; Sigma-Aldrich) was dissolved in water (150 ml) in a 250 ml 2-necked round bottom flask with continuous stirring. The solution of TMAOH in the round bottom flask was stirred in an ice bucket and cooled to 2 °C. The glassware used to prepare all of the titanium (IV) butoxide solutions was dried in an oven at 70 °C before use. Titanium (IV) butoxide

($Ti(OBu)_4$, 360.74 µl, 1 $g.ml^{-1}$, 340.32 $g.mol^{-1}$; Sigma-Aldrich) was added to n-butanol (10 ml; Sigma-Aldrich) and thoroughly mixed. When the temperature of the TMAOH solution reached 2 °C, the solution was rigorously stirred and the $Ti(OBu)_4$ solution in n-butanol (10 ml) was rapidly added. Immediately after addition, white precipitates of titanium hydroxide formed and the reaction mixture was left to stand for 10 min at 2 °C. The flask was then transferred to a reflux condenser and heated to 100 °C for 6 h under continuous argon flow. The precipitates eventually dispersed to form a fine white sol of TiO_2NP.TMAOH particles with complete anatase crystallinity, as previously reported.[16] The sol was then cooled to room temperature and stored in a darkened solution bottle at room temperature. Assuming that all the $Ti(OBu)_4$ reacted, the final concentration of TiO_2 present in the sol was 6.61 mM.

2.4.2 Thermal annealing of polyacrylic acid onto the TiO_2NP.TMAOH particles

Polyacrylic acid (PAA, 1.8 kDa; Sigma-Aldrich) was thermally annealed onto the surface of TiO_2 nanoparticles according to a previously reported protocol.[17] The as-synthesised TiO_2NP.TMAOH particle sol (30 ml) was placed in a round bottom flask and the water/butanol mixture was removed by rotary evaporation under reduced pressure at 60 °C. The dry TiO_2NP.TMAOH particle residue was weighed (*ca.* 6.5 mg) and dissolved in a 1% aqueous nitric acid solution (32.5 ml, pH 1; Fisher Scientific) to obtain a final TiO_2NP.TMAOH particle sol concentration of 20% w/v (6.10 mM TiO_2). The TiO_2NP.TMAOH particle sol was sonicated (30 min, 37 kHz) to disperse the nanoparticles. An aliquot of the acidified aqueous TiO_2NP.TMAOH particle sol (750 µl) was added to DMF (10 ml) in a 100 ml round bottom flask with continuous stirring. A solution of PAA (5 ml, 30 $mg.ml^{-1}$ in DMF) was prepared and added to the DMF solution containing the TiO_2NP.TMAOH particle sol. The mixture was then heated to 150 °C with continuous stirring for 30 min to remove the water, which reportedly hampers the annealing process.[17] A reflux condenser was then connected to the flask and the reaction was left stirring at 150 °C for a further 5.5 h. The reaction mixture containing *ca.* 0.305 mM TiO_2 equivalent of nanoparticles was cooled to room temperature and stored in a darkened solution bottle at room temperature.

An excess of THF (10 ml) was added to an aliquot of the TiO_2NP.PAA particle solution in DMF (5 ml). The white precipitates containing the TiO_2NP.PAA particles were collected by centrifugation at 2,000 xg at 4 °C for 10 min. The supernatant containing unbound PAA in

DMF was removed and the wash step was repeated a further two times. Following the third centrifugation, the pellets containing the TiO_2NP.PAA particles were readily dissolved in water (15 ml) to obtain a final nanoparticle concentration of *ca.* 0.102 mM TiO_2 equivalent (*ca.* 1% w/v).

Another method for removing DMF and eventually unbound PAA was attempted through rotary evaporation of the DMF reaction mixture containing TiO_2NP.PAA particles. An aliquot of the crude DMF reaction mixture (5 ml) was dried using rotary evaporation under reduced pressure at 70 °C. The TiO_2NP.PAA particle residue was redissolved in water (15 ml) although large aggregates were observed that remained even after sonication (37 kHz, 1 h).

2.4.3 Imaging of TiO_2NP.TMAOH and TiO_2NP.PAA particles

Samples of as-synthesised TiO_2NP.TMAOH particles, TiO_2NP.PAA particles in DMF, TiO_2NP.PAA particles purified using THF precipitation and TiO_2NP.PAA particles dried and reconstituted in water were imaged using TEM, as described in **section 2.1.6**.

2.4.4 Photocatalytic ·OH production using TiO_2NP.TMAOH particles - coumarin-3-carboxylic acid

A 10% v/v dilution of as-synthesised TiO_2NP.TMAOH particles in water (0.661 mM) was prepared in a solution of coumarin-3-carboxylic acid (3 ml, 0.5 mM in DMF; Sigma-Aldrich). The mixture was placed in a 3.5 ml stoppered quartz fluorescence cuvette and then exposed to UV light (254 nm, 1.12 $mW.cm^{-2}$) for 5 min using a 4W UVG-11 Mineralight® UV lamp. Fluorescence emission was recorded using a Hitachi F-4500 fluorimeter from 390 nm to 550 nm using excitation at 367 nm before, immediately after and 1 h after irradiation.

2.4.5 Photocatalytic ·OH production using TiO_2NP.TMAOH particles - methylene blue

An aqueous solution of methylene blue (1 ml, 10 μM, 373.19 $g.mol^{-1}$; Sigma-Aldrich) was placed in a 1.5 ml stoppered quartz UV-visible absorbance cuvette and exposed to UV light (254 nm, 1.12 $mW.cm^{-2}$) for 15 min. UV-visible absorption was measured every 5 min. The experiment was repeated in the presence of a 10% v/v dilution of as-synthesised TiO_2NP.TMAOH particles in water (0.661 mM TiO_2).

2.4.6 Sonocatalytic ·OH production using TiO_2NP.TMAOH particles - methylene blue

An aqueous solution of methylene blue (1 ml, 10 μM) was prepared and placed in a 1.5 ml stoppered quartz UV-visible absorbance cuvette. JPM ultrasound transmission gel (JPM Products Ltd.) was applied to one side of the cuvette and the solution was exposed to ultrasound irradiation (1 MHz, 0.5 $W.cm^{-2}$) for 15 min in the dark using a JPM KUP-200 Ultrasound Transducer (JPM Products Ltd.). UV-visible absorption was measured every 5 min. The experiment was repeated in the presence of a 10% v/v dilution of as-synthesised TiO_2NP.TMAOH particles in water (0.661 mM TiO_2).

2.4.7 *In situ* sol-gel synthesis of TiO_2NP.PAA particles

TiO_2 nanoparticles coated with PAA were synthesised according to an adapted version of a previously reported protocol.[18] An aqueous solution of PAA (4.5 g, 30 $mg.ml^{-1}$, 150 ml) was prepared in a 250 ml 2-necked round bottom flask and cooled to 2 °C in an ice bath with continuous stirring. A pre-prepared solution of $Ti(OBu)_4$ (360.74 μl in 10 ml THF) was then rapidly added and the cloudy white mixture was left to stand for 10 min at 2 °C. The flask was then transferred to a reflux condenser and heated to 100 °C for 6 h under continuous argon flow. The white TiO_2NP.PAA sol was then cooled to room temperature and stored in a darkened bottle at 4 °C. Assuming that all the $Ti(OBu)_4$ reacted, the final concentration of TiO_2 present in the sol was 6.61 mM.

2.4.8 Characterisation of TiO_2NP.TMAOH and TiO_2NP.PAA particles

As-synthesised TiO_2NP.TMAOH and TiO_2NP.PAA particles were characterised using UV-visible absorption spectrophotometry, Dynamic Light Scattering (DLS) and TEM imaging. DLS particle size analysis of the TiO_2NP.TMAOH or TiO_2NP.PAA particles (1 ml, 1% v/v dilution) was performed in a 1.5 ml stoppered quartz UV-visible absorbance cuvette using a Malvern Zetasizer Nano-ZS. TEM imaging was performed, as described in **section 2.1.6**.

2.4.9 Sonocatalytic singlet oxygen production using TiO_2NP.PAA particles - ADPA

Water (941.2 µl) was placed in a 1.5 ml stoppered quartz UV-visible absorbance cuvette and ADPA (58.8 µl, 1.7 mM stock in methanol) was added to obtain a final ADPA concentration of 100 µM. JPM ultrasound transmission gel was applied to one side of the cuvette and the solution was exposed to ultrasound irradiation (1 MHz, 0.5 $W.cm^{-2}$) for 15 min in the dark. UV-visible absorption spectra were recorded every 5 min. The experiment was repeated in the presence of a 10% v/v dilution of as-synthesised TiO_2NP.PAA in water (0.661 mM TiO_2).

Both experiments, with and without TiO_2NP.PAA, were repeated in methanol. Firstly, the effect of 15 min ultrasound (1 MHz, 0.5 $W.cm^{-2}$) on ADPA (100 µM, 1 ml in methanol) was assessed. In addition, a 10% v/v aqueous dilution of TiO_2NP.PAA (1 ml) was dried using rotary evaporation at 60 °C under reduced pressure. The sample was redissolved in methanol (941.2 µl) and ADPA (58.8 µl, 1.7 mM stock in methanol) was added to obtain a 100 µM solution of ADPA in methanol with a 10% v/v dilution of TiO_2NP.PAA (0.661 mM TiO_2). The effect of 15 min ultrasound (1 MHz, 0.5 $W.cm^{-2}$) on this sample was also assessed. UV-visible absorption spectra were recorded every 5 min during ultrasound irradiation.

2.4.10 Methanol as a scavenger for $^{\bullet}OH$ but not for singlet oxygen

Photobleaching of ADPA (100 µM in water, 1.7 mM stock in methanol) upon ultrasound exposure was repeated, as described in **section 2.4.9**, in the presence of methylene blue (10 µM). To investigate the effect of methanol on the ultrasound induced degradation of methylene blue, the experiment was also repeated in the absence of methanol. An aqueous solution of ADPA (100 µM, 1.7 mM stock in water) containing methylene blue (10 µM) was prepared and exposed to ultrasound irradiation for 15 min (1 MHz, 0.5 $W.cm^{-2}$), as described in **section 2.4.9**.

The sonocatalytic effect of TiO_2NP.PAA on the photobleaching of ADPA was compared in the presence or absence of methanol. The experiments on ultrasound irradiation of ADPA solutions in water with and without a 10% v/v dilution of TiO_2NP.PAA (0.661 mM TiO_2), as described in **section 2.4.9**, were repeated using stock solutions of ADPA in methanol or water (1.7 mM).

2.4.11 *In situ* sol-gel synthesis of dispersed TiO_2NP.PAA nanoparticles

The procedure in **section 2.4.7** describes the rapid addition of $Ti(OBu)_4$ (360.74 µl in 10 ml THF) to an aqueous solution of PAA (4.5 g, 30 $mg.ml^{-1}$, 150 ml). In this instance a THF solution (10 ml) containing both $Ti(OBu)_4$ (360.74 µl) and PAA (4.5 g) was prepared with the intention of adding water (150 ml) dropwise to control the hydrolysis of the $Ti(OBu)_4$. However, the moderately low solubility of PAA in THF resulted in a gel-like formation. Another THF solution (10 ml) was prepared using a 30-fold dilution of both the $Ti(OBu)_4$ (12.02 µl) and the PAA (150 mg); however, the solubility of the polymer was still low. The ratio of water:THF for the reaction was then decreased and 60 ml of THF was used to prepare a solution of $Ti(OBu)_4$ (12.02 µl) and PAA (150 mg). Stirring for 10 min was required to solubilise all the PAA to form a transparent colourless solution. Water (100 ml) was then added dropwise at a rate of 1 $drop.s^{-1}$ with continuous vigorous stirring. Once the addition of water was complete, the transparent colourless reaction mixture was heated to 80 °C for 1 h to remove the THF in order to increase the water:THF ratio and initiate the hydrolysis of the $Ti(OBu)_4$. As the THF evaporated, the reaction mixture became increasingly opaque. Boiling of the reaction mixture ceased after *ca.* 1 h of heating at 80 °C, indicating that most of the THF had evaporated. A reflux condenser was then connected to prevent water evaporation and the reaction was exposed to hydrothermal treatment at 90 °C for a further 5 h with rigorous stirring under continuous argon flow. The reaction mixture became transparent once again following *ca.* 3 h of hydrothermal treatment. The cooled solution of TiO_2NP.PAA (x/30) nanoparticles (0.353 mM TiO_2) was then stored in a darkened solution bottle at 4 °C. As-synthesised TiO_2NP.PAA (x/30) nanoparticles were characterised using UV-visible absorption spectrophotometry, DLS (**section 2.4.8**) and TEM imaging (**section 2.1.6**).

2.4.12 Purification of the TiO_2NP.PAA (x/30) nanoparticles

Removal of unbound PAA was initially attempted through repeated ultrafiltrations using Vivaspin™ 20 tubes (30 kDa MWCO, PES). Aliquots of as-synthesised TiO_2NP.PAA (x/30) nanoparticles (15 ml) were centrifuged in Vivaspin™ 20 tubes (30 kDa MWCO, PES) at 8,000 xg at 10 °C for 30 min. Water (15 ml) was then added to the TiO_2NP.PAA (x/30) nanoparticles and the ultrafiltration step was repeated a further 9 times. PAA content in the filtrate was assessed using the UV-visible absorption band centred at 217 nm. The TiO_2NP.PAA (x/30) nanoparticle samples were characterised using UV-visible absorption spectrophotometry following 5 and 10 filtration steps.

Gel filtration chromatography was also used in an attempt to remove unbound PAA. PD-10 desalting columns (5 kDa MWCO, 50 x 14 mm Sephadex® G-25; GE Healthcare Life Sciences) were conditioned according to the manufacturer's protocol. The buffer reservoir was removed and the column was equilibrated with 25 ml of water (2.5 ml aliquots). A freshly prepared sample of TiO_2NP.PAA (x/30) nanoparticles (*ca.* 100 ml) was concentrated to *ca.* 2.5 ml using rotary evaporation at 60 °C under reduced pressure and loaded onto the PD-10 column. The TiO_2NP.PAA (x/30) nanoparticle samples were then eluted with 10 x 3.5 ml aliquots of water. All elution fractions were then characterised using UV-visible absorption spectrophotometry. Elution fractions containing the highest TiO_2 content ($Abs_{270\ nm} \geq 1.5$) were pooled and concentrated to *ca.* 2.5 ml using rotary evaporation at 60 °C under reduced pressure. The PD-10 column was equilibrated once more with water (25 ml, 2.5 ml aliquots) and the nanoparticle concentrate (*ca.* 2.5 ml) was loaded onto the column again. This process was repeated a total of 3 times. All the elution fractions were characterised using UV-visible absorption spectrophotometry.

To obtain a higher resolution of separation between TiO_2NP.PAA and unbound PAA, a gel filtration chromatography column (300 x 14 mm) was packed with Sephadex® G-25 (5 kDa MWCO, Sigma-Aldrich) and equilibrated with 50 ml water. A peristaltic pump was used to increase the flow rate and separation resolution through the column. A freshly prepared sample of TiO_2NP.PAA (x/30) nanoparticles (*ca.* 100 ml) was concentrated to *ca.* 5 ml using rotary evaporation at 60 °C under reduced pressure and loaded onto the Sephadex® G-25 column. The sample was then eluted with 12 x 5 ml aliquots of water using a peristaltic pump and each elution fraction was characterised using UV-visible absorption spectrophotometry. Elution fractions containing the highest TiO_2 content ($Abs_{270\ nm} \geq 1.5$) were pooled, concentrated to *ca.* 5 ml using rotary evaporation at 60 °C under reduced pressure and loaded onto the Sephadex® G-25 column once again. All the elution

fractions were characterised using UV-visible absorption spectrophotometry. Elution fractions containing the highest TiO_2 content (Abs $_{270\,nm} \geq 1.5$) were pooled, concentrated to *ca.* 2.5 ml (*ca.* 14.13 mM TiO_2) using rotary evaporation at 60 °C under reduced pressure and stored at 4 °C.

2.4.13 Sonocatalytic efficiency of purified TiO_2NP.PAA (x/30) nanoparticles

In order to determine whether TiO_2NP.PAA (x/30) nanoparticle samples purified twice using the 300 x 14 mm Sephadex® G-25 column retained their ability to enhance the rate of ADPA photobleaching upon ultrasound irradiation, a 10% v/v aqueous dilution of the 2.5 ml purified sample (1.41 mM TiO_2) containing ADPA (100 μM) in water was prepared and exposed to 15 min ultrasound irradiation (1 MHz, 0.5 $W.cm^{-2}$), as described in **section 2.4.9**. UV-visible absorption spectra were recorded every 5 min. The photobleaching of ADPA was compared to that of an aqueous solution of ADPA (100 μM) without nanoparticles.

Additionally, the sonochemical degradation of methylene blue (10 μM) was investigated, as described in **section 2.4.6**, following 15 min ultrasound irradiation (1 MHz, 0.5 $W.cm^{-2}$) in the absence or presence of a 10% v/v dilution of the purified TiO_2NP.PAA (x/30) nanoparticles (1.41 mM TiO_2).

2.4.14 TEM and SEM imaging, and elemental analysis of purified TiO_2NP.PAA (x/30) nanoparticles

TEM imaging of the TiO_2NP.PAA (x/30) nanoparticle samples purified twice using the 300 x 14 mm Sephadex® G-25 column was performed as described in **section 2.4.12**. Scanning electron microscopy (SEM) was performed using a JEOL JSM 5900 LV scanning electron microscope. Two aliquots of purified TiO_2NP.PAA (x/30) nanoparticles (500 μl) were centrifuged in Vivaspin™ 500 (100 kDa MWCO, PES) tubes at 14,300 xg at 4 °C for 30 min. One aliquot was redispersed in water (500 μl) and the remaining aliquot was redispersed in HEPES buffered saline (500 μl; 10 mM HEPES, 150 mM NaCl, pH 7.4). The nanoparticle samples (3 x 100 μl aliquots) in water or HEPES buffered saline were placed onto aluminium SEM imaging stubs and dried in a 60 °C oven for 15 h. Samples were coated with gold prior to SEM imaging using a Quorum Technologies Gold Coater CC7640. Topographic contrast images and chemical contrast images were obtained using

secondary electron imaging (SEI) and backscatter electron imaging (BSEI) techniques, respectively. Elemental analysis of the TiO_2NP.PAA (x/30) nanoparticle sample in water was performed using an Oxford INCA Energy-Wave System integrated with the SEM microscope. The assistance of Dr Bertrand Leze (School of Environmental Sciences) who performed the SEM imaging is gratefully acknowledged.

2.4.15 HT-29 cell tolerance to ultrasound

HT-29 colon cancer cells were cultured in RPMI 1640 medium supplemented with 1.5 mM L-Gln and 10% FBS, as described in **section 2.2.3**. At *ca.* 75% confluency, the cells were trypsinised and seeded in transparent 6 well multidishes in 1 ml aliquots ($2x10^5$ cells per well) 24 h prior to ultrasound treatment. JPM ultrasound transmission gel was applied to the base of each well and the cells were then exposed to 0, 15, 30 or 60 s of ultrasound irradiation (1 MHz, 0.5 $W.cm^{-2}$). Staurosporine (20 μM) was used as a positive control for cytotoxicity.[10] The cells were then incubated for 48 h at 37 °C in a 5% CO_2 atmosphere. MTT reagent (100 μl, 5 $mg.ml^{-1}$ in PBS) was added to each well and the cells were incubated at 37 °C in a 5% CO_2 atmosphere for 4 h. The cell medium was then removed and the formazan crystals produced by the viable cells were dissolved in DMSO (6 ml). Aliquots of the well contents (200 μl) were transferred to transparent 96 well multidishes and the absorbance of the formazan at 550 nm was measured using a MRX-Dynatech plate reader. Background absorbance at 550 nm of RPMI 1640 medium alone incubated with MTT reagent was subtracted from all measurements. Cell viability was calculated as a percentage of absorbance at 550 nm of untreated, non-irradiated HT-29 cells. All assays were performed in triplicate.

2.4.16 Attenuation of ultrasound through 6 and 48 well multidishes

Solutions of ADPA (100 μM, 1 ml) in RPMI 1640 medium supplemented with 1.5 mM L-Gln and 10% FBS were prepared and placed in one well of a 6 well multidish or a 48 well multidish. JPM ultrasound transmission gel was applied to the base of each well and the ADPA solutions were exposed to 15 min of ultrasound irradiation (1 MHz, 0.5 $W.cm^{-2}$). At 5 min intervals, the ADPA solutions were removed from the wells, transferred to a 1.5 ml quartz cuvette and the UV-visible absorption spectra were recorded.

2.4.17 MTT viability assay of HT-29 cells following SDT using TiO_2NP.PAA (x/30) nanoparticles

HT-29 colon cancer cells were cultured in RPMI 1640 medium supplemented with 1.5 mM L-Gln and 10% FBS, as described in **section 2.2.3**. At *ca.* 75% confluency the cells were trypsinised and seeded onto 48 well multidishes in 1 ml aliquots (2.29×10^4 cells per well) 24 h prior to ultrasound treatment. The well contents were then removed, the cells were washed once in PBS (1 ml) and incubated for 3 h in RPMI 1640 medium supplemented with 1.5 mM L-Gln containing 0, 0.29, 0.74 or 1.47 mM TiO_2 equivalent of TiO_2NP.PAA (x/30) nanoparticles. The well contents were then removed and the cells were washed 3 times in PBS (1 ml). Finally, the cells were kept in RPMI 1640 medium (1 ml) supplemented with 10% FBS and 1.5 mM L-Gln. JPM ultrasound transmission gel was applied to the base of each well and the cells were then exposed to 30 s of ultrasound irradiation (1 MHz, 0.5 $W.cm^{-2}$). HT-29 cells incubated with the TiO_2 nanoparticles but not exposed to ultrasound irradiation were used as a control. Staurosporine (20 μM) was used as a positive control for cytotoxicity.[10] Following ultrasound irradiation, the cells were incubated at 37 °C in a 5% CO_2 atmosphere. 48 h after SDT treatment, an MTT viability assay was performed as described in **section 2.4.15**, with the variation that 12.5 μl MTT was added to each well and the formazan crystals were finally dissolved in 2 ml DMSO.

2.5 References

1. Hardman, K. D.; Ainsworth, C. F. *Biochemistry* **1976**, *15*, 1120-1128.
2. Wang, J.; Duan, T.; Sun, L.; Liu, D.; Wang, Z. *Anal. Biochem.* **2009**, *392*, 77-82.
3. Kim, T.; Lee, C. H.; Joo, S. W.; Lee, K. *J. Colloid Interface Sci.* **2008**, *318*, 238-243.
4. Obaid, G. *CHE-3FOY Final Year Research Project* **2009**, *University of East Anglia*.
5. Chambrier, I.; Cook, M. J.; Russell, D. A. *Synthesis* **1995**, 1283-1286.
6. Brust, M.; Walker, M.; Bethell, D.; Schiffrin, D. J. *J. Chem. Soc., Chem. Commun.* **1994**, *7*, 801-802.
7. Stuchinskaya, T.; Moreno, M.; Cook, M. J.; Edwards, D. R.; Russell, D. A. *Photochem. Photobiol. Sci.* **2011**, *10*, 822-831.
8. Camerin, M.; Magaraggia, M.; Soncin, M.; Jori, G.; Moreno, M.; Chambrier, I.; Cook, M. J.; Russell, D. A. *Eur. J. Cancer* **2010**, *46*, 1910-1918.
9. Lindig, B. A.; Rodgers, M. A. J.; Schaap, A. P. *J. Am. Chem. Soc.* **1980**, *102*, 5590-5593.
10. Bertrand, R.; Solary, E.; O'Connor, P.; Kohn, K. W.; Pommier, Y. *Exp. Cell Res.* **1994**, *211*, 314-321.
11. O'Brien, J.; Wilson, I.; Orton, T.; Pognan, F. *Eur. J. Biochem.* **2000**, *267*, 5421-5426.
12. Jeyaprakash, A. A.; Rani, P. G.; Reddy, G. B.; Banumathi, S.; Betzel, C.; Sekar, K.; Surolia, A.; Vijayan, M. *J. Mol. Biol.* **2002**, *321*, 637-645.
13. Obaid, G.; Chambrier, I.; Cook, M. J.; Russell, D. A. *Angew. Chem. Int. Ed.* **2012**, *51*, 6158-6162.
14. Sharma, A.; Sharma, S.; Khuller, G. K. *J. Antimicrob. Chemother.* **2004**, *54*, 761-766.
15. Reddy, G. R.; Thompson, W. C.; Miller, S. C. *J. Am. Chem. Soc.* **2010**, *132*, 13586-13587.
16. Chemseddine, A.; Moritz, T. *Eur. J. Inorg. Chem.* **1999**, *1999*, 235-245.
17. Kanehira, K.; Banzai, T.; Ogino, C.; Shimizu, N.; Kubota, Y.; Sonezaki, S. *Colloids Surf., B* **2008**, *64*, 10-15.
18. Chen, H. J.; Jian, P. C.; Chen, J. H.; Wang, L.; Chiu, W. Y. *Ceram. Int.* **2007**, *33*, 643-653.

Chapter 3

Concanavalin A conjugated phthalocyanine-PEG gold nanoparticles for targeted PDT of MCF-7 and SK-BR-3 human breast adenocarcinoma cells

This chapter describes the use of Concanavalin A (Con A) to target human breast adenocarcinoma cells for cancer specific photodynamic therapy with gold nanoparticles carrying a hydrophobic zinc phthalocyanine photosensitiser.

3.1 Introduction

3.1.1 Reactivity of Concanavalin A towards breast cancer cells

The discovery that some lectins could selectively agglutinate cancer cells gave a preliminary indication that differences in surface expressed carbohydrates are present between healthy and cancerous cells.[1,2] Concanavalin A (Con A) is a 104 kDa tetrameric α-mannose (α-Man)-binding lectin from the jack bean (*Canavalia ensiformis*), which has a greater affinity towards polymannose (450 Man residues, K_d 0.23 ± 0.02 μM) than to the α-Man monosaccharide (K_d 41 ± 5.4 μM).[3-5] Con A has been extensively studied due to the high prevalence of α-linked polymannose residues in many core glycoconjugate sequences found in yeast cell walls and mammalian T-lymphocytes, amongst several other glycan complexes.[4,6,7] Sumner first extracted Con A in 1918 and it was only discovered 17 years later that Con A had the capacity to agglutinate horse, dog, cat, rabbit, guinea pig, and rat erythrocytes.[8,9] It must be noted that Con A can weakly agglutinate human erythrocytes. However, its haemagglutinating activity considerably increases upon neuraminidase, pronase, papain, trypsin or chymotrypsin treatment of the erythrocytes.[9-11] Con A has been found to agglutinate some bacteria, spleen cells and lymphocytes.[4,9] The α-Man-specific lectin is also routinely used in research as a potent T-lymphocyte mitogen.[12] Con A is a typical homotetrameric hololectin (**Figure 3.1**), which contains a single calcium ion and a manganese ion at each of its four carbohydrate binding domains.[3,13] The tetravalance of Con A is responsible for the lectin's ability to crosslink glycoconjugates and cells.[4,13] Above pH 5.6 Con A is largely in its tetrameric form, existing as a pair of dimers associated with hydrogen bonds; however, below pH 5.6 Con A dissociates into dimers.[14,15]

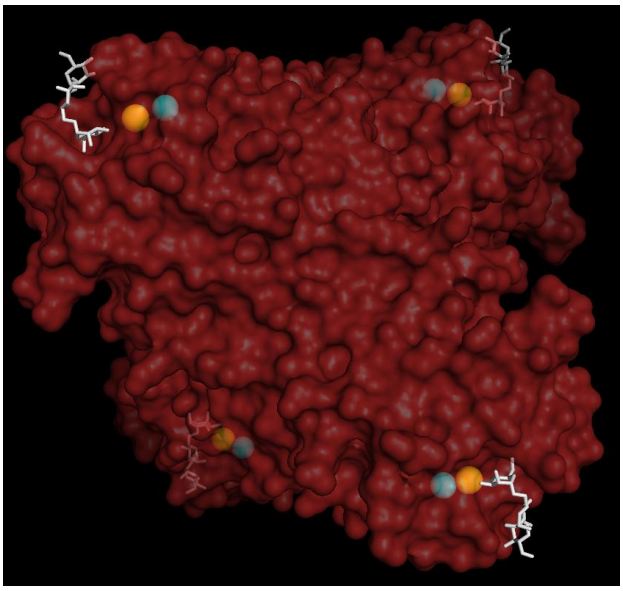

Figure 3.1 **A PyMOL generated image of Con A (PDB ID 1CVN[16]) bound to four synthetic trimannoside analogues (white). A calcium ion (orange) and a manganese ion (cyan) are present at each carbohydrate binding domain.**

Numerous studies have investigated the various applications of Con A, and some have demonstrated the ability of the lectin to selectively bind to tumour cells.[17] Furmanski *et al.* analysed a series of breast cancer biopsies and assessed the level of Con A reactivity towards the tumour homogenates.[17] The extent of Con A reactivity was correlated with the probability of tumour recurrence.[17] Voyles *et al.* conducted a cell-based study on the specificity of Con A towards tumour cells grown in culture.[18] The study concluded that Con A was reactive towards MCF-7, BT-20, MDA-MB 157, ALAB-496 and SK-BR-3 breast cancer cells.[18]

Further biological effects of Con A binding include apoptosis induction, which provides further potential for multimodal cancer therapy.[19] Liu *et al.* found that Con A interacts with glycoproteins on A375 melanoma cells and triggers apoptosis through both mitochondrial dependent and caspase dependent pathways.[19] Studies reviewed by Lei and Chang have shown that Con A can also induce autophagic cell death, activation of local T-lymphocytes, and induce hepatoma antigen specific T-cell memory.[20] Another study reported the *in vivo* inhibition of polyoma 3T3 tumour development in hamsters following intravenous administration of Con A (1 $mg.kg^{-1}$).[21] However, intravenous administration of the lectin also resulted in multiple adverse effects, such as liver injury through Con A induced hepatocyte apoptosis.[21] Such damage to hepatocytes resembles viral or autoimmune

hepatitis.[21] Indications of Con A within medicine are largely based on diagnostics, which involve quantification of cancer markers in the serum, such as α-fetoprotein (AFP).[22]

Nanoparticles have also been used with Con A for analytical assays that probe glycan expression. For example, both Con A and horseradish peroxidase (HRP) were bound onto gold nanoparticles and used in conjunction with nanohorn constructs to electrochemically monitor the dynamic carbohydrate expression of cancer cells in response to drugs.[23] Another study described the development of an electrochemical sensor using Con A functionalised gold nanoparticles and Con A coated gold electrodes for the qualitative and quantitative analysis of K562 leukaemia cell surface glycans.[24] Wang *et al.* also used gold nanoparticles functionalised with a series of lectins including Con A to colorimetrically probe the binding of these lectins to a number of cells lines.[25,26]

3.1.2 The dimeric succinylated derivative of Con A

Previous studies have found that by altering the quaternary structure of Con A, the biological effects the lectin exhibits can vary hugely.[4,27] A study by Gunther *et al*. investigated the biological activities of Con A and two dimeric derivatives of Con A: succinyl-Con A (S-Con A) and acetyl-Con A.[4] The mitogenicity of Con A towards mouse spleen lymphocytes was compared to that of S-Con A. It was found that S-Con A continued to stimulate cell proliferation at concentrations above 5 $\mu g.ml^{-1}$, whereas at those concentrations Con A became cytotoxic.[4] Sheep erythrocyte agglutination by the lectin was also greatly hindered by succinylation, possibly due to a decrease in its carbohydrate valence. Importantly, the individual glycan binding capacity of each Con A carbohydrate binding domain was unaltered following succinylation.[4] The structure of S-Con A is shown in **Figure 3.2**, highlighting the binding of the lectin to a synthetic bivalent mannoside derivative. The succinate molecule that serves to stabilise the dimeric lectin is also shown, in addition to the calcium and manganese metal ions at each carbohydrate binding domain.

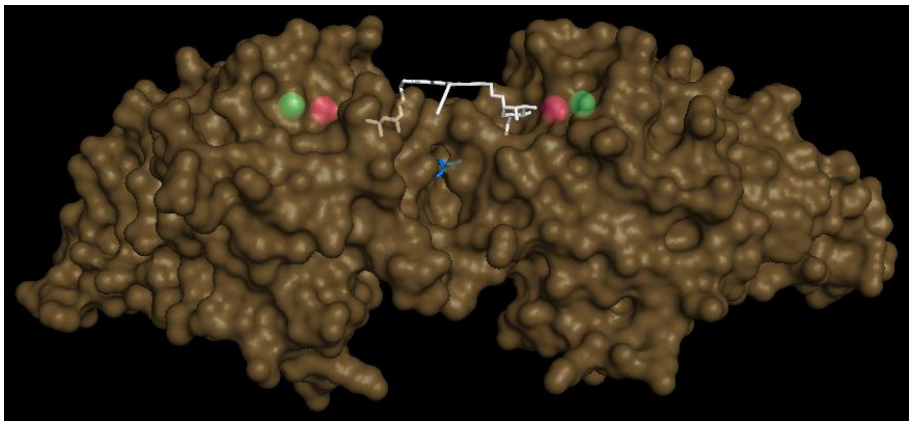

Figure 3.2 **A PyMOL generated image of S-Con A (PDB ID 1QGL[28]) bound to a synthetic bivalent mannoside ligand (white). The succinate molecule is shown in blue, the calcium ions are magenta and the manganese ions are green.**

S-Con A shows greater therapeutic potential than Con A for a number of reasons. S-Con A has a higher threshold for erythrocyte agglutination (>0.5 $mg.ml^{-1}$), it does not crosslink membrane receptors, and is less cytotoxic than the native lectin.[4] Unlike native Con A, S-Con A was also found to be unable to induce hepatitis *in vivo* within a mouse model, and was also unable to stimulate the secretion of MMP-2, an enzyme associated with cancer metastasis.[29,30]

Although initially S-Con A appears to be a more successful candidate for cancer cell targeting, it exhibits some limitations. The major potential limitation of using S-Con A for targeted treatment is its sustained mitogenic effect upon binding to cell surface glycans, with increasing concentrations of the lectin.[4] However, its superior characteristics mean that S-Con A could be an important targeting agent for selective PDT treatment.

3.2 Results and Discussion

3.2.1 Colorimetric labelling of breast cancer cells using lectin-gold nanoparticle conjugates

Citrate capped gold nanoparticles (*ca.* 16 nm in diameter) were synthesised according to an adapted version of the Turkevich method,[31] as described in **section 2.1.1**. Sodium citrate acts as both the reducing and capping agent, providing the gold nanoparticles with electrostatic stability in aqueous media. The nanoparticles exhibit an intense surface plasmon absorption band centred at 520 nm, as shown in the UV-visible absorption spectrum in **Figure 3.3** (**A**). The concentration of the nanoparticles was determined from the absorption band maximum at 520 nm using an extinction coefficient (ε_{520nm}) of 2.4×10^8 $M^{-1}.cm^{-1}$.[32] The surface plasmon absorption of the nanoparticles gives rise to the intense red colour observed in **Figure 3.3** (**B**).

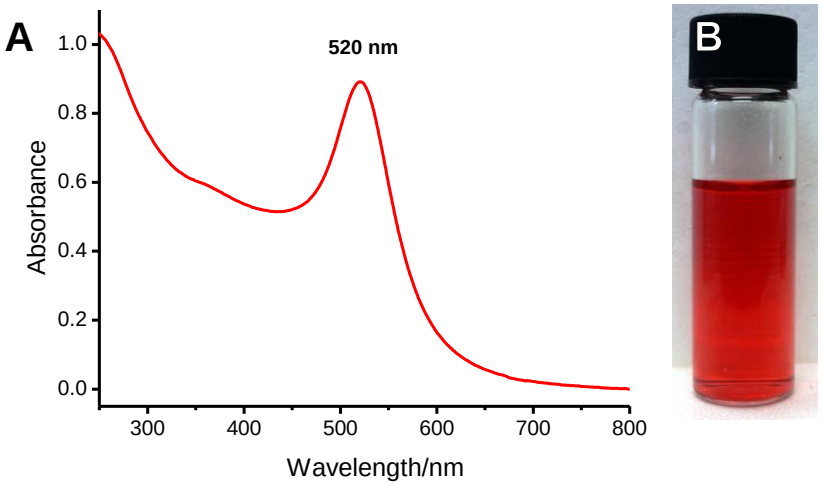

Figure 3.3 **A) A UV-visible absorption spectrum of citrate capped gold nanoparticles (3.72 nM) with a surface plasmon absorption band centred at 520 nm. B) An aqueous solution of the citrate capped gold nanoparticles.**

Plasmonic nanostructures, such as gold and silver nanoparticles display a variety of size and shape dependent colours, which can be used for diagnostics, bioimaging, sensing and bioanalytics.[33,34] The unique colouration of gold nanoparticles has been previously exploited for the colorimetric labelling of live cells using lectin functionalised particles.[25,26] In a study by Wang *et al.*,[25] streptavidin coated gold nanoparticles were functionalised with biotinylated lectins and used to assess the interaction of the conjugates with a

number of cancerous and healthy cell lines. This procedure was adapted in an attempt to colorimetrically assess the affinity of gold nanoparticles modified with Con A and S-Con A towards MCF-7 and SK-BR-3 human breast adenocarcinoma cells. The heterobifunctional linker, 3-(2-Pyridyldithio)propionic acid *N*-hydroxysuccinimide ester (SPDP) was used to modify the lectins for conjugation to the nanoparticles.[35] SPDP contains a terminal amine-reactive *N*-hydroxysuccinimide (NHS) ester moiety which forms an amide bond with lysine residues on proteins. Additionally, the linker contains a terminal dithiopyridine group that can autocleave and self-assemble onto gold surfaces.[35] Con A and S-Con A were activated with SPDP and conjugated to *ca.* 16 nm gold nanoparticles, as described in **section 2.1.2**, and outlined in the schematic shown in **Figure 3.4**.

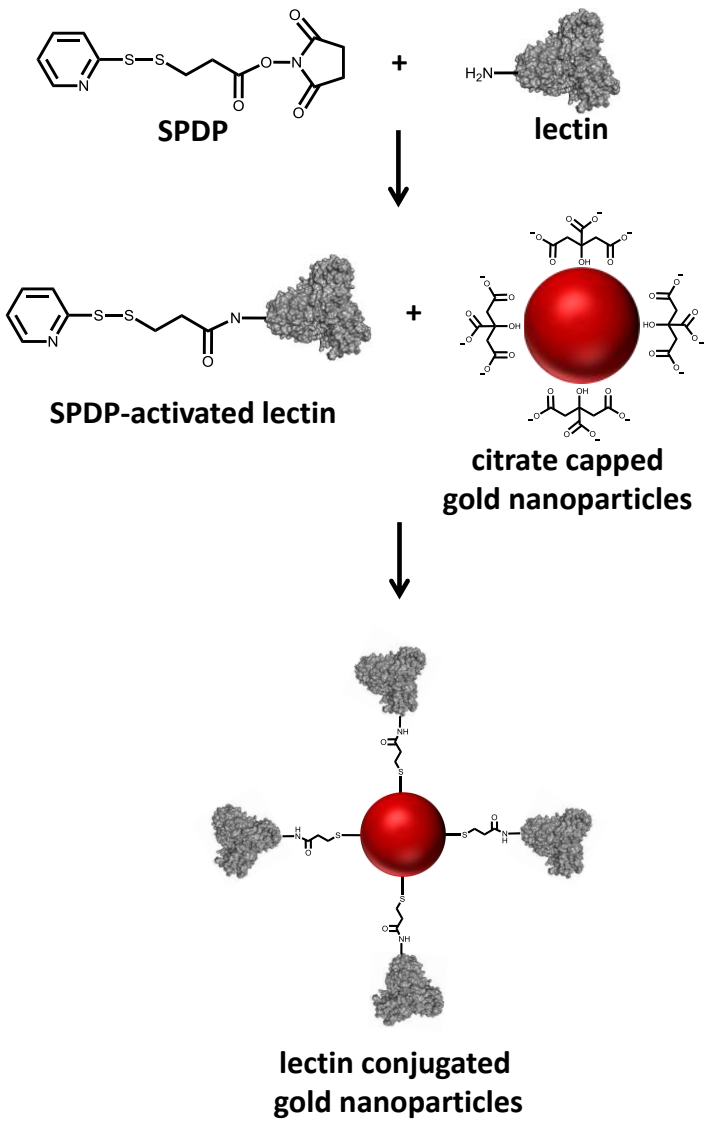

Figure 3.4 **Activation of a lectin using SPDP,[35] followed by the self-assembly of the SPDP-activated lectin onto citrate capped gold nanoparticles.**

Solutions of SPDP-activated Con A and S-Con A were prepared in D-Hank's buffer without NaCl and KCl to avoid nanoparticle aggregation upon addition of the SPDP-activated lectins to the citrate capped gold particles. Following the self-assembly of the SPDP-activated Con A or S-Con A, the gold nanoparticles were sterically stabilised in solutions with high ionic strengths, such as D-Hank's salt balanced buffer. **Figure 3.5** shows the UV-visible absorption spectra of citrate capped gold nanoparticles before and after the self-assembly of SPDP-activated Con A or S-Con A, following one centrifugation to remove the unbound lectins. Unmodified citrate capped gold nanoparticles exhibited a surface plasmon absorption band maximum at 520 nm, whereas the Con A conjugated and S-Con A conjugated gold nanoparticles exhibited red-shifted surface plasmon absorption band maxima centred at 529 nm and 522 nm, respectively. The red-shift is likely to be a result of a change in the refractive index at the surface of the gold nanoparticles, which is dependent on the molecular mass of the conjugated protein.[36]

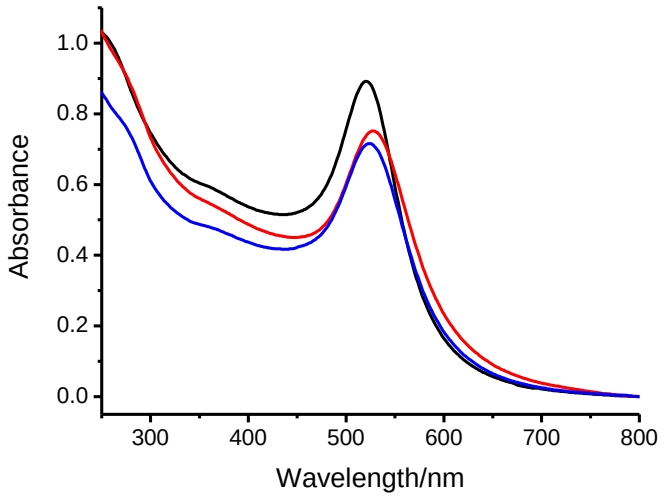

Figure 3.5 **UV-visible absorption spectra of citrate capped gold nanoparticles (black), and gold nanoparticles with Con A (red) or S-Con A (blue) conjugation. The nanoparticle samples were in D-Hank's salt balanced buffer.**

The Con A and S-Con A conjugates were prepared using a 100-fold molar excess of lectin to nanoparticles, as described in **section 2.1.2**. To obtain an approximation of the number of Con A or S-Con A molecules bound to the surface of each nanoparticle, an electrolyte induced aggregation assay was performed, as described in **section 2.1.3**. SPDP-activated Con A was self-assembled onto citrate capped gold nanoparticles at a 0, 5, 10, 15, 20, 25 or

200-fold molar excess to nanoparticles. The aggregation of gold nanoparticles with an incomplete monolayer of Con A was induced by the addition of a sodium chloride solution. The lowest molar excess of Con A required to prevent nanoparticle aggregation is representative of the number of Con A molecules present at the surface of each nanoparticle monolayer.[37,38] The same assay was repeated for S-Con A, although 0, 20, 30, 40 or 50-fold molar excesses of SPDP-activated S-Con A were used. Electrolyte induced aggregation of the particle conjugates was monitored as a decrease in absorbance intensity at the surface plasmon absorption band maxima (529 nm for the Con A conjugates and 522 nm for the S-Con A conjugates) and as an increase in absorbance intensity at 685 nm (**Figure 3.6** (**A** and **B**, respectively)). Aggregation of the Con A conjugates was found to plateau at a 10-15-fold molar excess of Con A to gold nanoparticles (**Figure 3.6** (**C**)), suggesting that *ca.* 10-15 molecules of Con A were bound to each particle. The aggregation of the S-Con A conjugates was found to plateau at a 20-30-fold molar excess of S-Con A to gold nanoparticles (**Figure 3.6** (**D**)), indicating that *ca.* 20-30 molecules of S-Con A are bound to each nanoparticle. It was expected that a higher number of SPDP-activated S-Con A molecules (52 kDa) than Con A molecules (104 kDa) would self-assemble onto each nanoparticle due to the smaller size of the dimeric S-Con A.

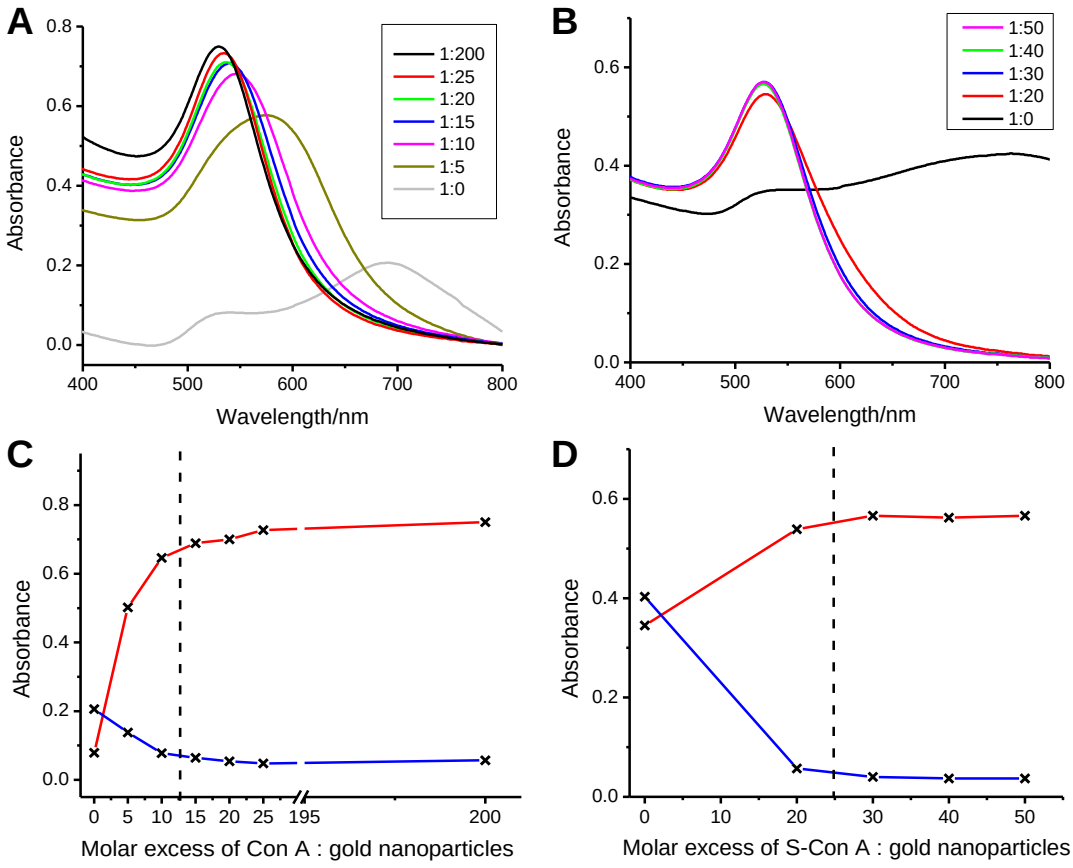

Figure 3.6 **UV-visible absorption spectra of A) Con A conjugated and B) S-Con A conjugated gold nanoparticles following the addition of NaCl (0.5 ml, 1.5 M). The conjugates were synthesised using SPDP-lectins at varying molar excesses to gold nanoparticles. C) Decreasing absorbance intensity at 529 nm (red) and increasing absorbance at 658 nm (blue) upon aggregation of the Con A conjugates. D) Decreasing absorbance intensity at 522 nm (red) and increasing absorbance at 658 nm (blue) upon aggregation of the S-Con A conjugates. The dotted lines in C) and D) refer to the approximate molar excess of lectins at which nanoparticle aggregation is prevented.**

Con A or S-Con A conjugated gold nanoparticles (8.4 nM) were prepared using a nanoparticle to lectin ratio of 1:100 and were incubated with MCF-7 cells or SK-BR-3 cells for 0, 1 or 2 h, as described in **section 2.1.4**. Extensive aggregation of Con A gold nanoparticle conjugates was observed following 2 h incubation with either MCF-7 cells or SK-BR-3 cells (**Figure 3.7** (**A** and **B**, respectively)). Although the aggregates were distributed over the base of the wells of the multidish, some aggregates appeared to bind to the MCF-7 cells and SK-BR-3 cells. However, due to the substantial instability of the Con A conjugates at physiological conditions, no conclusions regarding the affinity of the lectin nanoparticle conjugates towards the breast cancer cells could be drawn. It has been

reported that Con A can form temperature and pH dependent amorphous aggregates at physiological conditions (pH 7.4, 37 °C) in cell culture, which can be cytotoxic to LAN5 neuroblastoma cells.[39] The S-Con A nanoparticle conjugates appeared significantly more stable than the Con A conjugates, although no specific labelling of the MCF-7 cells or SK-BR-3 cells was observed (**Figure 3.7** (**C** and **D**, respectively)). The lack of any detectable binding could be attributed to the low affinity of the S-Con A nanoparticle conjugates towards the breast cancer cells, or due to a low sensitivity of the optical detection method used.

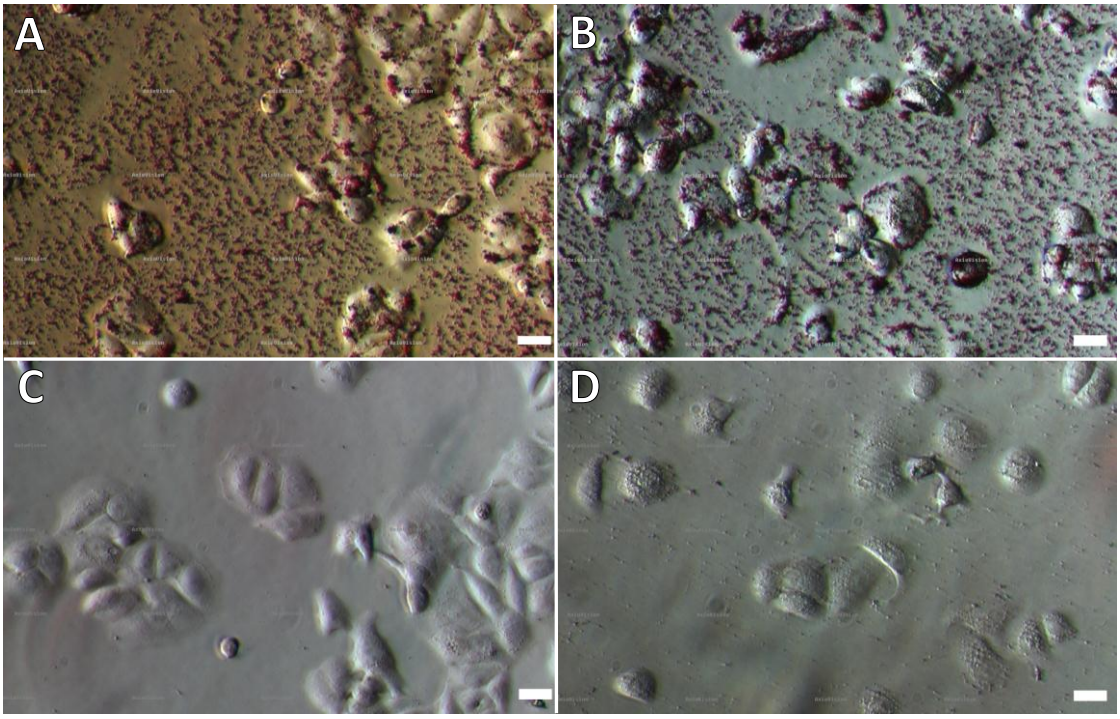

Figure 3.7 **Inverted optical microscope images of Con A conjugated (A and B) or S-Con A conjugated (C and D) gold nanoparticles (8.46 nM) incubated with MCF-7 cells (A and C) and SK-BR-3 cells (B and D) for 2 h at 37 °C. (Scale bars are 50 µm).**

The toxicity of the Con A conjugated nanoparticle aggregates was assessed using the fluorescent dye propidium iodide, which is a membrane-impermeable nucleotide interchelator that specifically binds to DNA once the cell membrane is damaged.[40] SK-BR-3 cells incubated with Con A conjugated gold nanoparticles for 1 h (**Figure 3.8** (**A**)) were further incubated with propidium iodide, as described in **section 2.1.4**. The nuclei of the majority of the SK-BR-3 cells incubated with the Con A conjugated nanoparticles stained positive with propidium iodide (**Figure 3.8** (**B**)) highlighting the significant cytotoxicity induced by the nanoparticle aggregates.

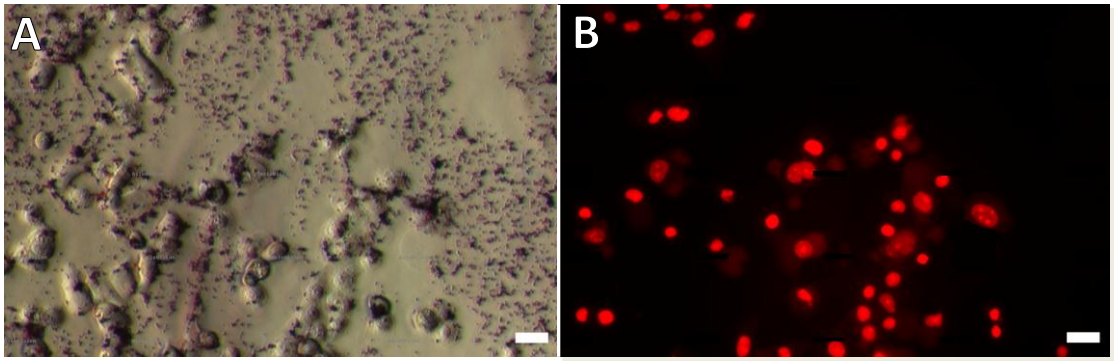

Figure 3.8 **A) An inverted optical microscope image of SK-BR-3 cells incubated with Con A conjugated gold nanoparticles (8.46 nM) for 1 h. B) Fluorescence microscope image of the SK-BR-3 cells in (A) incubated with propidium iodide (0.5 µg.ml^{-1} in D-Hank's buffer). Fluorescence images were acquired using excitation at 560 nm and emission at 630 nm. (Scale bars are 50 µm).**

To assess the dependence of the lectin type and the nanoparticle concentration on the aggregation of the Con A conjugates observed in **Figure 3.7** (**A** and **B**), Con A, *Erythrina cristagalli* lectin (ECL) and sheep serum albumin (SSA) gold nanoparticle conjugates (0.25, 0.50 or 1.00 nM) were prepared and incubated with MCF-7 cells, as described in **section 2.1.5**. ECL binds to the galactose (β-1,4) *N*-acetylgalactosamine disaccharide(Galβ-1,4GlcNAc-), also known as the cancer-associated Type II oligosaccharide antigen.[41,42] The Type II antigen is known to be overexpressed in MCF-7 breast cancer cells.[43] The SSA was used as a control. Following 1 h of incubation with the MCF-7 cells, no aggregation was observed with any of the nanoparticle conjugates. The conjugates were then incubated for a further 23 h with the cells and imaged once again. The Con A nanoparticle conjugates showed visible signs of aggregation at a concentration of 1.00 nM (**Figure 3.9** (**A**)), although aggregation was not as extensive as when using a nanoparticle concentration of 8.46 nM (**Figure 3.7** (**A** and **B**)). Significant aggregation of the ECL conjugated nanoparticles was observed at a concentration of 1.00 nM (**Figure 3.9** (**B**)) and, to a lesser extent, at 0.25 nM and 0.50 nM (data not shown). Finally, the SSA conjugated nanoparticles showed the least signs of aggregation (**Figure 3.9** (**C**)). These results indicate that the degree of nanoparticle aggregation was dependent on the concentration of the nanoparticles, the type of protein conjugated and the length of the incubation time. However, all SPDP-lectin nanoparticle conjugates appeared to exhibit some degree of colloidal instability at physiological conditions. A previous study has shown that protein conformation can be significantly altered when in close proximity to the surface of gold

nanoparticles (*ca.* 90 nm in diameter) through gold-sulfur interactions at physiological conditions (pH 7.5).[44] This destabilisation has been shown to result in the formation of higher order aggregates, which could explain the aggregation observed in the experiments reported in this section.

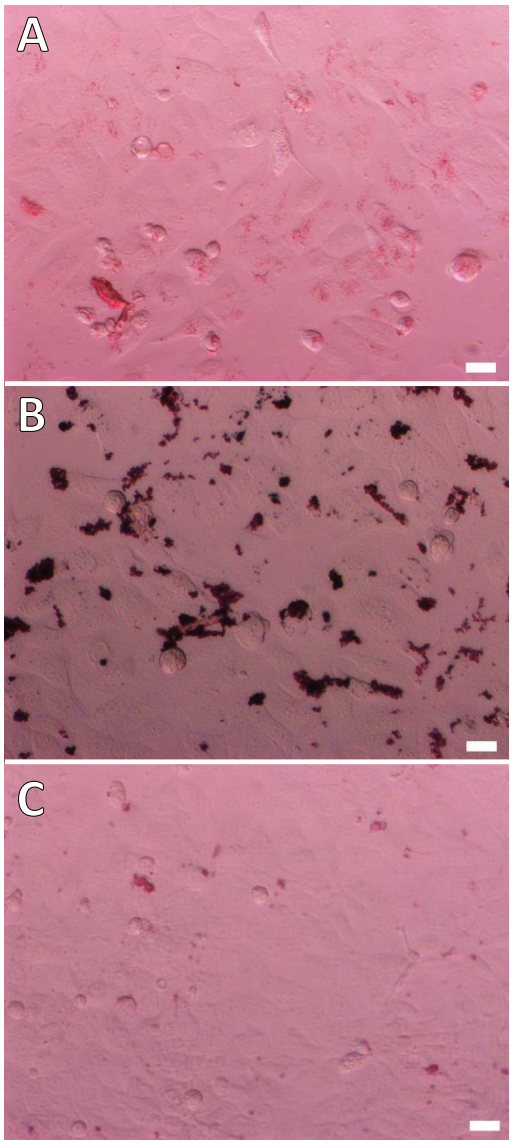

Figure 3.9 **Inverted optical microscope images of MCF-7 cells incubated with gold nanoparticles (1.00 nM) conjugated to A) Con A, B) ECL or C) SSA for 24 h in MEM + GlutaMAX™-I medium. (Scale bars are 50 µm).**

Citrate capped gold nanoparticles were modified with polyethylene glycol (PEG) prior to lectin conjugation, in order to enhance the stability of the particles and to distance the lectins from the nanoparticle surface.[45] Heterobifunctional α-thio-ω-carboxy PEG was self-assembled onto citrate capped gold nanoparticles, as described in **section 2.1.6**. The terminal thiol moiety on the PEG allows the self-assembly onto the nanoparticles, whilst the terminal carboxyl group allows for the conjugation of the lectins through EDC/sulfo-NHS chemistry. Following PEG modification, the gold nanoparticles were characterised using TEM imaging, as described in **section 2.1.6**.[46] The TEM image shown in **Figure 3.10** reveals that the PEG modified gold nanoparticles (*ca.* 16 nm) are mostly non-aggregated, with a predominantly spherical morphology.

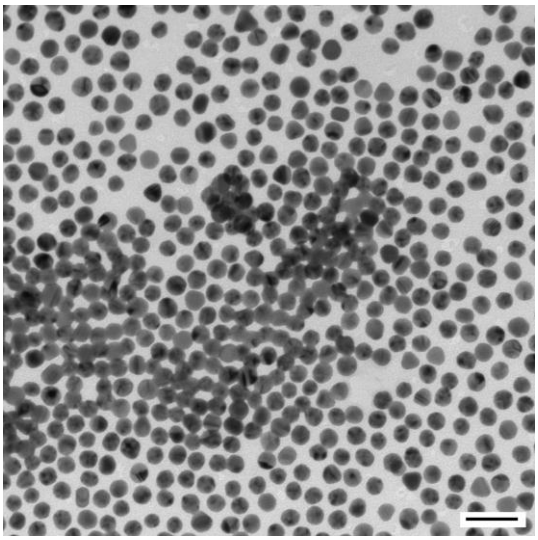

Figure 3.10 **A TEM image of gold nanoparticles (*ca.* 16 nm) following PEG attachment.[46] (Scale bar is 50 nm).**

EDC/sulfo-NHS chemistry was used to convert the terminal carboxyl moieties on the PEG attached to the gold nanoparticles into semi-stable, amine-reactive sulfo-NHS ester groups, as described in **section 2.1.6**. Con A, ECL and SSA were conjugated to the nanoparticles through amide bond formation with the sulfo-NHS ester modified PEG molecules. The nanoparticle conjugates were then characterised using UV-visible absorption spectrophotometry (**Figure 3.11**). Following PEG attachment, the surface plasmon absorption band maximum red-shifted by *ca*. 4 nm, which is likely to be due to the change in the refractive index at the nanoparticle surface.[36]

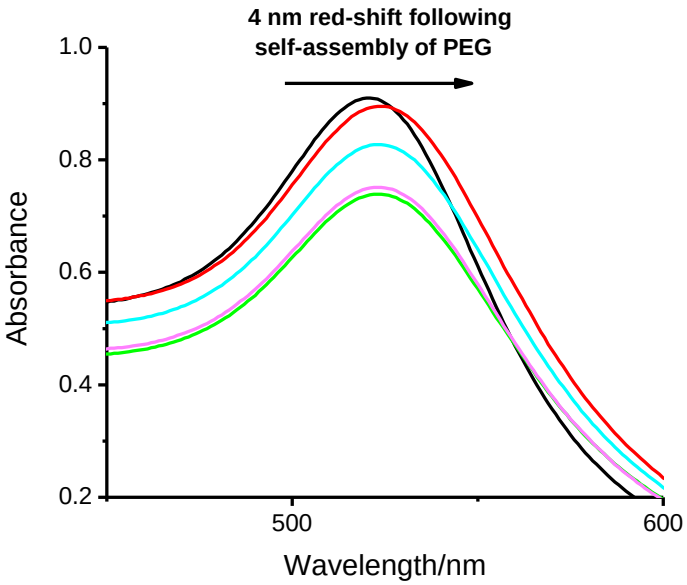

Figure 3.11 **UV-visible absorption spectra of the surface plasmon absorption band of the citrate capped gold nanoparticles before (black) and after PEG attachment (red), and following conjugation to Con A (green), ECL (blue) and SSA (pink).**

The Con A, ECL and SSA nanoparticle conjugates were incubated with MCF-7 cells at concentrations of 0.25, 0.50 or 1.00 nM for 24 h then imaged, as described in **section 2.1.7**. **Figure 3.12** shows that there was no visible aggregation of any of the nanoparticle conjugates at any concentration, demonstrating the stabilising effect that PEG has on the gold nanoparticles. However, no specific binding of the Con A or ECL conjugated PEG modified gold nanoparticles was observed following incubation with the MCF-7 cells.

It was thought that the aggregation of Con A conjugated gold nanoparticles observed in **Figure 3.7** was likely to be a result of a combination of Con A aggregation and the proximity of the Con A to the nanoparticle surface. The images in **Figure 3.7** suggest that the aggregation was further potentiated by using a high nanoparticle concentration (8.46 nM). Aggregation was significantly less when using a nanoparticle concentration of 1.00 nM (**Figure 3.9**). The findings of the colorimetric labelling assay were inconclusive, showing limited indications of specific binding of Con A or S-Con A nanoparticle conjugates to the MCF-7 and SK-BR-3 cells. However, the substantial improvement in nanoparticle stability following PEG modification suggests an important role for the use of such molecules in cell-based assays.

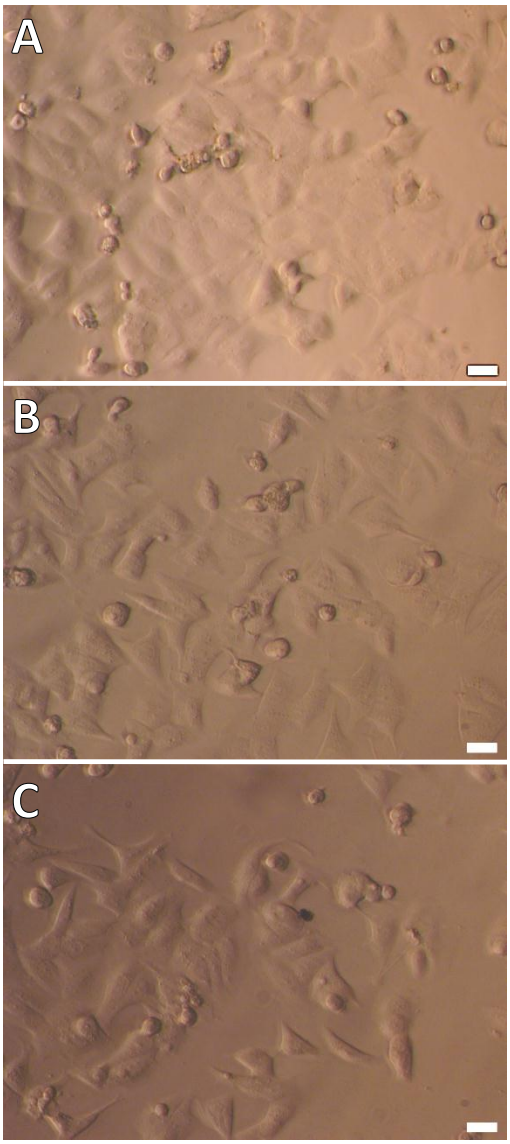

Figure 3.12 **Inverted optical microscope images of MCF-7 cells incubated with PEG modified gold nanoparticles (1 nM) conjugated to A) Con A, B) ECL or C) SSA for 24 h. (Scale bars are 50 µm).**

3.2.2 Lectin cytoadhesion assay

To directly assess the interactions of Con A or S-Con A with MCF-7 cells, a colorimetric formazan-based lectin cytoadhesion assay was performed, as described in **section 2.1.8**. Mitochondrial reductase within metabolically active cells convert the 3-(4,5-Dimethyl-2-thiazolyl)-2,5-diphenyl-2H-tetrazolium bromide (MTT) reagent into purple formazan crystals. Formazan is insoluble in aqueous media, and requires solubilisation with a

solvent, such as DMSO.[47] The conversion of the MTT reagent to formazan by viable cells that are specifically attached to the lectin-derivatised wells is shown in **Figure 3.13**.

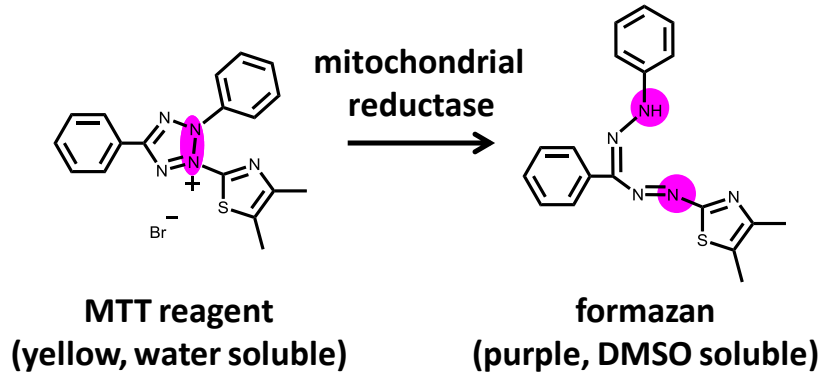

Figure 3.13 **Reduction of the MTT reagent by mitochondrial reductase activity within viable cells to produce formazan.[47]**

A cross-calibration assay was initially performed to establish the optimal lectin concentration required for adhesion to the multidish wells and to determine the MCF-7 cell density needed to achieve the highest binding to the lectin derivatised wells. Con A was adsorbed onto NUNC Nunclon™ Δ surface multidishes for the cross-calibration experiment, as described in **section 2.1.8**. The Nunclon™ Δ surface treatment increases the hydrophilicity of the polysterene multidishes to maximise the absorption of biomolecules and cells. The enzymatic treatment of cells with trypsin to detach them from their culture flasks can temporarily alter lectin binding patterns to the carbohydrates expressed at their surface.[10] Therefore the MCF-7 cells were detached using the calcium chelators EDTA and EGTA. The optimal Con A concentration for adsorption onto the surface of the wells in the multidishes was found to be 0.5 $mg.ml^{-1}$ (**Figure 3.14**). The optimum MCF-7 cell density was found to be $2x10^4$ cells per well. Therefore a lectin concentration of 0.5 $mg.ml^{-1}$ and a cell density of $2x10^4$ cells per well were used for all the cytoadhesion assays.

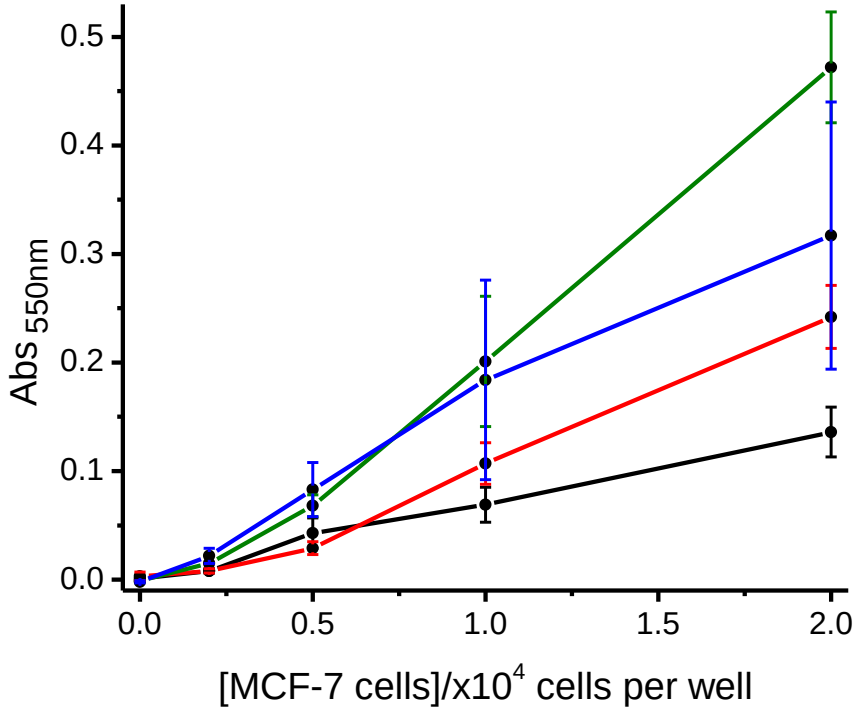

Figure 3.14 **Formazan absorbance at 500 nm following MTT incubation with MCF-7 cells that adhered to wells of a 96 well multidish pretreated with 0.0 (black), 0.1 (red), 0.5 (green) or 1.0 mg.ml^{-1} (blue) Con A. MCF-7 cell densities of 0.2x10^4, 0.5x10^4, 1.0x10^4 or 2.0x10^4 cells per well were used. (Error bars are ± standard error; n=3)**

Con A and S-Con A were adsorbed onto the multidishes and SSA was used as a control protein with no known selective binding capacity. The relative proportions of MCF-7 cells specifically bound to Con A and S-Con A was determined through the MTT cell viability assay. Formazan production was measured using the absorbance at 550 nm. The relative quantification of MCF-7 cells that specifically bound to Con A, S-Con A and the SSA control are shown in **Figure 3.15**. It is clear that the binding of MCF-7 cells to Con A is *ca.* 2-fold higher than to S-Con A and *ca.* 4.5-fold higher than to the SSA control. This pattern can be attributed to the tetravalent carbohydrate binding capacity of Con A, as compared to the bivalence of S-Con A. The limited binding of the MCF-7 cells to the SSA control is a result of non-specific cell adhesion.

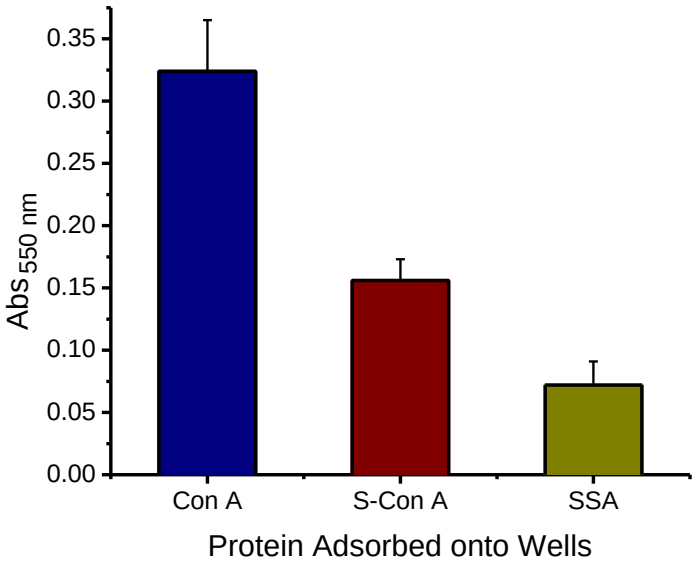

Figure 3.15 **Formazan production of viable MCF-7 cells interacting with Con A, S-Con A and the control protein SSA, adsorbed onto 96 well multidishes. Formazan production is expressed as the absorbance intensity at 550 nm. (Error bars are ± standard error; n=3).**

The same assay was repeated with Con A and S-Con A was compared to ECL (**Figure 3.16**). The binding pattern of MCF-7 cells with Con A and S-Con A is consistent with **Figure 3.15**, however the binding of MCF-7 cells to ECL is significantly higher than to Con A. The greater adhesion of MCF-7 cells to ECL than to Con A or S-Con A could be attributed to a higher binding affinity of ECL to the Galβ-1,4GlcNAc- disaccharide at the surface of the MCF-7 cells. However, the affinity any of ECL, Con A or S-Con A to the MCF-7 cells has not reported. Alternatively, the density of the Galβ-1,4GlcNAc- disaccharide at the surface of the MCF-7 cells could be higher than the density of cell surface α-Man residues.

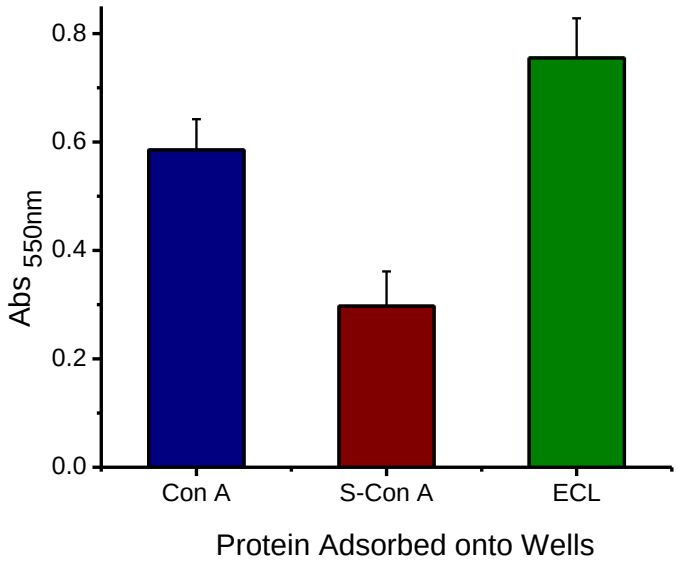

Figure 3.16 **Formazan production of viable MCF-7 cells interacting with Con A, S-Con A and ECL adsorbed onto 96 well multidishes. Formazan production is expressed as the absorbance intensity at 550 nm. (Error bars are ± standard error; n=3).**

3.2.3 Synthesis and characterisation of Con A conjugated C11Pc-PEG gold nanoparticles

Based on the findings of the lectin cytoadhesion assay, it was decided that only Con A would be used as a proof-of-concept to attempt targeted PDT on MCF-7 cells, as the binding of S-Con A to these cells appears to be significantly lower. The synthesis of 1,1',4,4',8,8',15,15',18,18',22,22'-tetradecakisdecyl-25,25'-(11,11'dithiodiundecyl) diphthalocyanine zinc (C11Pc), the photosensitiser used throughout the PDT experiments in this thesis, has been previously reported.[48] Using an adapted version of the Brust

method,[49] gold nanoparticles (*ca.* 4 nm in diameter) with a mixed monolayer of the disulfide C11Pc photosensitiser and thiolated carboxy PEG were synthesised, as described in **section 2.1.9**.[50] The PEG molecules provided colloidal stability and aqueous solubility to the nanoparticle system carrying the hydrophobic C11Pc photosensitiser. **Figure 3.17** is a schematic representation of the synthesis of the C11Pc-PEG gold nanoparticles.

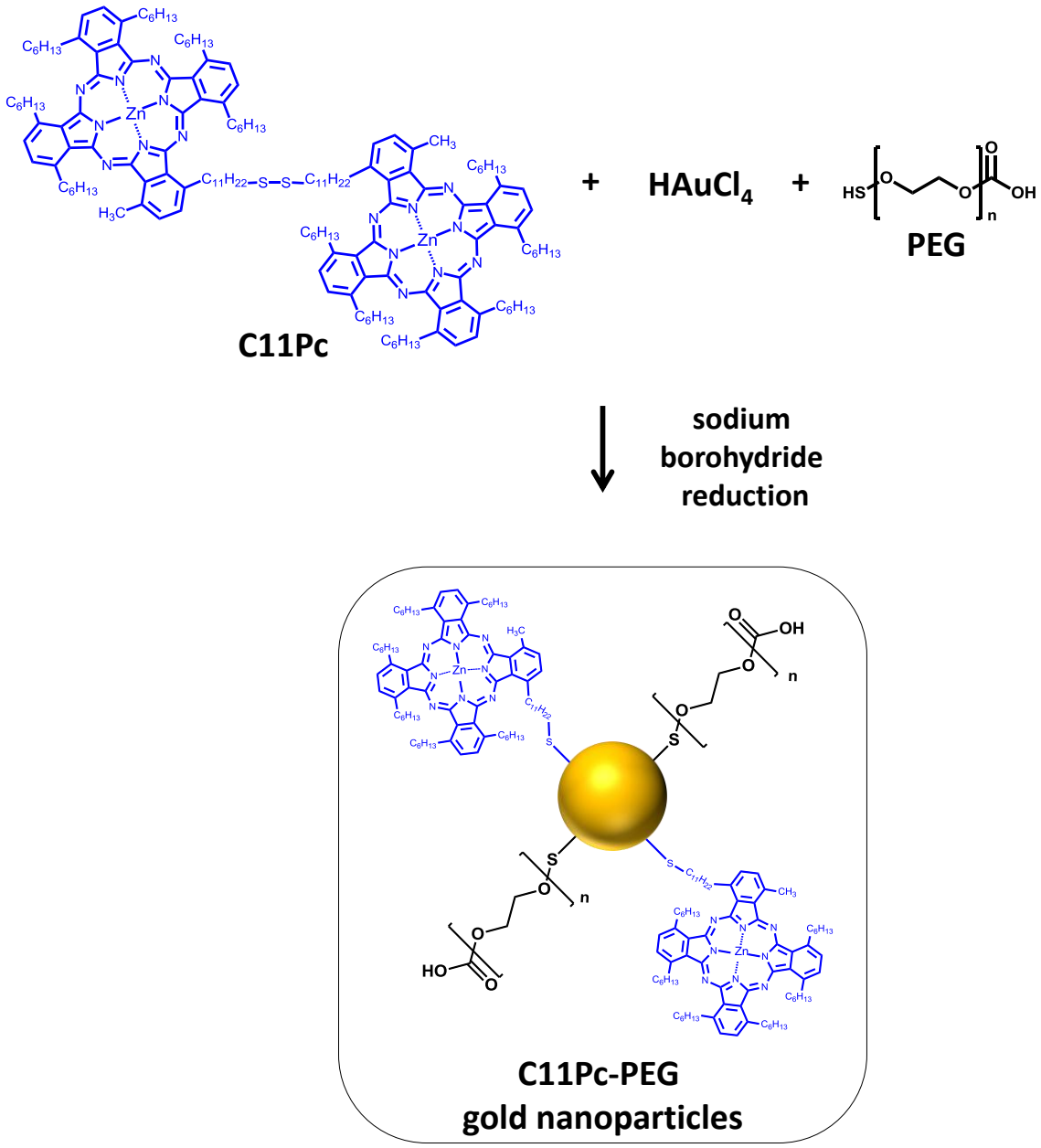

Figure 3.17 **Synthesis of the C11Pc-PEG gold nanoparticles following the reduction of gold chloride ($HAuCl_4$) in the presence of the C11Pc photosensitiser and thiolated carboxy PEG using sodium borohydride.**

The MES buffer used to dissolve the nanoparticles was at pH 5.5, as acidic buffers are optimal for the effective activation of the carboxyl groups on PEG using EDC/sulfo-NHS chemistry. Con A was covalently attached to the polyethylene glycol on the gold nanoparticles by amide coupling of the primary amine groups on the lectin to the terminal carboxyl groups of the PEG, as described in **section 2.1.10**. A diagrammatic representation of the Con A conjugated C11Pc-PEG gold nanoparticles is shown in **Figure 3.18**.

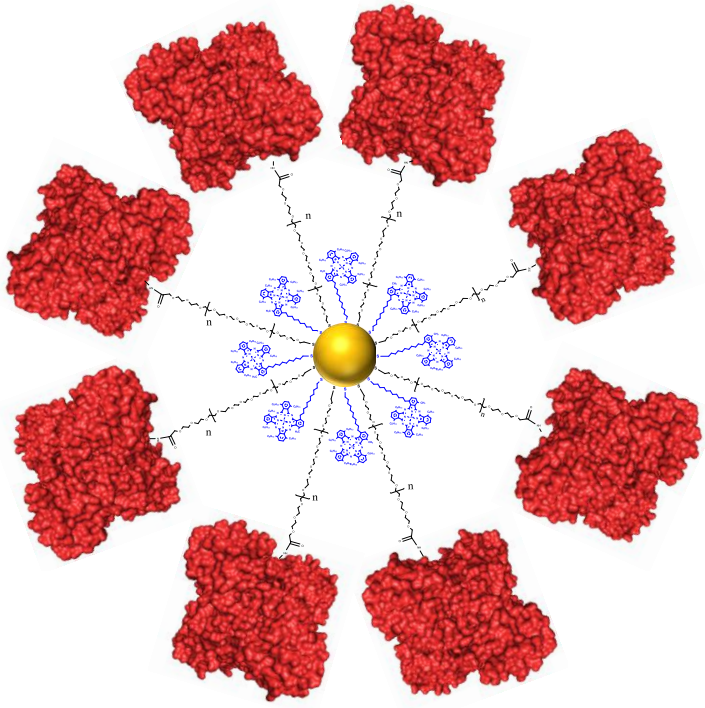

Figure 3.18 **A representation of the Con A conjugated C11Pc-PEG gold nanoparticles. The C11Pc photosensitiser is shown in blue, the PEG chains are black and the Con A molecules are shown in red (PDB ID 1CVN[16]).**

Following the removal of unbound Con A using ultrafiltration (**section 2.1.10**), the conjugated C11Pc-PEG gold nanoparticles were redispersed in serum-free Leibovitz's L15 medium. The use of serum in the PDT assays was avoided to prevent potential cross-reactivity of the Con A nanoparticle conjugates with glycoproteins expressing α-Man. The Con A conjugated and non-conjugated nanoparticles were characterised using UV-visible absorption spectrophotometry (**Figure 3.19**). The concentration of the C11Pc-PEG gold nanoparticles (C11Pc equivalent) was determined by the absorbance intensity of the phthalocyanine Q-band at 696 nm using an extinction coefficient ($\varepsilon_{696\,nm}$) of 2.23×10^5 M^{-}

^{1}.cm^{-1}.[51] The absence of the surface plasmon absorption band centred at *ca*. 520 nm indicates that the diameter of the gold nanoparticles is below *ca*. 5 nm.[52] As gold nanoparticles decrease in size, they exhibit quantum size effects that result in the dampening, broadening and blue-shifting of the surface plasmon absorption band towards the UV region of the spectrum (*ca.* 300-400 nm).[52]

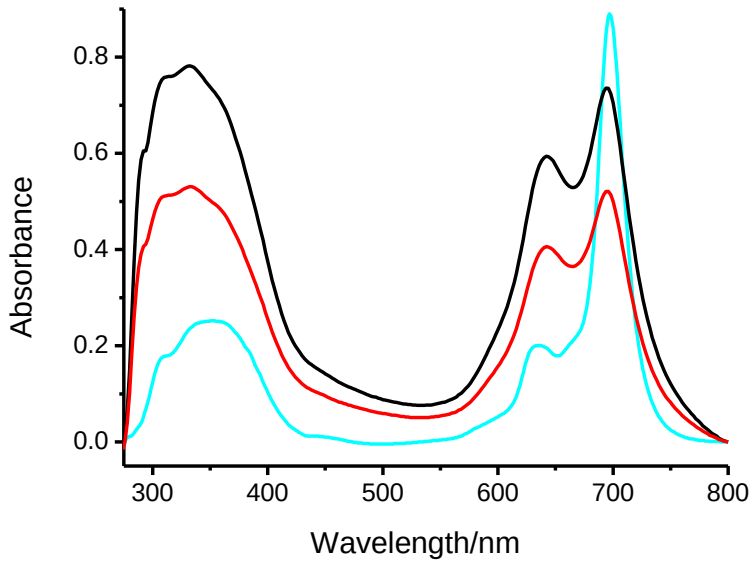

Figure 3.19 **UV-visible absorption spectra of the Con A conjugated (red) and non-conjugated (black) C11Pc-PEG gold nanoparticles. The nanoparticle samples were in serum-free Leibovitz's L15 medium without the phenol red indicator. The absorption spectrum of free C11Pc in THF is shown in blue. The intensity of the absorption band at 696 nm, with respect to the absorption band centred at 645 nm, indicates that the majority of the C11Pc supported onto the gold nanoparticles is present in the active monomeric form.**

The non-conjugated and Con A conjugated C11Pc-PEG gold nanoparticles were also characterised using TEM imaging (**Figure 3.20** (**A** and **B**, respectively)). The nanoparticles appeared non-aggregated with a narrow size distribution. The mean diameter of the Con A conjugated and the non-conjugated C11Pc-PEG gold nanoparticles was found to be 4.56 ± 0.3 nm and 4.16 ± 0.3 nm, respectively (mean ± 95% confidence interval, n=100). Histograms showing the size distribution of the non-conjugated and Con A conjugated nanoparticles are shown in **Figure 3.20** (**C** and **D**, respectively).

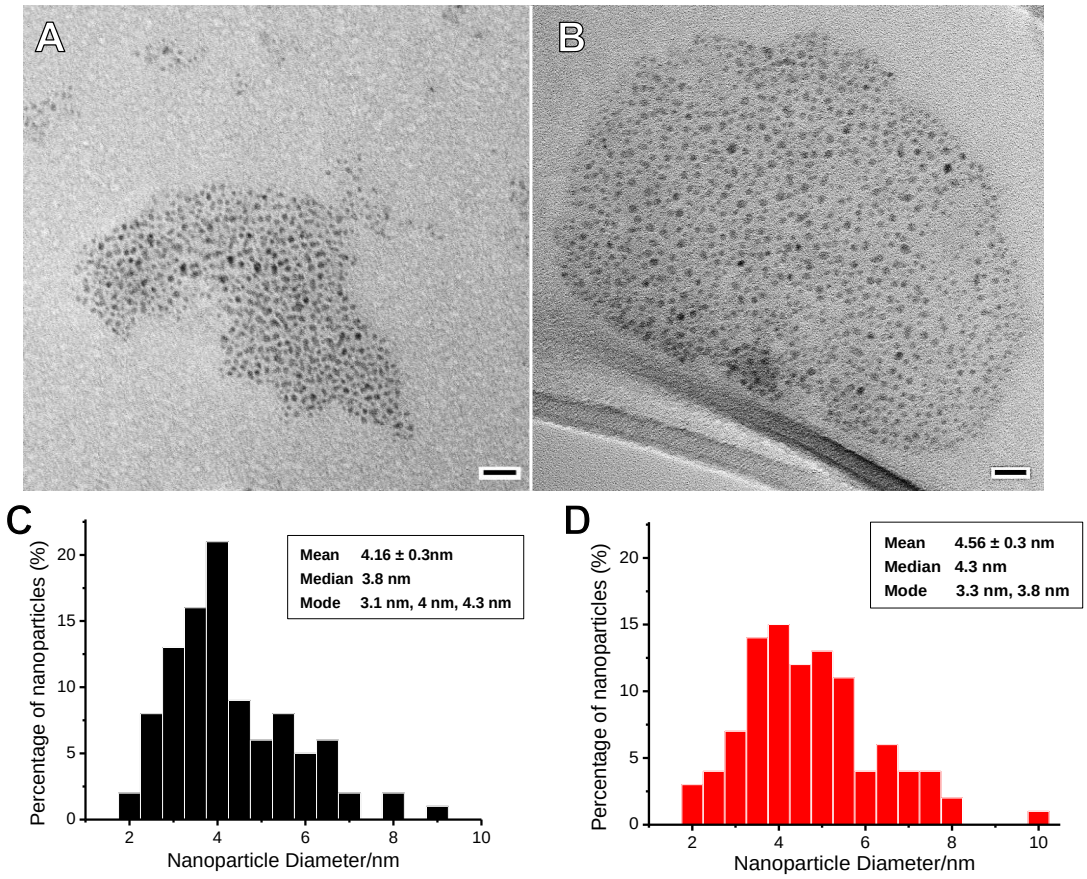

Figure 3.20 **TEM images of non-conjugated (A) and Con A conjugated (B) C11Pc-PEG gold nanoparticles in phosphate buffered saline. (Scale bars are 20 nm). C and D are histograms showing the size distribution of the non-conjugated (C) and Con A conjugated (D) nanoparticles.**

The photoactivity of the C11Pc-PEG gold nanoparticles was measured using the colorimetric singlet oxygen probe, anthracene-9,10-dipropionic acid disodium salt (ADPA).[53] ADPA exhibits characteristic absorption bands at *ca.* 300-420 nm. The reaction of singlet oxygen with ADPA yields a photobleached endoperoxide product (**Figure 3.21**).[53]

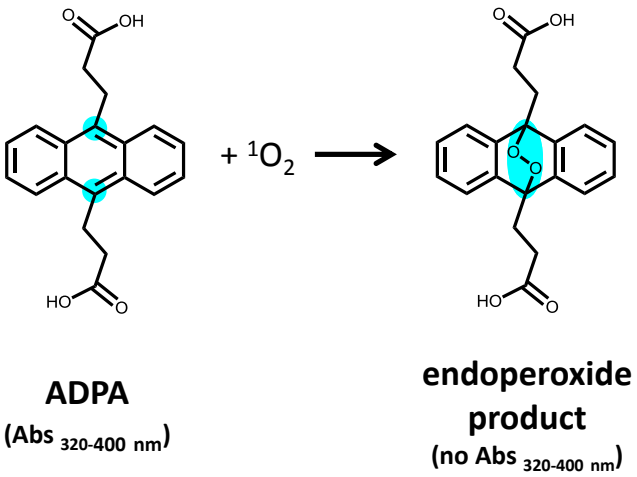

Figure 3.21 **The reaction of ADPA with singlet oxygen ($^1O_2$) to form a photobleached endoperoxide product. Figure adapted from Lindig *et al.*[53]**

Both the Con A conjugated and non-conjugated C11Pc-PEG gold nanoparticle samples in phosphate buffered saline were irradiated at 633 nm in the presence of ADPA, as described in **section 2.1.11**. The UV-visible absorption spectra of the non-conjugated and Con A conjugated nanoparticle solutions during the 30 min irradiation are shown in **Figure 3.22** (**A** and **B**, respectively). The decay in ADPA absorbance at 400 nm suggests that the probe is photobleached by the reaction with singlet oxygen following irradiation of the C11Pc-PEG gold nanoparticles at 633 nm (**Figure 3.22** (**C**)). The irradiation of the PEG gold nanoparticles not functionalised with C11Pc had no effect on the ADPA absorbance intensity showing that the C11Pc is essential for singlet oxygen production. Equation **3.1** was used to calculate the maximum rate of ADPA photobleaching, which was normalised to the C11Pc concentration. The maximum rate of ADPA photobleaching following the irradiation of the non-conjugated particles was 0.712% Abs $_{400\ nm}$/min/μM C11Pc. The maximum rate of ADPA photobleaching following the irradiation of the Con A-conjugated particles was found to be marginally lower at 0.613% Abs $_{400\ nm}$/min/μM C11Pc, although repeating the assay a number of times would establish if the decrease in singlet oxygen production was statistically significant. However, the increased cellular internalisation of the Con A nanoparticle conjugates could potentially overcome any decrease in singlet oxygen production observed.

$$\text{Maximum rate of ADPA Photobleaching } (\%\ \text{Abs}_{400}\ \text{nm/min/}\mu\text{M C11Pc}) = \frac{(\%\ \text{Abs}_{400}\ \text{at t=0 min}) - (\%\ \text{Abs}_{400}\ \text{at t=5 min})}{5\ (\text{min}) \times [\text{C11Pc}](\mu\text{M})} \quad (\mathbf{3.1})$$

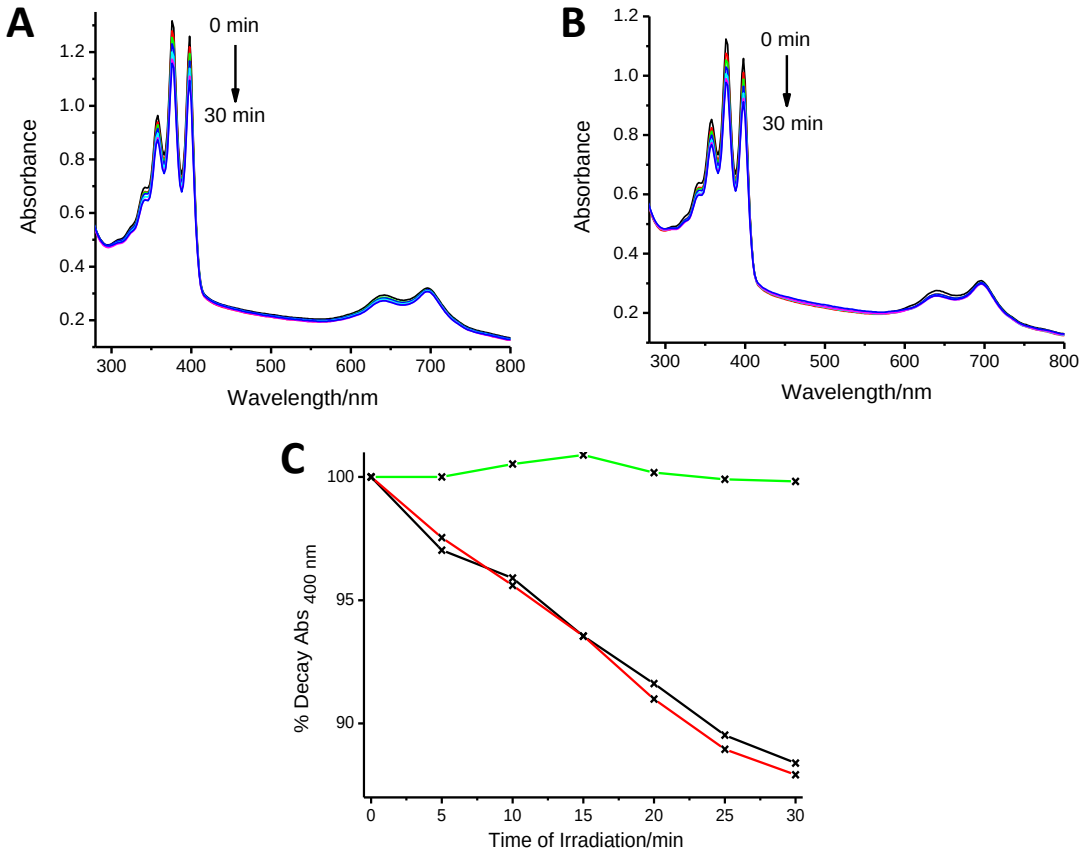

Figure 3.22 **UV-visible absorption spectra of phosphate buffered saline solutions of non-conjugated (A) and Con A conjugated (B) C11Pc-PEG gold nanoparticles in the presence of ADPA (0.17 mM), irradiated at 633 nm for 30 min. C) The progressive photobleaching of ADPA is shown as a percentage decay in absorbance intensity at 400 nm following the irradiation of non-conjugated (black) and Con A conjugated (red) C11Pc-PEG gold nanoparticles. The irradiation of PEG gold nanoparticles without C11Pc (green) were used as a control.**

3.2.4 Con A targeted PDT treatment of MCF-7 cells using C11Pc-PEG gold nanoparticles – MTT viability assay

After establishing that Con A binds to MCF-7 cells significantly more than S-Con A, and that the Con A C11Pc-PEG gold nanoparticle conjugates produce singlet oxygen upon irradiation, the PDT efficacy of the system was investigated using MCF-7 cells, as described in **section 2.1.12**. The Con A conjugated and non-conjugated C11Pc-PEG gold nanoparticles were incubated with the MCF-7 cells for 3 h at a concentration range of 0.0-0.5 μM C11Pc equivalent. The cells were irradiated for 5 min per well at 633 nm, giving a total light dose of 10.5 $J.cm^{-2}$. Staurosporine was used as a positive control for cytotoxicity inducing *ca.*93-98% cell death primarily through the apoptotic pathway.[54] Cell viability was assessed using the MTT assay and non-irradiated cells not incubated with the nanoparticle conjugates were used as a reference for 100% viable cells. The MTT assay was performed in phenol red-free Leibovitz's L15 medium to avoid interference of the phenol red indicator with the formazan absorbance readings at 550 nm. As seen in **Figure 3.23**, the cells not incubated with nanoparticles that were irradiated for 5 min per well exhibited only a *ca.* 5% reduction in viability. At nanoparticle concentrations of 0.0-0.5 μM C11Pc equivalent, the viability of the MCF-7 cells incubated with the non-conjugated (**Figure 3.23** (**A**)) or Con A conjugated particles (**Figure 3.23** (**B**)) was unaltered with or without irradiation. The lack of an observable PDT effect following the treatment of the MCF-7 cells suggests that there was insufficient cellular association or internalisation of the C11Pc-PEG gold nanoparticles, even with Con A conjugation.

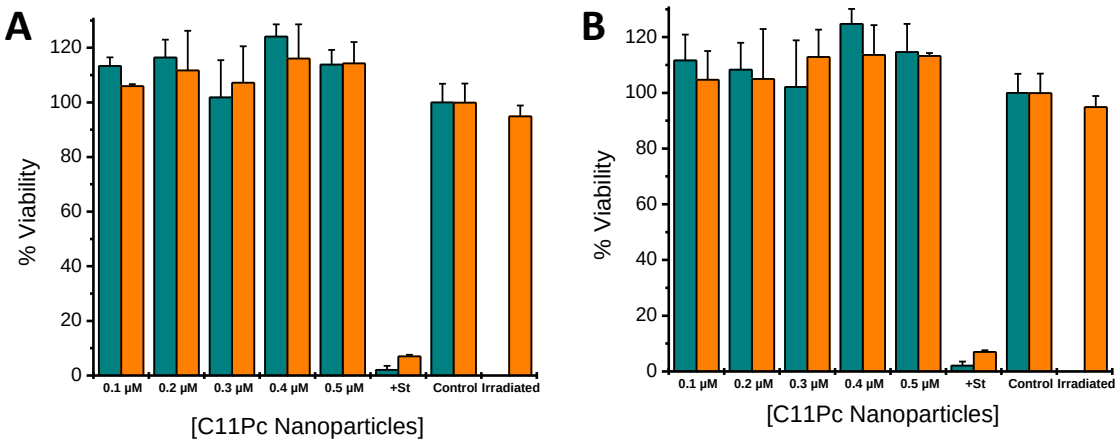

Figure 3.23 **MTT viability assay results of MCF-7 cells following PDT treatment using non-conjugated (A) and Con A conjugated (B) C11Pc-PEG gold nanoparticles. After a 3 h incubation with the nanoparticles, the cells were either irradiated for 5 min per well (orange) or non-irradiated (dark cyan). Viability is expressed as a percentage of non-irradiated cells not incubated with nanoparticles. 'Irradiated' refers to cells irradiated for 5 min per well but not incubated with nanoparticles. Staurosporine (+St; 20 µM) was used as a positive control for cytotoxicity. (Error bars are ± 95% confidence intervals; n=3).**

Following the synthesis of C11Pc-PEG gold nanoparticles in THF, as described in **section 2.1.9**, gold nanoparticles not functionalised with C11Pc were unstable in excess THF and precipitated. It was thought that some of these C11Pc-free PEG gold nanoparticles were not sufficiently removed from the C11Pc-PEG gold nanoparticles, and therefore competed for cellular internalisation. Therefore a further purification step was introduced to the synthetic procedure, which involved the centrifugation of the reaction mixture prior to removing the THF-water from the C11Pc-PEG gold nanoparticles. The MTT assay was then repeated following PDT treatment of MCF-7 cells incubated with the nanoparticles prepared using the additional purification procedure. However, the results of the MTT assay revealed no significant reduction in the viability of irradiated MCF-7 cells incubated with either non-conjugated (**Figure 3.24** (**A**)) or Con A conjugated (**Figure 3.24** (**B**)) C11Pc-PEG gold nanoparticles. It was proposed that the lack of phototoxicity of the treated MCF-7 cells was still a result of insufficient intracellular accumulation of the nanoparticles, which could be enhanced following a prolonged incubation of the conjugates at an increased particle concentration.

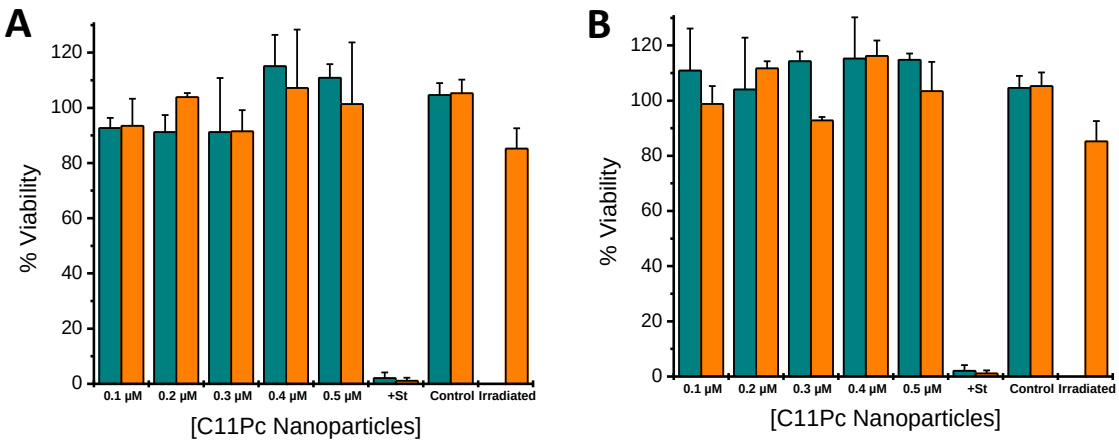

Figure 3.24 **MTT viability assay results of MCF-7 cells following PDT treatment using non-conjugated (A) and Con A conjugated (B) C11Pc-PEG gold nanoparticles. The nanoparticles were prepared using the additional purification step. After a 3 h incubation with the nanoparticles, the cells were either irradiated for 5 min per well (orange) or non-irradiated (dark cyan). Cells not incubated with nanoparticles were used as a control. 'Irradiated' refers to cells irradiated for 5 min per well but not incubated with nanoparticles. Staurosporine (+St; 20 µM) was used as a positive control for cytotoxicity. (Error bars are ± 95% confidence intervals; n=3).**

Non-conjugated and Con A conjugated C11Pc-PEG gold nanoparticles (0.00-1.44 µM C11Pc equivalent) were incubated with the MCF-7 cells for 24 h, as described in **section 2.1.12**, to maximise the internalisation of the conjugates. To increase the intracellular generation of singlet oxygen the MCF-7 cells were irradiated for 10 min per well, increasing the light dose to 23.13 $J.cm^{-2}$. The MTT assay was performed in MEM medium, which is the optimal culture medium for MCF-7 cells. **Figure 3.25** shows that the increased concentration of nanoparticles and prolonged incubation and irradiation times resulted in no phototoxicity. At the highest concentration of Con A conjugates (1.44 µM C11Pc equivalent) the viability of irradiated MCF-7 cells was reduced by *ca.* 30.24%. However, the dark toxicity of the particles resulted in a *ca.* 20.58% reduction in cell viability. The 95% confidence interval error bars were also high (45.13% for the irradiated control), which was likely to be due to the interference in formazan absorbance at 550 nm by residual phenol-red from the MEM medium. Residual MEM medium remaining in the wells prior to dissolution of the formazan crystals could also vary the pH of the final formazan solutions in DMSO. This variation in pH is known to induce a spectral shift in the absorbance of formazan, and therefore alter the true absorbance values at 550 nm.[55] This variability in absorbance at 550 nm can consequently reduce the reliability of the results.[55]

Although the targeted PDT efficacy of the nanoparticles was low in MCF-7 cells, the intracellular uptake of the Con A conjugated or non-conjugated C11Pc-PEG gold nanoparticles could be assessed using inductively coupled plasma-optical emission spectrometry (ICP-OES) analysis of the gold within cell homogenates.

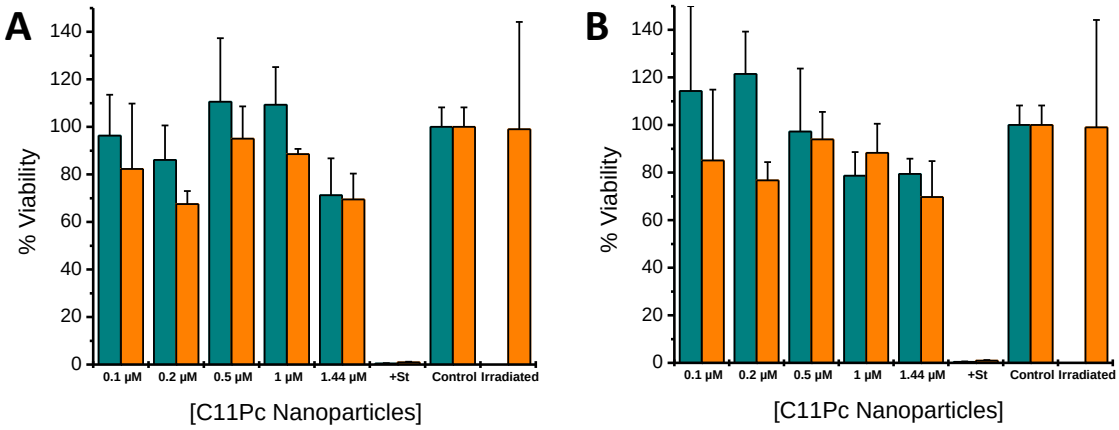

Figure 3.25 **MTT viability assay of MCF-7 cells following PDT treatment using non-conjugated (A) and Con A conjugated (B) C11Pc-PEG gold nanoparticles. After a 24 h incubation with the nanoparticles, the cells were either irradiated for 10 min per well (orange) or non-irradiated (dark cyan). Cells not incubated with nanoparticles were used as a control. 'Irradiated' refers to cells irradiated for 10 min per well but not incubated with the nanoparticles. Staurosporine (+St; 20 µM) was used as a positive control for cytotoxicity. (Error bars are ± 95% confidence intervals; n=3).**

3.2.5 Con A targeted PDT treatment of SK-BR-3 cells using C11Pc-PEG gold nanoparticles – CellTiter-Blue™ viability assay

Although Con A was not able to successfully target MCF-7 cells with C11Pc-PEG gold nanoparticles for an enhanced PDT effect, the targeted treatment was attempted on SK-BR-3 cells, as outlined in **section 2.1.13**. The fluorescence based CellTiter-Blue™ viability assay was used rather than the colorimetric MTT assay, as no solubilisation step for the assay product is required. The CellTiter-Blue™ reagent contains a non-fluorescent blue compound, resazurin, which is reduced by viable cells to the fluorescent product, resorufin, as outlined in **Figure 3.26**.[56]

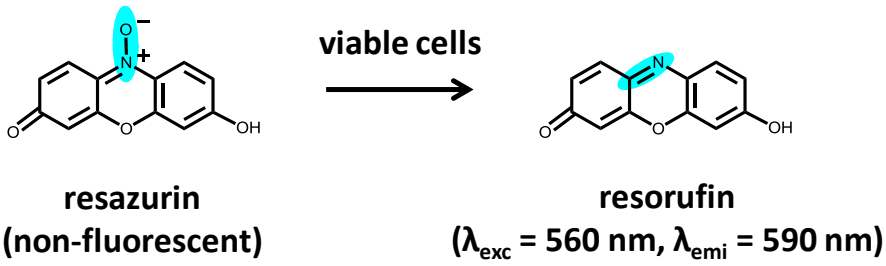

Figure 3.26 **The reduction of the non-fluorescent component of the CellTiter-Blue™ reagent, resazurin, to the fluorescent product, resorufin, by metabolically active viable cells.[56]**

Con A targeted PDT treatment of SK-BR-3 cells was performed using a nanoparticle concentration range of 0.00-1.44 μM C11Pc equivalent of Con A conjugated and non-conjugated C11Pc-PEG gold nanoparticles, as described in **section 2.1.13**. The SK-BR-3 cells were incubated with the nanoparticle conjugates for 24 h and irradiated for 10 min per well at 633 nm. The CellTiter-Blue™ assay was performed in DMEM medium 48 h following PDT treatment. Once again, no significant reduction in SK-BR-3 cell viability was observed in cells incubated with either the non-conjugated (**Figure 3.27** (**A**)) or Con A conjugated (**Figure 3.27** (**B**)) C11Pc-PEG nanoparticles, with or without irradiation.

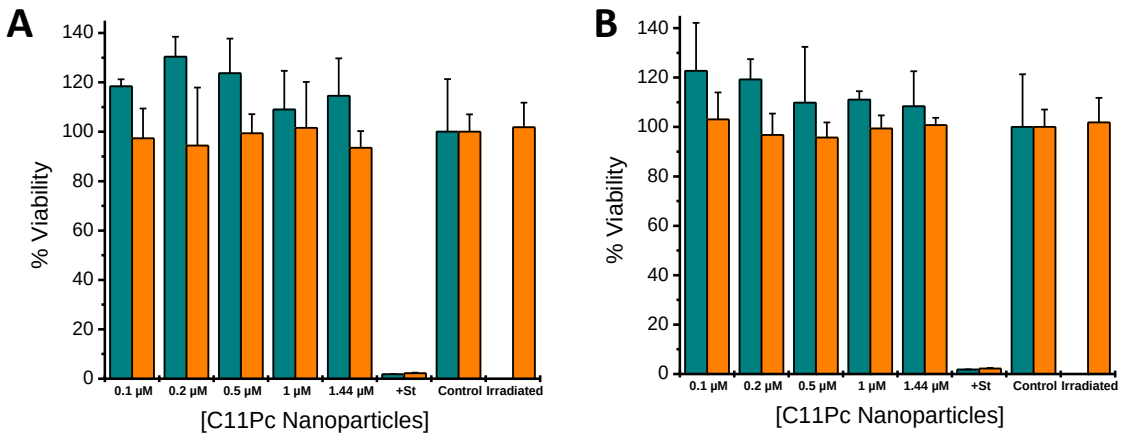

Figure 3.27 **CellTiter-Blue™ viability assay results of SK-BR-3 cells following PDT treatment using non-conjugated (A) and Con A conjugated (B) C11Pc-PEG gold nanoparticles. After a 24 h incubation with the nanoparticles, the cells were either irradiated for 10 min per well (orange) or non-irradiated (dark cyan). Cells not incubated with nanoparticles were used as a control. 'Irradiated' refers to cells irradiated for 10 min per well, but not incubated with the nanoparticles. Staurosporine (+St; 20 µM) was used as a positive control for cytotoxicity. (Error bars are ± 95% confidence intervals; n=3).**

The poor PDT efficacy observed suggests that even at the highest concentration of 1.44 µM C11Pc equivalent, with a 24 h incubation period and a light dose of up to 23.13 J.cm^{-2}, the Con A conjugates did not effectively target MCF-7 or SK-BR-3 breast cancer cells to induce any significant phototoxicity.

3.3 Conclusions

The aggregation of the gold nanoparticles (*ca.* 16 nm) functionalised with SPDP-activated lectins was found to be dependent on the type of lectin. The Con A conjugated nanoparticles (8.46 nM) aggregated substantially, whereas at the same concentration, the S-Con A conjugates remained largely stable at physiological conditions. Additionally, ECL conjugated nanoparticles (1 nM) were found to aggregate more than Con A or SSA nanoparticle conjugates. It was found that the aggregation was also dependent on concentration, as lower nanoparticle concentrations (0.25, 0.50 or 1.00 nM) of Con A, ECL or SSA conjugated gold nanoparticles did not aggregate following 1 h of incubation. Some aggregation was observed at nanoparticle concentrations of 0.25, 0.50 or 1.00 nM following a 24 h incubation period. Some evidence of the binding of the aggregated Con A

conjugates (1 nM and 8.46 nM) to MCF-7 cells and SK-BR-3 cells was observed, although the instability of the particles rendered these observations inconclusive. Following conjugation through PEG, Con A or S-Con A conjugated gold nanoparticles were unable to successfully label MCF-7 cells. In conclusion, it was found that PEG provides superior colloidal stability to gold nanoparticles (*ca.* 16 nm) functionalised with lectins, as compared to nanoparticles directly conjugated to SPDP-activated lectins. Therefore, by modifying the gold nanoparticles with PEG prior to lectin conjugation, the nanoparticles and more stable, and therefore useable for cells-based assays.

Overall, it was found that gold nanoparticles functionalised with Con A or S-Con A were not effective at colorimetrically labelling MCF-7 cells or SK-BR-3 cells. An assay with higher sensitivity, such as TEM imaging, could provide further information regarding the differential binding affinities of the Con A and S-Con A nanoparticle conjugates towards the MCF-7 cells and SK-BR-3 cells.

The lectin cytoadhesion assay, developed as part of this work, indicated that the binding affinity of Con A towards MCF-7 cells was 2-fold greater than that of S-Con A, and almost 4.5-fold greater than that of the SSA control. The significantly greater binding of Con A to the MCF-7 cells, as compared to S-Con A, resulted in the decision to use Con A as a proof-of-concept for lectin targeted PDT using C11Pc-PEG gold nanoparticles. Water soluble gold nanoparticles (*ca.* 4 nm) carrying the hydrophobic C11Pc photosensitiser and amphiphilic PEG derivative molecules were successfully synthesised. Singlet oxygen production of the aqueous nanoparticle system with and without Con A conjugation was confirmed through the photobleaching of the singlet oxygen molecular probe, ADPA, upon irradiation at 633 nm.

The targeted PDT efficacy of Con A conjugated C11Pc-PEG gold nanoparticles was investigated in MCF-7 and SK-BR-3 human breast adenocarcinoma cells, using non-conjugated nanoparticles as a control. The colorimetric MTT viability assay results showed no significant targeted phototoxicity of MCF-7 cells using the highest concentration (1.44 μM C11Pc equivalent) of Con A conjugated nanoparticles following a 24 h incubation period and 10 min irradiation. The results from the fluorometric CellTiter-Blue™ viability assay also showed no significant targeted phototoxicity of SK-BR-3 cells under the same conditions described. The poor PDT efficacy of the conjugates could be attributed to low binding of Con A conjugated nanoparticles to either MCF-7 or SK-BR-3 cells, resulting in insufficient intracellular accumulation of the photosensitiser functionalised nanoparticles.

Accumulation of the nanoparticles within the cells is dependent on the affinity of Con A to surface exposed α-Man residues, the density of the α-Man antigens at the cell surface, the extent of nanoparticle endocytosis and the loading efficiency of the sensitiser onto the particles. Further investigation into all these factors could provide a definitive reason for the low PDT efficacy of the Con A conjugated C11Pc-PEG gold nanoparticles.

This chapter has highlighted the effectiveness of a colorimetric formazan-based assay for assessing the interaction of lectins with breast cancer cells. Additionally, the methods and procedures for preparing photoactive, lectin functionalised gold nanoparticles carrying a hydrophobic sensitiser have been established. The parameters for performing the colorimetric MTT viability assay and the fluorometric CellTiter-Blue™ assay to investigate the efficacy of PDT treatment were also established. The following chapter demonstrates the targeting efficiency of an alternative lectin, jacalin, for the selective PDT treatment of HT-29 colon cancer cells expressing the tumour-associated carbohydrate T antigen.

3.4 References

1. Aub, J. C.; Tieslau, C.; Lankester, A. *Proc. Natl. Acad. Sci. U. S. A.* **1963**, *50*, 613-619.
2. Aub, J. C.; Sanford, B. H.; Wang, L. H. *Proc. Natl. Acad. Sci. U. S. A.* **1965**, *54*, 400-402.
3. Greer, J.; Kaufman, H. W.; Kalb, A. J. *J. Mol. Biol.* **1970**, *48*, 365-366.
4. Gunther, G. R.; Wang, J. L.; Yahara, I.; Cunningham, B. A.; Edelman, G. M. *Proc. Natl. Acad. Sci. U. S. A.* **1973**, *70*, 1012-1016.
5. Kussrow, A.; Kaltgrad, E.; Wolfenden, M. L.; Cloninger, M. J.; Finn, M. G.; Bornhop, D. J. *Anal. Chem.* **2009**, *81*, 4889-4897.
6. Tkacz, J. S.; Cybulska, E. B.; Lampen, J. O. *J. Bacteriol.* **1971**, *105*, 1-5.
7. Hardman, K. D.; Ainsworth, C. F. *Biochemistry* **1976**, *15*, 1120-1128.
8. Sharon, N.; Lis, H. *Glycobiology* **2004**, *14*, 53R-62R.
9. Sumner, J. B.; Howell, S. F. *J. Bacteriol.* **1936**, *32*, 227-237.
10. Schnebli, H. P.; Roeder, C.; Tarcsay, L. *Exp. Cell Res.* **1976**, *98*, 273-276.
11. Gokhale, S. M.; Mehta, N. G. *Biochem. J.* **1987**, *241*, 505-511.
12. Liener, I. E.; Sharon, N.; Goldstein, I. J. *The Lectins: properties, functions, and applications in biology and medicine*; Academic Press, **1986**.
13. Becker, J. W.; Reeke Jr, G. N.; Cunningham, B. A.; Edelman, G. M. *Nature* **1976**, *259*, 406-409.
14. McKenzie, G. H.; Sawyer, W. H.; Nichol, L. W. *Biochim. Biophys. Acta, Protein Struct. Mol. Enzymol.* **1972**, *263*, 283-293.
15. Reeke, G. N., Jr.; Becker, J. W.; Edelman, G. M. *J. Biol. Chem.* **1975**, *250*, 1525-1547.
16. Naismith, J. H.; Field, R. A. *J. Biol. Chem.* **1996**, *271*, 972-976.
17. Furmanski, P.; Kirkland, W. L.; Gargala, T.; Rich, M. A. *Cancer Res.* **1981**, *41*, 4087-4092.
18. Voyles, B. A.; Kirkland, W. L.; Furmanski, P.; McGrath, C. M. *Cancer Res.* **1978**, *38*, 1578-1583.
19. Liu, B.; Li, C. Y.; Bian, H. J.; Min, M. W.; Chen, L. F.; Bao, J. K. *Arch. Biochem. Biophys.* **2009**, *482*, 1-6.
20. Lei, H. Y.; Chang, C. P. *J. Biomed. Sci.* **2009**, *16*, 10.
21. Shoham, J.; Inbar, M.; Sachs, L. *Nature* **1970**, *227*, 1244-1246.
22. Mora, J.; Gascon, N.; Tabernero, J. M.; Germa, J. R.; Gonzalez, F. *Eur. J. Cancer* **1995**, *31A*, 2239-2242.
23. Ding, L.; Ji, Q.; Qian, R.; Cheng, W.; Ju, H. *Anal. Chem.* **2010**, *82*, 1292-1298.
24. Ding, C.; Qian, S.; Wang, Z.; Qu, B. *Anal. Biochem.* **2011**, *414*, 84-87.
25. Wang, J.; Duan, T.; Sun, L.; Liu, D.; Wang, Z. *Anal. Biochem.* **2009**, *392*, 77-82.

26. Wang, J.; Liu, D.; Wang, Z. *Anal. Methods* **2011**, *3*, 1745-1751.
27. Beppu, M.; Terao, T.; Osawa, T. *J. Biochem.* **1976**, *79*, 1113-1117.
28. Dimick, S. M.; Powell, S. C.; McMahon, S. A.; Moothoo, D. N.; Naismith, J. H.; Toone, E. J. *J. Am. Chem. Soc.* **1999**, *121*, 10286-10296.
29. Tiegs, G.; Hentschel, J.; Wendel, A. *J. Clin. Invest.* **1992**, *90*, 196-203.
30. Wilson, M. J.; Jiang, A.; Wiehr, C.; Wang, X.; Sinha, A. A.; Pei, D. *J. Androl.* **2004**, *25*, 274-285.
31. Turkevich, J.; Stevenson, P. C.; Hillier, J. *Discuss. Faraday Soc.* **1951**, *11*, 55-75.
32. Storhoff, J. J.; Elghanian, R.; Mirkin, C. A.; Letsinger, R. L. *Langmuir* **2002**, *18*, 6666-6670.
33. Szunerits, S.; Boukherroub, R. *Chem. Commun.* **2012**, *48*, 8999-9010.
34. Aslan, K.; Lakowicz, J. R.; Geddes, C. D. *Curr. Opin. Chem. Biol.* **2005**, *9*, 538-544.
35. Carlsson, J.; Drevin, H.; Axen, R. *Biochem. J.* **1978**, *173*, 723-737.
36. Chen, H.; Kou, X.; Yang, Z.; Ni, W.; Wang, J. *Langmuir* **2008**, *24*, 5233-5237.
37. Weisbecker, C. S.; Merritt, M. V.; Whitesides, G. M. *Langmuir* **1996**, *12*, 3763-3772.
38. Cañaveras, F.; Madueño, R.; Sevilla, J. M.; Blázquez, M.; Pineda, T. *J. Phys. Chem. C* **2012**, *116*, 10430-10437.
39. Vetri, V.; Carrotta, R.; Picone, P.; Di Carlo, M.; Militello, V. *Biochim. Biophys. Acta* **2010**, *1804*, 173-183.
40. Stoehr, M.; Vogt-Schaden, M. *Acta Pathol., Microbiol. Immunol. Scand., Sect. A* **1981**, *89*, 96-99.
41. Iglesias, J. L.; Lis, H.; Sharon, N. *Eur. J. Biochem.* **1982**, *123*, 247-252.
42. Baldus, S. E. *Int. J. Oncol.* **1996**, *9*, 43-48.
43. Choi, H. J.; Chung, T. W.; Kim, C. H.; Jeong, H. S.; Joo, M.; Youn, B.; Ha, K. T. *Biochem. Biophys. Res. Commun.* **2012**, *426*, 620-625.
44. Zhang, D. M.; Neumann, O.; Wang, H.; Yuwono, V. M.; Barhoumi, A.; Perham, M.; Hartgerink, J. D.; Wittung-Stafshede, P.; Halas, N. J. *Nano Lett.* **2009**, *9*, 666-671.
45. Paciotti, G. F.; Kingston, D. G. I.; Tamarkin, L. *Drug Dev. Res.* **2006**, *67*, 47-54.
46. Obaid, G. *CHE-3F0Y Final Year Research Project* **2009**, *University of East Anglia*.
47. Mosmann, T. *J. Immunol. Methods* **1983**, *65*, 55-63.
48. Chambrier, I.; Cook, M. J.; Russell, D. A. *Synthesis* **1995**, 1283-1286.
49. Brust, M.; Walker, M.; Bethell, D.; Schiffrin, D. J. *J. Chem. Soc., Chem. Commun.* **1994**, *7*, 801-802.
50. Stuchinskaya, T.; Moreno, M.; Cook, M. J.; Edwards, D. R.; Russell, D. A. *Photochem. Photobiol. Sci.* **2011**, *10*, 822-831.

51. Camerin, M.; Magaraggia, M.; Soncin, M.; Jori, G.; Moreno, M.; Chambrier, I.; Cook, M. J.; Russell, D. A. *Eur. J. Cancer* **2010**, *46*, 1910-1918.
52. Daniel, M. C.; Astruc, D. *Chem. Rev.* **2004**, *104*, 293-346.
53. Lindig, B. A.; Rodgers, M. A. J.; Schaap, A. P. *J. Am. Chem. Soc.* **1980**, *102*, 5590-5593.
54. Bertrand, R.; Solary, E.; O'Connor, P.; Kohn, K. W.; Pommier, Y. *Exp. Cell Res.* **1994**, *211*, 314-321.
55. Plumb, J. A.; Milroy, R.; Kaye, S. B. *Cancer Res.* **1989**, *49*, 4435-4440.
56. O'Brien, J.; Wilson, I.; Orton, T.; Pognan, F. *Eur. J. Biochem.* **2000**, *267*, 5421-5426.

Chapter 4

Targeting the oncofoetal T antigen disaccharide with jacalin functionalised phthalocyanine-PEG gold nanoparticles for selective PDT of HT-29 colon adenocarcinoma cells

This chapter describes the experiments performed to effectively target the tumour-associated T antigen at the surface of HT-29 human colon adenocarcinoma cells with jacalin functionalised gold nanoparticles carrying zinc phthalocyanine.

4.1 Introduction

4.1.1 The origin of the Thomsen-Friedenreich antigen

One of the most therapeutically attractive cancer-associated carbohydrates is the Thomsen-Friedenreich disaccharide antigen (T antigen), also known as the TF antigen, the core 1 glycan, or CD176.[1-3] The T antigen is a disaccharide consisting of galactose β1-3 *N*-acetylgalactosamine, *O*-linked to a glycoprotein through serine or threonine residues (Galβ1-3GalNAc-α-*O*-ser/thr; **Figure 4.1**). The T antigen is often referred to as being oncofoetal as it is a truncated *O*-glycan that is usually cryptic in normal cells but its exposure is restricted to developing embryonic cells or cancer cells.[3] The T antigen is expressed in more than 90% of primary human carcinomas including those from the lungs, pancreas, breasts, bladder, colon, oesophagus, ovaries and prostate.[4,5] Tumour initiating cells (cancer stem cells) of the lung, breast, liver and colon were also found to express the T antigen at their surface.[6] Consequently, the T antigen is an attractive target for cancer therapies.

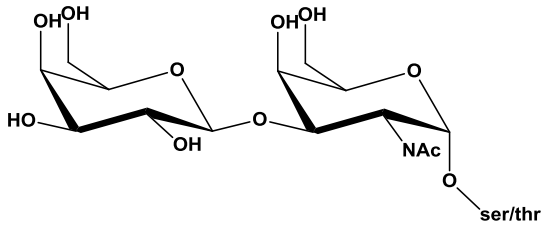

Figure 4.1 **Structure of the oncofoetal T antigen, Galβ1-3GalNAc-α-, *O*-linked to a serine or threonine residue on a cell surface glycoprotein.**

The exposure of the T antigen at the surface of cancer cells is a result of aberrant glycosylation mechanisms that hamper the maturation of the disaccharide. The pathways of *O*-glycan biosynthesis outlined in **Figure 4.2** show that the T antigen (core 1 glycan) is formed from an oncofoetal cancer-associated α-linked *N*-acetylgalactosamine glycan, also known as the Tn antigen. The T antigen is formed from the Tn antigen through Core 1 β3-galactose transferase activity by the addition of a galactose residue.[7,8] Colon cancer cell deficiencies in β3-galactose transferase activity are suggested to be responsible for the exposure of the Tn and sialyl-Tn antigens, both of which are also highly correlated with malignancy.[8] During normal *O*-glycan biosynthesis, the T antigen is further concealed by sulfate molecules, sialic acid, fucose or *N*-acetylglucoseamine residues, preventing further glycosylation. Alternatively, the T antigen can be matured into the core 2 glycan through core 2 β6-*N*-acetylglucosamine-transferase activity, leading to further branching. Colon cancer cells are also known to exhibit an increased expression of the core 1 glycan (T antigen), and a decrease in the expression of the core 3 glycan (*N*-acetylglucosamine β1-3 *N*-acetylgalactosamine, *O*-linked to serine or threonine).[9] Decreased synthesis of core 3 glycans in colon cancer cells has been attributed to a marked decrease in core 3 β3-*N*-acetylglucosamine transferase activity, leading to the prevalence of T antigen synthesis.[7] It is therefore crucial that the lectin used to target cancer cells can distinguish between the T antigen and other structures not associated with malignancy.

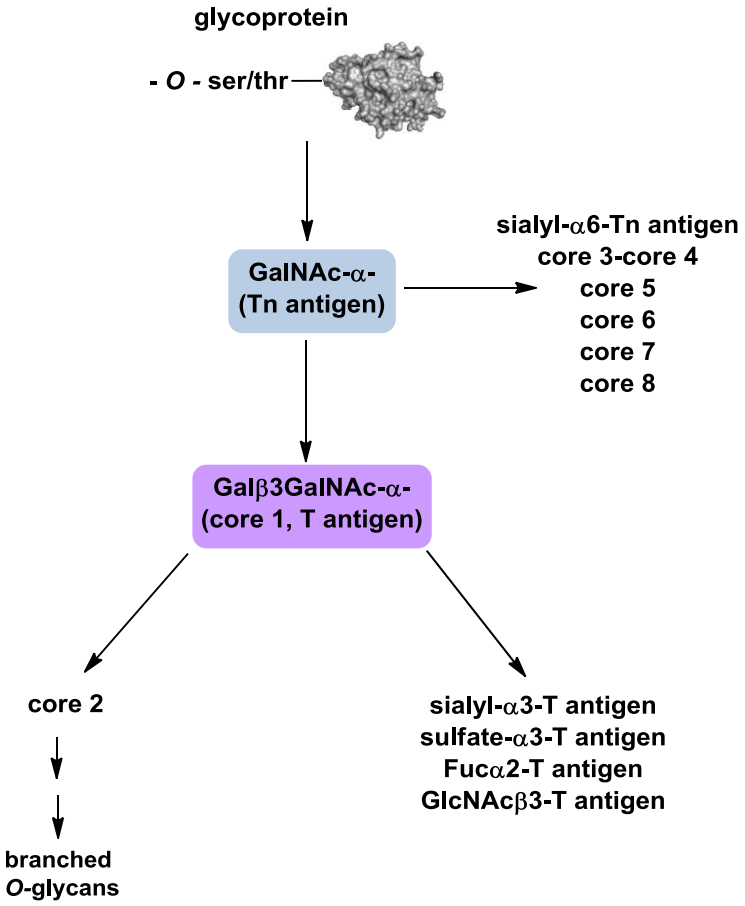

Figure 4.2 **Pathways of *O*-glycan biosynthesis showing the development of the T antigen on a glycoprotein. Figure adapted from Brockhausen (1999).**[7]

There are multiple factors thought to be responsible for incomplete *O*-glycan biosynthesis, and subsequent exposure of the T antigen. A decreased expression of carbohydrate sulfotransferases responsible for concealing the core 1 glycan through sulfation can lead to the exposure of the T antigen.[3] Furthermore, increased expression of the uridine diphosphate-galactose (UDP-Gal) transporter increases the bioavailability of UDP-Gal, and therefore up-regulates the synthesis of the T antigen.[3] In breast and colorectal cancer cells, T antigen expression was found to be highly dependent on the pH of the Golgi Apparatus. An increase of *ca.* 0.2 pH units in the Golgi Apparatus was sufficient to elevate the expression of the T antigen.[3,10]

As the T antigen is expressed in such a large number of cancers and cancer stem cells, and its exposure on non-developmental cells is restricted to malignant and premalignant tissue, it becomes an appealing molecular target for cancer therapies such as PDT.

4.1.2 Jacalin as a T antigen specific lectin

Jacalin is a 66 kDa tetrameric, galactose binding lectin (**Figure 4.3**) extracted from the jack fruit (*Artocarpus integrifolia*), which has a high specificity towards the T antigen.[11] Jacalin is one of several T antigen-specific lectins that can induce various biological responses following adhesion to membrane-bound glycoproteins. Some lectins can modulate cell proliferation by binding to glycosylated cell surface receptors and activate intracellular signaling pathways in a similar manner to growth factors.[12] For example, peanut agglutinin binds to the T antigen on glycosylated isoforms of the transmembrane CD44v6 receptor, thereby activating c-Met and mitogen-activated protein kinase (MAPK) signaling, and thereby increasing cell proliferation.[12,13] Similarly, the lectin Amaranthin causes an increase in cell proliferation upon binding.[14] Other lectins are known to induce a reversible inhibition in proliferation, such as the *Agaricus bisporus* lectin and jacalin.[14,15] Jacalin has been found to bind specifically to the T antigen expressed at the surface of HT-29 human colorectal adenocarcinoma cells, with a dissociation constant (K_d) of 500 ± 50nM, reaching maximum binding in 20 minutes at 4 °C.[14]

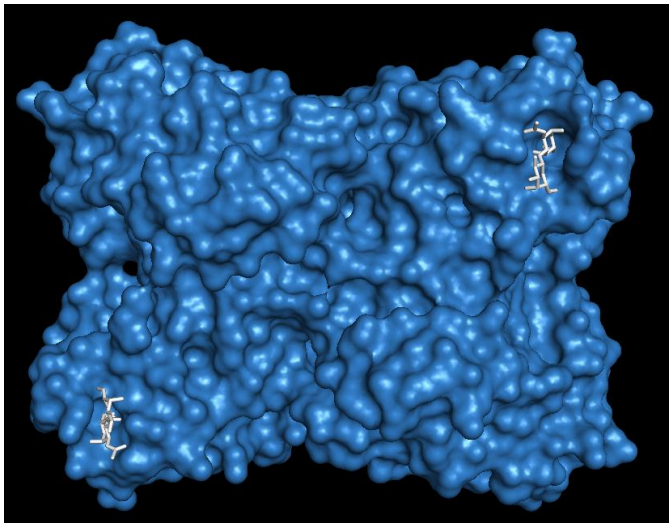

Figure 4.3 **A Pymol generated image (PDB ID 1M26[16]) of jacalin complexed to two individual T antigens (white). The remaining two T antigens are bound at the posterior face of the lectin.**

Jacalin has been previously used to detect the T antigen expressed on precancerous and cancerous colonic tissue.[17] Histological examination of T antigen expression using jacalin was compared to using the anti-T antigen antibody and the galactose oxidase-Schiff (GOS)

reaction. The GOS reaction colorimetrically labels tissue expressing the T antigen, following oxidation of the terminal galactose residue of the disacharride and treatment with Schiff's reagent (basic fuchsin).[18] Jacalin had the highest sensitivity of 84.3% for cancerous and precancerous tissue, as compared to the GOS reaction (75.7%) and immunostaining (50%).[17] However, the anti-T antigen antibody and the GOS reaction had the highest selectivity for the T antigen on cancerous and precancerous tissue (100%), whereas jacalin had only 80% selectivity.[17] It was suggested that jacalin cross-reacted with the sialyl-T antigen, which the lectin can also recognise.[17,19] However, the binding affinity of jacalin to the sialylated T antigen is weaker than its affinity for the T antigen.[19]

A number of photosensitising molecules have been reported to bind to jacalin with K_d values ranging from 0.42 mM to 7.69 μM. Binding was found to be at either the carbohydrate binding domain or at other regions of the lectin, depending on the sensitiser used.[20,21] These PDT agents include phycocyanin[22] (a phycobiliprotein from cyanobacteria and algae), meso-tetrasulfonatophenylporphyrin,[20,21] and zinc meso-tetrasulfonatophenylporphyrin.[20] Jacalin was therefore proposed to act as a potential tumour specific PDT vehicle, directing the photosensitising molecules to cancer cells expressing the T antigen. However, no studies have previously demonstrated the *in vitro* or *in vivo* efficacy of using jacalin for targeted PDT treatment of cancer.

A recent study by Poiroux *et al.*[23] has highlighted the potential of using lectins for targeted photodynamic cancer therapy. The T antigen, as well as the Tn antigen, expressed on Jurkat leukaemia cells were successfully targeted with the lectin, Morniga G, covalently conjugated to a water soluble porphyrin photosensitiser. Targeted PDT using the Morniga G-porphyrin conjugate reduced Jurkat leukaemia cell viability by more than 90%, whereas the non-conjugated sensitiser had no PDT effect at the same concentration.

The use of jacalin as a cancer-specific lectin to target gold nanoparticles for PDT is described for the first time in this chapter.[24] The oncofoetal T antigen at the surface of HT-29 human colon adenocarcinoma cells has been successfully targeted with jacalin functionalised C11Pc-PEG gold nanoparticles. Confocal microscopy revealed the enhanced intracellular uptake of the jacalin conjugates, as compared to the non-conjugated particles. By specifically targeting the T antigen, a dramatic reduction in cell viability was observed following PDT treatment. Phototoxicity of the targeted nanoparticle constructs was found to be predominantly through the necrotic pathway, with no signs of apoptosis.

4.2 Results and Discussion

4.2.1 Synthesis of jacalin conjugated C11Pc-PEG gold nanoparticles

C11Pc-PEG gold nanoparticles were synthesised in THF and conjugated to jacalin through covalent amide coupling to the PEG molecules, as described in **section 2.2.1**. A diagrammatic representation of the multifunctional jacalin conjugated C11Pc-PEG gold nanoparticles is shown in **Figure 4.4**.

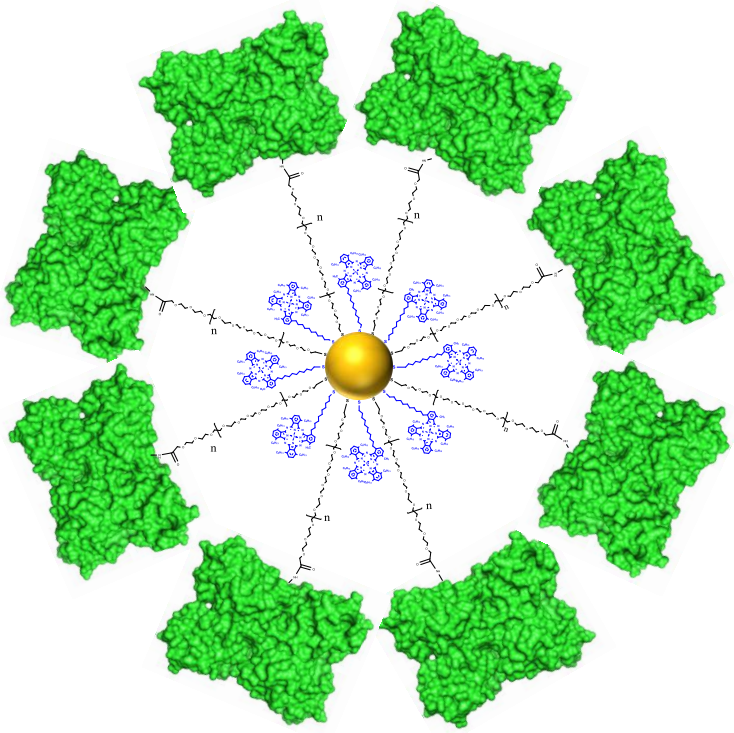

Figure 4.4 **A schematic representing the jacalin conjugated C11Pc-PEG gold nanoparticles composed of a mixed monolayer of the C11Pc photosensitiser (blue) and PEG molecules (black) covalently conjugated to jacalin (green, PDB ID 1M26[16]).**

The UV-visible absorption spectra of jacalin conjugated and non-conjugated C11Pc-PEG gold nanoparticles in serum-free RPMI 1640 cell culture medium are shown in **Figure 4.5**. It is clear that the monomeric, photoactive C11Pc species (absorption band maximum at *ca.* 696 nm) is predominant following self-assembly to the gold nanoparticles, and after covalent conjugation to jacalin.

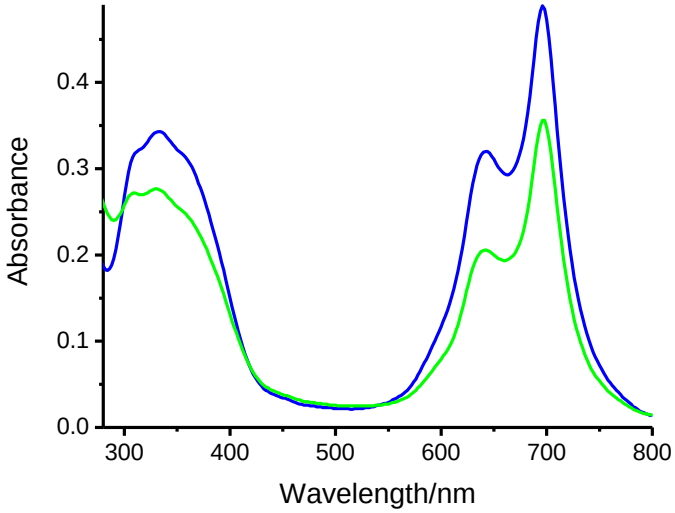

Figure 4.5 **UV-visible absorption spectra of C11Pc-PEG gold nanoparticles in serum-free RPMI 1640 medium with (green) and without (blue) jacalin conjugation.**

4.2.2 Singlet oxygen production by the C11Pc-PEG gold nanoparticles

To confirm that the C11Pc-PEG gold nanoparticles undergo a type II photosensitisation process to produce singlet oxygen, a study using deoxygenated and reoxygenated solutions of the nanoparticles was performed. A HEPES buffered saline solution of C11Pc-PEG gold nanoparticles containing APDA was deoxygenated by argon saturation and irradiated for 30 min at 633 nm, as described in **section 2.2.2**. **Figure 4.6** shows the UV-visible absorption spectra of the ADPA (*ca.* 300-420 nm; **Figure 4.6** (**A**)) and the C11Pc Q-band (*ca.* 550-750 nm; **Figure 4.6** (**B**)) during irradiation of the deoxygenated then reoxygenated solution of C11Pc-PEG gold nanoparticles. The decay in ADPA absorbance at 400 nm by singlet oxygen, following the irradiation of the C11Pc-PEG gold nanoparticles is shown in **Figure 4.6** (**C**). Singlet oxygen production by the C11Pc-PEG gold nanoparticles also resulted in a decay in the C11Pc absorbance intensity at 696 nm (**Figure 4.6** (**D**)). The decrease in C11Pc absorption can be attributed to the photooxidation of the C11Pc molecules to produce 3,6-bis-decylphthalimide following irradiation at 633 nm.[25] It is clear that during the irradiation of the deoxygenated nanoparticle solution, the rate of ADPA photobleaching was limited, as was the rate of C11Pc degradation. Upon reoxygenation of the nanoparticle solution, the rate of singlet oxygen production dramatically increased, as did the rate of C11Pc degradation. The oxygen dependence of the photobleaching of ADPA and the photodegradation of C11Pc suggest that both

processes are mediated by photosensitised singlet oxygen. The maximum rate of ADPA photobleaching upon irradiation of the nanoparticles in HEPES buffered saline was 4.83% Abs $_{400\ nm}$/min/μM C11Pc.

The singlet oxygen production of a HEPES buffered saline solution of jacalin conjugated C11Pc-PEG gold nanoparticles was also measured using ADPA. A maximum rate of ADPA photobleaching following irradiation of the jacalin nanoparticle conjugates was calculated to be 2.86% Abs $_{400\ nm}$/min/μM C11Pc.

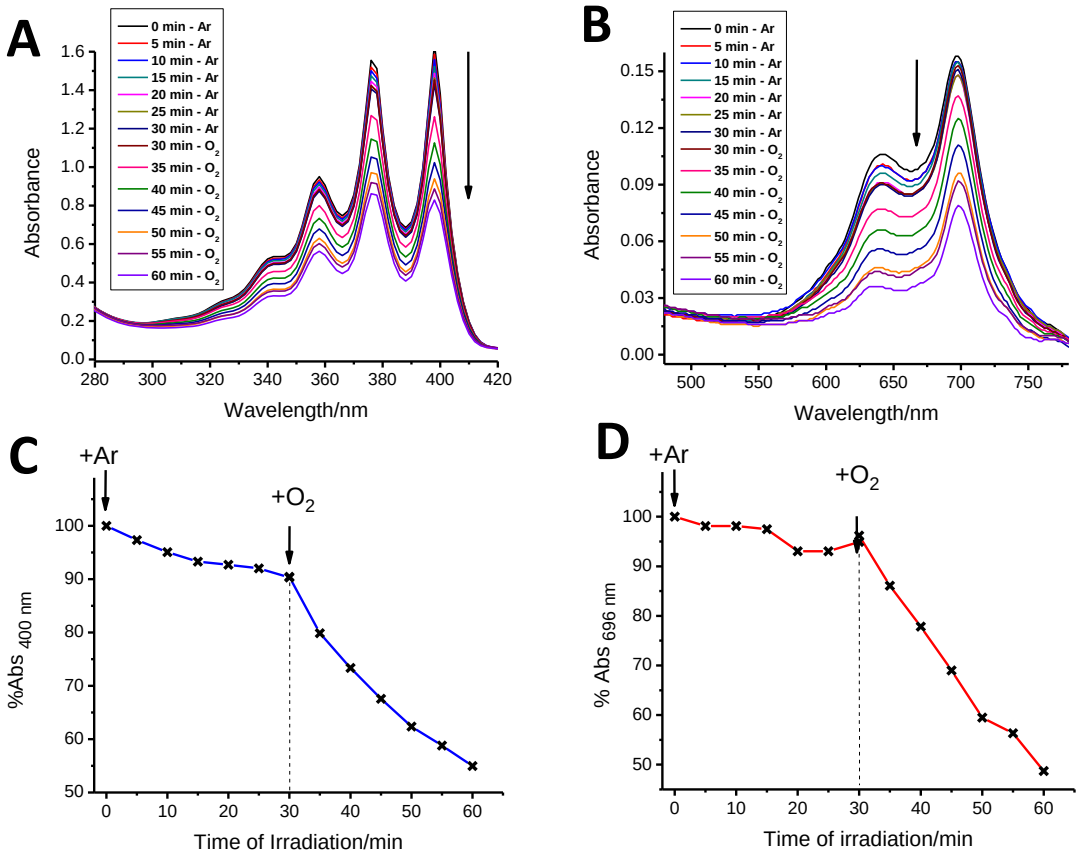

Figure 4.6 **UV-visible absorption spectra of a HEPES buffered solution of C11Pc-PEG gold nanoparticles containing the singlet oxygen molecular probe, ADPA (0.17 mM). The absorbance profiles of ADPA (A) and the C11Pc Q-band (B) are shown during the irradiation of the deoxygenated and reoxygenated solution at 633 nm. Progressive decay in absorbance of ADPA at 400 nm (C) and C11Pc at 696 nm (D) are a result of singlet oxygen production following irradiation.**

4.2.3 PDT of HT-29 cells using the jacalin conjugated C11Pc-PEG gold nanoparticles synthesised in THF

After confirming that both jacalin conjugated and non-conjugated C11Pc-PEG gold nanoparticles could produce significant quantities of singlet oxygen, the *in vitro* PDT efficacy of jacalin conjugated nanoparticles was investigated in HT-29 human colon adenocarcinoma cells. HT-29 cells have been shown to express *ca.* 4.4×10^7 T antigens per cell.[14] Jacalin conjugated or non-conjugated C11Pc-PEG gold nanoparticles were prepared as described in **section 2.2.1**. A range of concentrations between 0.00-1.15 μM C11Pc equivalent were incubated with the HT-29 cells for 3 h. Transparent 96 well multidishes were used to enable *in situ* optical imaging following PDT treatment. Following incubation with the nanoparticles, the cells were irradiated for 5 min per well at 633 nm. Inspection of the HT-29 cells using optical microscopy following PDT treatment using either non-conjugated or jacalin conjugated particles revealed no morphological changes associated with cell death. The viability of the cells was assessed using the MTT assay 48 h after irradiation, as described in **section 2.2.3**. The viability of the HT-29 cells following PDT treatment is expressed as a percentage of control cells not incubated with nanoparticles without irradiation (**Figure 4.7**). The non-ionic surfactant, Triton X-100, was used as a positive control for cytotoxicity. **Figure 4.7** (**A**) shows the HT-29 cell viability following incubation with 0.00-1.15 μM C11Pc equivalent of non-conjugated C11Pc-PEG gold nanoparticles. No significant changes in cell viability were observed in cells kept in the dark or those irradiated at 633 nm at any concentration of nanoparticles used. Similarly, **Figure 4.7** (**B**) shows that no significant difference in viability is observed between cells kept in the dark or those irradiated following incubation with jacalin-conjugated C11Pc-PEG gold nanoparticles. However, the jacalin conjugated C11Pc-PEG gold nanoparticles induced a substantial dose-dependent reduction in viability to a similar extent in cells with or without irradiation (*ca.* 60.70-62.51% reduction at 1.15 μM C11Pc equivalent, **Figure 4.7** (**B**)). Although the MTT results show a noticeable reduction in cell viability following incubation with the jacalin conjugated particles, the morphology of the HT-29 cells appeared largely unaltered, as compared to the untreated control cells. This reduction in viability of HT-29 cells incubated with the jacalin nanoparticle conjugates could be attributed to a non-cytotoxic inhibition of HT-29 cell proliferation upon jacalin binding. Previous findings have shown that jacalin (20 $\mu g.ml^{-1}$) can reversibly inhibit HT-29 cell proliferation by up to 46 ± 4% by down-regulating the extracellular signal-regulated kinase (ERK) signalling pathway through the activation of the tumour suppressor membrane protein, pp32.[14,26]

The results outlined in this section suggest that jacalin conjugated C11Pc-PEG gold nanoparticles bind to the HT-29 cells, as confirmed by the drastic anti-proliferative effects the conjugates exert. However, although sufficient concentrations of C11Pc were used in this experiment, it is likely that a low C11Pc loading efficiency onto the nanoparticles is responsible for the lack of an observable PDT effect. A low C11Pc loading efficiency can lead to insufficient intracellular accumulation of the sensitiser and a poor efficacy of phototoxicity, given that nanoparticle uptake may still be significant. Inductively coupled plasma-mass spectrometry (ICP-MS) analysis has previously shown that the C11Pc-PEG gold nanoparticles synthesised in THF have *ca.* 10 molecules of C11Pc per gold nanoparticle.[27] By increasing the C11Pc loading efficiency, an enhanced intracellular accumulation of the sensitiser may be achieved at the same concentration of C11Pc equivalent. The higher C11Pc loading efficiency could ultimately reduce the concentration of gold nanoparticles required to achieve effective cell kill when using the same concentration range of C11Pc equivalent (0.10-1.15 μM).

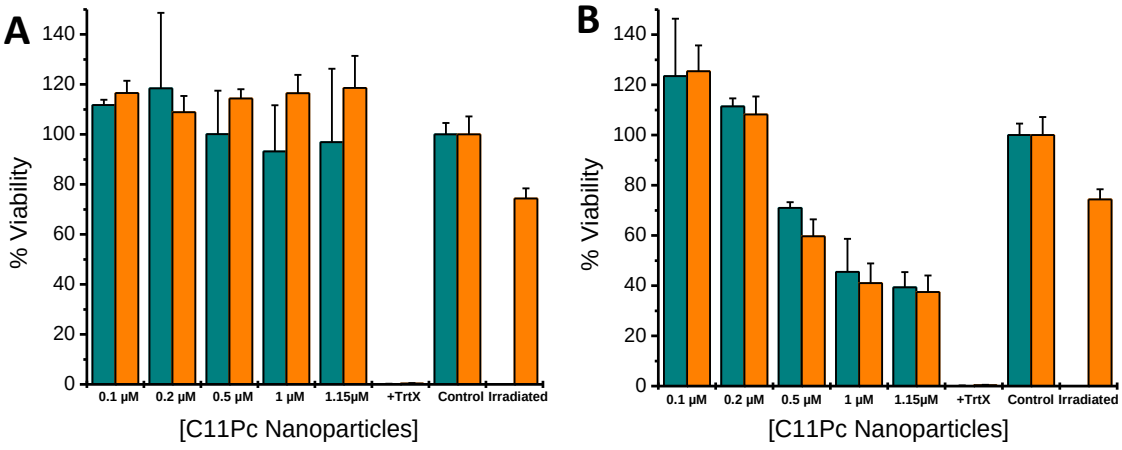

Figure 4.7 **MTT viability assay following PDT treatment of HT-29 cells using non-conjugated (A) and jacalin conjugated (B) C11Pc-PEG gold nanoparticles. HT-29 cells were seeded 24 h prior to incubation with the nanoparticles. After a 3 h incubation with the nanoparticles, the cells were either irradiated for 5 min per well (orange) or non-irradiated (dark cyan). Cells not incubated with nanoparticles were used as a control . 'Irradiated' refers to cells irradiated for 5 min per well but not incubated with nanoparticles. Triton X-100 (+TrtX; 1%) was used as a positive control for cytotoxicity. (Error bars are ± 95% confidence intervals, n=3).**

4.2.4 Synthesis and characterisation of high yield C11Pc-PEG gold nanoparticles in DMF

As discussed in **section 4.2.3**, the C11Pc-PEG gold nanoparticles synthesised in THF are likely to be carrying C11Pc at quantities insufficient for cell kill. The typical yield of C11Pc-PEG gold nanoparticles synthesised in THF was *ca.* 2 μM C11Pc equivalent. Following the reduction of gold (III) chloride by sodium borohydride, the instability of PEG gold nanoparticles (C11Pc-free) in excess THF during synthesis causes the particles to rapidly precipitate. This could possibly lead to a lower efficiency of C11Pc self-assembly, lower yields of C11Pc-PEG gold nanoparticles and a higher PEG:C11Pc ratio at the surface of the gold nanoparticles. To investigate whether enhancing the stability of the PEG nanoparticles during synthesis could increase the C11Pc loading and the yield of C11Pc-PEG gold nanoparticles, the use of an alternative solvent was explored. *N,N*-dimethylformamide (DMF) was used to incrementally replace THF in the synthesis of the nanoparticle conjugates. PEG gold nanoparticles without C11Pc were synthesised with varying ratios of DMF:THF, as described in **section 2.2.4**. Following 15 h of stirring, samples A to F (**Figure 4.8**) were visually inspected for nanoparticle precipitation. It is apparent that by increasing the ratio of DMF:THF, the PEG gold nanoparticles were increasingly more stable in the reaction solvent mixture.

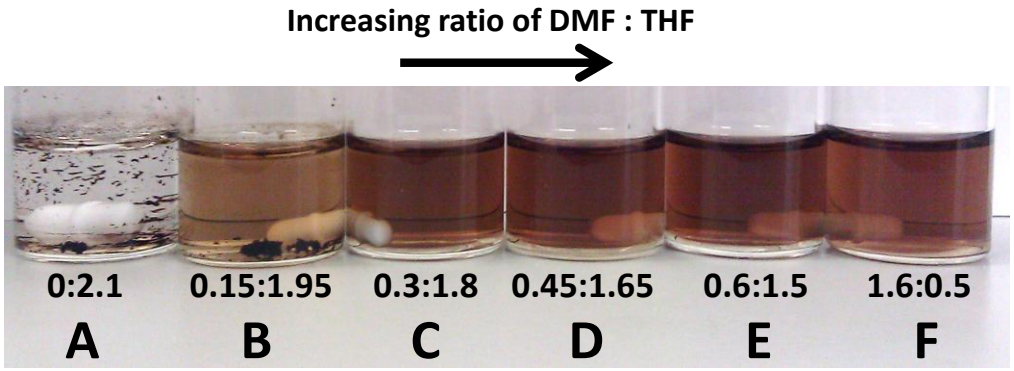

Figure 4.8 **Samples of PEG gold nanoparticles (C11Pc-free) synthesised using varying proportions of DMF to THF. As the ratio of DMF to THF increases, the stability of the brown PEG gold nanoparticles in the reaction mixture is enhanced.**

As the nanoparticles in sample F (**Figure 4.8**) appeared to be the most stable, the synthetic reaction conditions were used to synthesise C11Pc-PEG gold nanoparticles using DMF as the main solvent, as described in **section 2.2.4**. THF was only used to dissolve the C11Pc. Following 15 h of stirring, the C11Pc-PEG gold nanoparticle reaction mixture appeared more stable and the MES buffered solution of nanoparticles was *ca.* 6 µM C11Pc equivalent. The use of DMF as the main solvent was compared to using methanol, as PEG gold nanoparticles were also found to be highly stable in methanol. The MES buffered solutions of nanoparticles synthesised in DMF or methanol are shown in **Figure 4.9** (**A**). To confirm that the C11Pc present in the solution of nanoparticles was directly bound to the gold surface rather than non-covalently associated with the PEG, TLC separation of the nanoparticles synthesised in DMF or methanol was investigated (**Figure 4.9** (**B**) and (**C**), respectively). Following TLC separation of the nanoparticle sample synthesised in DMF, a blue residue of C11Pc-PEG gold nanoparticles remained at the stationary phase and some free C11Pc travelled with the mobile phase. When methanol was used as the main solvent, only brown PEG particles remained at the stationary phase and the majority of the C11Pc travelled with the mobile phase. It is therefore likely that the C11Pc was associated with the PEG at the surface of the nanoparticles synthesised in methanol, and was not directly bound to the gold particles. Therefore, it was concluded that C11Pc was only bound to the surface of gold nanoparticles synthesised using DMF as the main solvent. For this reason, DMF was used as the solvent of choice for nanoparticle synthesis for the remainder of the results reported in this chapter.

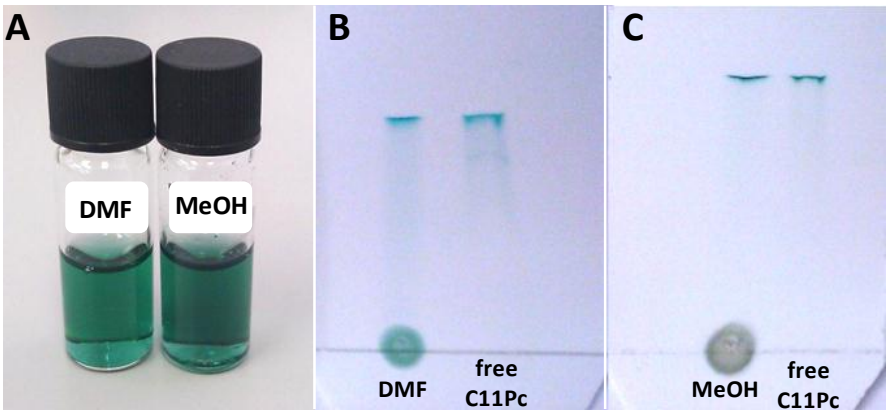

Figure 4.9 **A) C11Pc-PEG gold nanoparticles dissolved in MES buffer synthesised in DMF or methanol (MeOH). TLC separation of free C11Pc from the MES buffered solutions of gold nanoparticles (8 µl) synthesised in DMF (B) and in methanol (C). Free C11Pc in THF was used as a control. Toluene/methanol (98:2) was used as the mobile phase for the separation of unbound C11Pc from the nanoparticles.**

To confirm that the higher yield of C11Pc-PEG gold nanoparticles synthesised in DMF was due to the stabilisation of C11Pc by the nanoparticles, the synthesis was performed using 0.564 mM or 0.282 mM of gold (III) chloride. The image shown in **Figure 4.10** (**A**) demonstrates that the solution of nanoparticles synthesised in DMF using 0.564 mM gold (III) chloride appeared to contain a significantly higher amount of C11Pc than those synthesised using 0.282 mM gold (III) chloride. The UV-visible absorption spectra in **Figure 4.10** (**B**) shows that the yield of C11Pc-PEG gold nanoparticles was found to be dependent on the concentration of the gold (III) chloride used for the synthesis. The yield of the C11Pc-PEG gold nanoparticles synthesised using 0.282 mM gold (III) chloride (3.54 µM C11Pc equivalent) was significantly lower than the yield of nanoparticles synthesised using 0.564 mM gold (III) chloride (9.26 µM C11Pc equivalent). This difference further confirms that the gold nanoparticles were responsible for stabilising the C11Pc in aqueous media.

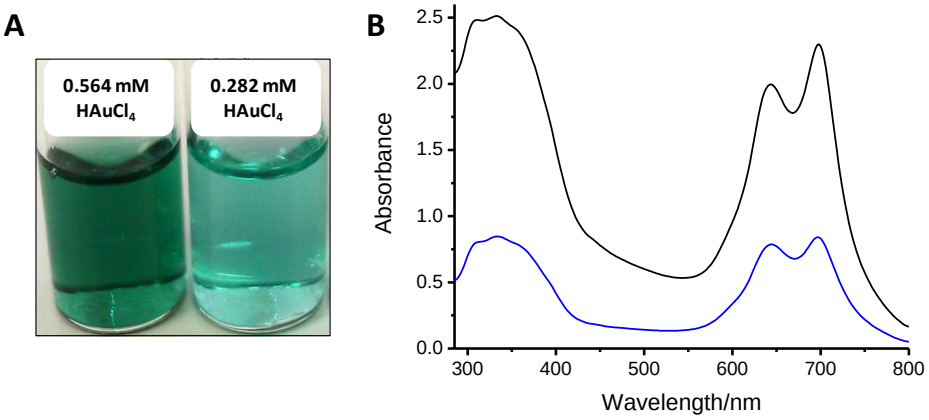

Figure 4.10 **A) Samples of C11Pc-PEG gold nanoparticles in MES buffer synthesised in DMF using 0.564 mM or 0.282 mM gold (III) chloride. B) UV-visible absorption spectra of MES buffered solutions of the C11Pc-PEG gold nanoparticles synthesised using 0.564 mM (black) or 0.282 mM (blue) gold (III) chloride.**

The singlet oxygen production by C11Pc-PEG gold nanoparticles synthesised in DMF was then investigated using ADPA as the singlet oxygen molecular probe, as described in **section 2.2.4**. The UV-visible absorption spectra of C11Pc-PEG gold nanoparticles in the presence of ADPA (0.17 mM) during 30 min of irradiation at 633 nm is shown in **Figure 4.11** (**A**). The characteristic ADPA absorption bands at *ca.* 300-420 nm (**Figure 4.11** (**B**)) decrease in intensity upon singlet oxygen generation following irradiation of the C11Pc-

PEG gold nanoparticles. Irradiation of the C11Pc-PEG gold nanoparticles also resulted in a decay in the C11Pc Q-band at *ca.* 550-750 nm upon irradiation at 633 nm (**Figure 4.11** (**C**)). The C11Pc Q-band decay is associated with photooxidation of the sensitiser following singlet oxygen generation, as discussed in **section 4.2.2**. The maximum rate of ADPA decay following irradiation at 633 nm of the nanoparticles in MES buffer was *ca.* 0.91% Abs $_{400\,nm}$/min/μM C11Pc (**Figure 4.11** (**D**)). This rate was found to be significantly lower than that obtained following the irradiation of a MES buffered solution of C11Pc-PEG gold nanoparticles synthesised in THF (*ca.* 3.73% Abs $_{400\,nm}$/min/μM C11Pc). The C11Pc-PEG gold nanoparticles synthesised in DMF were not sufficiently purified after synthesis. It is possible that the reason for this decrease in the maximum rate of ADPA decay, and rate of singlet oxygen production, is as a result of the presence of PEG gold nanoparticles, without C11Pc functionalisation. The presence of such particles could increase the light scattering and hinder C11Pc activation. Therefore, the removal of the PEG gold nanoparticles not functionalised with the phthalocyanine could be crucial in maximising the singlet oxygen production by the C11Pc-PEG gold nanoparticle conjugates.

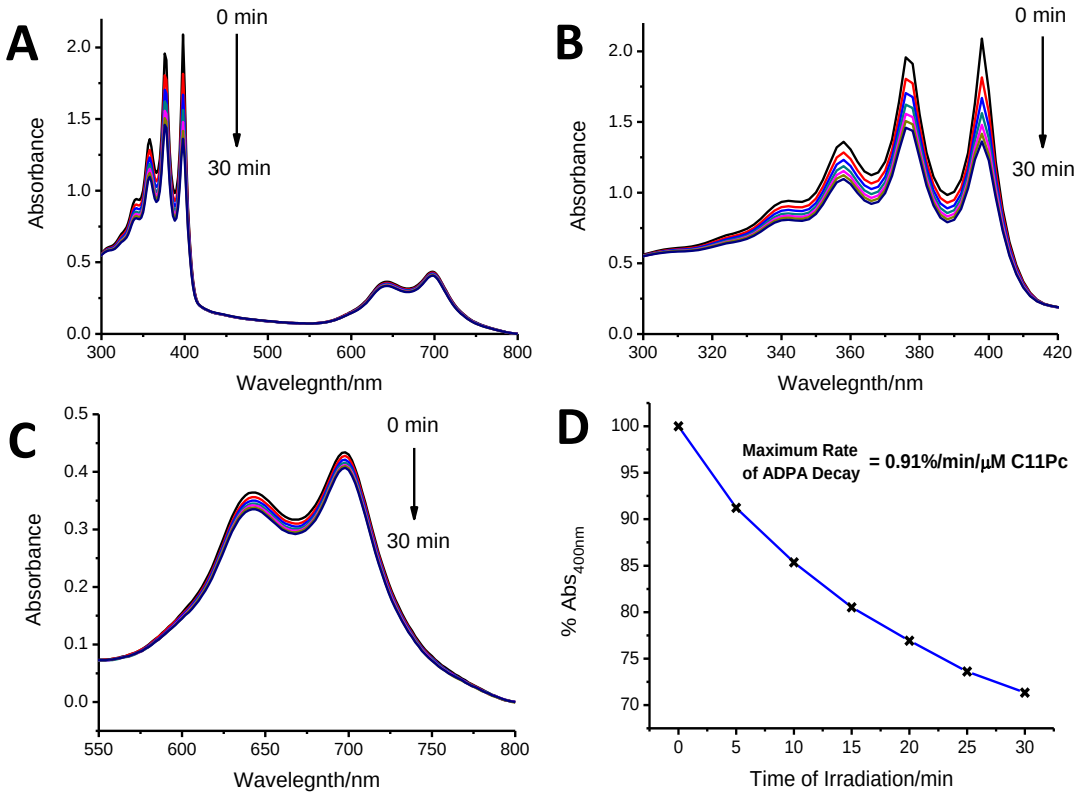

Figure 4.11 **A) UV-visible absorption spectra of a MES buffered solution of C11Pc-PEG gold nanoparticles (1.94 μM C11Pc equivalent) synthesised in DMF in the presence of ADPA (0.17 mM), irradiated at 633 nm for 30 min. B) Photobleaching of the ADPA absorption bands by singlet oxygen upon irradiation of the C11Pc-PEG gold nanoparticles. C) Decrease in the absorbance intensity of the phthalocyanine Q-band following singlet oxygen production upon irradiation. D) Progressive photobleaching of ADPA expressed as a percentage decay in absorbance intensity at 400 nm.**

Nanoparticles were synthesised again in DMF, as described in **section 2.2.4**, with an additional purification step that uses a THF extraction procedure to separate the nanoparticles functionalised with C11Pc from the dried nanoparticle mixture. The portion of the nanoparticles soluble in THF was dried and dissolved in MES buffer (THF extract) while the portion of the nanoparticles insoluble in THF was dissolved in water (water extract). The UV-visible absorption spectra of the two extracts are shown in **Figure 4.12**. The THF extract has a higher yield of C11Pc-PEG gold nanoparticles (4.35 μM C11Pc equivalent) than the water extract (3.92 μM C11Pc equivalent). The UV-visible absorption spectra in **Figure 4.12** show a greater absorption intensity between 300-400 nm, which suggests a higher content of gold nanoparticles in the water extract than in the THF

extract. Overall, it is apparent that the nanoparticles synthesised in DMF contain varying amounts of C11Pc at their surface. The particles with a higher degree of C11Pc functionalisation are more readily soluble in THF.

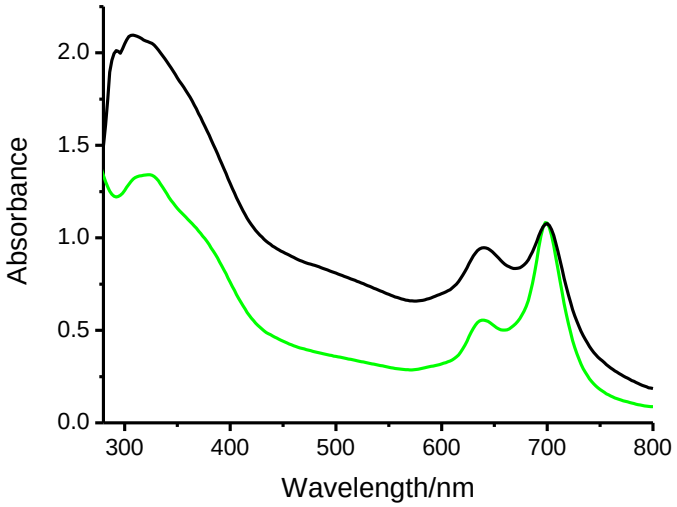

Figure 4.12 **UV-visible absorption spectra of C11Pc-PEG gold nanoparticles synthesised in DMF using an aqueous solution of sodium borohydride. A fraction of the C11Pc-PEG gold nanoparticles was soluble in both THF and water (THF extract, green, 4.35 μM C11Pc equivalent). The other fraction of nanoparticles was only soluble in water (water extract, black, 3.92 μM C11Pc equivalent).**

To investigate the effect of the absence of water on the C11Pc distribution on the nanoparticles, the synthesis of the C11Pc-PEG gold nanoparticles was repeated a further time using DMF. However, on this occasion DMF was also used as a solvent for the sodium borohydride, rather than water. The additional purification step using THF was also incorporated into this synthetic strategy. The UV-visible absorption spectra of the THF and water extracts of the C11Pc-PEG gold nanoparticles (**Figure 4.13**) show that the THF extract had a *ca.* 4.2-fold higher yield of C11Pc-PEG gold nanoparticles than the water extract. Additionally, the THF extract contained a *ca.* 1.55 μM C11Pc equivalent higher concentration of nanoparticles (**Figure 4.13**) than the THF extract of the particles shown in **Figure 4.12**. The higher C11Pc-PEG gold nanoparticle yield indicates that the absence of water during the synthesis leads to a more distinct separation between particles with a high C11Pc loading efficiency and particles with a low C11Pc loading efficiency.

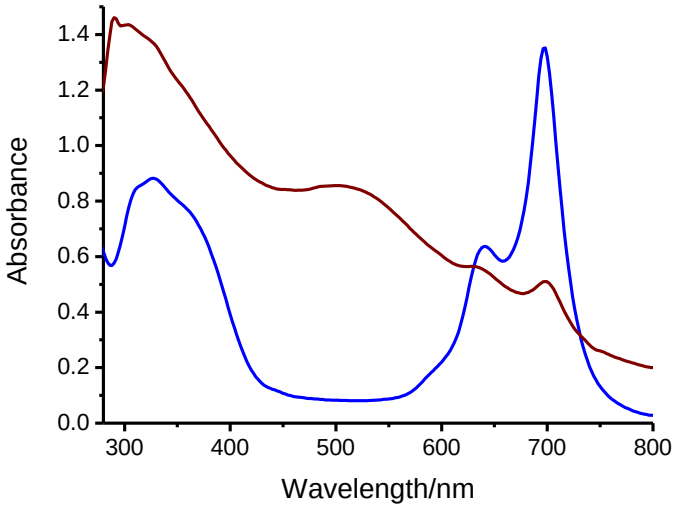

Figure 4.13 **UV-visible absorption spectra of the C11Pc-PEG gold nanoparticles synthesised in DMF using a DMF solution of sodium borohydride. A fraction of C11Pc-PEG gold nanoparticles was soluble in both THF and water (THF extract, blue, 5.9 µM C11Pc equivalent). The second fraction was only soluble in water (water extract, brown, 1.39 µM C11Pc equivalent).**

THF extracts of C11Pc-PEG gold nanoparticles synthesised in DMF, using either an aqueous solution or a DMF solution of sodium borohydride (**Figure 4.14** (**A**)), were spotted onto TLC plates. In both instances the free C11Pc was separated from the nanoparticle conjugates, as described in **section 2.2.4**. It is clear from **Figure 4.14** (**B**) that both THF extracts predominantly consisted of C11Pc-PEG gold nanoparticles and the amount of unbound C11Pc is negligible.

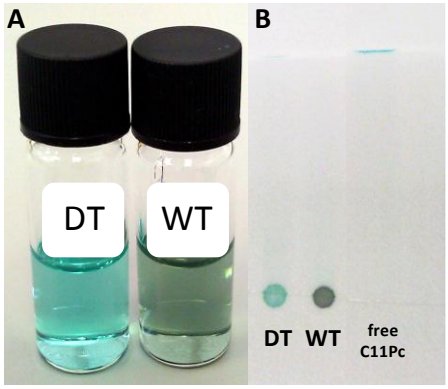

Figure 4.14 **A) THF extracts of C11Pc-PEG gold nanoparticles in MES buffer synthesised in DMF with either a DMF solution (DT) or an aqueous solution (WT) of sodium borohydride. B) TLC separation of free C11Pc from the THF extracts of C11Pc-PEG gold nanoparticles in MES buffer (8 µl). Both samples were synthesised in DMF using a DMF solution (DT) or an aqueous solution (WT) of sodium borohydride. Free C11Pc in THF was used as a control. The mobile phase used for the separation was toluene/methanol (98:2).**

As the yield of the C11Pc-PEG gold nanoparticles was higher when a DMF solution of sodium borohydride was used, this procedure was used for further investigations into singlet oxygen production. To facilitate the removal of the PEG gold nanoparticles not functionalised with C11Pc, a further purification step was introduced. Following the synthetic reaction of the nanoparticles, excess THF was added and the precipitated PEG gold nanoparticles not functionalised with C11Pc were removed by centrifugation. The remainder of the procedure was then performed as usual.

C11Pc-PEG gold nanoparticles were synthesised in DMF using a DMF solution of sodium borohydride, with the additional THF extraction purification steps. ADPA (0.17 mM) was used to measure the singlet oxygen production by the MES buffered solution of C11Pc-PEG gold nanoparticles following irradiation at 633 nm for 30 min. **Figure 4.15** shows that the maximum rate of ADPA decay was 2.70% $Abs_{400\,nm}$/min/µM C11Pc. This rate is greater than that of the C11Pc-PEG gold nanoparticles synthesised using an aqueous solution of sodium borohydride (0.91% $Abs_{400\,nm}$/min/µM C11Pc, **Figure 4.11** (**D**)). The increase in the maximum rate of ADPA decay confirms that the removal of C11Pc-free PEG gold nanoparticles enhanced the singlet oxygen production by the irradiation of the C11Pc-PEG gold nanoparticles. C11Pc-PEG gold nanoparticles in MES buffer were imaged using the TEM. **Figure 4.16** shows that the nanoparticles are non-aggregated with a diameter of *ca.* 2-4 nm.

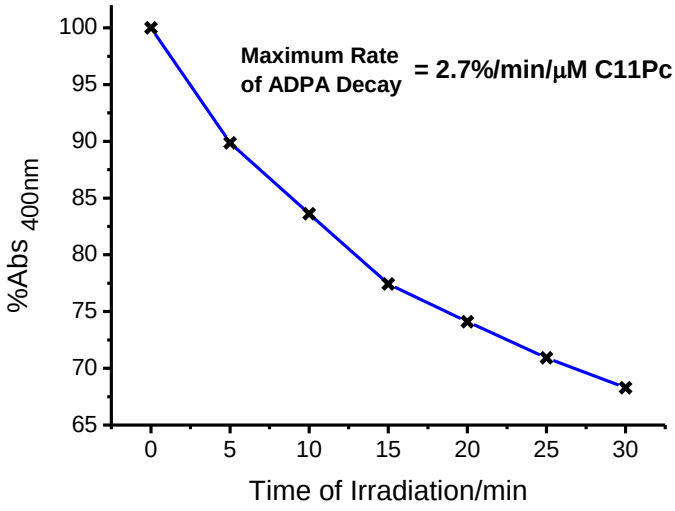

Figure 4.15 **The percentage decay in ADPA absorbance intensity at 400 nm upon singlet oxygen generation following irradiation of C11Pc-PEG gold nanoparticles in MES buffer.**

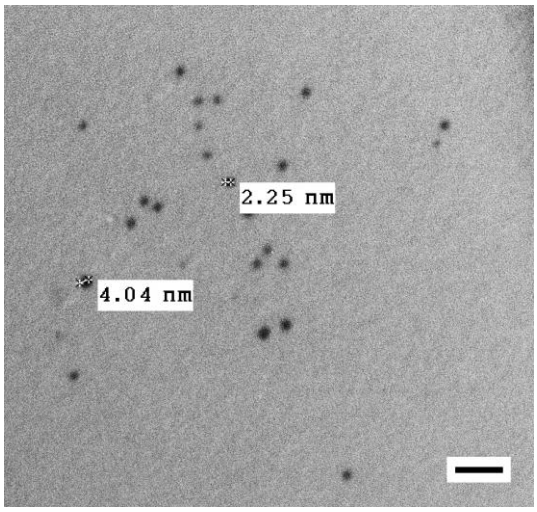

Figure 4.16 **A TEM image of C11Pc-PEG gold nanoparticles in MES buffer showing non-aggregated nanoparticles *ca.* 2-4 nm in diameter. (Scale bar is 20 nm).**

Table 4.1 summarises the finalised method for synthesising the C11Pc-PEG gold nanoparticles, which was used for the remainder of the experiments described in this thesis.

Table 4.1 The optimised experimental procedure for the synthesis of C11Pc-PEG gold nanoparticles.

Step	Procedure	Details
1	2 mg C11Pc in 1 ml THF	stirred continuously
2	7.5 mg PEG in 2 ml DMF	stirred with C11Pc for 5 min
3	1.2 mg gold (III) chloride in 1.2 ml DMF	stirred with C11Pc and PEG for 5 min
4	1.5 mg sodium borohydride in 1.2 ml DMF	added to the mixture and stirred for 15 h
5	5.4 ml THF added	stirred for 2 min
6	PEG gold nanoparticles (C11Pc free) removed	centrifuged at 200 xg for 2 min
7	solvent mixture removed	rotary evaporation at 70 °C
8	5.4 ml THF added	C11Pc-PEG gold nanoparticles extracted
9	THF removed	rotary evaporation at 70 °C
10	5.4 ml MES buffer added	C11Pc-PEG gold nanoparticles dissolved
11	free C11Pc removed	centrifuged at 21,913 xg for 30 min

Elemental analysis of the C11Pc-PEG gold nanoparticles using inductively coupled plasma-optical emission spectrometry (ICP-OES), as described in **section 2.2.5**, revealed that the as-synthesised nanoparticles had a gold concentration of 29.10 ± 0.05 $\mu g.ml^{-1}$ and a zinc concentration of 4.90 ± 0.005 $\mu g.ml^{-1}$. This gives a gold to zinc ratio of 1:0.168. Based on the approximation that *ca.* 4.2 nm diameter gold nanoparticles consist of a total of 923 atoms formed of 6 layers,[28] each 0.7 nm apart,[29] then *ca.* 155 C11Pc molecules were assembled onto each gold nanoparticle. Assuming that each thiol occupies *ca*. 21.4 $Å^2$ on a gold surface, the theoretical maximum number of thiol groups bound to a gold nanoparticle with a diameter of 4.2 nm is *ca.* 259 thiols per nanoparticle.[30] Consequently, a calculated value of 155 C11Pc molecules per nanoparticle does appear to be realistic. This calculated value is *ca.* 15.5-fold higher than that previously reported for C11Pc-PEG gold nanoparticles synthesised in THF.[27] Therefore, the alternative synthetic procedure described in this section increases both the C11Pc-PEG gold nanoparticle yield and the C11Pc loading efficiency.

Based on the approximation that an average of *ca.* 155 molecules of C11Pc are bound to each nanoparticle, a 6 μM solution of C11Pc-PEG gold nanoparticles contains *ca.* 38.7 nM gold nanoparticles. By reacting a *ca.* 38.7 nM solution of EDC/NHS-activated C11Pc-PEG gold nanoparticles with 0.24 μM jacalin, the lectin is at a 6.2-fold molar excess of gold nanoparticles.

4.2.5 Jacalin conjugation and characterisation of C11Pc-PEG gold nanoparticle conjugates

Jacalin was covalently conjugated to the C11Pc-PEG gold nanoparticles using EDC/NHS coupling, as described in **section 2.2.6**. The UV-visible absorption spectra of the jacalin conjugated and non-conjugated nanoparticles (**Figure 4.17**) reveal that the conjugation procedure and the removal of unbound jacalin did not alter the predominantly monomeric C11Pc at the surface of the nanoparticles. The jacalin conjugated C11Pc-PEG gold nanoparticles were also characterised using TEM imaging (**Figure 4.18**). The nanoparticles appear to be non-aggregated and monodisperse, with an average diameter of 4.30 ± 0.18 nm (mean ± 95% confidence interval, n=100).

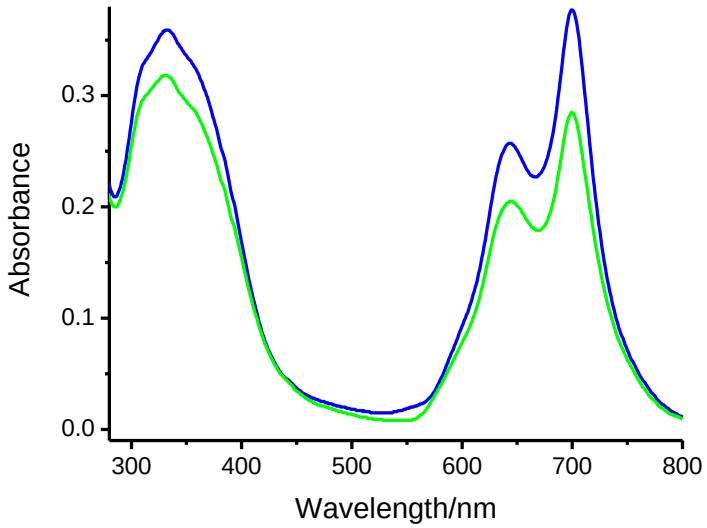

Figure 4.17 **UV-visible absorption spectra of C11Pc-PEG gold nanoparticles with (green) and without (blue) jacalin conjugation in serum-free RPMI 1640 medium.**

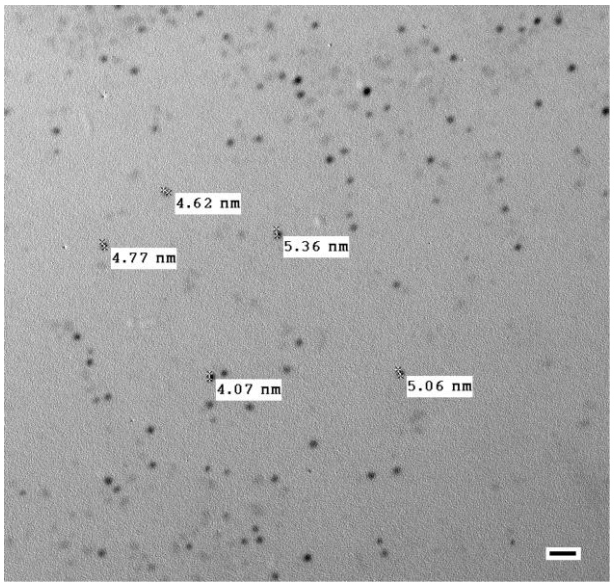

Figure 4.18 **A TEM image of the jacalin conjugated C11Pc-PEG gold nanoparticles in HEPES buffered saline. (Scale bar is 20 nm)**

The singlet oxygen production by the jacalin conjugated C11Pc-PEG gold nanoparticles in HEPES buffered saline was measured using ADPA, as described in **section 2.2.7**. The UV-visible absorption spectra of the nanoparticle conjugates in the presence of ADPA (0.17 mM) during 30 min of irradiation at 633 nm are shown in **Figure 4.19** (**A**). Singlet oxygen production was confirmed by the photobleaching of ADPA in addition to the photooxidation of the C11Pc. The maximum rate of ADPA decay of the jacalin conjugated C11Pc-PEG gold nanoparticles (**Figure 4.19** (**B**)) was found to be 2.82% $Abs_{400\ nm}$/min/μM C11Pc, as compared to 3.35% $Abs_{400\ nm}$/min/μM C11Pc for the non-conjugated nanoparticles (data not shown). Although jacalin conjugation decreased the maximum rate of ADPA decay, this potential limitation may be overcome if the cellular internalisation of the nanoparticles is significantly enhanced through targeting with jacalin.

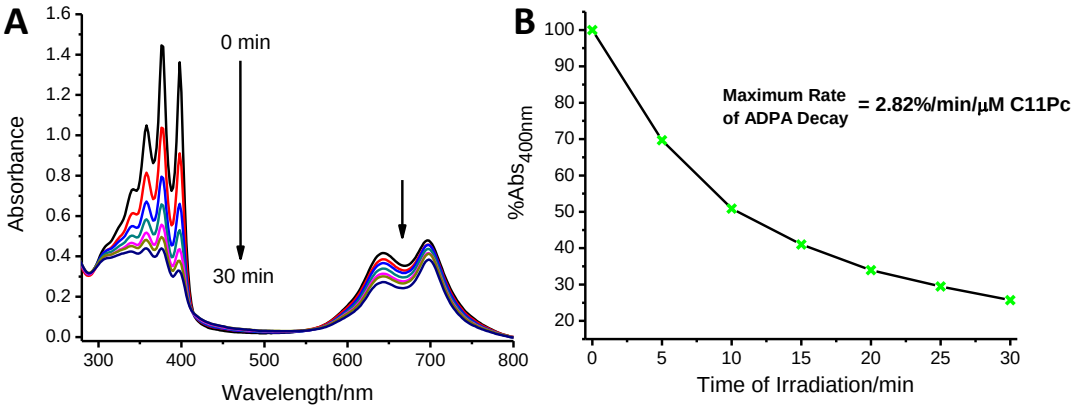

Figure 4.19 **A) UV-visible absorption spectra of a HEPES buffered solution of jacalin conjugated C11Pc-PEG gold nanoparticles (2.15 μM C11Pc equivalent) in the presence of ADPA (0.17 mM), irradiated at 633 nm for 30 min. B) Progressive photobleaching of ADPA following irradiation, expressed as a decay in percentage absorbance at 400 nm.**

4.2.6 Imaging of HT-29 cells subject to jacalin targeted PDT

HT-29 cells were seeded onto transparent multidishes and incubated with jacalin conjugated and non-conjugated C11Pc-PEG gold nanoparticles (0.00-1.15 μM C11Pc equivalent), as described in **section 2.2.8**. The higher yield of C11Pc-PEG gold nanoparticles synthesised in DMF could suggest a higher degree of C11Pc loading onto the nanoparticle surface. A higher loading efficiency of C11Pc is likely to enhance the intracellular accumulation of the sensitiser, leading to a greater PDT efficacy than that observed with the nanoparticles described in **section 4.2.3**. Following irradiation of the cells incubated with non-conjugated C11Pc-PEG gold nanoparticles, no visible changes in cell morphology were observed, even at the highest concentration of 1.15 μM C11Pc equivalent (**Figure 4.20** (**A** and **B**)). The jacalin conjugated nanoparticles appeared to induce minimal cell damage at the highest concentration of 1.15 μM C11Pc equivalent without irradiation (**Figure 4.20** (**C**)). However, following irradiation, the jacalin conjugated C11Pc-PEG gold nanoparticles induced drastic HT-29 cell morphological changes (**Figure 4.20** (**D**)), which was strongly indicative of PDT induced cytotoxicity.

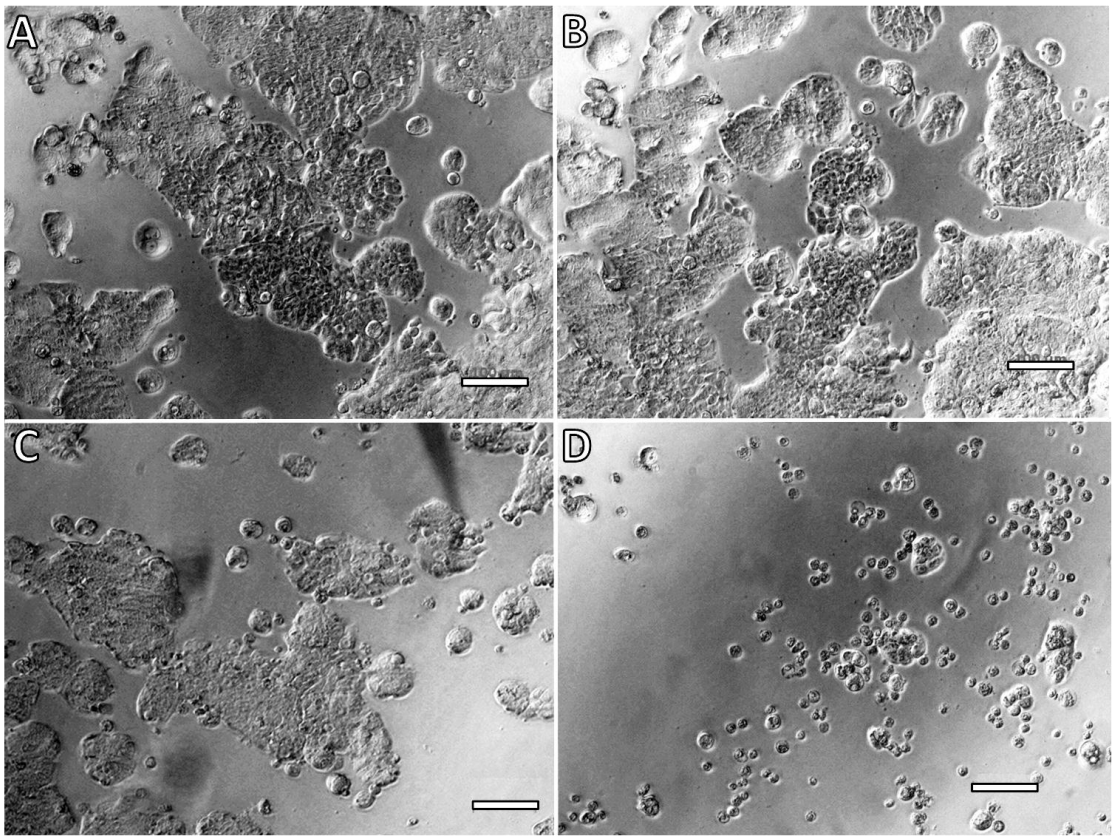

Figure 4.20 **Inverted optical microscope images of HT-29 cells incubated with 1.15 µM C11Pc equivalent of non-conjugated (A and B) and jacalin conjugated (C and D) C11Pc-PEG gold nanoparticles. The HT-29 cells were irradiated at 633 nm (B and D) for 5 min. (Scale bars are 100 µm).**

To confirm that the jacalin conjugated C11Pc-PEG gold nanoparticles were internalised by the HT-29 cells, the fluorescence of the C11Pc sensitiser was exploited in order to determine the localisation of the nanoparticle conjugates. The fluorescence excitation and emission spectra of the non-conjugated and jacalin conjugated C11Pc-PEG gold nanoparticles are shown in **Figure 4.21** (**A** and **B**, respectively). The C11Pc-PEG gold nanoparticles were excited at 633 nm, to mimic the excitation of the 633 nm HeNe laser of the laser scanning confocal microscope. Excitation at this wavelength resulted in a fluorescence emission band centred at 780 nm.

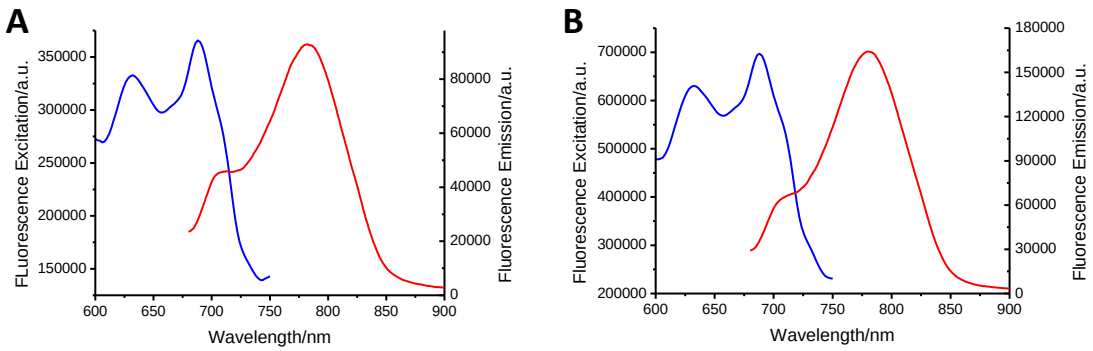

Figure 4.21 **Fluorescence excitation (blue)/emission (red) spectra of non-conjugated (A) and jacalin conjugated (B) C11Pc-PEG gold nanoparticles (1 μM C11Pc equivalent). Samples were in serum-free RPMI 1640 medium, excited at 633 nm with the emission centred at 780 nm.**

HT-29 cells were seeded onto glass coverslips, as described in **section 2.2.9**, and incubated with jacalin conjugated or non-conjugated C11Pc-PEG gold nanoparticles (1 μM or 2 μM C11Pc equivalent). Following irradiation, the cells were imaged using differential interference contrast (DIC) imaging overlaid with fluorescence images using excitation at 633 nm. **Figure 4.22** and **Figure 4.23** show the combined DIC and fluorescence images of the HT-29 cells incubated with 1 μM and 2 μM C11Pc equivalent of C11Pc-PEG gold nanoparticles, respectively. At both concentrations, it is apparent that the intracellular internalisation of the jacalin conjugated C11Pc-PEG gold nanoparticles (**Figure 4.22** and **Figure 4.23** (**A**)) was significantly more efficient than that of the non-conjugated C11Pc-PEG gold nanoparticles (**Figure 4.22** and **Figure 4.23** (**B**)). Following irradiation of the cells incubated with either concentration of jacalin conjugated nanoparticles, drastic changes in cellular morphology were observed (**Figure 4.22** and **Figure 4.23** (**C**)). The absence of apoptotic bodies strongly suggested that PDT cytotoxicity was not occurring through apoptosis. Cell membrane perforation and degradation is a key indicator of cell death *via* the necrotic pathway. Perforation of the cell membrane was assessed using the fluorescent marker propidium iodide. Propidium iodide is a membrane-impermeable nucleotide interchelator that specifically binds to DNA once the cell membrane is damaged.[31] The HT-29 cells incubated with the jacalin conjugated C11Pc-gold nanoparticles stained positive with propidium iodide following PDT treatment at both concentrations of nanoparticles (**Figure 4.22** and **Figure 4.23** (**D**)).

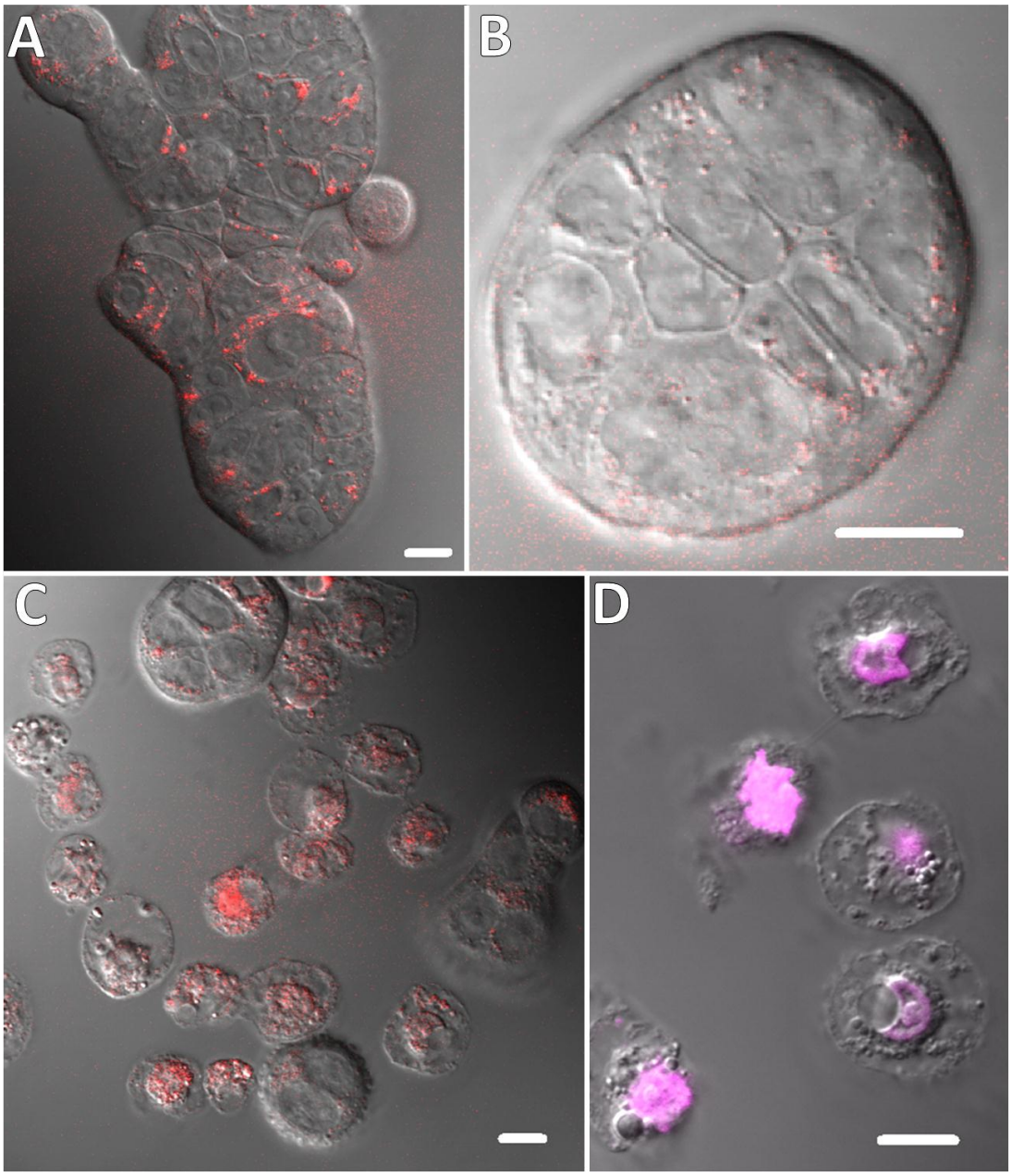

Figure 4.22 **Combined DIC and confocal fluorescence microscopy images of HT-29 cells incubated with jacalin conjugated (A) and non-conjugated (B) C11Pc-PEG gold nanoparticles (1 μM C11Pc equivalent). C) HT-29 cells incubated with jacalin conjugated C11Pc-PEG gold nanoparticles following irradiation at 633 nm for 6 min. D) HT-29 cells following jacalin targeted PDT, incubated with propidium iodide. (Scale bars are 10 μm).**

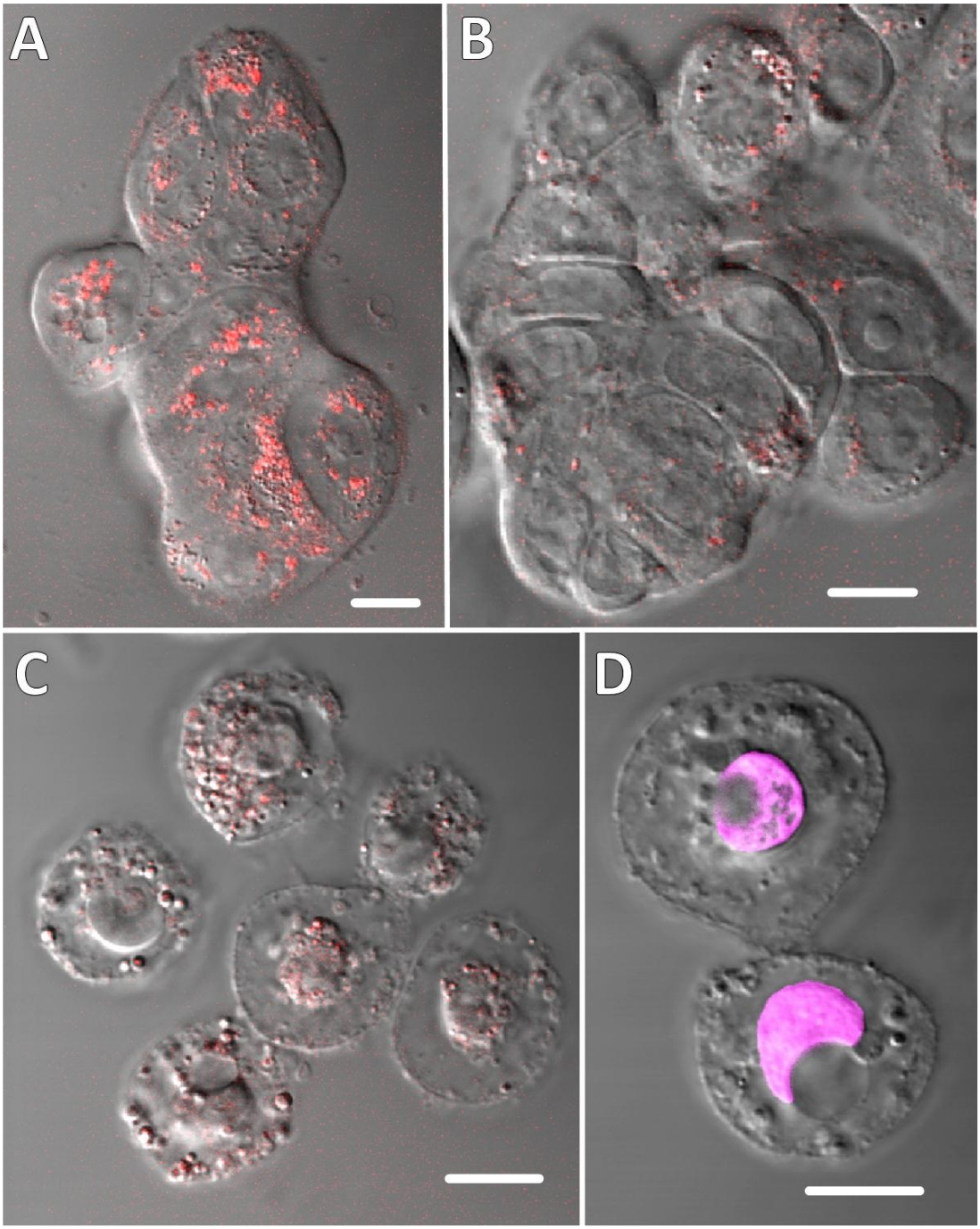

Figure 4.23 **Combined DIC and confocal fluorescence microscopy images of HT-29 cells incubated with jacalin conjugated (A) and non-conjugated (B) C11Pc-PEG gold nanoparticles (2 μM C11Pc equivalent). C) HT-29 cells incubated with jacalin conjugated C11Pc-PEG gold nanoparticles following irradiation at 633 nm for 6 min. D) HT-29 cells following jacalin targeted PDT, incubated with propidium iodide. (Scale bars are 10 μm).**

The confocal microscopy images in **Figure 4.22** and **Figure 4.23** demonstrate the significant improvement in intracellular accumulation of C11Pc-PEG gold nanoparticles, when conjugated to jacalin. PDT treatment of the HT-29 cells incubated with either 1 μM or 2 μM C11Pc equivalent of jacalin nanoparticle conjugates resulted in radical morphological changes associated with necrosis. Positive propidium iodide staining of the nuclei within the HT-29 cells following jacalin targeted PDT treatment further suggested that necrosis was induced. The findings detailed in this section reveal that the internalisation of the jacalin nanoparticle conjugates within HT-29 cells is responsible for the dramatic changes in morphology observed following irradiation at 633 nm. The effects on HT-29 cell viability following PDT treatment using the jacalin conjugated or non-conjugated C11PC-PEG gold nanoparticles are discussed in the next section.

4.2.7 Viability assessment of jacalin targeted PDT of HT-29 cells

The optical imaging and the laser scanning confocal microscopy demonstrated that the HT-29 cells could be targeted and subsequently killed with PDT using the jacalin conjugated C11Pc-PEG gold nanoparticles. To assess the degree of targeted phototoxicity of HT-29 cells by the jacalin nanoparticle conjugates, an MTT cell viability assay was performed using 0.00-1.15 μM C11Pc equivalent of jacalin conjugated and non-conjugated C11Pc-PEG gold nanoparticles, as described in **section 2.2.10**. Statistical significance was calculated using a one-tailed student's *t*-test. Without jacalin conjugation, no significant reduction in cell viability was observed at all concentrations used (**Figure 4.24** (**A**)). However, with jacalin conjugation, a significant photodynamic reduction in viability was observed at 0.5 μM C11Pc equivalent of jacalin conjugated nanoparticles (**Figure 4.24** (**B**), $P<0.05$). In the dark, viability of HT-29 cells incubated with 0.5 μM C11Pc equivalent of jacalin conjugated nanoparticles was *ca.* 100.2%, whereas cell viability following irradiation was at *ca.*79.3%. At 1 μM and 1.15 μM C11Pc equivalent of jacalin conjugated nanoparticles, cell viability reached a minimum of *ca.* 43%.

In **section 4.2.3** the MTT viability assay results following PDT treating using nanoparticles synthesised in THF show that incubation with jacalin conjugated particles reduced the proliferative activity of both the irradiated and non-irradiated HT-29 cells. In this section, incubation with jacalin conjugated nanoparticles at the same equivalent concentration of C11Pc did not induce the same reduction in HT-29 cell proliferation. This difference in anti-proliferative activity suggests that although the C11Pc concentration is consistent in

both experiments, the total concentration of jacalin nanoparticle conjugates incubated with the cells following the DMF synthetic method is significantly lower than that following synthesis using the THF method. Consequently, the jacalin targeted PDT effect on the HT-29 cells is dramatically improved.

The findings of the MTT assay indicate that jacalin effectively targeted the T antigen on HT-29 cells to induce an enhanced efficiency of photodynamic cell kill. However, it was suggested that the 633 nm HeNe laser beam diameter of 5 mm was insufficient for the direct irradiation of all the cells present in the wells of the multidishes. Therefore, by increasing the laser beam diameter, irradiation of a greater proportion of the monolayer of HT-29 cells in the wells may be achieved.

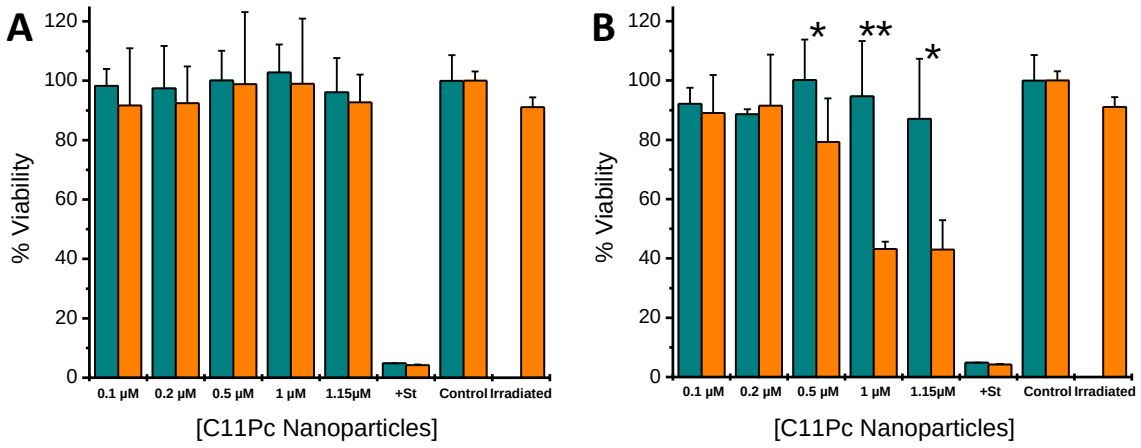

Figure 4.24 **MTT viability assay following PDT treatment of HT-29 cells using non-conjugated (A) and jacalin conjugated (B) C11Pc-PEG gold nanoparticles. After a 3 h incubation with the nanoparticles, the cells were either irradiated for 5 min per well (orange) or non-irradiated (dark cyan). Cells not incubated with nanoparticles were used as a control. 'Irradiated' refers to cells not incubated with nanoparticles but irradiated for 5 min per well. Staurosporine (+St; 20 µM) was used as a positive control for cytotoxicity. (Error bars are ± 95% confidence intervals, n=3. * indicates statistical significance at *P<0.05* and ** at *P<0.005* using a one-tailed *t*-test).**

To increase the beam diameter of the HeNe laser from 5 mm to 8 mm, the laser was fitted with a biconvexed divergent lens and positioned *ca.* 50 cm above the cells. Expanding the beam diameter reduced the laser fluency rate from 34 $mW.cm^{-2}$ to 29 $mW.cm^{-2}$. Therefore the irradiation time was increased to 6 min to maintain a consistent total light dose of 10.5 $J.cm^{-2}$. The jacalin targeted PDT treatment of the HT-29 cells was repeated using the laser

with the increased beam diameter. A minimal reduction in cell viability was observed with the non-conjugated C11Pc-PEG gold nanoparticles following 6 min irradiation at all concentrations used (**Figure 4.25** (**A**)). However, with jacalin conjugation, a substantial dose-dependent reduction in viability was observed following irradiation (**Figure 4.25** (**B**)) reaching a minimum of *ca.* 4-5% viability. The phototoxicity of the HT-29 cells following PDT treatment is shown in **Figure 4.25** (**C**). Irradiation of the cells incubated with non-conjugated C11Pc-PEG gold nanoparticles resulted in minimal phototoxicity at all nanoparticle concentrations used. However, irradiation of the cells incubated with the jacalin conjugated C11Pc-PEG gold nanoparticles induced considerable phototoxicity (*ca.* 95-96%) at 1.00-1.15 μM C11Pc equivalent, with a sigmoidal dose-dependent relationship.

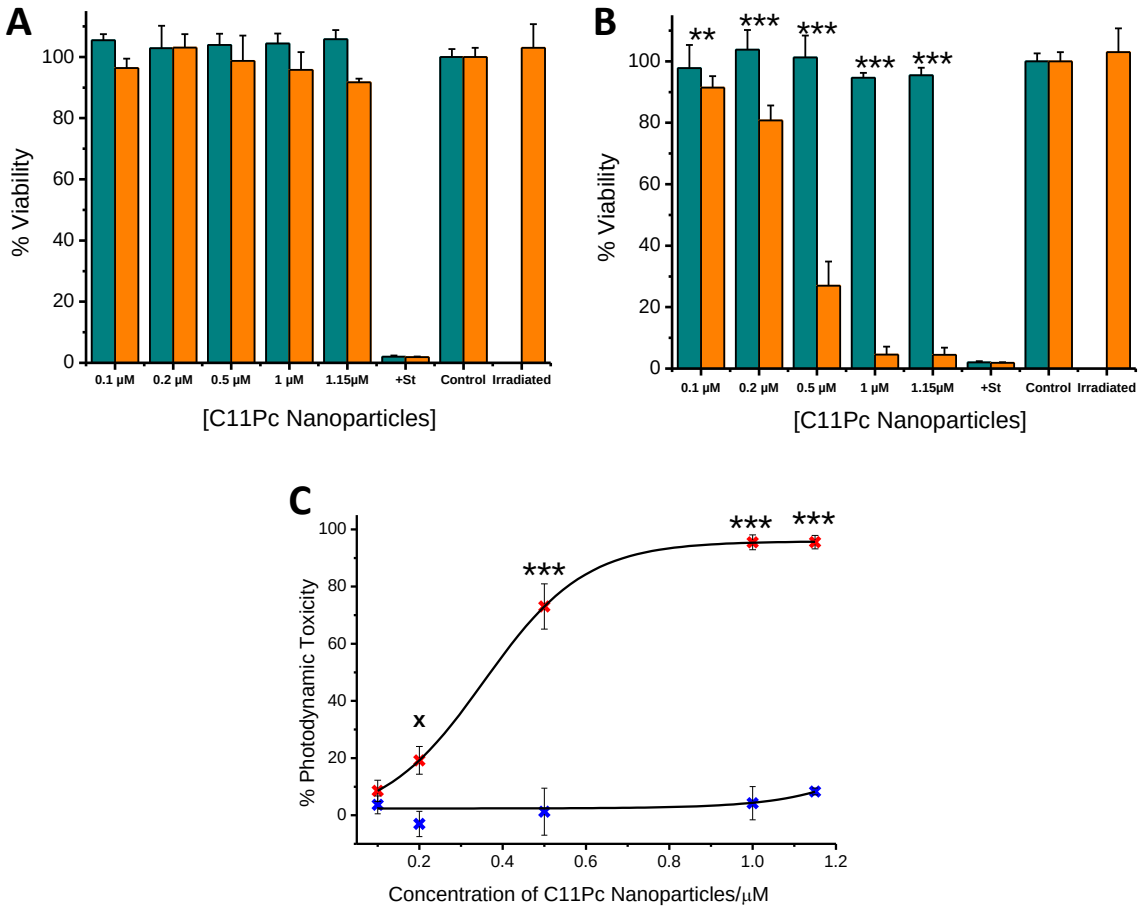

Figure 4.251 **MTT viability assay following PDT treatment of HT-29 cells using non-conjugated (A) or jacalin conjugated (B) C11Pc-PEG gold nanoparticles. After a 3 h incubation with the nanoparticles, the cells were irradiated for 6 min per well (orange) using a 633 nm HeNe laser fitted with a biconvexed divergent lens, or non-irradiated (dark cyan). Non-irradiated cells, not incubated with nanoparticles were used as a control. 'Irradiated' refers to cells irradiated at 633 nm, but not incubated with nanoparticles. Staurosporine (+St; 20 µM) was used as a positive control for cytotoxicity. C) Photodynamic toxicity of jacalin conjugated (X) and non-conjugated (X) nanoparticles following PDT treatment of HT-29 cells. (Error bars are 95% confidence intervals, n=3. ** indicates statistical significance at *P<0.005*, x at *P<0.001* and *** at *P<0.0005* using a one-tailed *t*-test).**

To confirm that the enhanced phototoxicity of the HT-29 cells was due to specific interactions between the jacalin functionalised C11Pc-PEG gold nanoparticles and the T antigen exposed at the cell surface, a competitive inhibition study was performed using methyl-α-D-galactopyranoside and asialofetuin. Simple sugars such as galactose (Gal) and *N*-acetylgalactosamine (GalNAc) have previously been used to inhibit the interaction

between jacalin and HT-29 cells at a concentration of 50 mM.[14] Studies of the carbohydrate specificity of jacalin showed that the lectin has a *ca.* 40-fold higher affinity to galactose when in the α-conformation, such as in methyl-α-D-galactopyranoside.[32] Asialofetuin, a glycoprotein expressing the T antigen, is known to bind to jacalin with a K_d of 0.4 nM.[33] Asialofetuin has been used to inhibit the binding of jacalin to HT-29 cells at a concentration of 40 μg.ml^{-1} (0.8 μM).[14] Consequently, methyl-α-D-galactopyranoside monohydrate and asialofetuin were both used to competitively inhibit the jacalin targeted phototoxicity of HT-29 cells, as described in **section 2.2.11**. It is clear from **Figure 4.26** that the presence of methyl-α-D-galactopyranoside or asialofetuin inhibited the photodynamic toxicity of the HT-29 cells by the jacalin conjugated C11Pc-PEG gold nanoparticles. A statistically significant inhibition of phototoxicity was observed at both concentrations of each inhibitor (*P<0.05*). The results of the competitive inhibition assay suggest that the enhanced photodynamic efficacy observed with the jacalin conjugated C11Pc-PEG gold nanoparticles was dependent on the targeted binding of jacalin to the T antigen on the HT-29 cell surface. Therefore, jacalin at the nanoparticle surface acts as a T antigen-specific endocytic ligand that transports the C11Pc-PEG gold nanoparticles into the HT-29 cells prior to photosensitisation.

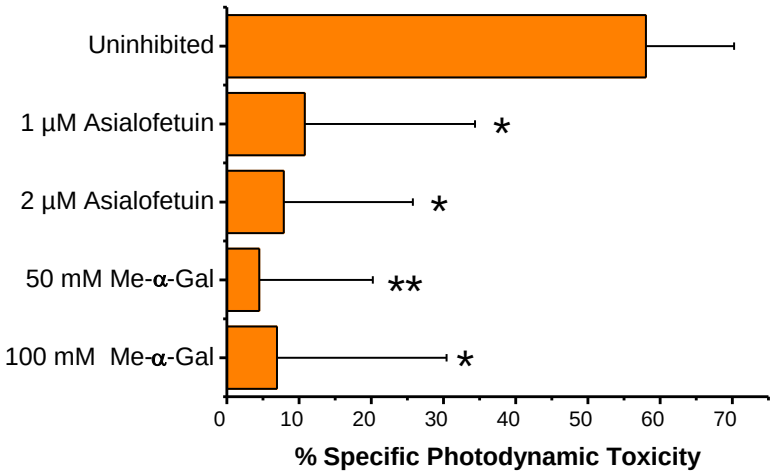

Figure 4.26 **Inhibition of the photodynamic toxicity of HT-29 cells by jacalin conjugated nanoparticles (0.5 μM C11Pc equivalent) using asialofetuin (1 μM or 2 μM) or methyl-α-D-galactopyranoside (50 mM or 100 mM, Me-α-Gal). (Error bars are 95% confidence intervals, n=3. * indicates statistical significance at *P<0.05* and ** at *P<0.005* using a one-tailed *t*-test).**

4.2.8 Determining the mechanism of jacalin targeted PDT cytotoxicity

Confocal imaging of HT-29 cells following jacalin targeted PDT treatment revealed that the cell nuclei stained positive with propidium iodide, suggesting that the primary mechanism of cell death was through necrosis. To establish the precise mechanism of jacalin mediated phototoxicity of the HT-29 cells, the ApoTox-Glo™ triplex assay was performed on the cells incubated with jacalin conjugated C11Pc-PEG gold nanoparticles 48 h following irradiation.

A viability/cytotoxicity reagent was prepared, as described in **section 2.2.12**, consisting of the viability substrate, glycylphenylalanyl-aminofluorocoumarin (GF-AFC), and the cytotoxicity substrate, bis-alanylalanyl-phenylalanyl-rhodamine 110 (bis-AAF-R110). The membrane permeable viability substrate, GF-AFC, is enzymatically cleaved by live cell proteases to release the fluorescent product aminofluorocoumarin (excitation at 405 nm, emission at 492 nm). The membrane impermeable cytotoxicity substrate bis-AAF-R110 is enzymatically cleaved by active dead cell proteases to release the fluorescent product rhodamine 110 (excitation at 492 nm, emission at 530 nm). The Caspase-Glo® 3/7 apoptosis reagent was also prepared, which contains a luminogenic substrate that is cleaved by active caspase 3/7 enzymes in apoptotic cells to release aminoluciferin. The reaction between UltraGlo™ luciferase and aminoluciferin results in bioluminescence centred at 576 nm.[34]

As can be seen from **Figure 4.27** (**A**), the viability of the HT-29 cells following jacalin targeted PDT treatment was reduced to *ca.* 5%, whereas no phototoxicity was observed with the cells incubated with non-conjugated C11Pc-PEG gold nanoparticles. These results are consistent with the MTT viability assay results shown in **Figure 4.25**. However, the results of the cytotoxicity component of the triplex assay shown in **Figure 4.27** (**B**) are inconsistent with the results of the viability component of the assay in **Figure 4.27** (**A**). It was expected that cytotoxicity would be observed following staurosporine treatment, although the levels of cytotoxicity found were comparable to those of the control. No cytotoxicity of the HT-29 cells was observed when the cells were incubated with non-conjugated nanoparticles with or without irradiation. Unexpectedly, some cytotoxicity was observed with jacalin conjugated nanoparticles without irradiation, although following irradiation, the cytotoxicity levels were below those of the control. The apoptosis component of the assay also gave unexpected results, as shown in **Figure 4.27** (**C**), with no apoptotic response detected above that of the cells under the control conditions. Treatment with staurosporine, which was used as a positive control for cytotoxicity

predominantly through apoptosis, caused no apparent increase in apoptosis. These results concluded that although the viability component of the assay was reliable, the cytotoxicity and apoptosis components of the assay were not effective 48 h following PDT treatment. It was thought that cytotoxicity or apoptosis of the HT-29 cells induced by PDT treatment or through staurosporine treatment was too extensive at 48 h following treatment. Therefore, at 48 h following PDT treatment, negligible activity of dead cell proteases or caspases were detected. It was therefore decided that the assay would be repeated 6 h following irradiation, at which time apoptosis induced DNA fragmentation in HT-29 cells following staurosporine treatment is observable.[35]

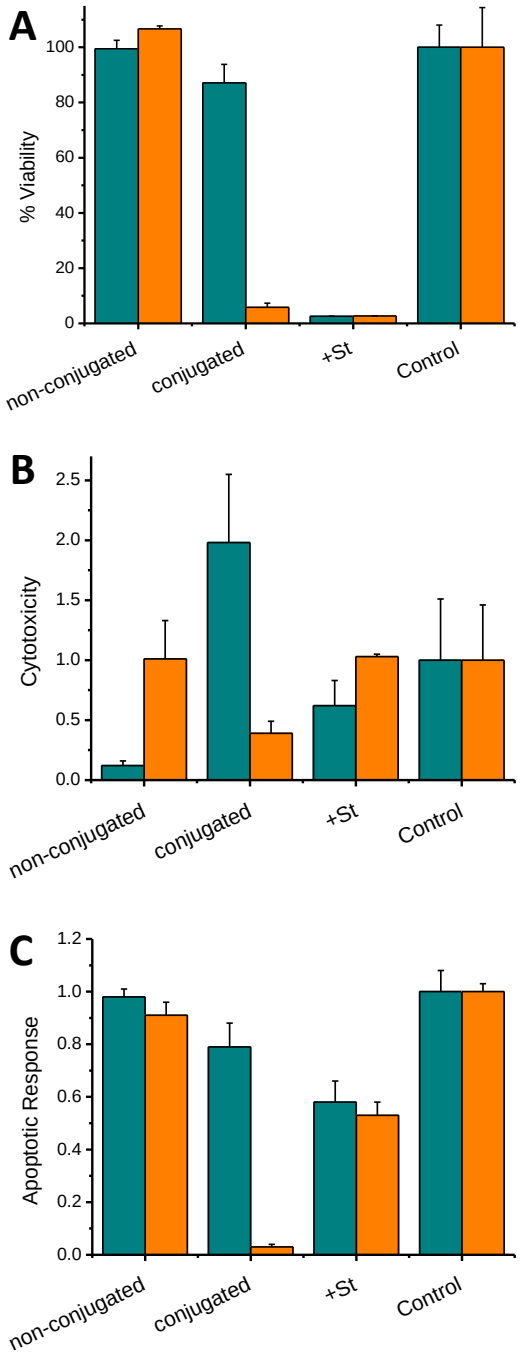

Figure 4.27 **Assessment of HT-29 cell viability (A), cytotoxicity (B) and apoptosis (C) using the ApoTox-Glo™ triplex assay performed 48 h after PDT treatment. The HT-29 cells were incubated for 3 h with C11Pc-PEG gold nanoparticles (1 µM C11Pc equivalent), with (conjugated) or without (non-conjugated) jacalin conjugation. Following incubation, the cells were either irradiated at 633 nm for 6 min per well (orange) or kept in the dark (dark cyan). Cells not incubated with nanoparticles were used as a control. Staurosporine (+St; 20 µM) was used as a positive control for cytotoxicity, predominantly through apoptosis. (Error bars are ± 95% confidence intervals, n=3).**

The ApoTox-Glo™ triplex assay was repeated, as described in **section 2.2.12**, on HT-29 cells incubated with either jacalin conjugated or non-conjugated C11Pc-PEG gold nanoparticles, 6 h after PDT treatment. Following irradiation, the viability of HT-29 cells incubated with jacalin conjugated nanoparticles (1 μM C11Pc equivalent) was drastically reduced to *ca.* 2.7% (*P<0.0005*), as shown in **Figure 4.28** (**A**). The viability of HT-29 cells incubated with non-conjugated C11Pc-PEG gold nanoparticles was reduced to *ca.* 57.2% (*P<0.0005*) following irradiation. HT-29 cell viability following irradiation of the cells incubated with non-conjugated nanoparticles (**Figure 4.28** (**A**)) is significantly lower than that observed when the assay was performed 48 h following irradiation (*ca.* 107%; **Figure 4.27** (**A**)). This difference suggests that the reduction in viability observed in **Figure 4.28** (**A**) is likely to be a temporary, non-cytotoxic inhibition in cell proliferation. Furthermore, no cytotoxicity or apoptosis is observed in HT-29 cells incubated with non-conjugated C11Pc-PEG gold nanoparticles following irradiation (**Figure 4.28** (**B** and **C**)). A reduction in viability (**Figure 4.28** (**A**)) that is not accompanied by any detectable cytotoxicity (**Figure 4.28** (**B**)) or apoptosis (**Figure 4.28** (**C**)) indicates that irradiation of HT-29 cells incubated with non-conjugated nanoparticles halts cell proliferation. Further investigations into cell growth and cell cycle arrest at varying time points following PDT treatment could give an insight into the extent of the cell damage induced by non-conjugated nanoparticles.[36] HT-29 cells incubated with jacalin conjugated C11Pc-PEG gold nanoparticles showed a *ca.* 5.2-fold increase in cytotoxicity following irradiation, as compared to the untreated control (*P<0.0005,* **Figure 4.28** (**B**)). Additionally, no increase in apoptosis of the HT-29 cells incubated with jacalin conjugated C11Pc-PEG gold nanoparticles was observed following irradiation (**Figure 4.28** (**C**)), thus confirming that jacalin targeted PDT of HT-29 cells induces cytotoxicity through necrosis at the defined conditions of the experiment. The mechanisms of PDT induced cytotoxicity are dependent on a large number of factors, which include the type and concentration of the photosensitiser used, the intracellular localisation of the PDT agent, the light dosage and the cell type investigated.[37] Following irradiation, a decrease in HT-29 cell viability and an increase in cytotoxicity were observed in cells incubated with 1 μM C11Pc equivalent of jacalin conjugated particles. Additionally, no indications of apoptosis were apparent. The findings of the ApoToxGlo™ triplex assay are consistent with the laser scanning confocal microscope images in **Figure 4.22** and **Figure 4.23**. Positive staining with propidium iodide, the lack of visible apoptotic bodies and the absence of an apoptotic response all strongly suggest that jacalin targeted PDT induces substantial necrosis in HT-29 cells expressing the T antigen.

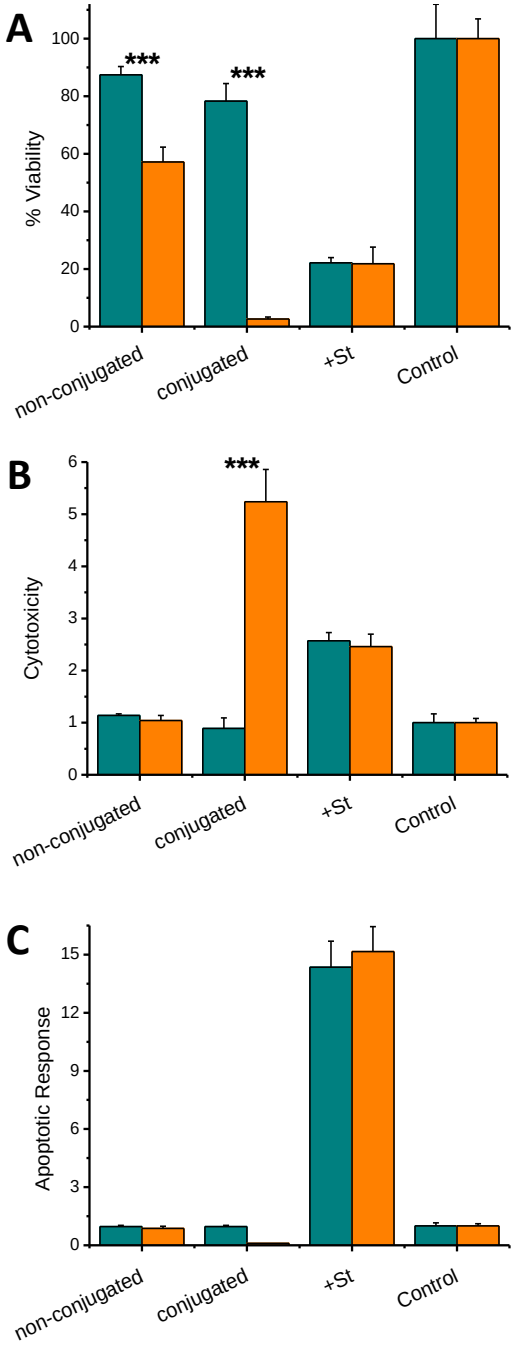

Figure 4.28 **Assessment of HT-29 cell viability (A), cytotoxicity (B) and apoptosis (C) using the ApoTox-Glo™ triplex assay performed 6 h after PDT treatment. The HT-29 cells were incubated for 3 h with the C11Pc-PEG gold nanoparticles (1 µM C11Pc equivalent), with (conjugated) or without (non-conjugated) jacalin conjugation. Following incubation, the cells were either irradiated at 633 nm for 6 min per well (orange) or non-irradiated (dark cyan). Cells not incubated with nanoparticles were used as a control. Staurosporine (+St; 20 µM) was used as a positive control for cytotoxicity, predominantly through apoptosis. (Error bars are ± 95% confidence intervals, n=3). *** indicates statistical significance at *P<0.0005*)**

4.3 Conclusions

The effective targeted PDT treatment of HT-29 human colon adenocarcinoma cells with jacalin conjugated C11Pc-PEG gold nanoparticles has been described in this chapter. Initially, the C11Pc-PEG gold nanoparticles synthesised in THF, with jacalin conjugation were ineffective against the HT-29 cells following irradiation at 633 nm. A dose-dependent reduction in viability was observed in both irradiated and non-irradiated HT-29 cells incubated with jacalin conjugated nanoparticles. The reduction in viability could be attributed to the non-cytotoxic inhibition in HT-29 cell proliferation following jacalin incubation.[14] The lack of PDT efficacy was possibly a result of a low number of C11Pc molecules per gold nanoparticle. The low C11Pc loading efficiency onto the nanoparticles could lead to insufficient intracellular accumulation of the sensitiser. It was previously reported that the C11Pc-PEG gold nanoparticles synthesised in THF have *ca.* 10 molecules of C11Pc per nanoparticle, as determined by ICP-MS analysis.[27] Therefore, an alternative synthetic procedure was explored to enhance the C11Pc loading efficiency onto the gold nanoparticles.

A novel protocol for synthesising C11Pc-PEG gold nanoparticles in DMF was introduced, which resulted in nanoparticles with a *ca.* 3-fold higher yield of C11Pc equivalent and *ca.* 155 molecules of C11Pc associated with each gold nanoparticle, as determined by ICP-OES analysis. The nanoparticle conjugates were *ca.* 4 nm in diameter and effectively generated singlet oxygen upon irradiation at 633 nm following conjugation to jacalin. Preliminary optical microscopy studies revealed the PDT efficacy of these jacalin nanoparticle conjugates on HT-29 cells. Cell morphology and integrity were severely compromised following targeted PDT treatment, whereas in the dark the cells remained largely unaffected. Non-conjugated C11Pc-PEG gold nanoparticles, at the same concentrations as the jacalin conjugates, induced no visible cell damage in the dark or following irradiation. Laser scanning confocal microscopy, in combination with differential interference contrast imaging, showed that jacalin conjugation vastly improves the intracellular accumulation of the C11Pc-PEG gold nanoparticles. Fluorescence confocal microscopy of the jacalin conjugated C11Pc-PEG gold nanoparticles following excitation with a 633 nm HeNe laser, revealed the intracellular localisation of the nanoparticles, which could be further confirmed using Z-stacked three-dimensional images. The intracellular distribution of the jacalin-nanoparticle conjugates indicates that their internalisation was likely to be through an endocytic pathway, as opposed to diffusion through the membrane to the cytoplasm. Following irradiation, the HT-29 cells incubated with jacalin conjugated particles

appeared spherical in morphology with a poorly defined cell periphery, typical of dead cells. The lack of apoptotic bodies indicate that cell death was predominantly through the necrotic pathway.[38] In addition, positive staining of the nuclei of those cells with propidium iodide suggested that cell membrane integrity was impaired.[31,38]

The MTT viability assay was used to investigate the extent and dose-dependence of jacalin targeted phototoxicity by the C11Pc-PEG gold nanoparticle conjugates. It was found that the jacalin conjugated C11Pc-PEG gold nanoparticles induced a significant reduction in viability (*ca.* 60% at 1.15 μM C11Pc equivalent), which was greatly enhanced following a *ca.* 3 mm increase in the beam diameter of the 633 nm HeNe laser used for irradiation. Statistical analysis using a one-tailed student's *t*-test revealed that a statistically significant reduction in viability was observed following the irradiation of the HT-29 cells incubated with all concentrations of the jacalin conjugates. It was found that a sigmoidal dose-dependence in cytotoxicity was observed with the jacalin conjugated C11Pc-PEG gold nanoparticles, reaching a maximum of *ca.* 96% at 1.15 μM C11Pc equivalent concentration. Conversely, the non-conjugated C11Pc-PEG gold nanoparticles exhibited minimal phototoxicity, suggesting that jacalin significantly promotes the specific endocytosis of the nanoparticle conjugates. The MTT assay was also utilised to perform a competitive inhibition study to determine the significance of the carbohydrate binding capacity of jacalin conjugated particles on their PDT efficacy. Methyl-α-D-galactopyranoside and asialofetuin have been previously used to inhibit the selective binding of jacalin to carbohydrates.[14,32] It was found that both methyl-α-D-galactopyranoside and asialofetuin significantly inhibited the phototoxicity of jacalin conjugated C11Pc-PEG gold nanoparticles (0.5 μM C11Pc equivalent). Inhibition of phototoxicity of the jacalin conjugated nanoparticles confirmed that the enhanced PDT effect observed with the HT-29 cells was a result of jacalin binding to the T antigen at the surface of the cells. Therefore, jacalin conjugation significantly increases the specific internalisation of the C11Pc-PEG gold nanoparticle conjugates within the HT-29 cells, as compared to the non-conjugated nanoparticles.

Preliminary indications that necrosis was the mechanism of jacalin mediated PDT cytotoxicity were suggested by the morphology of the treated cells and by the positive staining of the cell nuclei with propidium iodide. The ApoTox-Glo™ triplex assay, which assesses cell viability, cytotoxicity and apoptosis, further indicated that necrosis was predominant following jacalin targeted PDT. Following incubation with jacalin conjugated C11Pc-PEG gold nanoparticles and irradiation at 633 nm, the HT-29 cells exhibited a

significant decrease in viability and a marked increase in cytotoxicity. Furthermore, no indications of apoptosis were observed.

In conclusion, it was found that by conjugating the lectin jacalin to C11Pc-PEG gold nanoparticles, the oncofoetal T antigen disaccharide was successfully targeted at the surface of HT-29 cells. Following recognition and binding to the T antigen at the HT-29 cell surface, the jacalin conjugated C11Pc-PEG gold nanoparticles were delivered intracellularly, as confirmed by laser scanning confocal microscopy. Irradiation of the intracellular nanoparticle conjugates at 633 nm induced cell death of a remarkable proportion of HT-29 cancer cells (*ca*. 95-98%) *via* necrosis. Conversely, no significant dark toxicity was observed in the non-irradiated HT-29 cells incubated with the jacalin conjugated nanoparticles. HT-29 cells incubated with non-conjugated nanoparticles exhibited no significant reduction in viability, even following irradiation, although some reduction in viability was observed at 1 μM C11Pc equivalent, only at 6 h following irradiation. Since the T antigen is expressed by more than 90% of primary human carcinomas[4] and by a number of cancer stem cells,[6] it is an appealing target for a range of cancer therapies. The ability to target the T antigen with jacalin conjugated C11Pc-PEG gold nanoparticles and then to efficiently destroy the cells with PDT is a significant first, and potentially an important development in cancer therapy. In the following chapter, the efficacy of using lectins as cancer targeting ligands will be compared to the use of monoclonal antibodies for selective PDT.

4.4 References

1. Samuel, J.; Noujaim, A. A.; MacLean, G. D.; Suresh, M. R.; Longenecker, B. M. *Cancer Res.* **1990**, *50*, 4801-4808.
2. Cao, Y.; Merling, A.; Karsten, U.; Goletz, S.; Punzel, M.; Kraft, R.; Butschak, G.; Schwartz-Albiez, R. *Int. J. Cancer* **2008**, *123*, 89-99.
3. Yu, L.-G. *Glycoconjugate J.* **2007**, *24*, 411-420.
4. Springer, G. F. *Science* **1984**, *224*, 1198-1206.
5. Dube, D. H.; Bertozzi, C. R. *Nat. Rev. Drug Discovery* **2005**, *4*, 477-488.
6. Lin, W. M.; Karsten, U.; Goletz, S.; Cheng, R. C.; Cao, Y. *Int. J. Exp. Pathol.* **2011**, *92*, 97-105.
7. Brockhausen, I. *Biochim. Biophys. Acta* **1999**, *1473*, 67-95.
8. Brockhausen, I.; Yang, J.; Dickinson, N.; Ogata, S.; Itzkowitz, S. H. *Glycoconjugate J.* **1998**, *15*, 595-603.
9. Brockhausen, I. *EMBO Rep.* **2006**, *7*, 599-604.
10. Rivinoja, A.; Kokkonen, N.; Kellokumpu, I.; Kellokumpu, S. *J. Cell. Physiol.* **2006**, *208*, 167-174.
11. Sastry, M. V.; Banarjee, P.; Patanjali, S. R.; Swamy, M. J.; Swarnalatha, G. V.; Surolia, A. *J. Biol. Chem.* **1986**, *261*, 11726-11733.
12. Singh, R.; Subramanian, S.; Rhodes, J. M.; Campbell, B. J. *Glycobiology* **2006**, *16*, 594-601.
13. Ryder, S. D.; Smith, J. A.; Rhodes, J. M. *J. Natl. Cancer Inst.* **1992**, *84*, 1410-1416.
14. Yu, L.-G.; Milton, J. D.; Fernig, D. G.; Rhodes, J. M. *J. Cell. Physiol.* **2001**, *186*, 282-287.
15. Yu, L.-G.; Fernig, D. G.; Smith, J. A.; Milton, J. D.; Rhodes, J. M. *Cancer Res.* **1993**, *53*, 4627-4632.
16. Jeyaprakash, A. A.; Rani, P. G.; Reddy, G. B.; Banumathi, S.; Betzel, C.; Sekar, K.; Surolia, A.; Vijayan, M. *J. Mol. Biol.* **2002**, *321*, 637-645.
17. Said, I. T.; Shamsuddin, A. M.; Sherief, M. A.; Taleb, S. G.; Aref, W. F.; Kumar, D. *Histol. Histopathol.* **1999**, *14*, 351-357.
18. Yang, G. Y.; Shamsuddin, A. M. *Histol. Histopathol.* **1996**, *11*, 801-806.
19. Wu, A. M.; Wu, J. H.; Lin, L. H.; Lin, S. H.; Liu, J. H. *Life Sci.* **2003**, *72*, 2285-2302.
20. Komath, S. S.; Bhanu, K.; Maiya, B. G.; Swamy, M. J. *Biosci. Rep.* **2000**, *20*, 265-276.
21. Goel, M.; Anuradha, P.; Kaur, K. J.; Maiya, B. G.; Swamy, M. J.; Salunke, D. M. *Acta Crystallogr., Sect. D: Biol. Crystallogr.* **2004**, *60*, 281-288.
22. Pandey, G.; Fatma, T.; Cowsik, S. M.; Komath, S. S. *J. Photochem. Photobiol., B* **2009**, *97*, 87-93.

23. Poiroux, G.; Pitié, M.; Culerrier, R.; Ségui, B.; Van Damme, E. J.; Peumans, W. J.; Bernadou, J.; Levade, T.; Rougé, P.; Barre, A.; Benoist, H. *Photochem. Photobiol.* **2011**, *87*, 370-377.
24. Obaid, G.; Chambrier, I.; Cook, M. J.; Russell, D. A. *Angew. Chem. Int. Ed.* **2012**, *51*, 6158-6162.
25. Cook, M. J.; Chambrier, I.; Cracknell, S. J.; Mayes, D. A.; Russell, D. A. *Photochem. Photobiol.* **1995**, *62*, 542-545.
26. Yu, L. G.; Packman, L. C.; Weldon, M.; Hamlett, J.; Rhodes, J. M. *J. Biol. Chem.* **2004**, *279*, 41377-41383.
27. Stuchinskaya, T.; Moreno, M.; Cook, M. J.; Edwards, D. R.; Russell, D. A. *Photochem. Photobiol. Sci.* **2011**, *10*, 822-831.
28. Daniel, M. C.; Astruc, D. *Chem. Rev.* **2004**, *104*, 293-346.
29. Schmid, G.; Bäumle, M.; Geerkens, M.; Helm, I.; Osemann, C.; Sawitowski, T. *Chem. Soc. Rev* **1999**, *28*, 179-185.
30. Sellers, H.; Ulman, A.; Shnidman, Y.; Eilers, J. E. *J. Am. Chem. Soc.* **1993**, *115*, 9389-9401.
31. Stoehr, M.; Vogt-Schaden, M. *Acta Pathol., Microbiol. Immunol. Scand., Sect. A* **1981**, *89*, 96-99.
32. Jeyaprakash, A. A.; Katiyar, S.; Swaminathan, C. P.; Sekar, K.; Surolia, A.; Vijayan, M. *J. Mol. Biol.* **2003**, *332*, 217-228.
33. Milton, J. D.; Fernig, D. G.; Rhodes, J. M. *Glycoconjugate J.* **2001**, *18*, 565-569.
34. Reddy, G. R.; Thompson, W. C.; Miller, S. C. *J. Am. Chem. Soc.* **2010**, *132*, 13586-13587.
35. Bertrand, R.; Solary, E.; O'Connor, P.; Kohn, K. W.; Pommier, Y. *Exp. Cell Res.* **1994**, *211*, 314-321.
36. Haywood-Small, S. L.; Vernon, D. I.; Griffiths, J.; Schofield, J.; Brown, S. B. *Biochem. Biophys. Res. Commun.* **2006**, *339*, 569-576.
37. Mroz, P.; Yaroslavsky, A.; Kharkwal, G. B.; Hamblin, M. R. *Cancers* **2011**, *3*, 2516-2539.
38. Andrade, R.; Crisol, L.; Prado, R.; Boyano, M. D.; Arluzea, J.; Arachaga, J. *Biol. Cell* **2010**, *102*, 25-35.

Chapter 5

A comparative study of targeted phototoxicity of HT-29 colon and SK-BR-3 breast adenocarcinoma cells using jacalin or anti-HER-2 antibodies

In this chapter, the PDT targeting efficiency of jacalin is compared to that of anti-HER-2 antibodies. Both proteins were covalently conjugated to zinc phthalocyanine-PEG gold nanoparticles and the photodynamic efficacy of the conjugates was investigated using HT-29 human colon adenocarcinoma cells and SK-BR-3 human breast adenocarcinoma cells. The experiments performed to compare the targeted PDT efficacy of the lectin and the antibody are described. Further investigations into the mechanisms of targeted cell death and the intracellular localisation of the nanoparticle conjugates are detailed in this chapter.

5.1 Introduction

5.1.1 Cancer targeting ligands

Active targeting of cancer tissue relies on the identification of specific cancer-associated molecular targets and their respective exogenous targeting ligands. Cancer-associated molecular targets include overexpressed cell surface receptors or newly expressed receptors that are not usually expressed in healthy cells (neoexpression). An example of an overexpressed cell surface molecular target is the folate receptor, which is overexpressed in more than 90% of human ovarian cancer cells.[1] The folate receptor can be targeted with anticancer agents conjugated to folic acid that enables the preferential accumulation of the anticancer agents within the tumour cells. An example of receptor neoexpression during the transformation of healthy cells to malignant cells is the appearance of N-cadherin, which is observed in 44% of colonic carcinoma tissue.[2] Neoexpression of N-cadherin is suggested to play a role in cancer cell invasion and metastasis.[2] Receptors expressed at the surface of angiogenic vessels can also be targeted to impede the blood supply to tumours. Receptors expressed in tumour vessels include

vascular endothelial growth factor receptor (VEGFR) and vascular cell adhesion molecule-1 (VCAM-1).[3]

Natural ligands of tumour-associated receptors can be exploited to specifically deliver an anticancer agent to cancer cells expressing the target receptor. For example transferrin bioconjugates have been widely used for monitoring disease progression and targeted therapy of cancer cells overexpressing the transferrin receptor.[4]

Studies screening peptide sequences for specific affinities towards cancer-associated targets have established a number of oligopeptides with potential for cancer targeting.[5-8] For example, peptides containing the arginine-glycine-aspartate (RGD) sequence are commonly used to target $\alpha_v\beta_3$ integrins and $\alpha_v\beta_5$ integrins that are overexpressed by a number of cancer cells and activated angiogenic vascular endothelial cells.[6-9] Additionally, peptides containing the asparagine-glycine-arginine (NGR) sequences target the CD13 receptor, which is overexpressed by several tumour and endothelial cells.[5,8]

Aptamers are low molecular weight oligonucleotide sequences (DNA or RNA) that exhibit high specificity towards target molecules.[10] The generation of aptamers typically involves the screening and selection of oligonucleotides from a pool of sequences based on their affinity towards molecular targets. Aptamers can be specific for individual cancer-associated proteins, such as MUC-1,[11] or even for whole live cancer cells.[12] Binding affinities of aptamers to their targets can have equilibrium dissociation constants (K_d) from the nanomolar to the picomolar range, making them highly attractive targeting ligands.[12] Additionally, aptamers are non-immunogenic allowing for repeated intravenous administration without a decline in efficacy.[10]

Carbohydrates have also been used to directly target endogenous lectins that are overexpressed by cancer cells or tumour vessels. For example, mannose receptors have been found to be overexpressed by MCF-7, MDA-MB-231 and HCT-116 cells.[13] Silica nanoparticles functionalised with mannose have been used to target mannose receptors expressed by HCT-116 tumours.[14] Tumour targeting using mannose has been shown to enhance the delivery of a photosensitiser to the tumour and to improve the *in vivo* efficacy of PDT.[14] Human serum albumin conjugated to mannose-6-phosphate has also been shown to effectively deliver a chemotherapeutic agent, doxorubicin, to cancer cells expressing the mannose-6-phosphate receptor, both *in vitro* and *in vivo*.[13] As discussed in **Chapter 1** and **Chapter 4**, exogenous lectins have also been used for the reverse targeting of cell surface carbohydrates.

Tumour cells can also be targeted by exploiting abnormal protease expression that is up-regulated during malignancy. Such proteases include matrix metalloproteases -2 and -9 (MMP-2 and MMP-9), which are overexpressed by human cancer cells such as HCT-116 colon cancer cells, PC3 prostate cancer cells, and Hep2 epidermoid cancer cells.[15] A tumour-specific pro-drug is usually formulated by conjugating a therapeutic agent to a neutralising agent through a peptide. The peptide linker used for conjugation is a substrate for a cancer-associated protease. Cleavage of the pro-drug by the extracellular proteases up-regulated in tumours results in the selective extracellular activation of the drug and subsequent accumulation of the drug within the cancer cells.[15]

Antibodies are of the most commonly used targeting agents due to the high affinity for the respective antigen (K_d values typically in the nanomolar range) and due to the feasibility of generating antibodies for virtually any given antigen.[16] Examples of the use of antibodies for targeted cancer therapies are described in greater detail in **section 5.1.2**.

5.1.2 Antibodies

Antibodies are immunological proteins that exhibit unique individual specificity for a broad range of antigens.[17] Antibodies, also known as immunoglobulins (Ig), are synthesised by B lymphocytes within the mammalian immune system to target foreign invading bodies.[17-19] Initially, antibodies are restricted to the membrane of B cells, each of which express antibodies of an individual antigen specificity. Following the interaction of the surface-bound antibodies with their specific immunogenic target, the B cells become activated and the synthesis of soluble extracellular antibodies is initiated.[17-19] This immunisation phenomenon is exploited for the generation of antibodies for diagnostic and therapeutic applications. Polyclonal antibodies consist of a mixture of antibodies, each with affinities for different epitopes on the same antigen. These are typically extracted from the immunised host species using affinity chromatography with an antigen derivatised separation column.[17] Monoclonal antibodies are generated by the fusion of a single activated B lymphocyte with an immortalised cell line to form a hybridoma. The hybridoma produces antibodies with a single antigen epitope specificity.[17,18]

The typical structure of a monomeric antibody is depicted in **Figure 5.1**.[17] Antibody monomers consist of two heavy chains and two light chains. The N-terminus at each of the four chains form the two antigen binding fragments (Fab). The C-terminus at each of the two heavy chains form the constant fragment (Fc), which is responsible for the initiation

of the immune response.[17] There are several primary classes of antibodies that are distinguished by their heavy chains, which serve different functions at their physiological site of action. These antibody classes are denoted IgA, IgD, IgE, IgG and IgM. IgA antibodies exist either monomers or dimers, IgD, IgE and IgG antibodies are typically monomers, and IgM antibodies are usually pentameric.[17-19] Furthermore, each heavy chain is glycosylated at the Fc region with exposed aldehyde groups, which play a role in antigen clearance.[19,20] The aldehyde group is commonly used for antibody modification. The aldehyde is typically oxidised using periodate and bound to an amine group or hydrazine derivative on the conjugate molecule.[21]

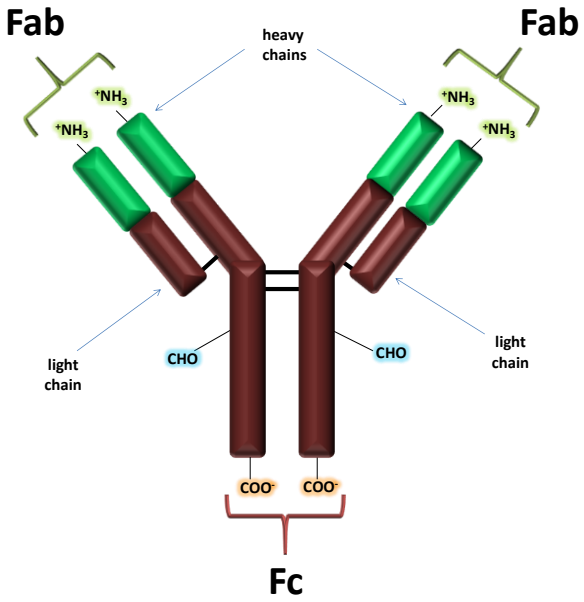

Figure 5.1 **A schematic representation of a monomeric antibody with bivalent antigen specificity. The two antigen binding fragments (Fab) at the N-terminus exhibit antigen recognition. The constant fragment (Fc) at the C-terminus contains exposed aldehyde groups (CHO) at the antibody glycosylation sites.**

Antibodies or antibody fragments are of the most commonly used cancer targeting ligands.[16] Antibody conjugates, also known as immunoconjugates, have seen wide-spread use for *in vitro*, *in vivo* and clinical applications.[16] Immunogenicity and subsequent physiological clearance of antibody immunoconjugates by the human immune system are of the major limitations of using antibodies and other globular proteins for targeted therapy.[16] Imunogenicity can be overcome by the generation of chimeric antibodies (*ca.*

66% human DNA) or humanised antibodies (*ca.* 90% human DNA), which are fusions of human Fc fragments with cancer-specific animal monoclonal Fab fragments.[16,22] The use of antibodies for targeted cancer treatment also includes the functional blocking of signalling pathways involved in cancer survival and progression.[23] For example, the clinically approved humanised IgG1 monoclonal antibody, Avastin®, is used to block VEGF signalling, and thus inhibits angiogenesis and other downstream signalling effects associated with the disease.[23,24]

Within PDT, a large number of studies have reported the direct conjugation of a photosensitiser with a cancer-targeting antibody to yield photoimmunoconjugates for selective photodynamic treatment.[25] Two isothiocyanate derivatives of water soluble porphyrin photosensitisers have been synthesised and conjugated to monoclonal antibodies that target cell internalising receptors (FSP 77 and 17.1A antibodies) and a non-internalising receptor (35A7 antibody).[26] The photoimmunoconjugates retained the binding specificities of the unmodified antibodies and enhanced the tumour localisation of the sensitisers in mouse tumour models bearing a subcutaneously implanted LS174T colon carcinoma (35A7 photoimmunoconjugates) and an SKOV ovarian carcinoma (FSP 77 photoimmunoconjugates). Furthermore, the FSP 77 cell internalising photoimmunoconjugates induced a greater level of phototoxicity in SKOv3-CEA-1B9 cells than the non-internalising 35A7 conjugates.[26]

NIH:OVCAR-5 human ovarian carcinoma cells overexpressing the epidermal growth factor receptor (EGFR) have been targeted with an anti-EGFR monoclonal antibody conjugated to the photosensitiser benzoporphyrin derivative monoacid ring A.[27] Treatment of the ovarian cancer cells and EGFR-positive Chinese hamster ovary cells with the photoimmunoconjugate directly blocked EGFR receptor signalling and enhanced the cellular uptake and phototoxicity of the PDT agent.[27]

Anti-HER-2 antibodies have been used for targeting human breast cancer cells overexpressing the HER-2 receptor with zinc phthalocyanine functionalised gold nanoparticles.[28] Following irradiation, the antibody conjugated nanoparticles were able to selectively reduce the viability of HER-2 overexpressing cells. Cells not expressing the HER-2 receptor and subnormal, non-transformed MCF-10A breast epithelial cells were unaffected by the treatment.[28]

HepG2 hepatocellular carcinoma cells were successfully targeted with anti-CD44 antibody functionalised liposomal formulations encapsulating the anticancer drug doxorubicin.[29]

Antibody targeted treatment with the liposomal doxorubicin formulation increased the percentage of apoptotic cells, as compared to treatment with the free drug. Furthermore, the targeted liposomal preparation was found to dramatically enhance the accumulation of doxorubicin within a hepatocellular carcinoma murine tumour model *in vivo.*[29]

Antibodies have also been conjugated to toxins (immunotoxins) that selectively induce cytotoxicity in cancer cells.[16] The process of photochemical internalisation (PCI) has been used in conjunction with immunotoxin administration to facilitate cytoplasmic release of the targeted conjugate and potentiate its toxicity.[30] PCI treatment using immunotoxins was performed on the HER-2 receptor-positive cell line, Zr-75-1, which is resistant to functional blocking treatment with anti-HER-2 antibodies. Tetraphenylchlorin disulfonate was used as the photosensitiser for endosomal compartment rupture following incubation with the anti-HER-2 anitbody-saponin toxin conjugate.[30] It was found that the immunotoxin was significantly more effective at reducing cell viability following PCI than the toxin alone, highlighting the enhanced cellular homing of the targeted immunotoxin.[30]

A number of other studies have highlighted the enhanced therapeutic effect of antibody targeted treatments for cancer by improving tumour accumulation and by minimising peripheral damage to healthy tissue.[23] Functional blocking of signalling pathways is one of the main mechanisms of antibody treatments currently used, and combinatory mechanisms of targeting using antibody-drug conjugates are proving to be of increasing significance.[23,31,32]

5.1.3 The EGFR family of receptors

Epidermal growth factor receptors (EGFRs), also known as human epidermal growth factor receptors (HERs) or erythroblastoma gene B (ErbB) receptors, are a tyrosine kinase family of transmembrane receptors that modulate cellular growth and proliferation.[33] Upon ligand binding, EGFRs activate a complex network of intracellular signalling pathways.[33] The receptor family consists of four homologues of the receptor: EGFR (ErbB-1), HER-2 (ErbB-2/neu), HER-3 (ErbB-3) and HER-4 (ErbB-4).[33] There are 13 natural ligands identified to date, which specifically bind to and activate the EGFR receptor family.[34] The natural ligands of EGFR include EGF, amphiregulin (AR), betacellulin (BTC), transforming growth factor-α (TGF-α), epiregulin (EPR), heparin-binding ERGF-like growth factor (HB-EGF) and epigen. The ligands that recognise HER-3 include neuregulins 1 and 2 (NRG-1 and NRG-2, respectively) and Herregulins 1 and 2 (HRG-1 and HRG-2,

respectively), although the receptor lacks intrinsic tyrosine kinase activity and is dependent on dimerisation with another EGFR receptor. The natural ligands of HER-4 include HRG-1, -2, -3 and -4, BTC, EPR, NRG-1, -2, -3 and -4, and HB-EGF.[34]

The HER-2 receptor is an orphan receptor as it has no ligand binding capacity.[34] Therefore, activation of the receptor is dependent on heterodimerisation with another EGFR.[34] The functional blocking monoclonal antibody trastuzumab (Herceptin®) binds to the HER-2 receptor and prevents its dimerization and activation.[35] It has been found that although no ligand binds to HER-2, the transmembrane mucin, MUC4, stabilises the receptor, interacts with it and activates its signalling pathways within pancreatic and ovarian cancer cells.[36,37] Homodimerisation or heterodimerisation of the four EGFR receptors results in a total of ten possible dimer combinations that are responsible for the complex EGFR signalling network.[35] Homodimerisation of the enzymatically inactive HER-3 receptors leads to no signal transductions, and homodimerisation of the remaining EGFR receptors leads to weak signalling.[35]

The EGFR signalling network regulates apoptosis, migration, proliferation, growth, adhesion and proliferation, and thus plays a crucial role in maintaining healthy cellular function.[33] Intracellular signalling pathways controlled by the EGFR signalling network include the Ras-mitogen-activated protein kinase (Ras-MAPK) pathway and the AKT pathway.[16,33] These pathways are responsible for the transcription of proto-oncogenes such as *myc*, *fos* and *jun*, amongst other genes.[17,35] Within cancer, deregulation of the EGFR signalling network by the overexpression or underexpression of EGFR receptors (or their respective ligands) results in a variety of abnormal cellular processes.[34,35] Deregulation of the EGFR network is associated with tumourigenesis and the occurrence of cancers of the breast, colon, head and neck, pancreas and ovaries, amongst others.[34,35]

HER-2 is of particular importance in cancer due to its specific downstream intracellular effects upon overexpression.[35] The overexpression of the HER-2 receptor is usually a result of the amplification of its proto-oncogene, ERBB2.[38] Elevated levels of cell surface HER-2 receptor expression promote the heterodimerisation of the receptor with either of the remaining three EGFRs.[35] The receptor is activated following heterodimerisation and the binding of EGF or NRG factors.[35] HER-2 activation is typically accompanied by low-specificity ligand interactions, prolonged ligand association and prolonged signalling responses.[35] The HER-2 receptor is overexpressed in 10-34% of human breast cancers, and the overexpression is correlated with disease prognosis and clinical outcome.[39] The

effects of the overexpression of the HER-2 receptor directly increase cancer cell proliferation and migration, and also result in apoptosis resistance and resistance to therapy.[35,37] As the overexpression of the HER-2 receptor is related to cancer progression, and the activation of the receptor can be effectively blocked with monoclonal antibodies, the receptor has proven to be a viable target for selective cancer therapies using antibodies.

In this chapter, the targeting of the HER-2 receptor was achieved using a rat monoclonal IgG2a antibody that is specific for the extracellular domain of the receptor. The antibody was covalently conjugated to the PEG molecules on C11Pc-PEG gold nanoparticles. The nanoparticle conjugates were used to comparatively study the targeted PDT efficacy with that of jacalin conjugated nanoparticles described in **Chapter 4**. The HER-2 receptor is overexpressed in SK-BR-3 human breast adenocarcinoma cells and in HT-29 human colorectal adenocarcinoma cells.[40-43] SK-BR-3 cells are known to express *ca.* 1-2x10^6 HER-2 receptors per cell,[44] and IgG anti-HER-2 monoclonal antibodies are known to bind to these cells with a K_d of 14-36 nM.[45] Moreover, HT-29 cells express *ca.* 4.4 ± 0.3x10^7 T antigens per cell, which jacalin binds to with a K_d of 500 ± 50 nM.[46] The significance of cell surface receptor density and targeting ligand binding affinity on the efficacy of targeted PDT using C11Pc-PEG gold nanoparticles are discussed in this chapter. The phototoxicity of these two targeting systems has been investigated using both SK-BR-3 and HT-29 cells and the intracellular localisation was determined using confocal fluorescence microscopy.

5.2 Results and Discussion

5.2.1 Jacalin and anti-HER-2 antibody C11Pc-PEG gold nanoparticle conjugates

C11Pc-PEG gold nanoparticles were synthesised as described in **section 2.2.4**. Jacalin and anti-HER-2 rat monoclonal IgG2a antibodies were conjugated to the gold nanoparticles using EDC/NHS coupling, as described in **section 2.3.1**. The jacalin or anti-HER-2 antibodies were reacted with the EDC/NHS activated nanoparticles at a molar ratio of 6.2:1. **Figure 5.2** shows schematic representations of jacalin conjugated (**A**) and anti-HER-2 antibody conjugated (**B**) C11Pc-PEG gold nanoparticles. The degree of jacalin or antibody grafting onto the nanoparticle conjugates could be approximated by dynamic light scattering (DLS) particle size analysis before and after conjugation. Additionally, ζ potential measurements of the C11Pc-PEG gold nanoparticles before and after jacalin or antibody conjugation could give further insight into the extent of biofunctionalisation.

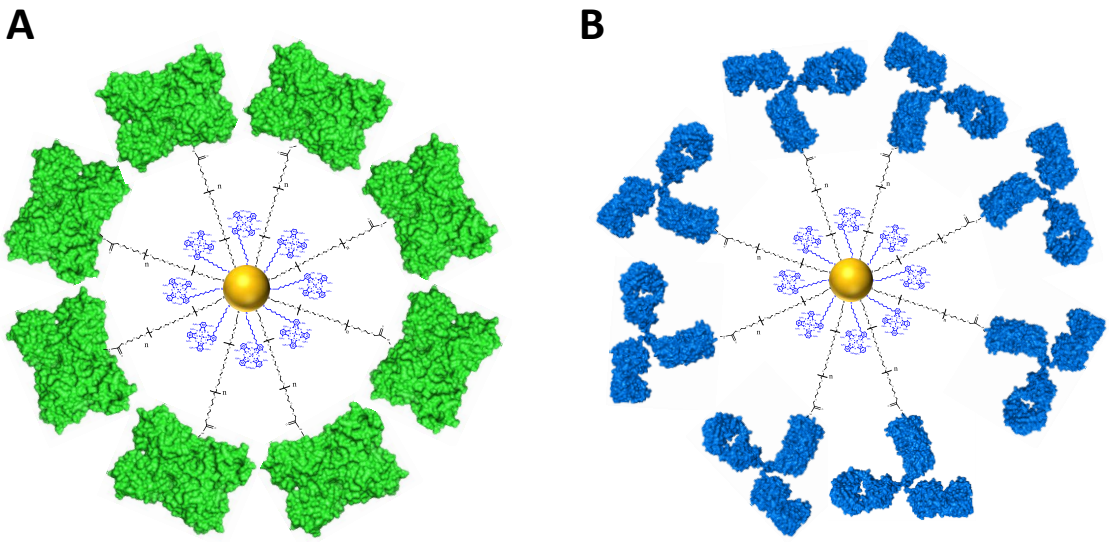

Figure 5.2 **A schematic representation of C11Pc-PEG gold nanoparticles functionalised with A) jacalin or B) anti-HER-2 antibodies. Images of jacalin (PDB ID 1M26[47]) and the IgG2a antibody (PDB ID 1IGT[48]) were generated using PyMOL.**

Following the conjugation of jacalin or anti-HER-2 antibodies to the gold nanoparticles, the nanoparticle conjugates were characterised using UV-visible absorption spectrophotometry. As can be seen from the absorption spectra in **Figure 5.3**, both types of nanoparticle conjugates retain the optical characteristics of predominantly monomeric C11Pc.

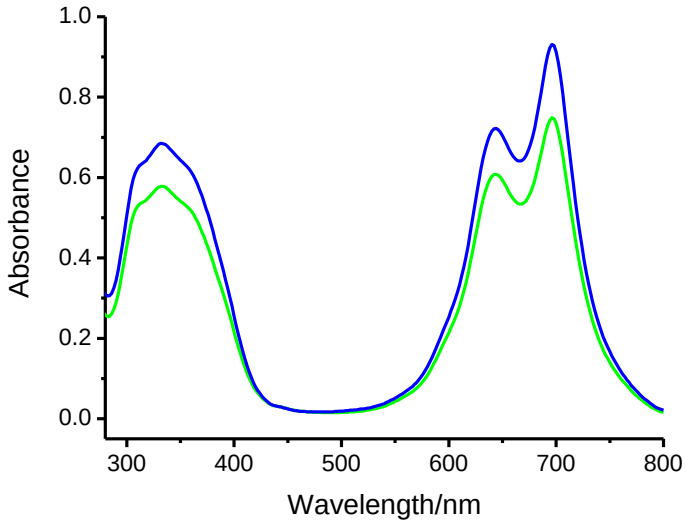

Figure 5.3 **UV-visible absorption spectra of jacalin (green) or anti-HER-2 antibody (blue) conjugated C11P-PEG gold nanoparticles in serum-free RPMI 1640 medium.**

To effectively compare the targeting efficiency of jacalin conjugates with anti-HER-2 antibody conjugates, the singlet oxygen production following the irradiation of the conjugated C11Pc-PEG gold nanoparticles was compared, as described in **section 2.3.2**. Non-conjugated C11Pc-PEG gold nanoparticles were used as a control. Singlet oxygen production was measured in phosphate buffered saline using ADPA as the colorimetric singlet oxygen probe. The quantification of singlet oxygen was calculated using a 1:1 stoichiometry of singlet oxygen to ADPA. The number of moles of singlet oxygen produced were normalised to the concentration of C11Pc equivalent present within the samples of nanoparticle conjugates. It is clear from the graph shown in **Figure 5.4** that there is no significant difference in singlet oxygen production by the irradiation of the C11Pc-PEG gold nanoparticles conjugated to either jacalin (**Figure 5.4**, **green**) or the anti-HER-2 antibody (**Figure 5.4**, **blue**). Following conjugation to either targeting ligands, the singlet oxygen production of the nanoparticle conjugates is slightly reduced, as compared to the higher photoactivity of the non-conjugated C11Pc-PEG gold nanoparticles (**Figure 5.4**, **black**). However, if targeting significantly enhances the cellular internalisation of the nanoparticle conjugates as compared to the non-conjugated nanoparticles, the slight reduction in photoactivity following conjugation may be overcome.

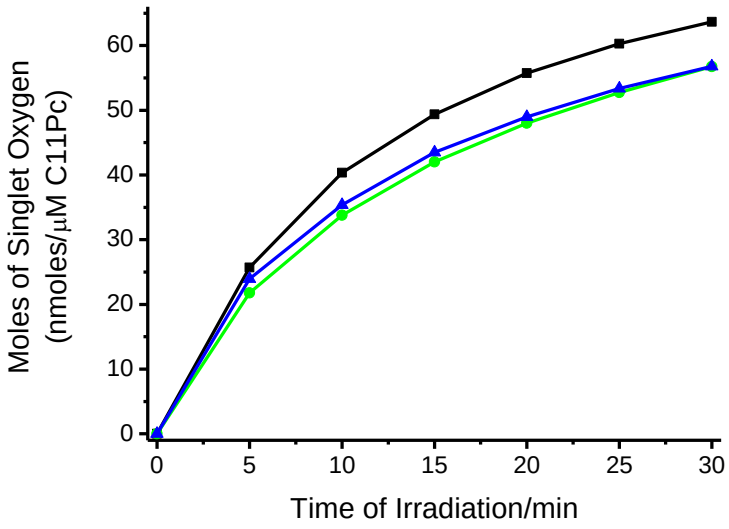

Figure 5.4 **Singlet oxygen production (nmoles/μM C11Pc) by the irradiation at 633 nm of non-conjugated (black), jacalin conjugated (green) and anti-HER-2 antibody (blue) conjugated C11P-PEG gold nanoparticles. Nanoparticle samples were in phosphate buffered saline (10 mM, 150 mM NaCl, pH 7.4).**

5.2.2 Targeted PDT of HT-29 cells – MTT viability assay

HT-29 cells were incubated with non-conjugated, jacalin conjugated or anti-HER-2 antibody conjugated C11Pc-PEG gold nanoparticles and irradiated at 633 nm (0.00-1.15 μM C11Pc equivalent), as described in **section 2.3.3**. 48 h following PDT treatment, an MTT viability assay was performed on the HT-29 cells. **Figure 5.5** shows the viability of the cells following jacalin targeted (**A**) or anti-HER-2 antibody targeted (**B**) PDT. Statistical significance was calculated using a one-tailed student's *t*-test. Following irradiation, viability of the HT-29 cells incubated with the jacalin conjugated or anti-HER-2 antibody conjugated nanoparticles was significantly reduced to *ca.* 10.1% and *ca*. 19.2%, respectively (using 1.15 μM C11Pc equivalent of nanoparticles). However, without irradiation at the same nanoparticle concentration, viability remained at *ca.* 62.0% and *ca.* 77.3%, respectively. No significant difference in the dose-dependent phototoxicity of the HT-29 cells was observed following targeted PDT treatment using jacalin conjugated (**Figure 5.5** (**C**), **green**) or anti-HER-2 antibody conjugated (**Figure 5.5** (**C**), **blue**) nanoparticles at concentrations of 0.0-0.5 μM C11Pc equivalent. However, at 1.15 μM C11Pc equivalent, phototoxicity induced by the jacalin conjugated nanoparticles was *ca.* 9.3% higher than that induced by the anti-HER-2 antibody conjugated particles (*P<0.05*).

The greater reduction in HT-29 cell viability following jacalin targeted PDT could also be attributed to a greater level of dark toxicity (*ca.* 38% reduction in viability), as compared to incubation with the antibody conjugates (*ca.* 23% reduction in viability) when using a nanoparticle concentration of 1.15 μM C11Pc equivalent.

Irradiation of HT-29 cells incubated with 0.00-1.15 μM C11Pc equivalent of non-conjugated nanoparticles did not result in any significant phototoxicity (**Figure 5.5** (**C**), **black**). At nanoparticle concentrations of 0.20-1.15 μM C11Pc equivalent, targeted PDT treatment using either jacalin or anti-HER-2 antibody conjugates significantly enhanced the phototoxicity of the HT-29 cells, as compared to non-targeted treatment ($P<0.05$).

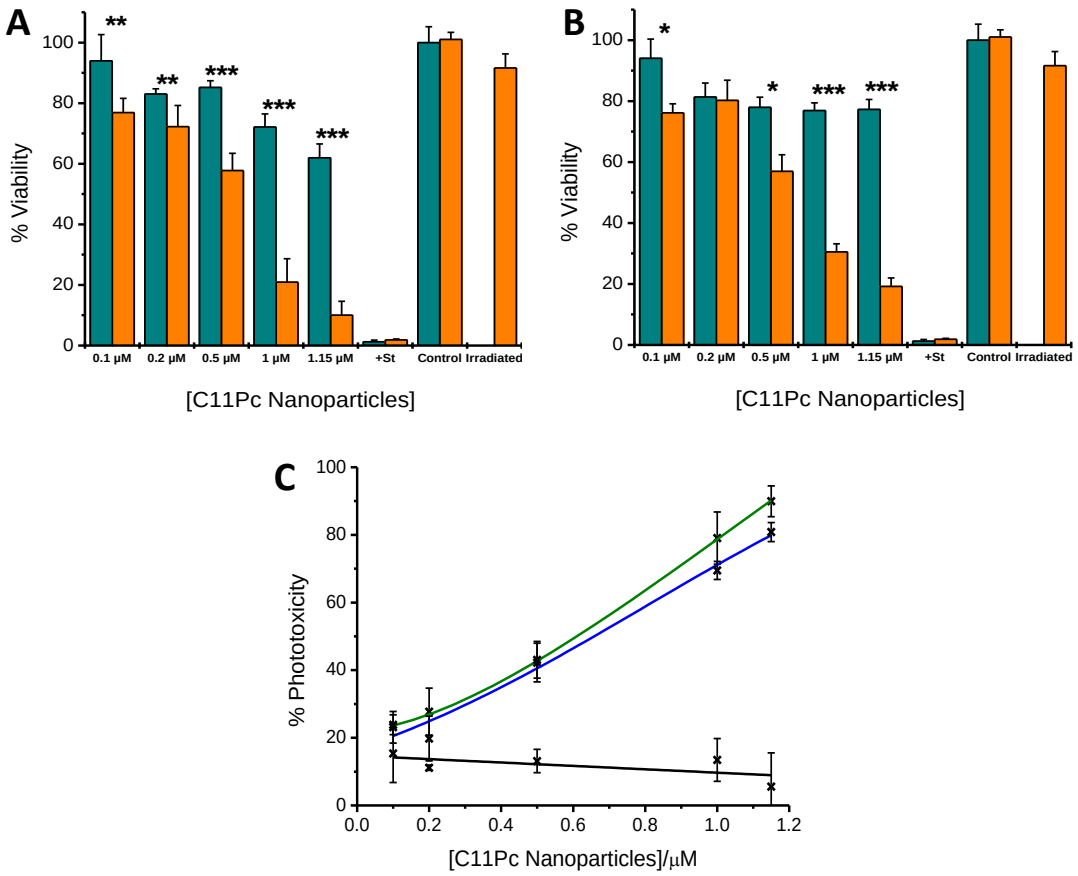

Figure 5.5 **MTT viability assay results of HT-29 cells following PDT treatment with the jacalin conjugated (A) or anti-HER-2 antibody conjugated (B) C11Pc-PEG gold nanoparticles. Cells were irradiated at 633 nm for 6 min per well (orange) or non-irradiated (dark cyan). C) Phototoxicity of HT-29 cells incubated with the jacalin conjugated (green), anti-HER-2 antibody conjugated (blue) or non-conjugated (black) nanoparticles. Staurosporine (+St, 20 µM) was used as a positive control for cytotoxicity. (Error bars are ± 95% confidence intervals, n=3. * indicates statistical significance in viability reduction following irradiation at *P<0.005*, ** at *P<0.0025* and *** at *P<0.0005* using a one-tailed *t*-test).**

5.2.3 Targeted PDT of SK-BR-3 cells – CellTiter-Blue™ viability assay

Targeted PDT using jacalin or anti-HER-2 antibody nanoparticle conjugates was then investigated on SK-BR-3 cells, as described in **section 2.3.4**. An MTT assay was attempted on SK-BR-3 cells following targeted PDT treatment; however, residual DMEM medium in the wells during the formazan solubilisation step caused significant variation in the formazan colour (data not shown).[49] Therefore, the CellTiter-Blue™ fluorometric cell

viability assay was performed on SK-BR-3 cells following targeted PDT treatment as no solubilisation step is involved with this assay.

As shown in **Figure 5.6**, the viability of the SK-BR-3 cells appeared to be significantly lower than that of the HT-29 cells following targeted PDT treatment with the same range of nanoparticle concentrations. The lower viability of the SK-BR-3 cells could be attributed to variation resulting from the use of different viability assays for each cell line. Alternatively, the SK-BR-3 cells could be more susceptible to phototoxicity or have less repair mechanisms than the HT-29 cells to recover from oxidative damage.[50]

At 0.5 μM C11Pc equivalent of jacalin conjugated nanoparticles, PDT treatment dramatically reduced SK-BR-3 cell viability to *ca.* 2.6%, whereas without irradiation viability remained at *ca.* 86.4% (**Figure 5.6** (**A**)). Similarly, at the same concentration of nanoparticles, anti-HER-2 antibody targeted PDT reduced cell viability to *ca.* 5.4%, whilst the viability of non-irradiated cells was at *ca.* 111.4% (**Figure 5.6** (**B**)). The limited dark toxicity of the anti-HER-2 antibody conjugates offers an obvious advantage over the jacalin conjugates. At nanoparticle concentrations of 1 μM and 1.15 μM C11Pc equivalent, both jacalin and anti-HER-2 antibody targeted PDT induced >99% cell kill, whereas viability in the dark remained at *ca.* 58.9-70.2% (**Figure 5.6** (**A**)) and *ca.* 85.5-98.5% (**Figure 5.6** (**B**)), respectively. As observed with the HT-29 cells, the phototoxicity of the SK-BR-3 cells induced by non-conjugated C11Pc-PEG gold nanoparticles was negligible at the concentrations used for this experiment (**Figure 5.6** (**C**)). A dose-dependent phototoxicity of the SK-BR-3 cells incubated with the jacalin or anti-HER-2 antibody conjugated particles was also observed. Jacalin conjugation appeared to provide a statistically significant improved PDT effect at 0.10 μM C11Pc equivalent, as compared to anti-HER-2 antibody conjugation (*P<0.05*). The marginally greater PDT efficacy observed with the jacalin conjugated particles, as compared to the anti-HER-2 antibody conjugated nanoparticles, could be attributed to higher binding kinetics of jacalin. However, the viability of the SK-BR-3 cells incubated with the jacalin conjugates (0.10 μM C11Pc equivalent) was *ca.* 4% lower than when incubated with the anti-HER-2 antibody conjugates at the same concentration. Further investigations into the variations in dark toxicity, binding affinity, kinetics and uptake of the two nanoparticle conjugates would provide a more conclusive explanation. The cellular uptake rates of jacalin conjugated and antibody conjugated nanoparticle can be determined using fluorescence-activated cell sorting (FACS) analysis in addition to quantitative gold and zinc ICP-OES elemental analysis at varying time points during nanoparticle incubation.

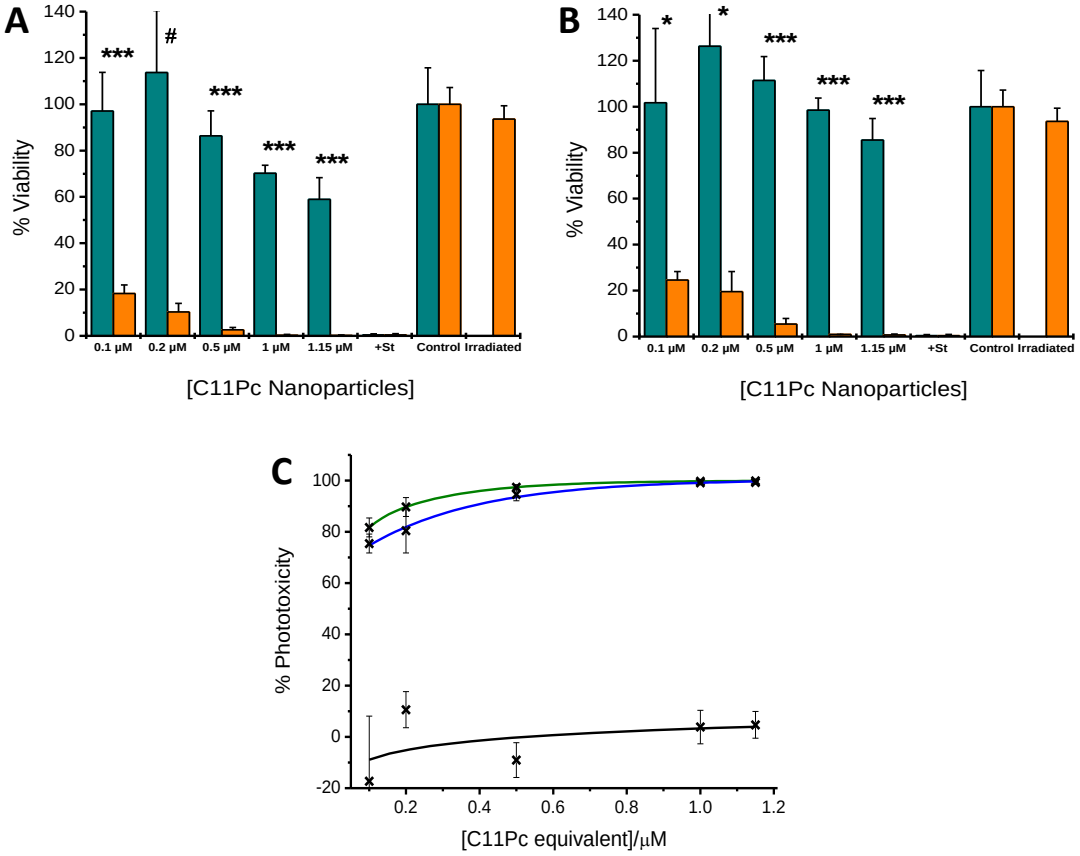

Figure 5.6 **CellTiter-Blue™ viability assay results of SK-BR-3 cells following PDT treatment with the jacalin conjugated (A) or anti-HER-2 antibody conjugated (B) C11Pc-PEG gold nanoparticles. Cells were irradiated at 633 nm for 6 min per well (orange) or non-irradiated (dark cyan). C) Phototoxicity of HT-29 cells incubated with the jacalin conjugated (green), anti-HER-2 antibody conjugated (blue) and non-conjugated (black) nanoparticles. Staurosporine (+St, 20 µM) was used as a positive control for cytotoxicity. (Error bars are ± 95% confidence intervals, n=3. # indicates statistical significance in viability reduction following irradiation at *P<0.001*, * at *P<0.005* and *** at *P<0.0005* using a one-tailed *t*-test).**

5.2.4 Comparative study of targeted PDT – ApoTox-Glo™ triplex assay

In order to investigate whether different pathways of cell death were induced following targeted PDT using either jacalin or anti-HER-2 antibody targeted PDT, the ApoTox-Glo™ triplex assay was performed, as described in **section 2.3.5**. Additionally, the effect of nanoparticle concentration on the cell death mechanism was explored by using either 0.1 µM or 1 µM C11Pc equivalent of nanoparticle conjugates. The significance of non-specific protein-cell interactions on enhancing the PDT efficacy of conjugated C11Pc-PEG gold

nanoparticles was also examined by using sheep serum albumin (SSA) conjugated nanoparticles as a control.

As can be seen from **Figure 5.7** (**A**), viability levels of irradiated HT-29 cells incubated with 0.1 μM C11Pc equivalent of jacalin, anti-HER-2 antibody or SSA conjugated nanoparticles are similar (*ca.* 80-85%). However, at 1 μM C11Pc equivalent, nanoparticles conjugated to jacalin reduced HT-29 cell viability to *ca.* 31.3%, which were significantly more effective than SSA conjugated nanoparticles (*ca.* 51.5% viability, $P<0.001$). Anti-HER-2 antibody conjugated nanoparticles were also significantly more efficient than SSA conjugated nanoparticles at reducing HT-29 cell viability (*ca.* 42.7% viability, $P<0.05$).

The viability of irradiated SK-BR-3 cells incubated with 1 μM C11Pc equivalent of nanoparticles conjugated to jacalin, anti-HER 2 antibodies or SSA was reduced to *ca.* 1.6%, 3.3% and 4.9%, respectively (**Figure 5.7** (**B**)). At this concentration, phototoxicity was extensive with all types of nanoparticles, suggesting that selective cellular uptake is not observed at higher concentration of particle conjugates. Additionally, the jacalin conjugated nanoparticles (1 μM C11Pc equivalent) were more efficient than the anti-HER-2 antibody conjugated particles at reducing SK-BR-3 cell viability ($P<0.001$). However, non-irradiated SK-BR-3 cells incubated with the jacalin conjugates exhibit a *ca.* 22.7% lower viability than those incubated with the antibody conjugates (data not shown). Therefore, a greater level of dark toxicity could contribute to the apparent improvement in jacalin targeted PDT using a particle concentration of 1 μM C11Pc equivalent. At 0.1 μM C11Pc equivalent of nanoparticle conjugates, the difference between targeted PDT and non-targeted SSA-mediated PDT becomes more apparent. Both jacalin and anti-HER-2 antibody conjugated nanoparticles were significantly more effective at reducing cell viability than the SSA conjugated particles ($P<0.0005$). The viability of irradiated SK-BR-3 cells incubated with the jacalin conjugated, anti-HER-2 antibody conjugated or SSA conjugated particles was reduced to *ca.* 22.0%, 34.8% and 77.9%, respectively. At a nanoparticle concentration of 0.1 μM C11Pc equivalent, jacalin targeting appeared to be more effective at reducing irradiated SK-BR-3 cell viability than anti-HER-2 antibody targeting ($P<0.005$). However, the viability of the non-irradiated cells incubated with the jacalin conjugates was *ca.* 5% lower than the viability of the cells incubated with the antibody conjugates (data not shown).te

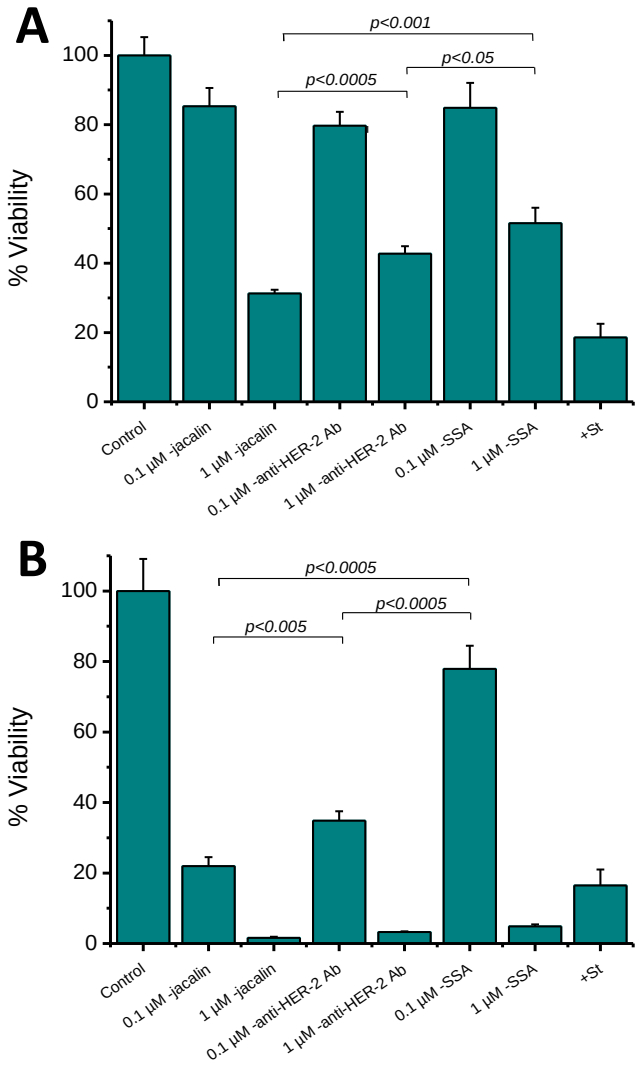

Figure 5.7 **Viability results of the ApoTox-Glo™ triplex assay showing the viability of HT-29 cells (A) and SK-BR-3 cells (B) incubated with 0.1 µM or 1 µM C11Pc equivalent of C11Pc-PEG gold nanoparticles following irradiation at 633 nm. The nanoparticles were conjugated to jacalin (-jacalin), anti-HER-2 antibodies (-anti-HER-2 Ab) or sheep serum albumin (-SSA). Viability is expressed as a percentage of fluorescence emission of the untreated control cells at 492 nm. Staurosporine (+St, 20 µM) was used as a positive control for cytotoxicity. (Error bars are ± 95% confidence intervals, n=3).**

Irradiated HT-29 cells incubated with 1 μM C11Pc equivalent of jacalin conjugated or anti-HER-2 antibody conjugated nanoparticles exhibited a *ca.* 2.8-fold and 1.7-fold increase in cytotoxicity, respectively, as compared to the untreated control cells (**Figure 5.8** (**A**)). Incubation with either 0.1 μM or 1 μM C11Pc equivalent of SSA conjugated nanoparticles induced no cytotoxicity of the HT-29 cell following irradiation. Therefore, specific ligand-receptor interactions are likely to be responsible for the enhanced PDT effect observed in the HT-29 cells incubated with the jacalin conjugated or anti-HER-2 antibody conjugated nanoparticles. Moreover, the selective uptake of the jacalin conjugated or anti-HER-2 antibody conjugated nanoparticles by the HT-29 cells is more apparent at higher concentrations.

As can be seen in (**Figure 5.8** (**B**)), the cytotoxicity of SK-BR-3 cells was more extensive than that of HT-29 cells following PDT treatment, which agrees with the viability results (**Figure 5.7** (**B**)). At 0.1 μM C11Pc equivalent, jacalin or anti-HER-2 antibody conjugated nanoparticles induced similar levels of cytotoxicity in SK-BR-3 cells (*ca.* 5.6-fold increase in cytotoxicity), as compared to the SSA conjugated particles (*ca.* 1.6-fold increase in cytotoxicity, $P<0.0005$). At a higher nanoparticle concentration of 1 μM C11Pc equivalent, jacalin conjugated and anti-HER-2 antibody conjugated particles induced a *ca.* 7.5-fold and a *ca.* 5.7-fold increase in cytotoxicity in irradiated SK-BR-3 cells. At a nanoparticle concentration of 1 μM C11Pc equivalent, greater cytotoxicity of irradiated SK-BR-3 cells was observed following incubation with the SSA conjugated particles (7.8-fold increase in cytotoxicity). These findings further suggest that above a certain critical nanoparticle concentration, cellular internalisation of the conjugates into the SK-BR-3 cells becomes non-specific. Therefore at lower nanoparticle concentrations, the selective enhancement in phototoxicity using targeted nanoparticle conjugates is observed. Dead cell protease activity is largely dependent on the time delay between PDT treatment and assay execution. Performing the triplex assay at varying time points following initiation of PDT within the SK-BR-3 cells would give further insight into the time dependence and extent of targeted and non-targeted PDT cell damage.

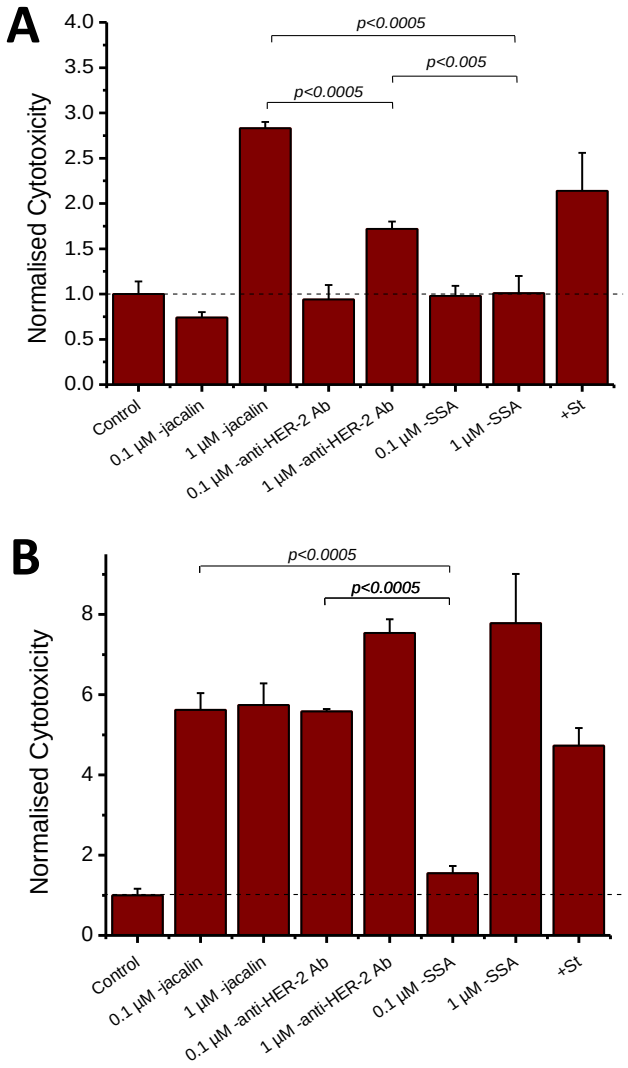

Figure 5.8 **ApoTox-Glo™ triplex assay results showing the cytotoxicity of irradiated HT-29 cells (A) and SK-BR-3 cells (B) incubated with 0.1 µM or 1 µM C11Pc equivalent of C11Pc-PEG gold nanoparticles. The nanoparticles were conjugated to jacalin (-jacalin), anti-HER-2 antibodies (-anti-HER-2 Ab) or sheep serum albumin (-SSA). Cytotoxicity is expressed as a normalised fluorescence emission at 530 nm. Staurosporine (+St, 20 µM) was used as a positive control for cytotoxicity predominantly through apoptosis. (Error bars are ± 95% confidence intervals, n=3).**

The apoptotic response of irradiated HT-29 cells (**Figure 5.9** (**A**)) and SK-BR-3 cells (**Figure 5.9** (**B**)) following nanoparticle incubation (0.1 μM or 1 μM C11Pc equivalent) indicates that targeted PDT treatment using jacalin conjugated or anti-HER-2 antibody conjugated nanoparticles did not induce apoptosis. Furthermore, SSA conjugated nanoparticles did not induce apoptosis at both concentrations in either cell line. Apoptosis was only observed in the positive control cells incubated with staurosporine (20 μM).

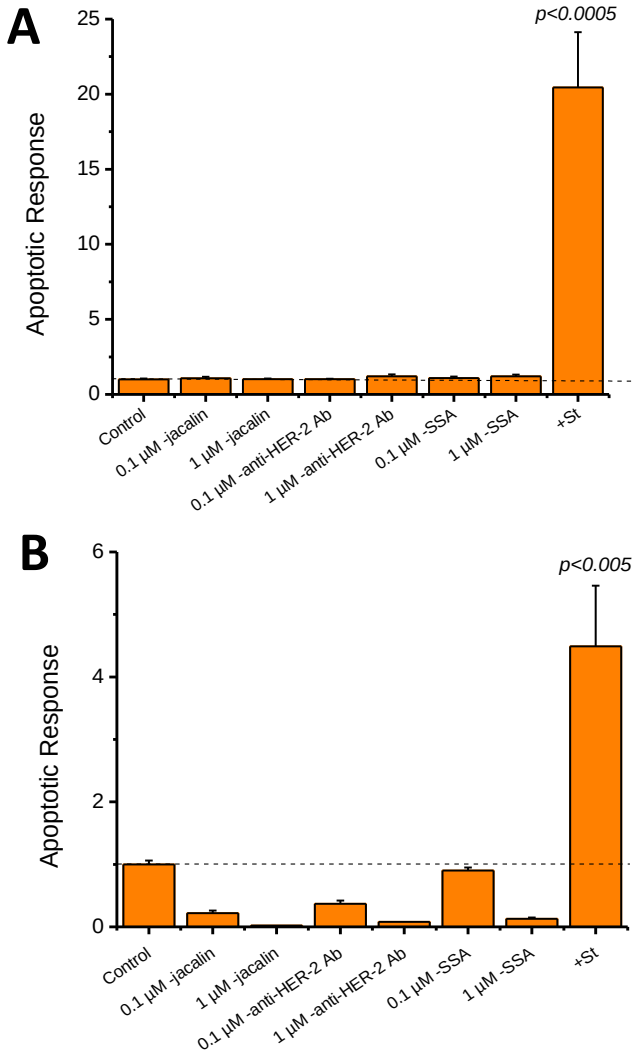

Figure 5.9 **ApoTox-Glo™ triplex assay results showing the apoptotic response of irradiated HT-29 cells (A) and SK-BR-3 (B) cells incubated with 0.1 μM or 1 μM C11Pc equivalent of C11Pc-PEG gold nanoparticles. The nanoparticles were conjugated to jacalin (-jacalin), anti-HER-2 antibodies (-anti-HER-2 Ab) or sheep serum albumin (-SSA). Apoptosis is expressed as a normalised bioluminescence emission at 576 nm.[51] Staurosporine (+St, 20 μM) was used as a positive control for cytotoxicity predominantly through apoptosis.[52] (Error bars are ± 95% confidence intervals, n=3).**

5.2.5 Lysosomal colocalisation of targeted nanoparticle conjugates

After establishing the PDT efficacy of jacalin conjugated and anti-HER-2 antibody conjugated C11Pc-PEG gold nanoparticles on both HT-29 cells and SK-BR-3 cells, the intracellular fate of both nanoparticle conjugates was investigated using laser scanning confocal microscopy. HT-29 cells and SK-BR-3 cells were incubated with C11Pc-PEG gold nanoparticles (1 μM C11Pc equivalent) with jacalin or anti-HER-2 antibody conjugation. The cells were also incubated with LysoSensor™ Green DND-189, a marker of acidic organelles, as described in **section 2.3.6**. It has been shown that nanoparticles can be uptaken into cells through a receptor mediated endocytic pathway, which results in intracellular nanoparticle accumulation within the endosomal compartments.[53,54] Maturation of endosomes leads to their eventual acidification through combination with lysosomes down the endocytic degradation pathway.[55] Internalised nanoparticles present in endosomes may also be redirected to the extracellular domain prior to endosomal maturation and acidification.[53] Colocalisation of nanoparticle conjugates with acidic organelle markers would suggest that the conjugates are uptaken through an endocytic pathway.[55] Acidic organelles within the HT-29 cells and SK-BR-3 cells were visualised using the green fluorescent marker LysoSensor™ Green DND-189 (1 μM) using excitation at 458 nm. Conjugated C11Pc-PEG gold nanoparticles (1 μM C11Pc equivalent) were visualised by exploiting the fluorescence of C11Pc upon excitation at 633 nm. Colocalisation of the nanoparticle conjugates with LysoSensor™ Green DND-189 was assessed using the colocalisation analysis function within the BioImageXD software. Regions of colocalised red and green fluorescence from the conjugated C11Pc-PEG gold nanoparticles and the acidic organelles, respectively, were isolated and false coloured yellow. An upper colocalisation threshold of 4095 and a lower colocalisation threshold of 705 was used throughout the analyses of all the images. Quantitative colocalisation analysis of three random images of SK-BR-3 cells or HT-29 cells incubated with the jacalin or anti-HER-2 antibody conjugated nanoparticles was performed using the BioImageXD software. Colocalisation was quantified as a percentage of voxels (volumetric pixels) in the red channel (C11Pc-PEG gold nanoparticles) that were colocalised with the voxels in the green channel (LysoSensor™ Green DND-189) (**Table 5.1**). It appears that there is a significantly greater error in the mean % voxel colocalisation values of the jacalin conjugated nanoparticles than the anti-HER-2 antibody conjugated particles in both cell lines analysed. This suggests that there are likely to be differences between the cellular uptake processes of both nanoparticle conjugates, as their respective cell surface targets differ in nature.

Table 5.1 **Mean percentage voxel colocalisation of jacalin conjugated or anti-HER-2 antibody conjugated C11Pc-PEG gold nanoparticles (red channel) with LysoSensor™ Green DND-189 (green channel).**

Adenocarcinoma Cell Line	Ligand Conjugated to the Nanoparticles	Mean % Voxel Colocalisation with the LysoSensor™ ± 95% Confidence Interval
HT-29	jacalin	27.60 ± 20.09
HT-29	anti-HER-2 antibody	30.51 ± 7.48
SK-BR-3	jacalin	43.19 ± 27.68
SK-BR-3	anti-HER-2 antibody	22.42 ± 2.24

Figure 5.10 shows the laser scanning confocal microscope images of HT-29 cells incubated with the jacalin conjugated C11Pc-PEG gold nanoparticles (**A**) and LysoSensor™ Green DND-189 (**B**). The brightness of the green channel was reduced by 9% and the contrast of the red channel was increased by 10% for clarity. However, colocalisation isolation and quantitative image analysis was performed on unaltered images, as-obtained. Regions of colocalisation of the nanoparticles with the LysoSensor™ are shown in yellow (**Figure 5.10** (**C**)). A merge of the differential interference contrast (DIC) image with the fluorescence images of the conjugated C11Pc-PEG gold nanoparticles and the LysoSensor™ is shown in (**Figure 5.10** (**D**)).

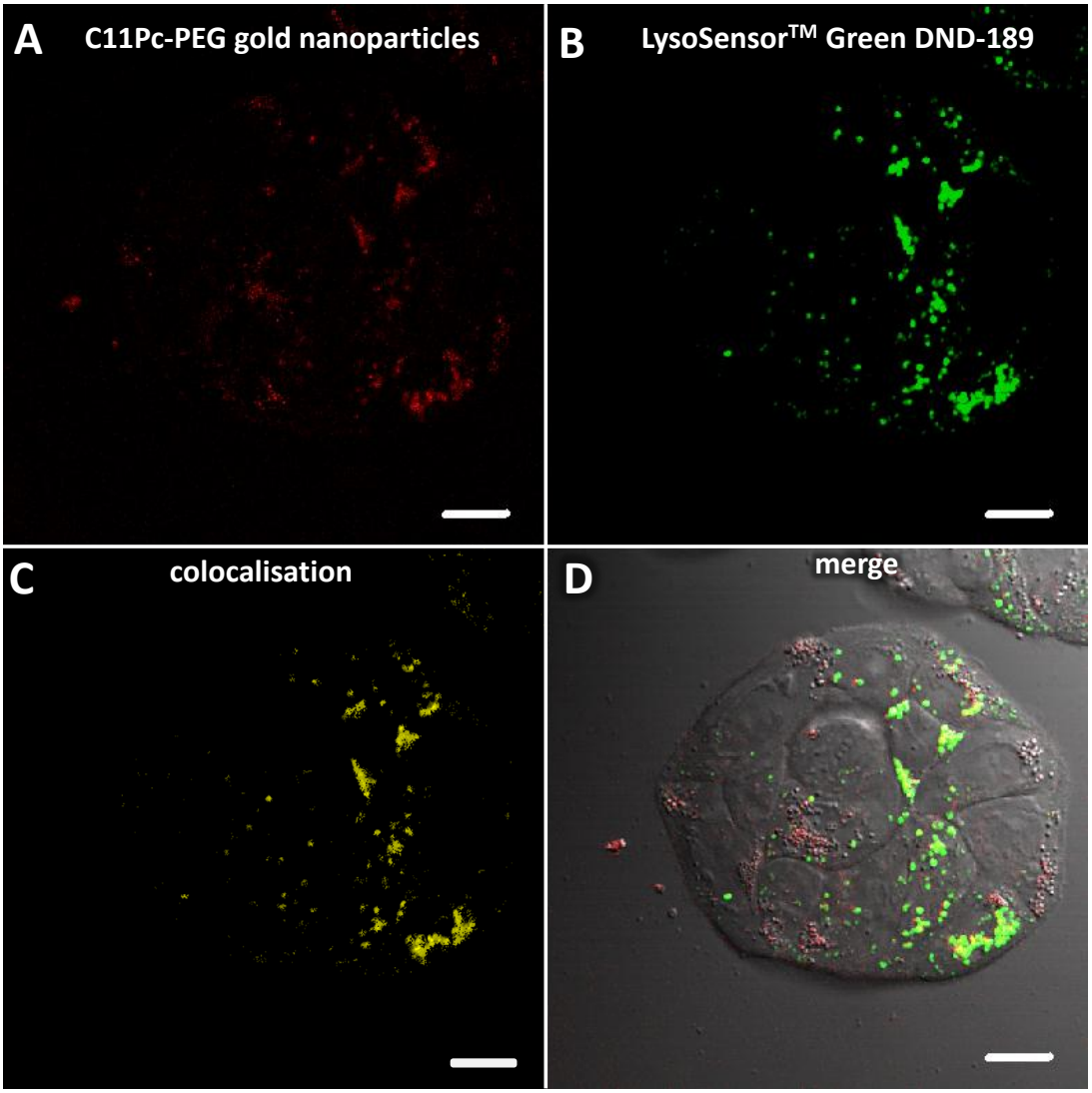

Figure 5.10 **Confocal microscope images of HT-29 cells incubated with the jacalin conjugated C11Pc-PEG gold nanoparticles (1 µM C11Pc equivalent). A) Excitation at 633 nm resulted in a red fluorescence emission of the conjugated C11Pc-PEG gold nanoparticles. B) Acidic organelles were visualised by the green fluorescence emission of LysoSensor™ Green DND-189 upon excitation at 458 nm. C) Colocalisation of the conjugated C11Pc-PEG gold nanoparticles and the LysoSensor™ is shown in yellow. D) The DIC image and the fluorescence images of C11Pc and the LysoSensor™ were merged. (Scale bars are 10 µm).**

Figure 5.11 shows the confocal microscope images of HT-29 cells incubated with the anti-HER-2 antibody conjugated C11Pc-PEG gold nanoparticles (1 μM C11Pc equivalent). The brightness of the green channel was reduced by 9% and the contrast of the red channel was increased by 10% for clarity. Colocalisation isolation and quantitative image analysis was performed on unaltered images.

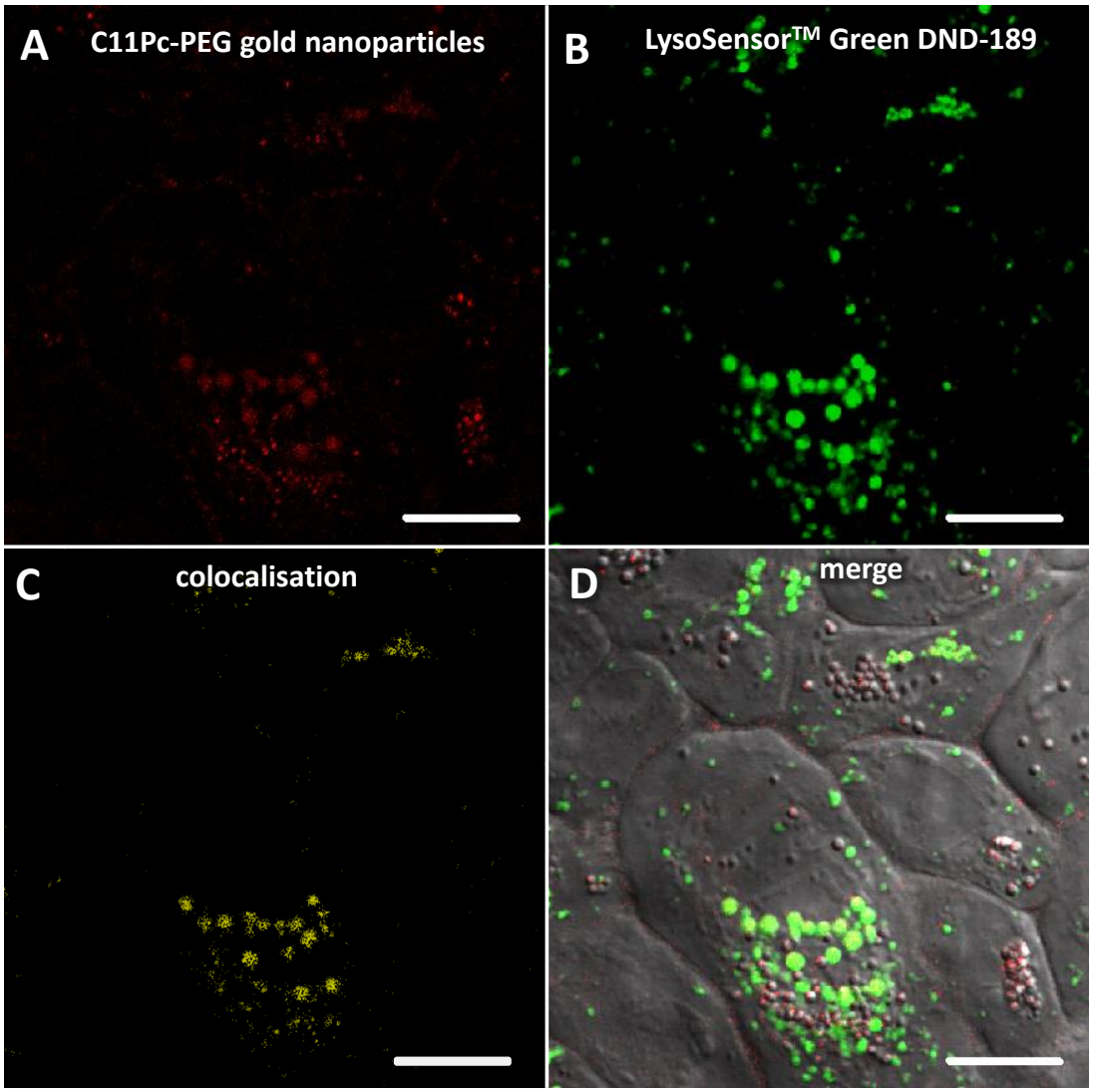

Figure 5.11 **Confocal microscope images of HT-29 cells incubated with the anti-HER-2 antibody conjugated C11Pc-PEG gold nanoparticles (1 μM C11Pc equivalent). A) Excitation of the conjugated C11Pc-PEG gold nanoparticles at 633 nm results in red fluorescence emission. B) Acidic organelles are visualised by the green fluorescence emission of LysoSensor™ Green DND-189 upon excitation at 458 nm. C) Colocalisation of the conjugated C11Pc-PEG gold nanoparticles and the LysoSensor™ is shown in yellow. D) The DIC image and the fluorescence images of C11Pc and the LysoSensor™ were merged. (Scale bars are 10 μm).**

Figure 5.12 is a collection of the confocal microscope images of SK-BR-3 cells incubated with the jacalin conjugated C11Pc-PEG gold nanoparticles (1 μM C11Pc equivalent). The brightness of the green channel was reduced by 9% for clarity; however, colocalisation isolation and analysis was performed on unaltered images.

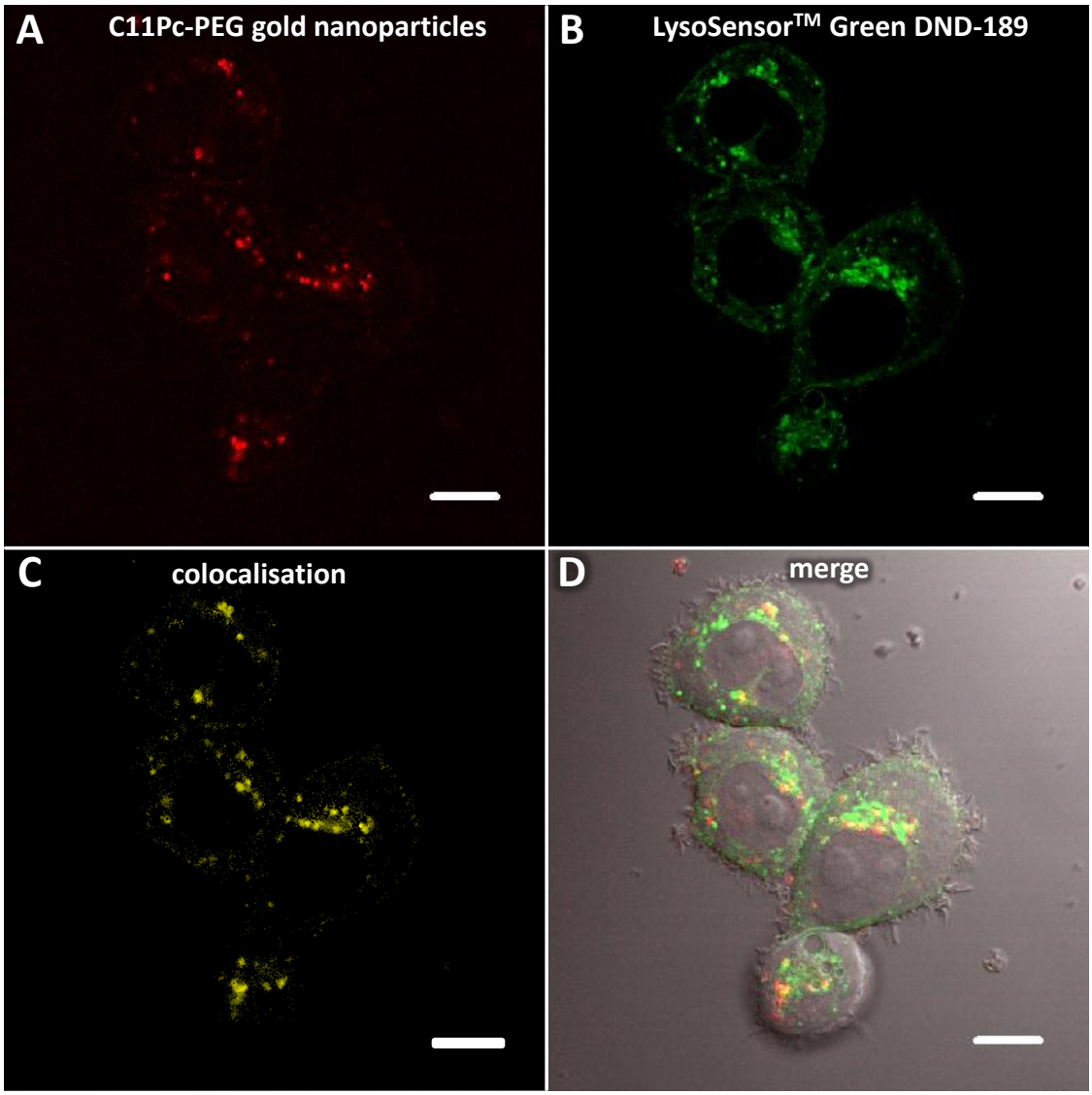

Figure 5.12 **Confocal microscope images of SK-BR-3 cells incubated with the jacalin conjugated C11Pc-PEG gold nanoparticles (1 μM C11Pc equivalent). A) Excitation of the conjugated C11Pc-PEG gold nanoparticles at 633 nm results in red fluorescence emission. B) Acidic organelles are visualised by the green fluorescence emission of LysoSensor™ Green DND-189 upon excitation at 458 nm. C) Colocalisation of the conjugated C11Pc-PEG gold nanoparticles and the LysoSensor™ is shown in yellow. D) The DIC image and the fluorescence images of C11Pc and the LysoSensor™ were merged. (Scale bars are 10 μm).**

The confocal microscope images of SK-BR-3 cells incubated with C11Pc-PEG gold nanoparticles conjugated to anti-HER-2 antibodies (1 μM C11Pc equivalent) are shown in **Figure 5.13**. The brightness and contrast of all the images are as-obtained.

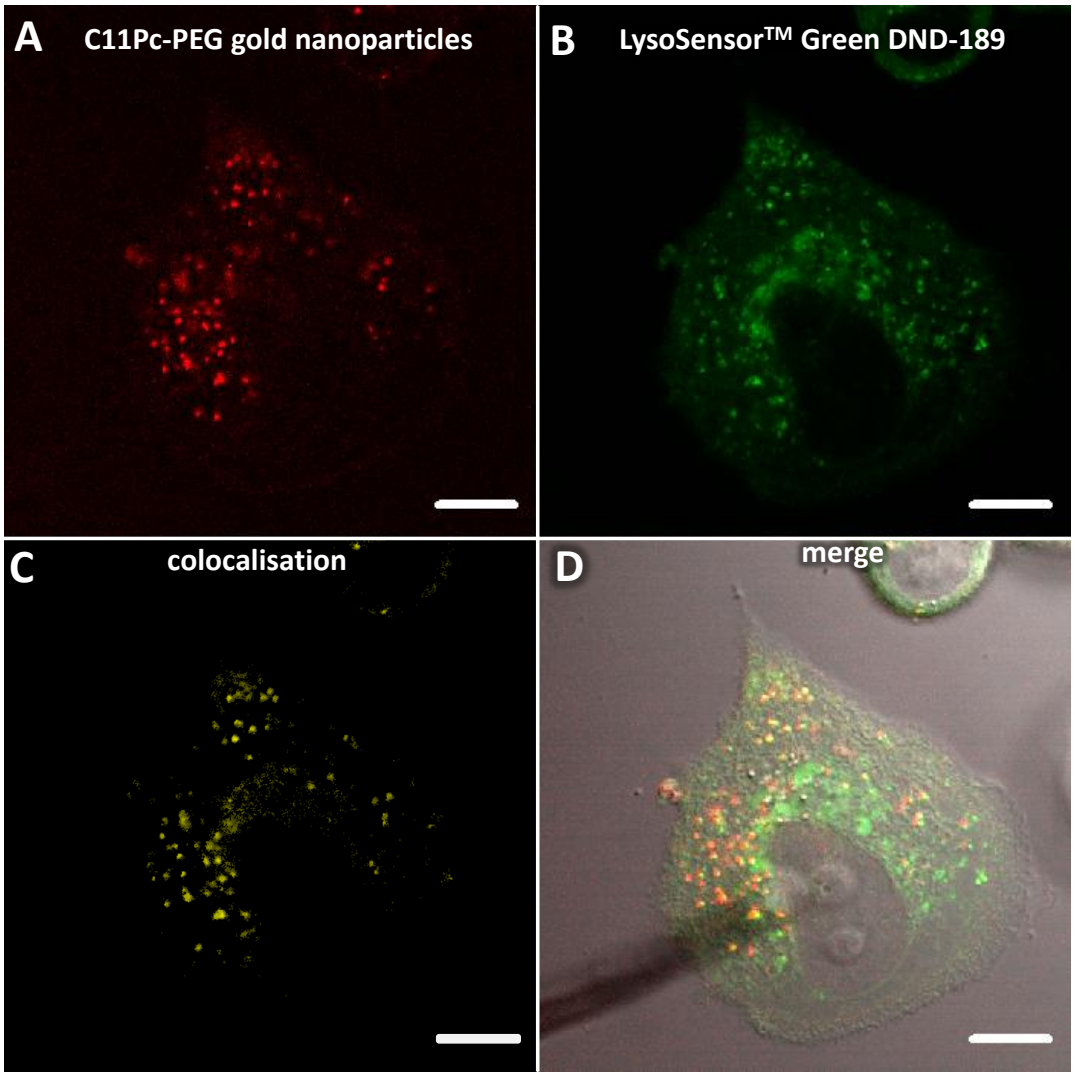

Figure 5.13 **Confocal microscope images of SK-BR-3 cells incubated with anti-HER-2 antibody conjugated C11Pc-PEG gold nanoparticles (1 μM C11Pc equivalent). A) Excitation of the conjugated C11Pc-PEG gold nanoparticles at 633 nm results in red fluorescence emission. B) Acidic organelles are visualised by the green fluorescence emission of LysoSensor™ Green DND-189 upon excitation at 458 nm. C) Colocalisation of the conjugated C11Pc-PEG gold nanoparticles and the LysoSensor™ is shown in yellow. D) The DIC image and the fluorescence images of C11Pc and the LysoSensor™ were merged. (Scale bars are 10 μm).**

The findings of the laser scanning confocal microscopy imaging experiments strongly suggest that both jacalin and anti-HER-2 antibody conjugated C11Pc-PEG gold nanoparticles partially accumulate within the acidic organelles within the HT-29 cells and the SK-BR-3 cells. Regions of red fluorescence that are not colocalised with the LysoSensor™ are possibly nanoparticle conjugates within endosomal compartments that have not yet matured into late endosomes or have been redirected back to the surface.[53] Thus, conjugated C11Pc-PEG gold nanoparticles targeted to HT-29 colon cancer and SK-BR-3 breast cancer cells using jacalin or anti-HER-2 antibodies are likely to enter the cells through a receptor mediated endocytic pathway and remain within the endosomal compartments.

5.3 Conclusions

In this chapter, the efficacy of using the lectin jacalin as a cancer-specific targeting protein was compared to anti-HER-2 antibodies. Both targeting ligands were covalently conjugated to C11Pc-PEG gold nanoparticles and were found to produce similar quantities of singlet oxygen upon irradiation at 633 nm. By using the MTT viability assay, it was shown that nanoparticles conjugated to either jacalin or anti-HER-2 antibodies significantly reduced HT-29 cell viability, as compared to the non-conjugated particles. At a nanoparticle concentration of 1.15 μM C11Pc equivalent, HT-29 cell viability was reduced to *ca.* 10% and 19% following jacalin or anti-HER-2 antibody targeted PDT treatment, respectively. However, at the same concentration, viability of HT-29 cells incubated with non-conjugated particles remained at *ca.* 94%. The SK-BR-3 cells appeared to be more susceptible to PDT damage than the HT-29 cells. At a nanoparticle concentration of 1.15 μM C11Pc equivalent, SK-BR-3 cell viability was reduced to *ca.* 3% and 5% following targeted PDT treatment with nanoparticles conjugated to jacalin or anti-HER-2 antibodies, respectively. However, at the same concentration, non-conjugated nanoparticles reduced SK-BR-3 cell viability by only *ca.* 5% following irradiation.

The ApoTox-Glo™ triplex assay was performed on both HT-29 cells and SK-BR-3 cells to investigate whether using the different targeting ligands would result in variations in the cell death mechanisms. The effect of nanoparticle concentration on the cell death pathway was also investigated by comparing particles at 0.1 μM and 1 μM C11Pc equivalent. Nanoparticles conjugated to SSA were used as a control to explore any non-specific enhancement in PDT cytotoxicity. It was found that at 0.1 μM C11Pc equivalent, no

significant difference in HT-29 cell viability reduction was observed between SSA conjugated and jacalin or anti-HER-2 antibody conjugated nanoparticles. At 1 μM C11Pc equivalent, jacalin and anti-HER-2 antibody conjugated nanoparticles reduced HT-29 cell viability significantly more than SSA conjugated particles (*P<0.05*). Cytotoxicity of irradiated HT-29 cells was only detected when the cells were incubated with the jacalin or anti-HER-2 antibody conjugated nanoparticles at 1 μM C11Pc equivalent. SSA conjugated particles failed to induce HT-29 cell cytotoxicity at either concentration. Therefore the enhanced PDT effect on the HT-29 cells observed with the jacalin or anti-HER-2 antibody conjugated nanoparticles is largely due to specific ligand-receptor interactions. Apoptosis, however, was not observed in HT-29 cells following PDT treatment with any of the C11Pc-PEG gold nanoparticle conjugates at any concentration.

At 0.1 μM C11Pc equivalent, the jacalin conjugated and anti-HER-2 antibody conjugated nanoparticles reduced SK-BR-3 cell viability significantly more than the SSA conjugated particles (*P<0.0005*). At 1 μM C11Pc equivalent a dramatic reduction in SK-BR-3 cell viability was observed with all three types of nanoparticles (*ca.* 95.0-98.5%). However, both jacalin and anti-HER-2 antibody conjugated nanoparticles were more effective than SSA conjugated particles (*P<0.05*). Cytotoxicity of SK-BR-3 cells was observed with both concentrations of the jacalin conjugated or anti-HER-2 antibody conjugated C11Pc-PEG gold nanoparticles (*ca.* 5.6-7.5 fold increase in cytotoxicity). However, the SSA conjugated nanoparticles only induced a significant level of SK-BR-3 cell cytotoxicity (*ca.* 7.8-fold increase in cytotoxicity) when using a nanoparticle concentration of 1 μM C11Pc equivalent. At a lower nanoparticle concentration of 0.1 μM C11Pc equivalent only a *ca.* 1.6-fold increase in cytotoxicity was observed. The concentration dependence in SSA-mediated cytotoxicity suggests that above a certain nanoparticle concentration, active targeting is overcome by non-specific particle uptake in the SK-BR-3 cells. A concentration course viability assay following targeted and non-targeted PDT treatment would define the nanoparticle concentration range at which active cancer cell targeting is optimal.

As with the HT-29 cells, no apoptosis was observed in the SK-BR-3 cells following PDT treatment with any of the nanoparticle conjugates at both concentrations used. Once again, the jacalin conjugated particles were more effective than the anti-HER-2 antibody conjugated nanoparticles at reducing SK-BR-3 viability at both concentrations of 0.1 μM and 1 μM C11Pc equivalent (*P<0.005*). However, the cytotoxicity of SK-BR-3 cells incubated with anti-HER-2 antibody conjugated and SSA conjugated particles was higher than those incubated with the jacalin conjugated particles at 1 μM C11Pc equivalent

(*P<0.005*). This difference suggests a role in the time dependence of dead cell protease activity, which may not entirely correlate with the viability analysis.

The intracellular localisation of the jacalin conjugated or anti-HER-2 antibody conjugated C11Pc-PEG gold nanoparticles was investigated in HT-29 cells and SK-BR-3 cells using laser scanning confocal microscopy. Accumulation of the targeted nanoparticle conjugates within acidic organelles was assessed by the colocalisation of the red C11Pc fluorescence from the conjugated nanoparticles with the green LysoSensor™ Green DND-189 fluorescence. The degree of colocalisation was analysed using the BioImageXD software. It was found that both the jacalin conjugated and anti-HER-2 antibody conjugated nanoparticles partially colocalised with the LysoSensor™ Green DND-189 and remained in the acidic organelles within both the HT-29 cells and the SK-BR-3 cells. Colocalisation suggests that both types of nanoparticle conjugates were internalised through receptor mediated endocytosis. Unlike the anti-HER-2 antibody conjugated particles, the high variability of the colocalisation analyses of the jacalin conjugated particles with the LysoSensor™ Green DND-189 in both cells lines could indicate a difference in the mechanism of endocytosis. Further investigations into the internalisation and recycling of the HER-2 receptor and the T antigen-bearing glycoproteins could provide valuable insight into the differences in cellular uptake of the targeted nanoparticle conjugates. Additionally, the intracellular integrity of the conjugated C11Pc-PEG gold nanoparticles could be studied by using dark-field microscopy to determine the localisation of the gold nanoparticles with respect to the C11Pc fluorescence.

In conclusion, this chapter outlines a number of investigations comparing the efficacy of the lectin, jacalin, with the anti-HER-2 antibody as cancer-specific targeting ligands. Both targeting ligands conjugated to C11Pc-PEG gold nanoparticles significantly reduced the viability of HT-29 colon adenocarcinoma cells and SK-BR-3 breast adenocarcinoma cells following irradiation at 633 nm. Cytotoxicity was observed following targeted PDT using either the lectin or the antibody, whereas no evidence of apoptosis was observed. Evidence suggests that at certain nanoparticle concentrations, jacalin conjugation was more effective than anti-HER-2 antibody conjugation at targeted PDT cell kill; however, this could be attributed to the higher levels of dark toxicity induced by the jacalin conjugates. Based on the dissociation constants of jacalin binding to HT-29 cells (500 ± 50 nM)[46] and anti-HER-2 antibodies binding to SK-BR-3 cells (14-36 nM),[45] it was expected that antibody targeting would be more efficient than lectin targeting. However, SK-BR-3 cells express *ca.* 1-2x10^6 HER-2 receptors per cell,[44] whereas HT-29 cells express *ca.*

$4.4x10^7$ T antigens per cell.[46] These findings suggest an important role for cell surface receptor density on the outcome of targeted PDT treatments for cancer. Investigations into the binding kinetics of the nanoparticle conjugates to the cells could help explain the differences between using the lectin or the antibody. The studies described in this chapter outline how lectins, such as jacalin, may have great potential for targeted cancer therapy by exploiting the high levels of cancer-associated carbohydrate antigen expression, *e.g*. $4.4x10^7$ T antigens per cell.

5.4 References

1. Sudimack, J.; Lee, R. J. *Adv. Drug Delivery Rev.* **2000**, *41*, 147-162.
2. Rosivatz, E.; Becker, I.; Bamba, M.; Schott, C.; Diebold, J.; Mayr, D.; Hofler, H.; Becker, K. F. *Int. J. Cancer* **2004**, *111*, 711-719.
3. Thorpe, P. E. *Clin. Cancer Res.* **2004**, *10*, 415-427.
4. Hogemann-Savellano, D.; Bos, E.; Blondet, C.; Sato, F.; Abe, T.; Josephson, L.; Weissleder, R.; Gaudet, J.; Sgroi, D.; Peters, P. J.; Basilion, J. P. *Neoplasia* **2003**, *5*, 495-506.
5. Arap, W.; Pasqualini, R.; Ruoslahti, E. *Science* **1998**, *279*, 377-380.
6. Aina, O. H.; Sroka, T. C.; Chen, M. L.; Lam, K. S. *Biopolymers* **2002**, *66*, 184-199.
7. Li, Z. J.; Cho, C. H. *J. Transl. Med.* **2012**, *10 Suppl 1*, S1.
8. Kapoor, P.; Singh, H.; Gautam, A.; Chaudhary, K.; Kumar, R.; Raghava, G. P. S. *PLoS ONE* **2012**, *7*, e35187.
9. Kopelman, R.; Koo, Y.-E. L.; Philbert, M.; Moffat, B. A.; Reddy, G. R.; McConville, P.; Hall, D. E.; Chenevert, T. L.; Bhojani, M. S.; Buck, S. M.; Rehemtulla, A.; Ross, B. D. *J. Magn. Magn. Mater.* **2005**, *293*, 404-410.
10. Esposito, C. L.; Catuogno, S.; de Franciscis, V.; Cerchia, L. *Discov. Med.* **2011**, *11*, 487-496.
11. Cai, L.; Chen, Z. Z.; Chen, M. Y.; Tang, H. W.; Pang, D. W. *Biomaterials* **2013**, *34*, 371-381.
12. Shangguan, D.; Li, Y.; Tang, Z.; Cao, Z. C.; Chen, H. W.; Mallikaratchy, P.; Sefah, K.; Yang, C. J.; Tan, W. *Proc. Natl. Acad. Sci. U. S. A.* **2006**, *103*, 11838-11843.
13. Prakash, J.; Beljaars, L.; Harapanahalli, A. K.; Zeinstra-Smith, M.; de Jager-Krikken, A.; Hessing, M.; Steen, H.; Poelstra, K. *Int. J. Cancer* **2010**, *126*, 1966-1981.
14. Gary-Bobo, M.; Mir, Y.; Rouxel, C.; Brevet, D.; Basile, I.; Maynadier, M.; Vaillant, O.; Mongin, O.; Blanchard-Desce, M.; Morère, A.; Garcia, M.; Durand, J. O.; Raehm, L. *Angew. Chem. Int. Ed.* **2011**, *50*, 11425-11429.
15. Olson, E. S.; Aguilera, T. A.; Jiang, T.; Ellies, L. G.; Nguyen, Q. T.; Wong, E. H.; Gross, L. A.; Tsien, R. Y. *Integr. Biol.* **2009**, *1*, 382-393.
16. Schrama, D.; Reisfeld, R. A.; Becker, J. C. *Nat. Rev. Drug Discovery* **2006**, *5*, 147-159.
17. Alberts, B., Johnson, A., Lewis, J., Raff, M., Roberts, K., Walter, P. *Molecular Biology of the Cell*; 4th ed.; Garland Science, **2002**.
18. Coico, R.; Sunshine, G. *Immunology: A Short Course*; 6th ed.; Wiley, **2009**.
19. Nelson, D. L.; Osgood, M.; Cox, M. M.; Ocorr, K. *Lehninger Principles of Biochemistry*; 4th ed.; Macmillan Higher Education, **2004**.

20. Wright, A.; Morrison, S. L. *Trends Biotechnol.* **1997**, *15*, 26-32.
21. Hermanson, G. T. *Bioconjugate Techniques*; 2nd ed.; Academic Press, **2008**.
22. Smith, B. T. *Concepts in Immunology and Immunotherapeutics*; 4th ed.; American Society of Health-System Pharmacists, **2007**.
23. Scott, A. M.; Allison, J. P.; Wolchok, J. D. *Cancer Immunol. Immunother.* **2012**, *12*, 14.
24. Ellis, L. M.; Hicklin, D. J. *Nat. Rev. Cancer* **2008**, *8*, 579-591.
25. Bullous, A. J.; Alonso, C. M.; Boyle, R. W. *Photochem. Photobiol. Sci.* **2011**, *10*, 721-750.
26. Hudson, R.; Carcenac, M.; Smith, K.; Madden, L.; Clarke, O. J.; Pelegrin, A.; Greenman, J.; Boyle, R. W. *Br. J. Cancer* **2005**, *92*, 1442-1449.
27. Abu-Yousif, A. O.; Moor, A. C.; Zheng, X.; Savellano, M. D.; Yu, W.; Selbo, P. K.; Hasan, T. *Cancer Lett.* **2012**, *321*, 120-127.
28. Stuchinskaya, T.; Moreno, M.; Cook, M. J.; Edwards, D. R.; Russell, D. A. *Photochem. Photobiol. Sci.* **2011**, *10*, 822-831.
29. Wang, L.; Su, W.; Liu, Z.; Zhou, M.; Chen, S.; Chen, Y.; Lu, D.; Liu, Y.; Fan, Y.; Zheng, Y.; Han, Z.; Kong, D.; Wu, J. C.; Xiang, R.; Li, Z. *Biomaterials* **2012**, *33*, 5107-5114.
30. Berstad, M. B.; Weyergang, A.; Berg, K. *Biochim. Biophys. Acta* **2012**, *1820*, 1849-1858.
31. Hughes, B. *Nat. Rev. Drug Discovery* **2010**, *9*, 665-667.
32. Firer, M. A.; Gellerman, G. *J. Hematol. Oncol.* **2012**, *5*, 70.
33. Bazley, L. A.; Gullick, W. J. *Endocr.-Relat. Cancer* **2005**, *12 Suppl 1*, S17-27.
34. Seshacharyulu, P.; Ponnusamy, M. P.; Haridas, D.; Jain, M.; Ganti, A. K.; Batra, S. K. *Expert Opin. Ther. Targets* **2012**, *16*, 15-31.
35. Yarden, Y.; Sliwkowski, M. X. *Nat. Rev. Mol. Cell Biol.* **2001**, *2*, 127-137.
36. Chaturvedi, P.; Singh, A. P.; Chakraborty, S.; Chauhan, S. C.; Bafna, S.; Meza, J. L.; Singh, P. K.; Hollingsworth, M. A.; Mehta, P. P.; Batra, S. K. *Cancer Res.* **2008**, *68*, 2065-2070.
37. Ponnusamy, M. P.; Singh, A. P.; Jain, M.; Chakraborty, S.; Moniaux, N.; Batra, S. K. *Br. J. Cancer* **2008**, *99*, 520-526.
38. Yu, D.; Hung, M. C. *Oncogene* **2000**, *19*, 6115-6121.
39. Ross, J. S.; Fletcher, J. A. *Stem Cells* **1998**, *16*, 413-428.
40. Kim, W. K.; Bang, M. H.; Kim, E. S.; Kang, N. E.; Jung, K. C.; Cho, H. J.; Park, J. H. *J. Nutr. Biochem.* **2005**, *16*, 155-162.
41. Lewis, G. D.; Figari, I.; Fendly, B.; Wong, W. L.; Carter, P.; Gorman, C.; Shepard, H. M. *Cancer Immunol. Immunother.* **1993**, *37*, 255-263.

42. Pohl, M.; Stricker, I.; Schoeneck, A.; Schulmann, K.; Klein-Scory, S.; Schwarte-Waldhoff, I.; Hasmann, M.; Tannapfel, A.; Schmiegel, W.; Reinacher-Schick, A. *J. Cancer Res. Clin. Oncol.* **2009**, *135*, 1377-1386.
43. Xu, H.; Yu, Y.; Marciniak, D.; Rishi, A. K.; Sarkar, F. H.; Kucuk, O.; Majumdar, A. P. *Mol. Cancer Ther.* **2005**, *4*, 435-442.
44. Orlova, A.; Bruskin, A.; Sivaev, I.; Sjöberg, S.; Lundqvist, H.; Tolmachev, V. *Anticancer Res.* **2006**, *26*, 1217-1223.
45. Tang, Y.; Wang, J.; Scollard, D. A.; Mondal, H.; Holloway, C.; Kahn, H. J.; Reilly, R. M. *Nucl. Med. Biol.* **2005**, *32*, 51-58.
46. Yu, L.-G.; Milton, J. D.; Fernig, D. G.; Rhodes, J. M. *J. Cell. Physiol.* **2001**, *186*, 282-287.
47. Jeyaprakash, A. A.; Rani, P. G.; Reddy, G. B.; Banumathi, S.; Betzel, C.; Sekar, K.; Surolia, A.; Vijayan, M. *J. Mol. Biol.* **2002**, *321*, 637-645.
48. Harris, L. J.; Larson, S. B.; Hasel, K. W.; McPherson, A. *Biochemistry* **1997**, *36*, 1581-1597.
49. Wang, H.; Wang, F.; Tao, X.; Cheng, H. *Anal. Biochem.* **2012**, *421*, 324-326.
50. Schafer, F. Q.; Buettner, G. R. *Photochem. Photobiol.* **1999**, *70*, 858-867.
51. Reddy, G. R.; Thompson, W. C.; Miller, S. C. *J. Am. Chem. Soc.* **2010**, *132*, 13586-13587.
52. Bertrand, R.; Solary, E.; O'Connor, P.; Kohn, K. W.; Pommier, Y. *Exp. Cell Res.* **1994**, *211*, 314-321.
53. Zhang, S.; Li, J.; Lykotrafitis, G.; Bao, G.; Suresh, S. *Adv Mater* **2009**, *21*, 419-424.
54. Vácha, R.; Martinez-Veracoechea, F. J.; Frenkel, D. *Nano Lett.* **2011**, *11*, 5391-5395.
55. Iversen, T. G.; Skotland, T.; Sandvig, K. *Nano Today* **2011**, *6*, 176-185.

Chapter 6

Sonodynamic therapy of HT-29 colon adenocarcinoma cells using titanium dioxide nanoparticles

This chapter describes the synthesis and characterisation of stable polyacrylic acid coated titanium dioxide nanoparticles. The potential of sonocatalytic enhancement in the production of reactive oxygen species is investigated and *in vitro* sonodynamic therapy of HT-29 cells is explored.

6.1 Introduction

6.1.1 Sonochemistry

Acoustic waves are longitudinal propagations of mechanical vibrations travelling through a medium, the frequencies of which are expressed as Hertz (Hz, cycles per second).[1] Ultrasound waves consist of cycles of low pressure (rarefaction) and high pressure (compression), which oscillate at frequencies greater than 16 kHz.[1] High frequency ultrasound (1-20 MHz) is widely used for medical imaging and diagnostics. The frequency of ultrasound waves is inversely proportional to the tissue penetration depth; with increasing frequency, transmission through tissue is attenuated.[2] For example, ultrasound penetration through soft tissue is *ca.* 150 mm when using an ultrasound frequency of 3.5 MHz; however, penetration is reduced to *ca.* 20 mm when using 10 MHz ultrasound.[3] Additionally, the spatial resolution of ultrasound images is improved with increasing frequency.[3] High intensity focused ultrasound has been exploited for selective surgical tissue necrosis, and has been utilised for the selective ablation of a variety of tumours using ultrasound frequencies of 0.8-4 MHz and intensities of 1,000-20,000 $W.cm^{-2}$.[4]

The physical effects of ultrasound on water can lead to the sonochemical generation of several cytotoxic reactive oxygen species (ROS), including radicals and singlet oxygen.[1,5] Sonochemical reactions are initiated by the violent collapse of cavitation bubbles formed by the exertion of an ultrasonic field in a liquid medium. Acoustic cavitation of water begins with the nucleation of a gas or vapour filled microbubble upon oscillating cycles of compression and rarefaction within the applied ultrasonic field.[6] Two distinct yet

interconnected mechanisms of cavitation exist: stable and transient cavitation.[6,7] During stable acoustic cavitation, the diameter of the bubble stably oscillates with the incident acoustic frequency. However, during transient acoustic cavitation, the bubble forms and rapidly grows with the oscillating cycles of compression and rarefaction. Once the microbubble reaches an unstable size, it violently collapses. At this stage, the liquid-gas interface velocity of the collapsing bubble nears that of the speed of sound, which results in hotspots with extreme localised temperatures and pressures, *i.e.* 2,000 °C and 10,000 atm, respectively.[6] The processes during transient acoustic cavitation are explained in **Figure 6.1**.

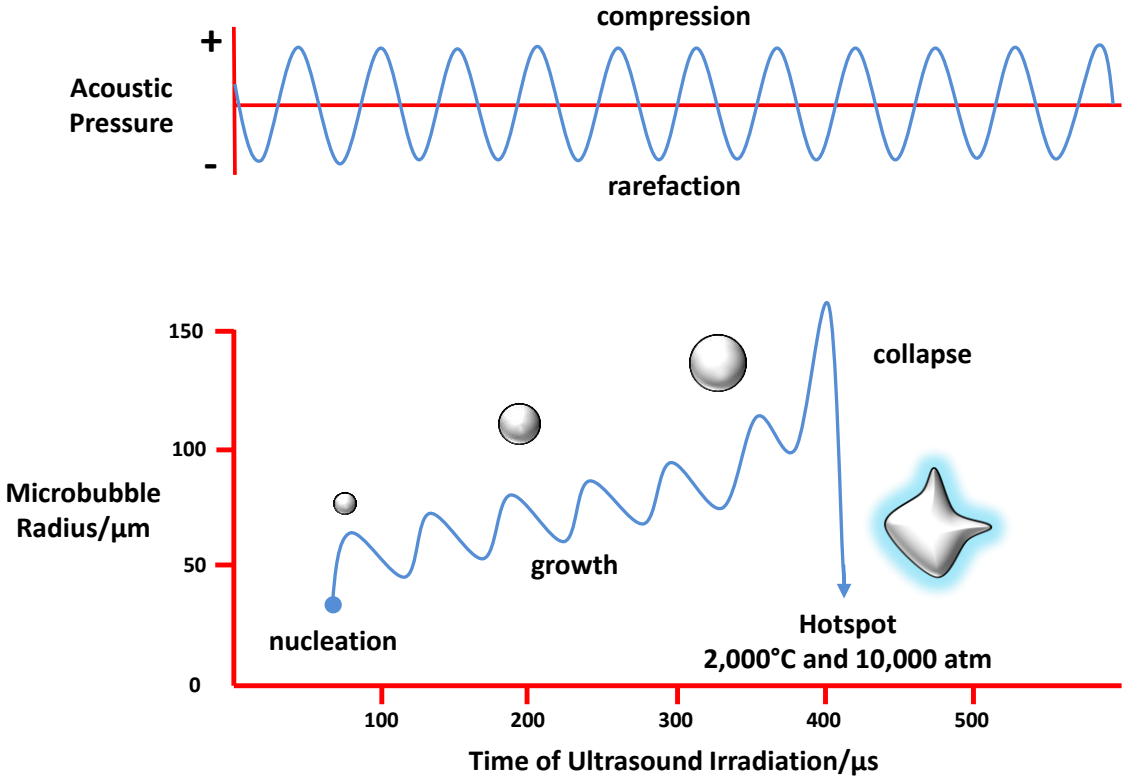

Figure 6.1 **The processes involved in transient acoustic cavitation during ultrasound irradiation. Upon oscillating waves of acoustic compression and rarefaction, gas or vapour filled microbubbles are formed, expand, and then collapse to generate hotspots with areas of high temperatures and pressures. Figure adapted from Suslick.[8]**

Visible light is also emitted during cavitation; this phenomenon is known as sonoluminescence.[7,9,10] The first sonochemical reaction to occur during ultrasonic irradiation of water is the sonolysis of H_2O into $H^{\bullet}$ and $^{\bullet}OH$ radicals.[6] Light spanning the UV-visible and near-infrared regions of the spectrum is emitted during cavitation as a result of radiative recombination of radicals, in addition to the radiative relaxation of excited species formed during cavitation.[7] The optical properties of sonoluminescence in water are influenced by the frequency of the ultrasound and the nature of the gases dissolved in the water.[7] For example, sonoluminescence emission maxima centred at 310 nm, 360 nm and 430 nm are observed upon the exposure of air saturated water to ultrasound (450 kHz).[7] The sonolysis of water propagates a variety of radical chain reactions producing strongly oxidising species such as hydroxyl radicals ($^{\bullet}OH$) and hydrogen peroxide (H_2O_2), amongst others.[6] The possible reactions that occur during cavitation bubble collapse are described in equations **6.1**-**6.12**.[1,6,11] Additionally, the presence of oxygen within a cavitation bubble has been reported to result in the formation of singlet oxygen in addition to peroxy radicals.[5] Sonolysis of water results in the production of hydrogen radicals and hydroxyl radicals (**6.1**). These radicals can recombine to form water once again (**6.2**).[6]

$$H_2O \rightarrow H^{\bullet} + {}^{\bullet}OH \quad (\mathbf{6.1})$$

$$H^{\bullet} + {}^{\bullet}OH \rightarrow H_2O \quad (\mathbf{6.2})$$

Alternatively, the combination of two hydroxyl radicals can result in the formation of hydrogen peroxide (**6.3**), hydrogen and oxygen (**6.4**), or water and oxygen (**6.5**). Hydroxyl radical attack of water can also lead to the production of hydrogen peroxide and oxygen radicals (**6.6**).[6]

$$^{\bullet}OH + {}^{\bullet}OH \rightarrow H_2O_2 \quad (\mathbf{6.3})$$

$$^{\bullet}OH + {}^{\bullet}OH \rightarrow H_2 + O_2 \quad (\mathbf{6.4})$$

$$2{}^{\bullet}OH + 2{}^{\bullet}OH \rightarrow 2H_2O + O_2 \quad (\mathbf{6.5})$$

$$^{\bullet}OH + H_2O \rightarrow H_2O_2 + O^{\bullet} \quad (\mathbf{6.6})$$

The combination of two hydrogen radicals can result in the formation of hydrogen gas (**6.7**). Hydrogen radicals can also react with hydrogen peroxide to produce hydroxyl radicals and water (**6.8**). The reaction of hydrogen radicals with oxygen leads to the generation of hydroperoxyl radicals (**6.9**). Hydroperoxyl radicals may further react with hydrogen radicals to produce hydrogen peroxide (**6.10**).[6]

$H^{\bullet} + H^{\bullet} \rightarrow H_2$ (**6.7**)

$H^{\bullet} + H_2O_2 \rightarrow {}^{\bullet}OH + H_2O$ (**6.8**)

$H^{\bullet} + O_2 \rightarrow HO_2^{\bullet}$ (**6.9**)

$HO_2^{\bullet} + H^{\bullet} \rightarrow H_2O_2$ (**6.10**)

The combination of two hydroperoxyl radicals may lead to the generation of hydrogen peroxide and oxygen (**6.11**). Additionally, hydroperoxyl radicals may react with oxygen radicals to produce hydrogen peroxide (**6.12**). [6]

$HO_2^{\bullet} + HO_2^{\bullet} \rightarrow H_2O_2 + O_2$ (**6.11**)

$H_2O^{\bullet} + O^{\bullet} \rightarrow H_2O_2$ (**6.12**)

The large variety of radical intermediates and ROS species produced during the exposure of water to ultrasound has led to a significant number of studies exploring the therapeutic potential of ultrasound.[12]

6.1.2 Sonosensitisers and ultrasound enhanced chemotherapeutics

Sonosensitisers are agents that become sensitising following exposure to ultrasound frequencies, leading to the generation of ROS. It has been shown that a large number of photosensitisers act as sonosensitisers that produce singlet oxygen amongst other ROS species following exposure to ultrasound.[12] Sonoluminescence is thought to be primarily responsible for the photoexcitation of the sensitisers through typical type I and type II reactions. The ultrasonic irradiation of other non-photosensitising compounds and chemotherapeutics, such as Adriamycin® and 5-fluorouracil, has also been found to exhibit a synergistic antitumour effect.[12] The mechanisms underlying ultrasound enhanced

chemotherapy differ from those of sonoluminescent activation of photo/sonosensitisers.[12] Ultrasound is suggested to play a role in the sonoporation of cells, promoting the transport of drugs through the cell membrane.[12] Additionally, chemotherapeutics are thought to assist the shear forces during ultrasound exposure that can physically destabilise cell membranes. Sonochemically generated alkoxyl and peroxyl radicals produced from chemotherapeutic sonosensitisers are also responsible for cell membrane lipid peroxidation through radical chain reactions.[12]

6.1.3 *In vitro* and *in vivo* sonodynamic therapy

Reports of using photosensitisers for sonodynamic therapy (SDT) demonstrate the clinical prospects for using a combination of chemical agents and ultrasound to reduce cancer cell viability and inhibit tumour growth. SDT treatment of an implanted S180 sarcoma tumour using protoporphyrin IX and haematoporphyrin showed a *ca.* 43% and 35% inhibition of tumour growth, respectively, when administration of the photo/sonosensitisers was combined with ultrasound exposure (2.2 MHz, 5 $W.cm^{-2}$).[13] The use of haematoporphyrin as a sonosensitiser was also investigated on hepatoma 22 cells.[14] Sonodynamic toxicity of hepatoma 22 cells was observed in both an ultrasound exposure time-dependent manner and a sensitiser concentration-dependent manner. Reduction in cell viability was most effective when the cells were incubated with haematoporphyrin (200 $\mu g.ml^{-1}$) and exposed to 60 s of ultrasound irradiation (1.43 MHz, 2 $W.cm^{-2}$).[14] *In vivo*, haematoporphyrin administration followed by ultrasound irradiation exhibited a synergistic antitumour effect on implanted hepatoma 22 cells, which was reported to significantly inhibit tumour growth.[14]

C6 glioma cells were also responsive to SDT treatment using a monoethyl ether derivative of haematoporphyrin.[15] SDT treatment by the combination of ultrasound (1 MHz, 1 $W.cm^{-2}$) and the haematoporphyrin derivative induced a significant increase in intracellular production of ROS and an increase in the rate of C6 cell apoptosis. A marked decrease in the mitochondrial membrane potential in the C6 cells was also observed.

A comparative investigation into the anticancer effects of photodynamic and sonodynamic therapies has been reported using chloroaluminium phthalocyanine disulfonate incubated with B16FO murine melanoma cells and NIH3T3 murine fibroblast cells.[16] A drastic reduction in the viability of both cell lines was observed following PDT treatment (660 nm,

15 J.cm^{-2}) and following SDT treatment (1 MHz, 2 W.cm^{-2}) at all concentrations of the sensitiser used (0.5-100 μM).

The sonodynamic efficacy of chlorin e6 has been investigated in a SPCA-1 human lung adenocarcinoma mouse tumour xenograft model.[17] Sensitiser administration alone or ultrasound irradiation of the tumour without the sensitiser did not lead to an observable effect on tumour size. However, sonodynamic treatment using sensitiser administration followed by ultrasound irradiation induced a dose-dependent and ultrasound intensity-dependent inhibition of tumour growth. Maximal antitumour effects were observed at 40 mg.kg^{-1} of chlorin e6 in combination with ultrasound (1 MHz 1.6 W.cm^{-2}).

Recently, a systematic study on the *in vitro* and *in vivo* efficacy of indocyanine green as both a photosensitiser and a sonosensitiser has been reported.[18] RIF-1 murine fibrosarcoma cells incubated with indocyanine green were exposed to ultrasound irradiation alone (1 MHz, 2 W.cm^{-2}), which reduced cell viability by *ca.* 65%. Cells incubated with the sensitiser irradiated with near infrared light (880 nm, 37.8 J.cm^{-2}) followed by exposure to ultrasound (1 MHz, 2 W.cm^{-2}) exhibited a *ca.* 90% reduction in viability. Following intratumoural administration of indocyanine green, a *ca.* 42% inhibition of tumour growth was observed after PDT alone, a *ca.* 67% inhibition was observed after SDT alone, and a *ca.* 98% tumour growth inhibition was exerted after a combination of PDT and SDT. These results, amongst others, outline the potential of using deeply penetrating ultrasound to activate sensitisers for effective cancer treatment. The reports also suggest an important role for ultrasound in assisting conventional PDT modalities.

6.1.4 Titanium dioxide as a sonosensitiser

Nanostructured titanium dioxide (TiO_2) is a widely used material with various applications in photocatalysis, photovoltaics, electrochemistry, hydrogen storage and gas sensing.[19] TiO_2 nanoparticles are semiconductors, which photocatalytically generate ROS at their surface following irradiation. Upon photoirradiation, the presence of a positive hole and an electron at the surface of the TiO_2 results in the generation of cytotoxic ROS species. **Figure 6.2** (**A**) demonstrates the photogeneration of hydrogen peroxide (H_2O_2) and superoxide anions ($^{\bullet}O_2^-$) from water at the site of the surface electron(e^-). At the site of the positive hole (h^+), hydroxyl radicals ($^{\bullet}OH$) are also generated from molecular oxygen.

The direct energy transfer from photoexcited TiO_2 can also result in singlet oxygen production through a type II photosensitisation reaction.[20]

TiO_2 nanoparticles have also proven to be useful for a number of anticancer indications using SDT. The sonodynamic enhancement of ROS production by TiO_2 nanoparticles occurs through multiple mechanisms that can overlap. Given that the sonoluminescent emission during acoustic cavitation is of an appropriate wavelength and a sufficient intensity to excite the TiO_2, ROS production can be amplified in the presence of the nanoparticles (**Figure 6.2** (**B**, top)).[20] Furthermore, crevices and defects at the surface of the TiO_2 nanoparticles can act as gas pockets at the solid-liquid interface that can stabilise micronuclei during acoustic cavitation.[1,21,22] Stabilisation of the micronuclei during cavitation through this 'Crevice Model' can act to lower the threshold for cavitation.[1,6,21,23] A lower threshold for cavitation leads to an enhancement in the sonochemical generation of ROS (**Figure 6.2** (**B**, bottom)).

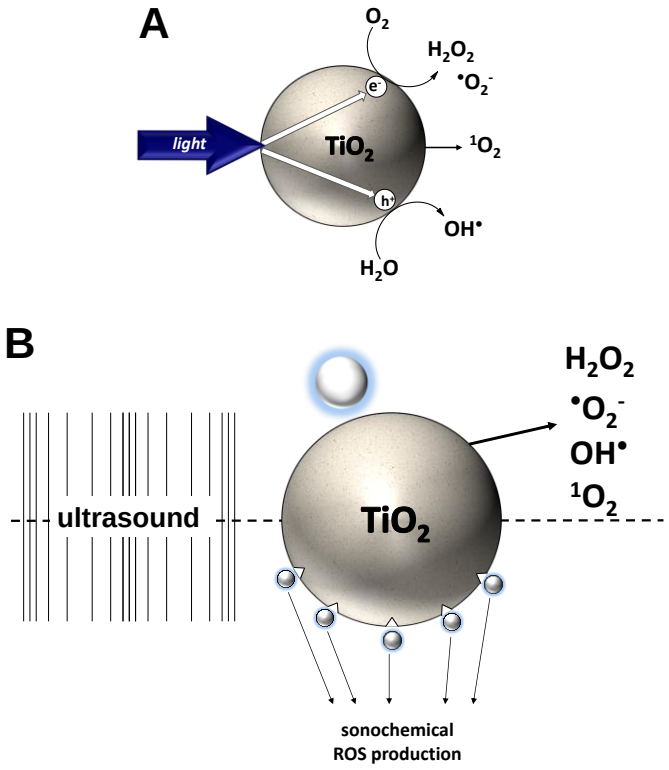

Figure 6.2 **A) A schematic representation of a photoexcited TiO_2 nanoparticle generating ROS species at surface trapped h^+ and e^-. Singlet oxygen is also produced through energy transfer from the photoexcited nanoparticle. B, top) Sonoluminescent activation of a TiO_2 nanoparticle producing ROS species upon exposure to ultrasound. B, bottom) Enhanced cavitation of water at the surface crevices and defects of the TiO_2 nanoparticle, leading to the sonochemical ROS production.**

Within SDT, recent reports highlight the potential use of TiO_2 nanoparticles for the effective SDT treatment of cancer. Commercial TiO_2 nanoparticles with a diameter of *ca.* 102 nm have been coated with polyacrylic acid and further modified with the pre-S1/S2 protein, extracted from the hepatitis B virus.[24] The nanoparticle-protein conjugates, with selectivity towards hepatocytes were used to target HepG2 human hepatocellular carcinoma cells. The intracellular localisation of the nanoparticles was confirmed by immunostaining of the targeting ligand. Exposure of the cells to ultrasound (1 MHz, 0.4 $W.cm^{-2}$) caused an increase in membrane damage, which was significantly enhanced by the presence of non-conjugated TiO_2 nanoparticles. Membrane damage was markedly higher following SDT treatment using the pre-S1/S2 protein nanoparticle conjugates.

SDT treatment using TiO_2 nanoparticles (*ca.* 6 nm) was also effective against C32 melanoma cells *in vitro* and against subcutaneously implanted C32 solid melanoma tumours in mice.[25] C32 cells were incubated with 0.025% or 0.050% nanoparticle preparations and exposed to ultrasound irradiation (1 MHz, 1 $W.cm^{-2}$). Cell viability was reduced to *ca.* 81.3% and *ca.* 53.6%, respectively, following exposure to ultrasound. Administration of the TiO_2 nanoparticles alone or exposure to ultrasound alone had no significant antitumour effect. However, SDT treatment induced by the combination of both nanoparticle administration and ultrasound irradiation had a noticeable inhibitory effect on tumour growth.

PEG modified TiO_2 nanoparticles (*ca.* 50 nm) also exhibited a sonodynamic effect on U251 human glioblastoma cells.[26] Incubation of the glioblastoma cells with TiO_2 nanoparticles (100 $\mu g.ml^{-1}$) followed by ultrasound irradiation (1 MHz, 1 $W.cm^{-2}$) for 50 s reduced cell viability to *ca.* 10%. Conversely, in order to reduce U251 cell viability to *ca.* 10% with PDT using the TiO_2 nanoparticles, UV irradiation at 360 nm (5 $mW.cm^{-2}$) for 1 h was required. The presence of the radical scavenger, glutathione, inhibited PDT induced cytotoxicity significantly more than sonodynamic toxicity. This difference in inhibition of cytotoxicity was suggested to be due to a synergistic role of TiO_2 nanoparticles in enhancing mechanical cavitation stress to cells in addition to ROS generation.

These reports, amongst others, demonstrate the efficacy of TiO_2 nanoparticles as sonosensitisers for the SDT treatment of cancer. The synthesis of biocompatible TiO_2 nanoparticles for the SDT treatment of HT-29 human colon adenocarcinoma cells is described in this chapter. The nanoparticles were capped with polyacrylic acid to provide the particles with multiple carboxyl functionalities to enable the bioconjugation of

targeting ligands. Investigations into the nature of the sonochemically generated ROS species are outlined, in addition to preliminary *in vitro* SDT studies.

6.2 Results and Discussion

6.2.1 Synthesis and characterisation of cation stabilised TiO_2 nanoparticles

The synthesis of TiO_2 nanoparticles capped with tetramethylammonium hydroxide (TMAOH) was performed as described in **section 2.4.1**. **Figure 6.3** shows the structure of TMAOH stabilised TiO_2 nanoparticles (TiO_2NP.TMAOH).

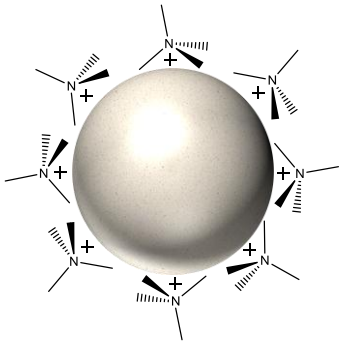

Figure 6.3 **Schematic representation of TiO_2 nanoparticles stabilised by the tetramethylammonium cation.**

The synthesis of the nanoparticles proceeds *via* a two-step reaction, as previously reported.[27] The initial step involves the hydrolysis of titanium (IV) butoxide to form titanium hydroxide clusters (**6.13**). The second step is the polycondensation of titanium hydroxide upon hydrothermal treatment to form the TiO_2 nanoparticles, which is catalysed by the TMAOH (**6.14**). TMAOH also serves to stabilise the condensed nanoparticles by capping their exposed surface –OH groups with a tetramethylammonium ion (TMA^+) (**6.15**).[27] The notations 'x', 'y' and 'z' refer to the proportions of the titanium, oxygen, and hydrogen atoms, respectively, within a TiO_2 nanoparticle.

$$Ti(OBu)_4 + 4\ H_2O \rightarrow Ti(OH)_4 + 4\ BuOH \quad (\mathbf{6.13})$$

$$TiOH + TMAOH \rightarrow TiO^- + TMA^+ + H_2O \quad (\mathbf{6.14})$$

$$Ti_xO_yH_z + TMAOH \rightarrow (Ti_xO_yH_{z-1})TMA^+ + H_2O \quad (\mathbf{6.15})$$

The TEM images of as-synthesised TiO_2NP.TMAOH particles are shown in **Figure 6.4**. The particles appear to be clusters (*ca.* 100-150 nm) of smaller nanoparticles. It is likely that the aggregation of the particles was due to a lack of stability provided by the TMAOH. Acidification of the nanoparticle solution could protonate the capping molecules, thus enabling electrostatic stabilisation of the nanoparticles.

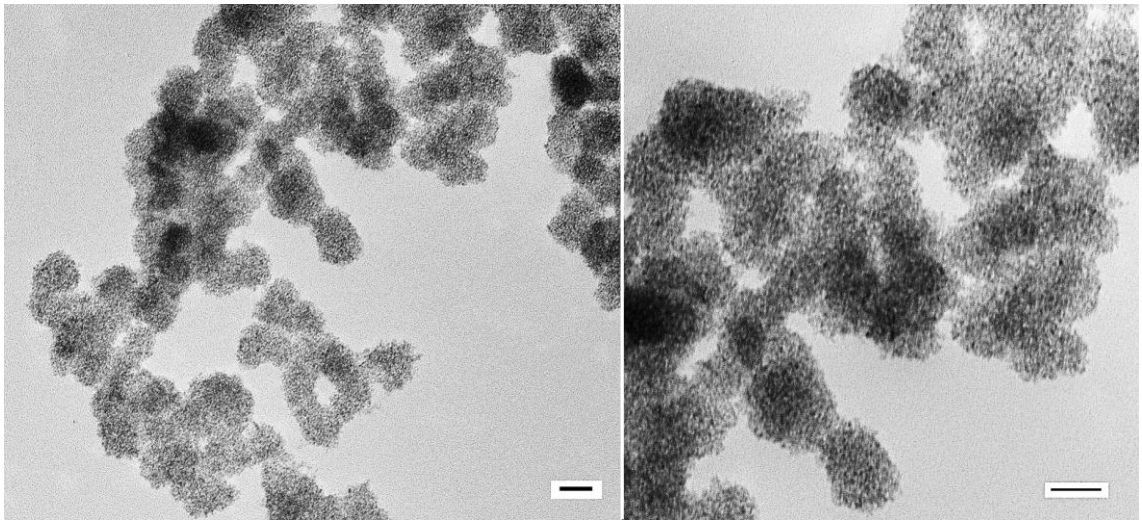

Figure 6.4 **TEM Images of as-synthesised TiO_2NP.TMAOH particles in water. (Scale bars are 100 nm).**

To enhance the biocompatibility of the TiO_2 nanoparticles and to allow for further conjugation to targeting biomolecules, modification with polyacrylic acid (PAA) containing multiple carboxyl groups was attempted. The initial protocol for modification with PAA was adapted from Kanehira *et al.*[28] The procedure involved the thermal annealing of the polymer onto the TiO_2NP.TMAOH nanoparticles in acidified *N,N*-dimethylformamide (DMF). Following removal of the water/butanol mixture present following the synthesis reaction, the nanoparticles were redispersed in 1% nitric acid and imaged using TEM, as

described in **section 2.4.3**. The TEM image of the nanoparticles after ultrasonic dispersion in nitric acid (**Figure 6.5**) revealed that the nanoparticles (*ca.* 5-10 nm in diameter) were largely non-aggregated. The prevalence of the non-aggregated, dispersed particles allowed for further modification of the individual nanoparticles with PAA.

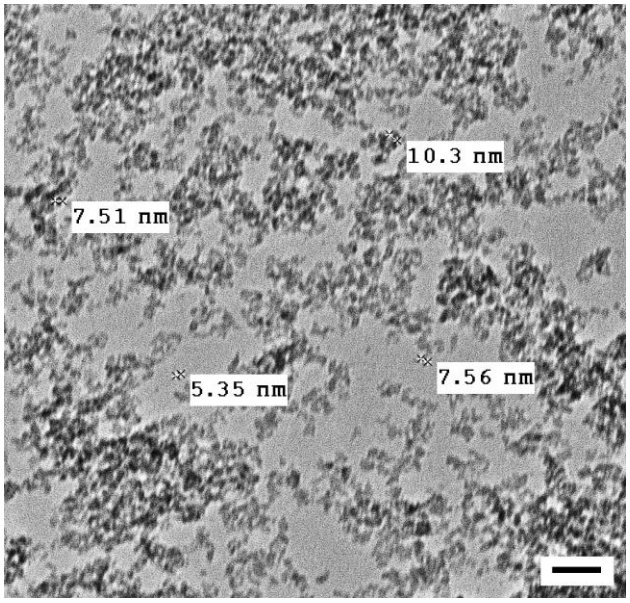

Figure 6.5 **TEM image of TiO_2NP.TMAOH nanoparticles in 1% nitric acid following ultrasonic dispersion. (Scale bar is 50 nm).**

The UV-visible absorption spectra of the as-synthesised TiO_2NP.TMAOH particles before and after sonication (**Figure 6.6** (**A**)) show that the as-synthesised nanoparticle aggregates have a significantly lower extinction in the UV region, as compared to the dispersed particles. The absorption band maximum of the aggregated particles is centred at 320 nm, whereas the dispersed particles exhibit a blue shift in the absorption band maximum, which is centred at 270 nm. This spectroscopic shift is typical for TiO_2 nanoparticles, which exhibit a blue shift in the absorption band maximum with a decreasing particle diameter.[29] The TiO_2NP.TMAOH particles sonicated in a nitric acid solution exhibit two distinct absorption bands centred at 270 nm and 320 nm, (**Figure 6.6** (**B**)) which correspond to a mixed species of dispersed and aggregated particles, respectively.

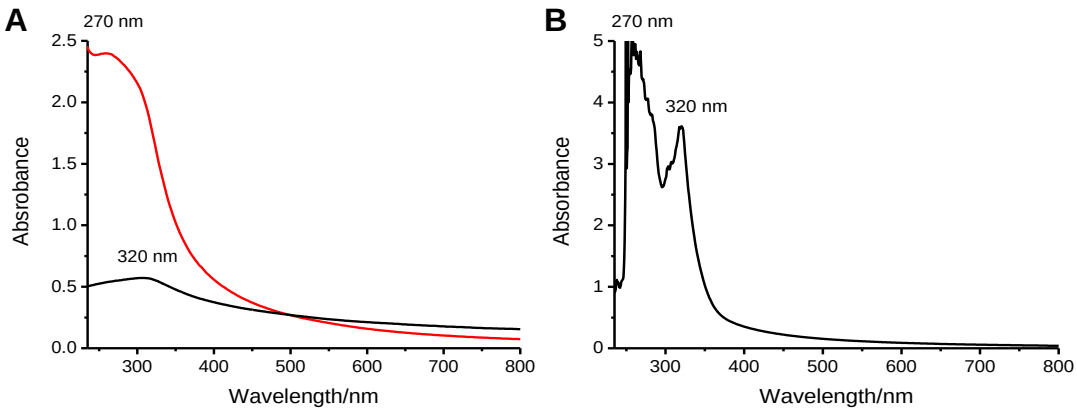

Figure 6.6 **A) UV-visible absorption spectra of 10% v/v dilutions of as-synthesised TiO_2NP.TMAOH particles in water before (black) and after (red) 15 min of ultrasonic dispersion. B) UV-visible absorption spectrum of a 20% w/v solution of TiO_2NP.TMAOH particles in 1% nitric acid, dispersed by 30 min of sonication.**

Following ultrasonic dispersion of the TiO_2NP.TMAOH particles in nitric acid, PAA was thermally annealed onto the nanoparticles in DMF, as described in **section 2.4.2**. Removal of DMF and unbound PAA from the TiO_2 nanoparticles capped with PAA (TiO_2NP.PAA, **Figure 6.7**) was reported to be achieved through precipitation of the particles with isopropanol.[28] However, to avoid Fisher esterification between exposed carboxyl groups on the TiO_2NP.PAA particles and isopropanol, precipitation with an excess of THF was attempted. Furthermore, removal of the DMF following the thermal annealing reaction was also attempted using rotary evaporation, as described in **section 2.4.2**.

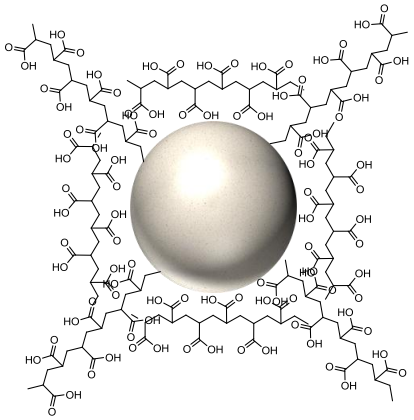

Figure 6.7 **Schematic representation of PAA capped TiO_2 nanoparticles (TiO_2NP.PAA).**

F**igure 6.8** shows the TEM images of the TiO_2NP.PAA nanoparticle samples in DMF following the thermal annealing of PAA (**Figure 6.8** (**A**)). The TEM images of the TiO_2NP.PAA particles precipitated with THF (**Figure 6.8** (**B**)) or rotary evaporated (**Figure 6.8** (**C**)) are also shown. Following the thermal annealing reaction of PAA onto the TiO_2 particles in DMF the nanoparticles appeared stable and non-aggregated, with a diameter of *ca.* 4 nm (**Figure 6.8** (**A**)). Although the nanoparticles were successfully precipitated upon addition of excess THF, the recovery of the nanoparticles was poor as no particles were observed during TEM imaging (**Figure 6.8** (**B**)). Rotary evaporation was successful at removing the DMF following the thermal annealing reaction; however, the nanoparticles appeared to aggregate on drying, and dissolution in water was unsuccessful (**Figure 6.8** (**C**)). The macroscopic TiO_2NP.PAA aggregates present following rotary evaporation failed to redisperse in water even after 1 h of sonication.

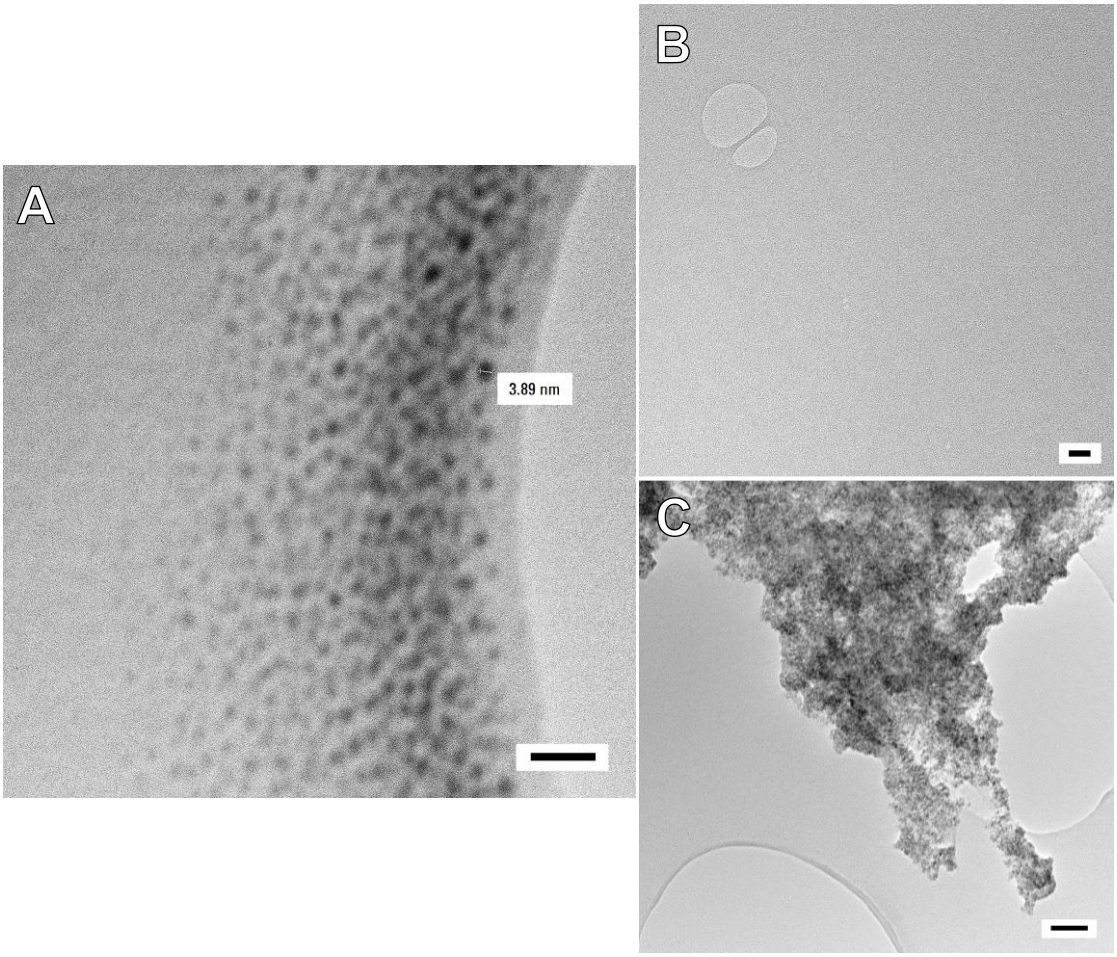

Figure 6.8 **A) TEM image of TiO_2NP.PAA following thermal annealing of PAA in DMF (scale bar is 20 nm). The nanoparticles were precipitated using excess THF and redissolved in water (B) or rotary evaporated and redissolved in water (C).(Scale bars in B and C are 100 nm).**

6.2.2 Photocatalytic and sonocatalytic ·OH generation by TiO_2NP.TMAOH particles

Preliminary attempts to remove the DMF and unbound PAA were largely unsuccessful, therefore it was decided that the photocatalytic activity of the TiO_2NP.TMAOH particles would be investigated prior to further attempts to synthesise TiO_2NP.PAA nanoparticles. It has been reported that coumarin-3-carboxylic acid (3-CCA) incorporated into polymeric nanoparticles can act as a fluorescent probe for sensing ·OH species.[30] 3-CCA was initially used to monitor ·OH production following UV irradiation (245 nm) of DMF in the absence or presence of TiO_2NP.TMAOH particles, as described in **section 2.4.4**. When excited at 367 nm, no fluorescence emission at 450 nm was observed in the 3-CCA solutions with or without nanoparticles. The lack of fluorescence was unexpected as 7-hydroxy-coumarin-3-carboxylic acid, the product of the reaction between 3-CCA and ·OH, exhibits a fluorescence emission band centred at 450 nm.[30] Therefore methylene blue was explored as an alternative probe for ·OH production. Methylene blue has been reported to be mineralised by ·OH into CO_2, water, sulphates and nitrates;[31] and has therefore been used as a colorimetric probe for the detection of ·OH species.[32] The photocatalytic degradation of methylene blue by the UV irradiation (245 nm) of the TiO_2NP.TMAOH particles was therefore investigated in water, as described in **section 2.4.5**. **Figure 6.9** (**A**) shows that the UV irradiation (245 nm, 15 min) of aqueous methylene blue (10 μM) resulted in minimal degradation of the dye. However, in the presence of TiO_2NP.TMAOH particles (**Figure 6.9** (**B**)) the degradation of methylene blue is significantly enhanced, demonstrating the photocatalytic activity of the nanoparticles. Due to the light scattering by the TiO_2NP.TMAOH particles, degradation of methylene blue was shown as the decay in the absorbance intensity at 664 nm (**Figure 6.9** (**C**)).

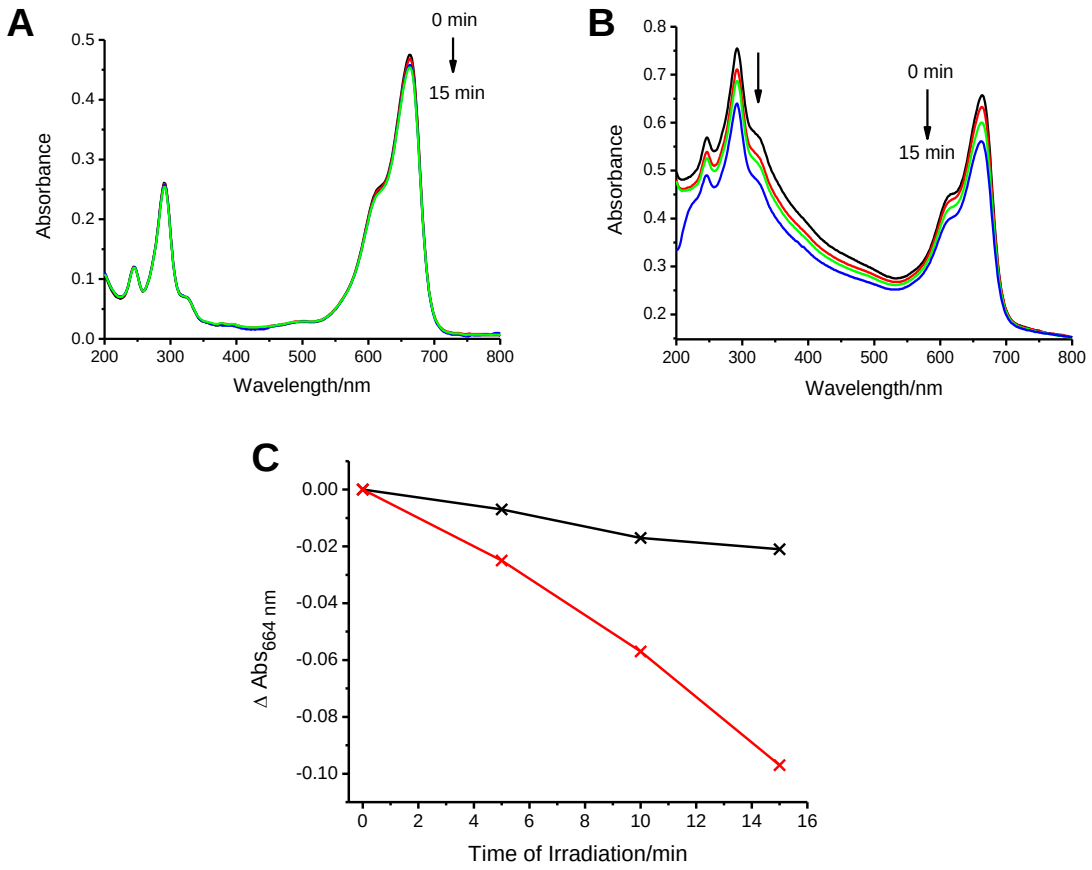

Figure 6.9 **UV-visible absorption spectra of the photocatalytic degradation of A) aqueous methylene blue (10 µM) and B) methylene blue (10 µM) in the presence of a 10% v/v dilution of TiO_2NP.TMAOH particles upon 15 min UV irradiation (245 nm). C) Degradation of methylene blue shown as a decay in absorbance intensity at 664 nm following UV irradiation (254 nm) in the absence (black) or presence (red) of a 10% v/v dilution of TiO_2NP.TMAOH particles.**

Exposure of TiO_2 pellets to ultrasound irradiation has previously been reported to sonocatalytically enhance the degradation of aqueous methylene blue.[33] Cavitation bubble collapse during ultrasound irradiation is thought to be responsible for the degradation of methylene blue following sonochemical •OH production.[33] This was further supported by the observation that mannitol and dimethylsulfoxide (•OH scavengers) inhibited the sonocatalytic degradation of methylene blue.[33]

An aqueous solution of methylene blue (10 µM) was exposed to ultrasound irradiation (1 MHz, 0.5 $W.cm^{-2}$) for 15 min, as described in **section 2.4.6**. The exposure of the methylene

blue to ultrasound resulted in the substantial degradation of the dye (**Figure 6.10** (**A**)). However, the presence of the TiO_2NP.TMAOH particles prevented any sonochemical degradation of methylene blue, thus indicating that the nanoparticles are ineffective for the sonocatalytic enhancement of •OH production (**Figure 6.10** (**B**)). Absorption in the UV region of the spectra shown in **Figure 6.10** (**B**) significantly increases upon ultrasound irradiation, as the TiO_2NP.TMAOH particles are dispersed. **Figure 6.10** (**C**) shows the decay in absorbance intensity at 664 nm following the sonochemical degradation of methylene blue in the absence or presence of the TiO_2NP.TMAOH particles.

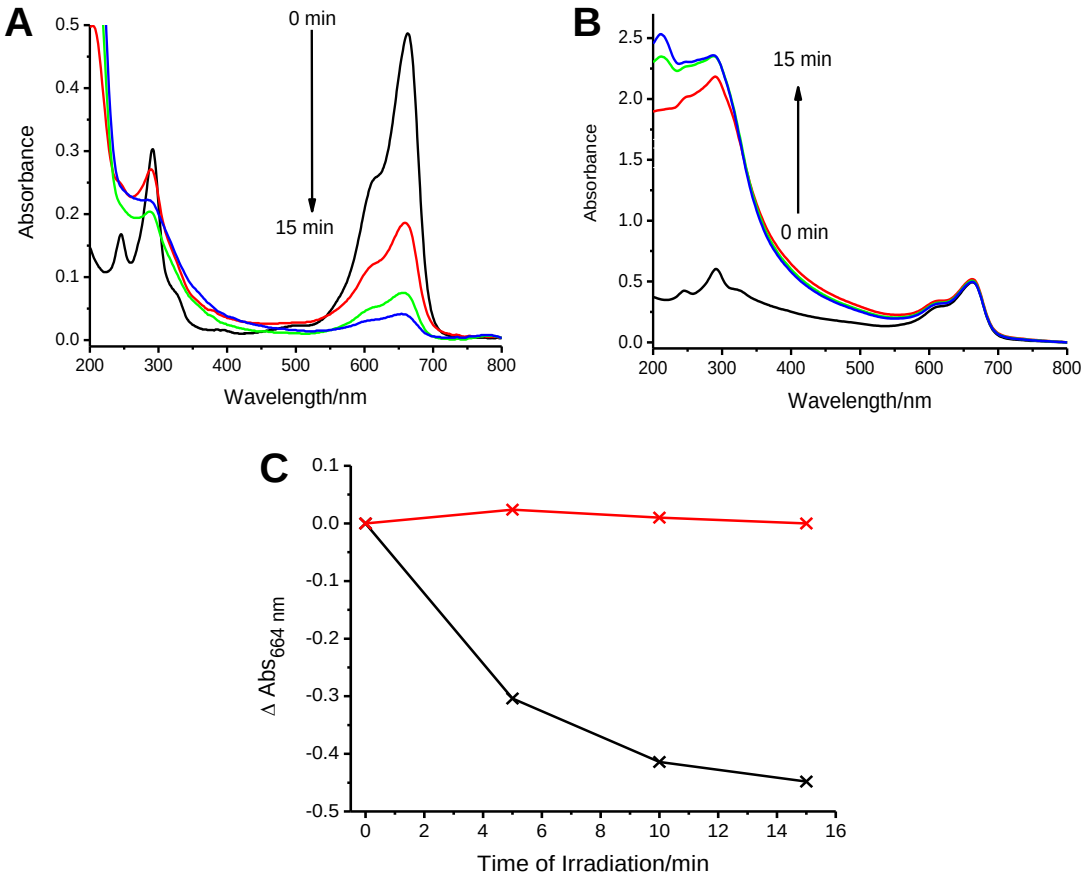

Figure 6.10 **UV-visible absorption spectra of the sonocatalytic degradation of A) aqueous methylene blue (10 µM) and B) methylene blue (10 µM) in the presence of a 10% v/v dilution of TiO_2NP.TMAOH particles following ultrasound irradiation (1 MHz, 0.5 W.cm^{-2}). C) Degradation of methylene blue is shown as a decay in absorbance intensity at 664 nm upon ultrasound irradiation in the absence (black) and presence (red) of a 10% v/v dilution of TiO_2NP.TMAOH particles.**

6.2.3 *In situ* synthesis of PAA capped TiO_2 particles

Although methylene blue was found to be an effective colorimetric probe for sonochemical •OH generation, the TiO_2NP.TMAOH particles appeared to have an inhibitory effect on the production of the radical. Chen *et al*.[34] have previously reported the synthesis of TiO_2 nanoparticles in the presence of PAA. The PAA acts as both a chelator and a stabilising agent for the nanoparticles formed. This protocol was therefore adapted and used to synthesise TiO_2NP.PAA nanoparticles *in situ*, as described in **section 2.4.7**, without the need for TMAOH. The butanol used in the reported protocol[34] was replaced with THF to avoid Fisher esterification between the alcohol and the carboxyl groups of PAA.

To compare the colloidal stability of the TiO_2NP.PAA particles and the TiO_2NP.TMAOH particles, both solutions were sonicated for 1 h then left to stand for 15 h. **Figure 6.11** shows that the TiO_2NP.PAA particles synthesised *in situ* exhibited higher colloidal stability than the TiO_2NP.TMAOH particles. The latter particles sedimented when left to stand for 15 h. Therefore, the PAA plays an important role in nanoparticle stabilisation in addition to biocompatibility.

Figure 6.11 **Aqueous solutions of as-synthesised TiO_2NP.TMAOH particles (left) and TiO_2NP.PAA particles synthesised *in situ* (right). Following synthesis, the particles were dispersed by 1 h sonication then left to stand for 15 h.**

Dynamic light scattering (DLS) size analysis by intensity shows the relative intensities of the light scattering of particles, which is proportional to the sixth power of their diameter. The histograms in **Figure 6.12** (**A** and **B**) show the size distribution by intensity of the TiO_2NP.TMAOH particles and the TiO_2NP.PAA particles, respectively. The size distribution of the aggregates is emphasised as a result of the increased intensity of light scattered by the aggregates, as compared to the smaller particle species. DLS analysis by number applies a spherical correlation function for the particles and corrects for the increased light scattering of larger particles. Therefore, the size approximation of non-spherical

particles may not be accurate, although the number of the predominant particle species is more representative of the sample. DLS analysis by number revealed that both the TiO_2NP.TMAOH particles and the TiO_2NP.PAA particles have similar hydrodynamic diameters. The TiO_2NP.TMAOH particles were mostly *ca.* 197.3 nm in diameter (**Figure 6.12 (C)**). The TiO_2NP.PAA particles were mostly *ca.* 189.9 nm in diameter, although the sample also contained a negligible amount of larger aggregates *ca.* 1.69 µm in diameter (**Figure 6.12 (D)**).

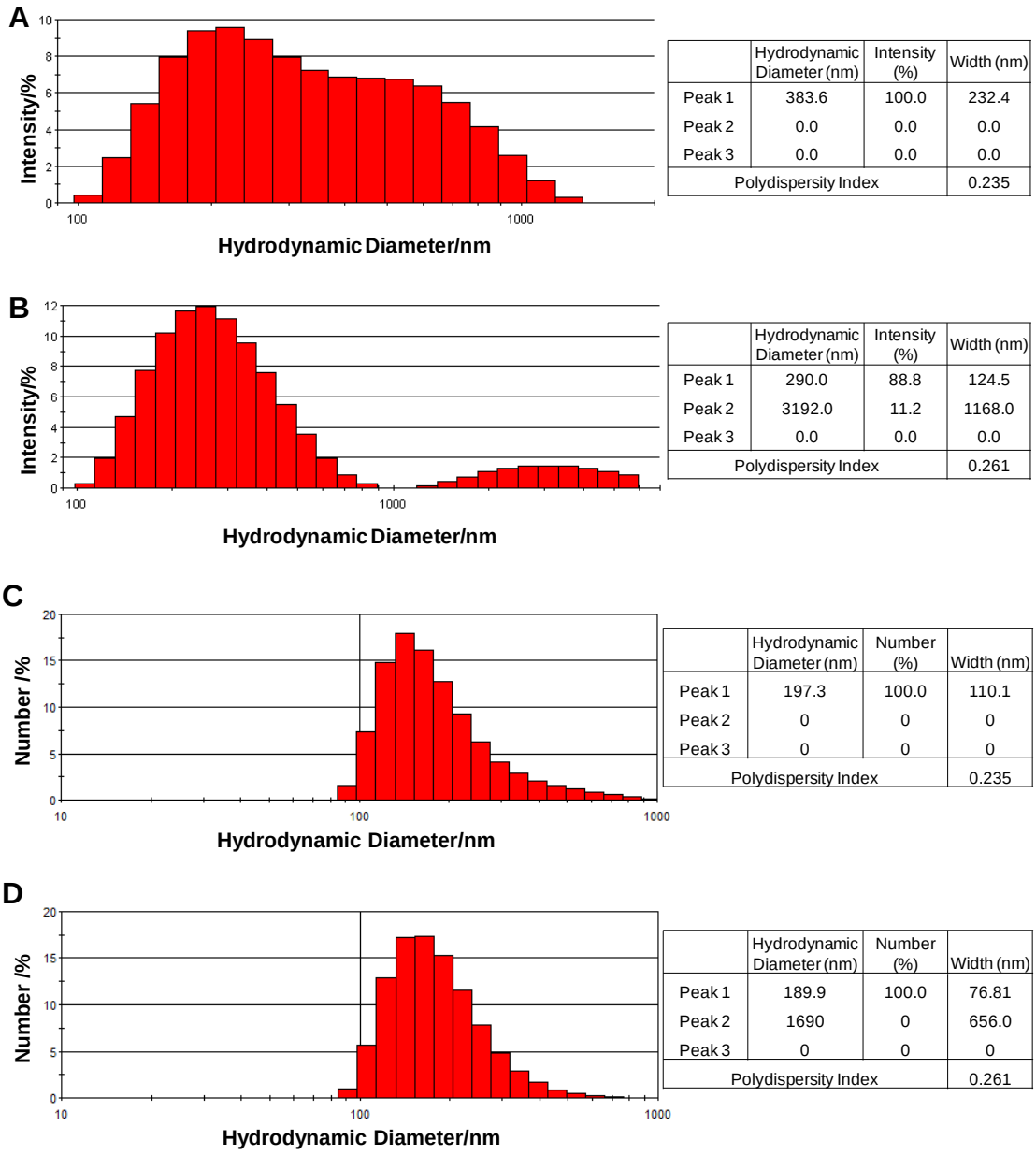

	Hydrodynamic Diameter (nm)	Intensity (%)	Width (nm)
Peak 1	383.6	100.0	232.4
Peak 2	0.0	0.0	0.0
Peak 3	0.0	0.0	0.0
Polydispersity Index			0.235

	Hydrodynamic Diameter (nm)	Intensity (%)	Width (nm)
Peak 1	290.0	88.8	124.5
Peak 2	3192.0	11.2	1168.0
Peak 3	0.0	0.0	0.0
Polydispersity Index			0.261

	Hydrodynamic Diameter (nm)	Number (%)	Width (nm)
Peak 1	197.3	100.0	110.1
Peak 2	0	0	0
Peak 3	0	0	0
Polydispersity Index			0.235

	Hydrodynamic Diameter (nm)	Number (%)	Width (nm)
Peak 1	189.9	100.0	76.81
Peak 2	1690	0	656.0
Peak 3	0	0	0
Polydispersity Index			0.261

Figure 6.12 **A and B) DLS particle size analysis by intensity of a 1% v/v dilution of TiO_2NP.T0MAOH particles TiO_2NP.PAA particles, respectively, in water. C and D) DLS particle size analysis by number of the TiO_2NP.T0MAOH particles TiO_2NP.PAA particles, respectively.**

Although both types of nanoparticles are present in clusters of *ca.* 190-200 nm in diameter, it is apparent that PAA provides the particles with a superior level of colloidal stability than TMAOH. The TEM images of the TiO_2NP.TMAOH and TiO_2NP.PAA particles (**Figure 6.13** (**A** and **B**, respectively)) revealed that both types of particles exist as aggregates that are too large to be effectively used for the SDT treatment of cancer cells.

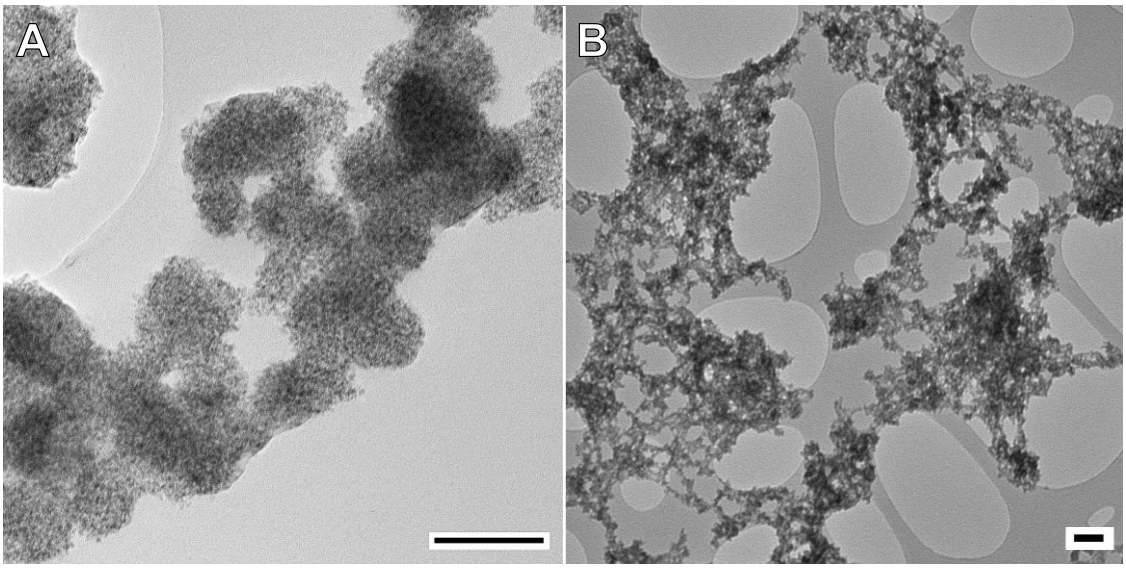

Figure 6.13 TEM images of A) TiO_2NP.TMAOH particles and B) TiO_2NP.PAA particles in water. (Scale bars are 200 nm).

6.2.4 Sonocatalytic singlet oxygen and ·OH generation by TiO_2NP.PAA particles

To explore the potential of singlet oxygen production upon the ultrasound irradiation of water, an aqueous solution of the singlet oxygen probed ADPA (100 μM) was exposed to 15 min of ultrasound irradiation (1 MHz, 0.5W.cm^{-2}), as described in **section 2.4.9**. As can be seen from **Figure 6.14** (**A**), the absorbance intensity of ADPA decreases upon the ultrasound irradiation of water indicating that singlet oxygen was being produced. The stock solution of ADPA used (1.7 mM) was prepared in methanol. Methanol is a known scavenger for ·OH, therefore the observed decay in ADPA absorbance is likely to be due to singlet oxygen production rather than degradation by radicals such as ·OH.[35] In the presence of the TiO_2NP.PAA particles the photobleaching of ADPA was enhanced (**Figure 6.14** (**B**)). The enhanced photobleaching of ADPA in the presence of the particles suggests that the TiO_2NP.PAA sample acts as a sonocatalyst for singlet oxygen production (**Figure 6.14** (**C**)). The photobleaching of ADPA is shown as the decay in absorbance intensity at 400 nm, as the TiO_2NP.PAA sample also contributes to the overall absorption at 400 nm.

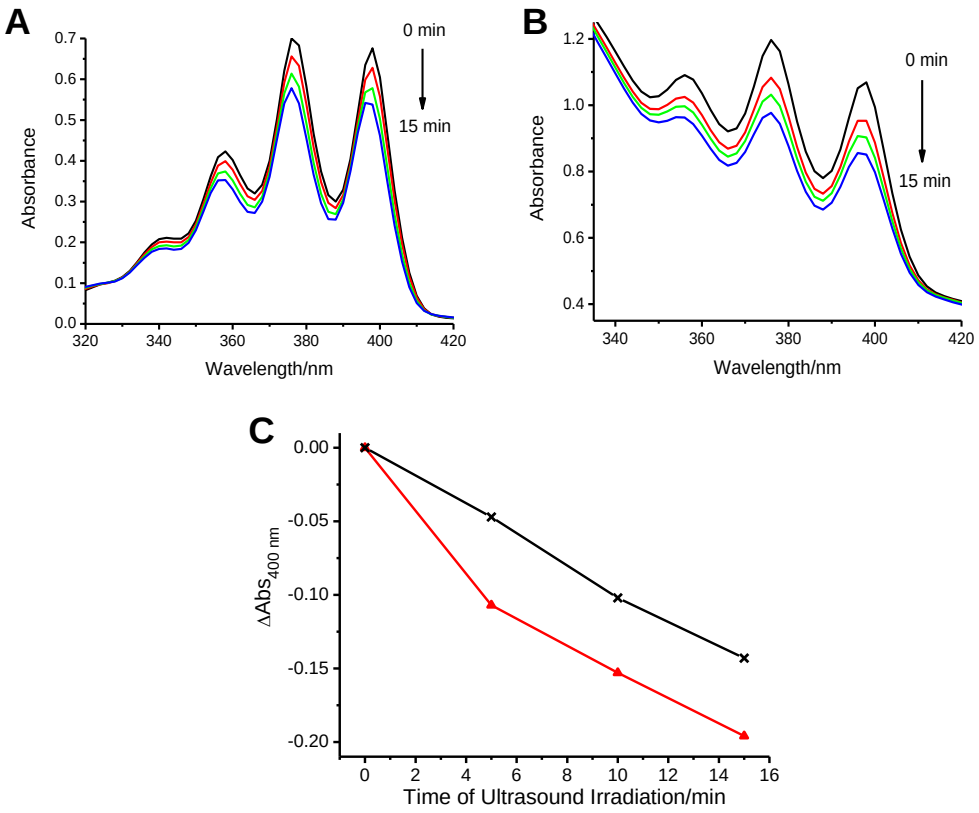

Figure 6.14 **Photobleaching of ADPA (100 µM from 1.7 mM stock in methanol) upon ultrasound irradiation (1 MHz, 0.5 W.cm^{-2}) of A) water or B) a 10% v/v dilution of TiO_2NP.PAA particles in water. C) Photobleaching of ADPA is shown as a decay in the absorbance intensity at 400 nm in the absence (black) or presence (red) of TiO_2NP.PAA particles in water following ultrasound irradiation.**

To confirm that the photobleaching of ADPA was as a result of cavitation bubble collapse in water, and the consequent generation of singlet oxygen, the experiment was repeated in methanol (in the absence of water), as described in **section 2.4.9**. As can be seen from **Figure 6.15,** no decay of ADPA absorption occurs in the absence or presence of the TiO_2NP.PAA particle solutions in methanol (**A** or **B**, respectively). This confirms that the sonochemical photobleaching of ADPA is a process that is dependent on the ultrasonic irradiation of water that can be further enhanced by the presence of the TiO_2NP.PAA particles. **Figure 6.15** (**C**) shows the minimal changes in the ADPA absorbance intensity at 400 nm following ultrasound irradiation in the absence and presence of the TiO_2NP.PAA particles. It is likely that the enhancement in ADPA photobleaching, and therefore singlet oxygen production, is the result of a combination of sonoluminescent activation of the TiO_2NP.PAA particles leading to the photogeneration of ROS, in addition to the increased rate of cavitation at the surface of the particles.

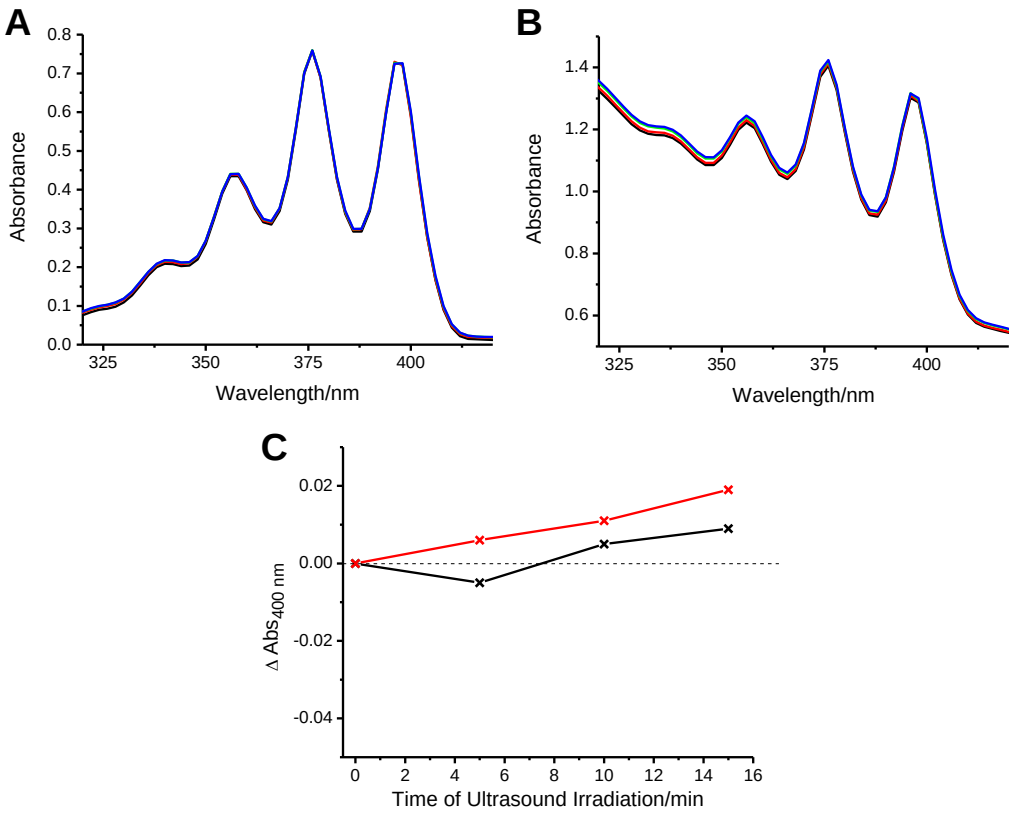

Figure 6.15 **Changes in the UV-visible absorption bands of ADPA (100 µM) upon ultrasound irradiation (1 MHz, 0.5 W.cm^{-2}) of A) methanol or B) a 10% v/v dilution of TiO_2NP.PAA particles in methanol. C) Changes in ADPA absorbance intensity at 400 nm with (red) and without the TiO_2NP.PAA particles (black) in methanol upon ultrasound irradiation.**

To confirm that methanol was acting as a selective scavenger for •OH, and therefore singlet oxygen was responsible for the decay in the absorption of ADPA, two aqueous solutions were prepared each containing both ADPA (100 µM) and methylene blue (10 µM). One of the combined ADPA-methylene blue samples was prepared using a methanol stock solution of ADPA (1.7 mM) and the second sample was prepared using an aqueous stock solution of ADPA (1.7 mM). Both solutions were exposed to 15 min of ultrasound irradiation (1 MHz, 0.5 W.cm^{-2}), as described in **section 2.4.10**. When using a methanol stock solution of ADPA (**Figure 6.16** (**A**)) the absorption of ADPA decreases upon ultrasound exposure, although there is no decay in the absorbance intensity of methylene blue. When using an aqueous stock solution of ADPA (**Figure 6.16** (**B**)) the absorption of both ADPA and methylene blue decreases upon exposure to ultrasound irradiation. This confirms that methanol prevents radical attack of either methylene blue or ADPA, and that the ADPA photobleaching observed is a result of singlet oxygen production.

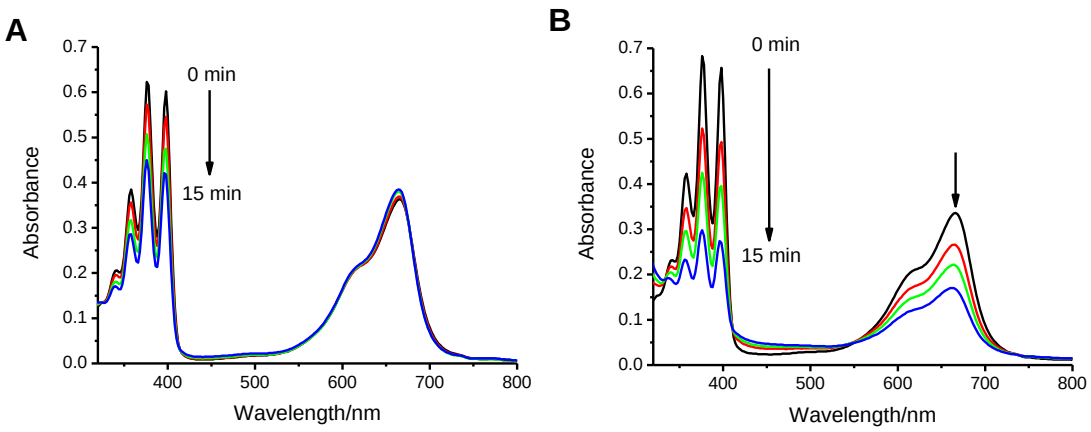

Figure 6.16 **Ultrasound irradiation (1 MHz, 0.5 W.cm^{-2}) of combined solutions containing both ADPA (100 µM) and methylene blue (10 µM) prepared using either A) a methanol stock solution of ADPA or B) an aqueous stock solution of ADPA.**

The enhancement in the sonochemical photobleaching of ADPA by the presence of the TiO_2NP.PAA particles was also investigated using either a methanol or aqueous stock solution of ADPA, as described in **section 2.4.10**. In the absence of methanol, a greater decay in ADPA absorption was observed than when using a methanol stock solution of ADPA (**Figure 6.17**). This difference could be attributed to the small quantity of methanol present (5.88% v/v) when using a methanol stock solution of ADPA to prepare the samples. The presence of methanol could decrease the surface tension of the water, thereby increasing the threshold for acoustic cavitation.[36] In both instances, the TiO_2NP.PAA particles enhanced the photobleaching of ADPA upon ultrasound irradiation showing that the particles contributed to the sonochemical generation of singlet oxygen.

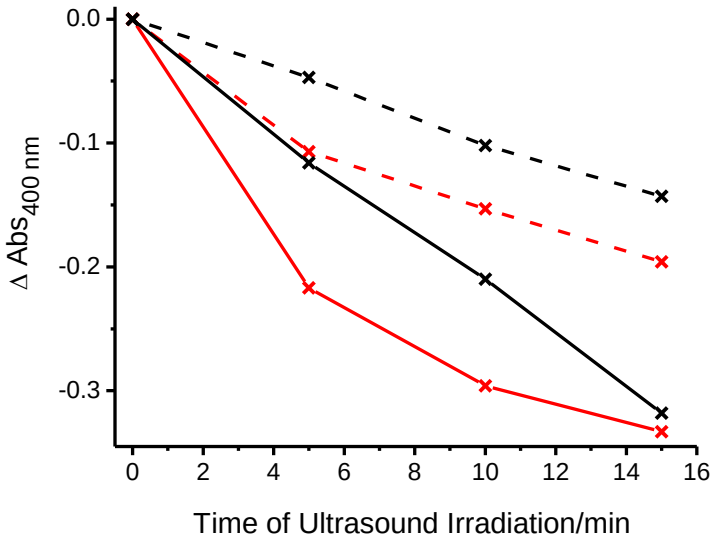

Figure 6.171 **Decay in absorbance intensity at 400 nm following ultrasound irradiation (1 MHz, 0.5 W.cm^{-2}) of an aqueous solution of ADPA (100 µM) prepared using a methanol (dash) or aqueous (line) ADPA stock solution, in the absence (black) or presence (red) of a 10% v/v dilution of TiO_2NP.PAA particles.**

6.2.5 *In situ* synthesis of monodisperse PAA capped TiO_2 nanoparticles

Although it was shown that TiO_2NP.PAA particles can enhance the sonochemical generation of singlet oxygen, the nanoparticles synthesised *in situ* described in **section 6.2.3** were aggregated and had a hydrodynamic diameter of *ca.* 190 nm. The synthesis procedures of TMAOH capped and PAA capped TiO_2 nanoparticles described in **sections 2.4.1** and **2.4.7**, respectively, involve the rapid addition of titanium (IV) butoxide to aqueous solutions of the capping agents. It was thought that the controlled hydrolysis of the titanium (IV) butoxide by the dropwise addition of water would yield non-aggregated, monodisperse nanoparticles. A THF solution of titanium (IV) butoxide and PAA was prepared, as described in **section 2.4.11**. The same molar ratios of titanium (IV) butoxide to PAA used for the *in situ* synthesis of TiO_2NP.PAA particles in **section 6.2.3** were maintained. However the reaction was performed using a 30-fold dilution of all the reactants to enable complete solubilisation of PAA. Water was then added dropwise to gradually initiate the hydrolysis of the titanium (IV) butoxide in the presence of PAA to form dispersed TiO_2 nanoparticles capped with PAA (TiO_2NP.PAA (x/30)). The resultant nanoparticle preparation appeared transparent with no visible sedimentation of nanoparticle aggregates (**Figure 6.18** (**A**)). The TEM image of the TiO_2NP.PAA (x/30)

nanoparticles (**Figure 6.18** (**B**)) shows that the samples were mostly non-aggregated with a mean diameter of 65.67 ± 8.73 nm (mean ± 95% confidence interval; n = 20). However, the resolution of the TEM image was low at the magnification used, possibly due to the presence of unbound PAA. DLS analysis by intensity (**Figure 6.18** (**C**)) reveals the presence of aggregates at 207.9 nm and 477.5 nm. DLS analysis by number (**Figure 6.18** (**D**)) shows that the hydrodynamic diameter of 98% of the nanoparticles was 62.75 nm with a polydispersity index of 0.462, which agrees with the size determined by TEM imaging. However, 1.6% and 0.4% of the sample were found to be aggregates with approximate hydrodynamic diameters of 194.9 nm and 466.2 nm, respectively. These aggregates could eventually be removed by centrifugation or filtration using a 220 nm syringe driven filter unit.

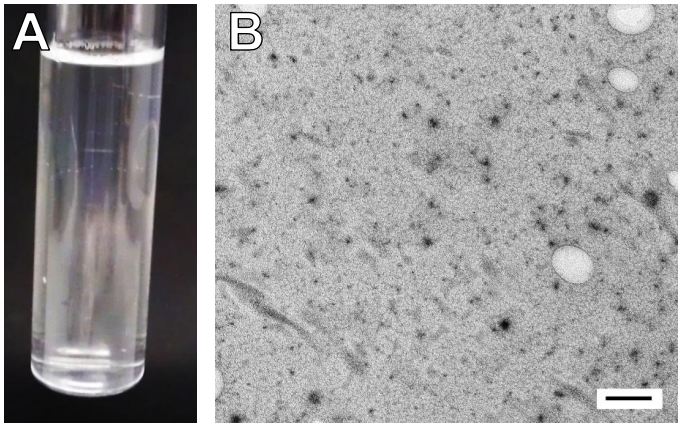

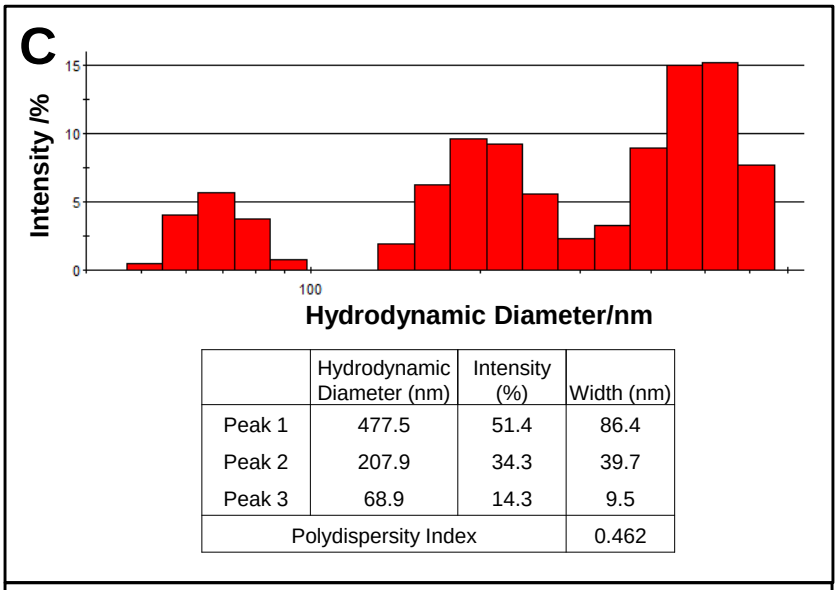

	Hydrodynamic Diameter (nm)	Intensity (%)	Width (nm)
Peak 1	477.5	51.4	86.4
Peak 2	207.9	34.3	39.7
Peak 3	68.9	14.3	9.5
Polydispersity Index			0.462

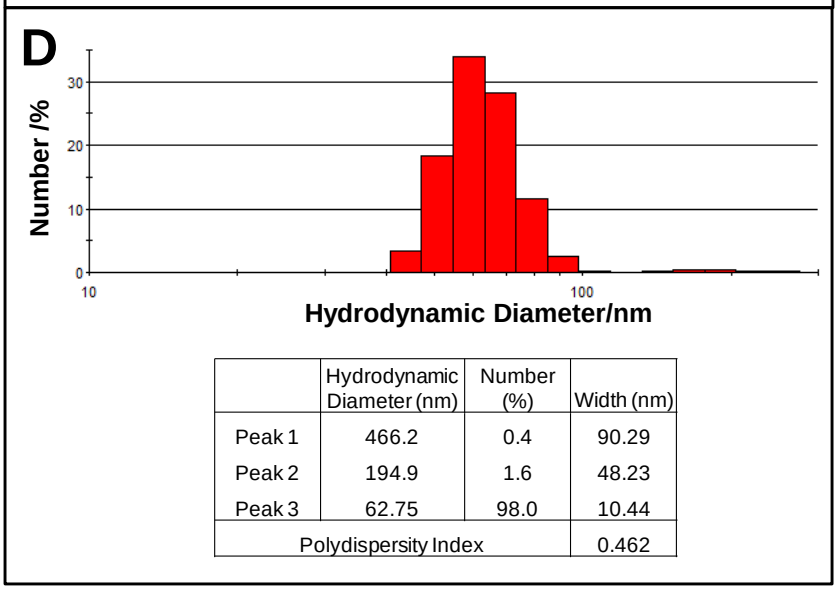

	Hydrodynamic Diameter (nm)	Number (%)	Width (nm)
Peak 1	466.2	0.4	90.29
Peak 2	194.9	1.6	48.23
Peak 3	62.75	98.0	10.44
Polydispersity Index			0.462

Figure 6.18 **A) Photograph, B) TEM image (Scale bar is 500 nm), C) DLS size analysis by intensity and D) DLS size analysis by number of the as-synthesised TiO_2NP.PAA (x/30) nanoparticles in water.**

Removal of unbound PAA (1.8 kDa) was initially attempted by repeated ultrafiltrations using Vivaspin™ 20 tubes with a molecular weight cut-off of 30 kDa, as described in **section 2.4.12**. The UV-visible absorption spectra shown in **Figure 6.19** (**A**) show the absorption profiles of the filtrates of the Vivaspin™ 20 tubes during 5 ultrafiltration cycles. Some free PAA was still observed in the fifth filtrate as determined by the absorbance at *ca.* 217 nm, therefore the nanoparticles were subject to a further 5 cycles of ultrafiltration. However, following the sixth filtration, aggregates of the TiO_2NP.PAA (x/30) nanoparticles were observed. Additionally, the nanoparticles themselves were found in the sixth filtrate, as confirmed by the absorption band centred at *ca.* 270 nm (**Figure 6.19** (**B**)). The particles were not sufficiently stable for the complete removal of unbound PAA using ultrafiltration, therefore an alternative purification procedure was explored.

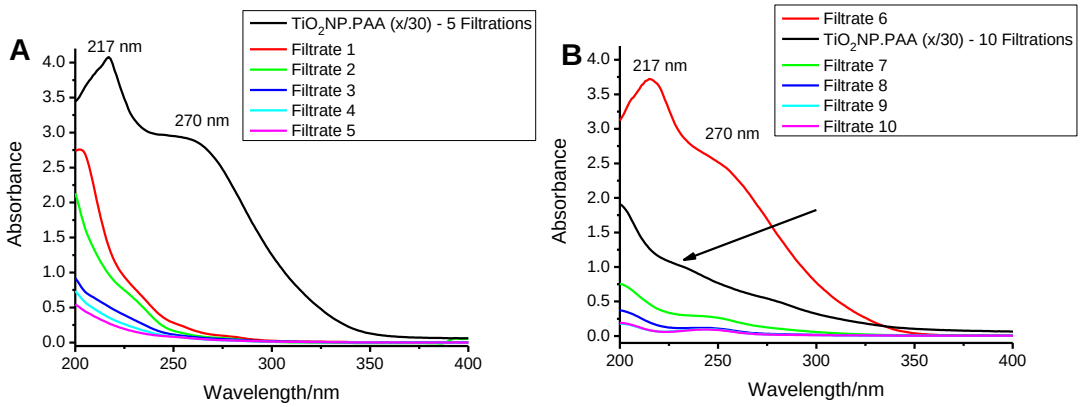

Figure 6.19 **UV-visible absorption spectra of a solution of TiO_2NP.PAA (x/30) nanoparticles during A) 5 ultrafiltrations using a Vivaspin™ 20 (30 kDa MWCO, PES), followed by B) a further 5 ultrafiltrations of TiO_2NP.PAA (x/30). The arrow shown in B highlights the absorption profile of TiO_2NP.PAA (x/30) nanoparticles following 10 cycles of ultrafiltration.**

Removal of free PAA was then attempted by gel filtration chromatography using PD-10 desalting columns, which have a molecular weight cut off of 5 kDa. As synthesised TiO_2NP.PAA (x/30) nanoparticles were concentrated to *ca.* 2.5 ml from *ca* 100 ml, as described in **section 2.4.12**, and loaded onto the PD-10 desalting columns. By monitoring the UV-visible absorption spectra of each eluent, it was apparent that fractions 2, 3 and 4 contained the highest nanoparticle content ($Abs_{270\,nm} \geq 1.5$). Following three cycles of gel filtration chromatography using the PD-10 desalting columns it was apparent that the

separation resolution of the PD-10 columns was too low for the efficient separation of unbound PAA from the TiO_2NP.PAA (x/30) nanoparticles. Both PAA (217 nm, **Figure 6.20** (**A**)) and the TiO_2NP.PAA (x/30) nanoparticles (270nm, **Figure 6.20** (**B**)) were found to be in the same elution fractions in all three cycles of gel filtration.

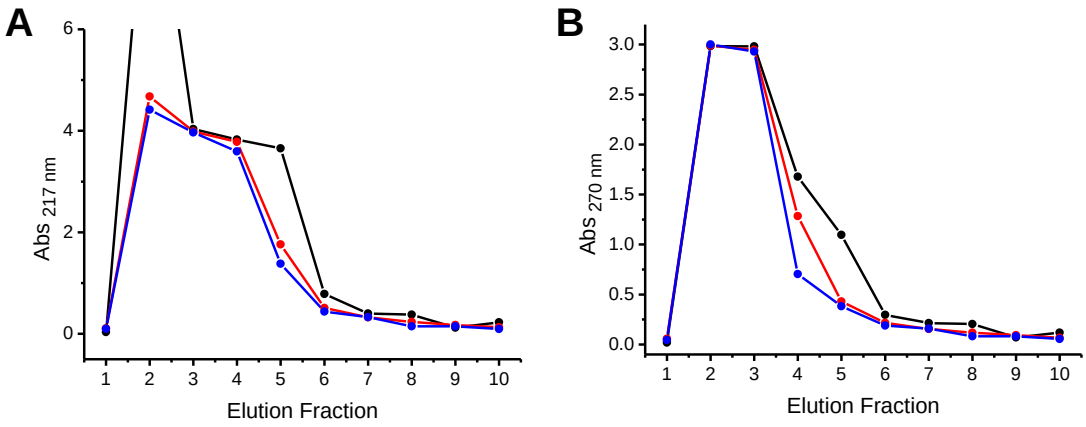

Figure 6.20 **The PAA content (A, 217 nm) and the TiO_2NP.PAA (x/30) nanoparticle content (B, 270 nm) in the elution fractions of the first (black), second (red) and third (blue) cycles of gel filtration using a PD-10 desalting column.**

In order to increase the resolution of separation, Sephadex® G-25 (5 kDa MWCO) was packed into a 300 x 14 mm column and the crude concentrated nanoparticle mixture was loaded onto the Sephadex® G-25 column, as described in **section 2.4.12**. It was thought that the greater separation distance of the 300 x 14 mm Sephadex® G-25 column would enhance the separation efficiency, as compared to the 15 x 14 mm PD-10 desalting column. The graph shown in **Figure 6.21** (**A**) reveals that PAA is retained by the Sephadex® G-25 column for longer than the PD-10 column. **Figure 6.21** (**B**) shows that the nanoparticle content in the elution fractions decreased as the particles were eluted from the column, whilst the PAA content remained high until the end of the first cycle of gel filtration. Elution fractions 4-8 with the highest nanoparticle content ($Abs_{270\ nm} \geq 1.5$) were pooled, concentrated, and loaded onto the Sephadex® G-25 column once more. **Figure 6.21** (**C**) shows that by elution fraction 12 of the second cycle of gel filtration, the absorbance intensity of the PAA (217 nm) and the nanoparticles (270 nm) was similar. The little difference observed between the content of PAA and the nanoparticles suggests that two cycles of gel filtration may be sufficient for the removal of the majority of the unbound PAA from the TiO_2NP.PAA (x/30) nanoparticles.

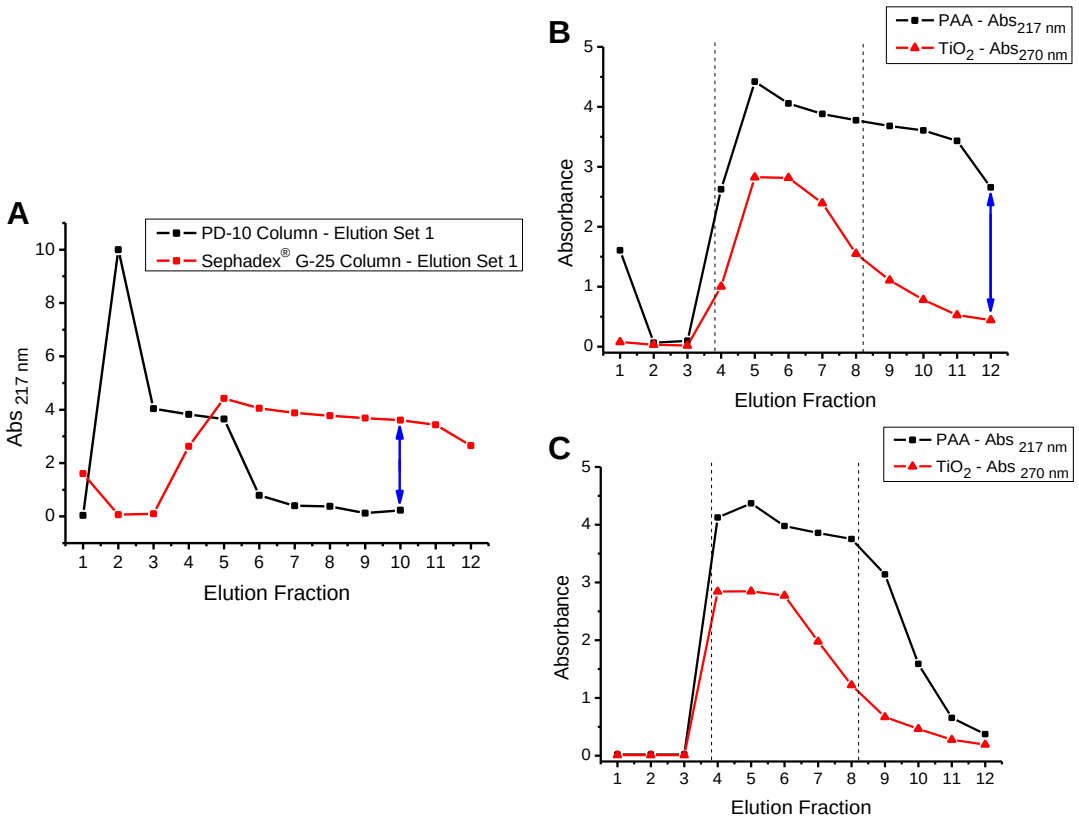

Figure 6.21 **A) Improved retention of PAA on the Sephadex® G-25 column as compared to the PD-10 column, as determined by the absorbance at 217 nm. The nanoparticle content (270 nm) and the PAA content (217 nm) in the 12 elution fractions of first (B) and second (C) cycles of gel filtration are shown. The blue arrows in A) and B) highlight the retention of the PAA on the gel filtration columns.**

To investigate the sonocatalytic enhancement of singlet oxygen generation by the purified TiO_2NP.PAA (x/30) nanoparticles, an aqueous solution of ADPA (100 µM) was exposed to ultrasound irradiation (1 MHz, 0.5 W.cm^{-2}) in the presence of a 10% v/v dilution of the purified nanoparticles (**section 2.4.13**). **Figure 6.22** (**A**) demonstrates the effective photobleaching of an aqueous solution of ADPA following ultrasound irradiation. In the presence of the purified TiO_2NP.PAA (x/30) nanoparticles, the rate of ADPA photobleaching is considerably enhanced (**Figure 6.22** (**B**)). The decay in ADPA absorbance at 400 nm is shown in **Figure 6.22** (**C**) following the sonochemical photobleaching of the probe in the absence and presence of the nanoparticles.

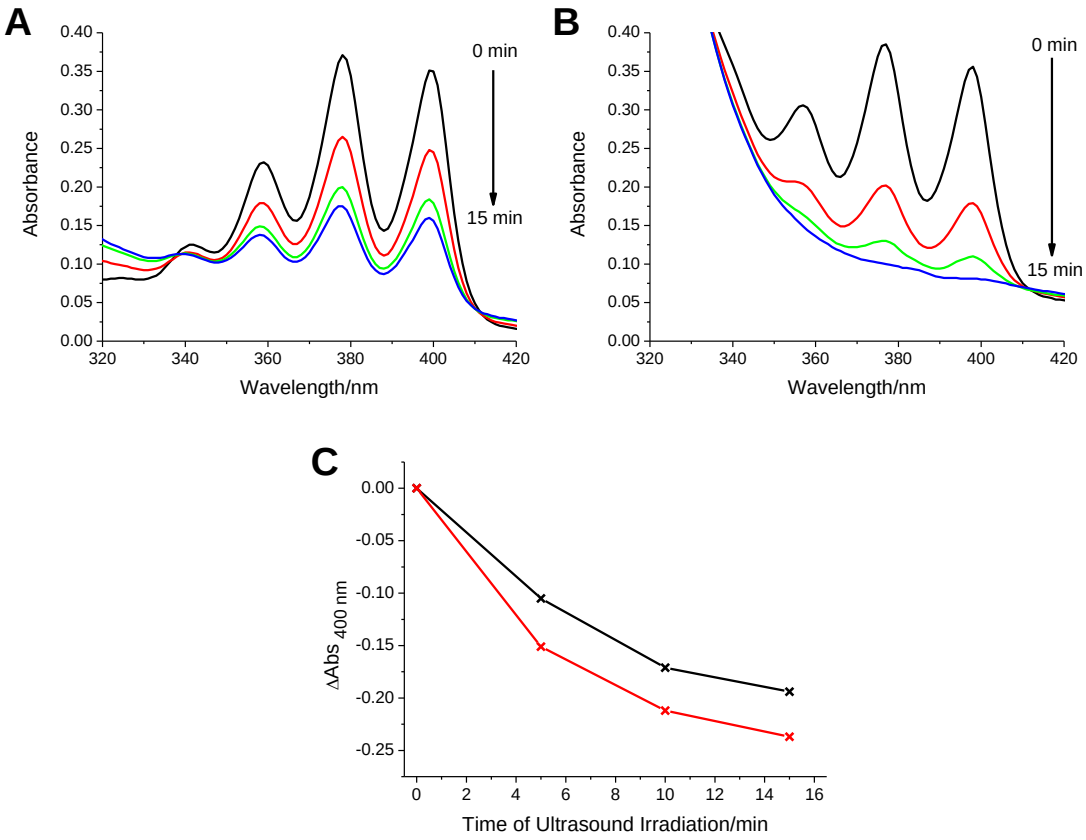

Figure 6.22 **Photobleaching of ADPA (100 µM from 1.7 mM aqueous stock) upon ultrasound irradiation (1 MHz, 0.5 W.cm^{-2}) of A) water or B) a 10% v/v dilution of TiO_2NP.PAA (x/30) nanoparticles in water purified using a Sephadex® G-25 column. C) Photobleaching of ADPA shown as a decay in absorbance intensity at 400 nm in the absence (black) or presence (red) of TiO_2NP.PAA (x/30) nanoparticles in water upon ultrasound irradiation.**

To explore the effect of the presence of the purified TiO_2NP.PAA (x/30) nanoparticles on the sonochemical degradation of methylene blue, an aqueous solution of the dye was exposed to ultrasound irradiation in the absence or presence of a 10% v/v dilution of the purified nanoparticles, as described in **section 2.4.13**. The spectrum of the methylene blue solution containing the nanoparticles shows that the dye is sonochemically degraded during the 15 min of ultrasound irradiation (**Figure 6.23** (**A**)). However, the presence of the particles has an inhibitory effect on the degradation of methylene blue (**Figure 6.23** (**B**)). This could be attributed to the quenching of •OH by the PAA coating on the particle surface.

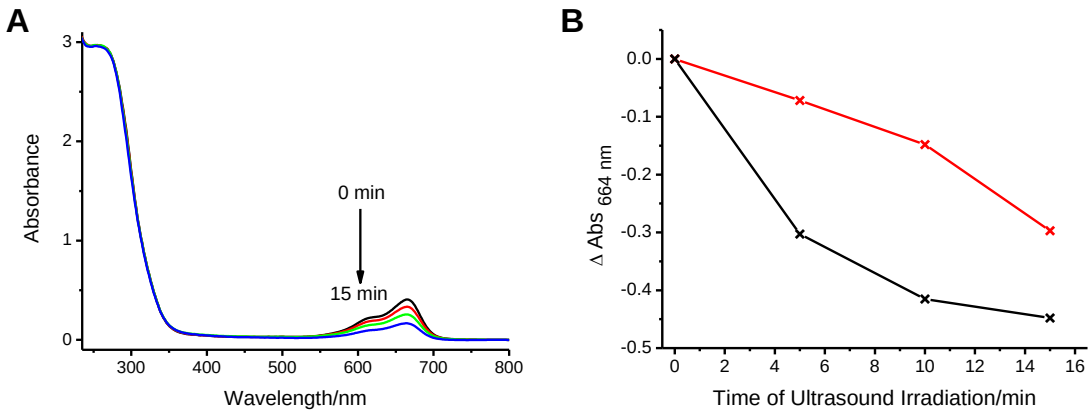

Figure 6.23 **A) UV-visible absorption spectrum of an aqueous solution of methylene blue (10 µM) in the presence of a 10% v/v dilution of the purified TiO_2NP.PAA (x/30) nanoparticles exposed to 15 min ultrasound irradiation (1 MHz, 0.5 W.cm^{-2}). B) Decay in the methylene blue absorbance intensity at 664 nm following the ultrasound irradiation of water in the absence (black) or presence (red) of the nanoparticles.**

Scanning electron microscopy (SEM) was used to investigate the morphology of the purified TiO_2NP.PAA (x/30) nanoparticles, as described in **section 2.4.14**. The images in **Figure 6.24** (**A** and **B**) are secondary electron images, also known as topical contrast images, that analyse the outer surface of the sample. It is clear that following purification, there is still a considerable matrix of PAA embedded with the TiO_2NP.PAA (x/30) nanoparticles. Thus the surface morphology of the nanoparticles cannot be seen. Complete removal of unbound PAA can be attempted using density gradient centrifugation which separates the nanoparticles from the free capping polymer.

The image shown in **Figure 6.24** (**C**) is a secondary electron image of the purified nanoparticles in HEPES buffered saline. Numerous surface spots were visible, which preliminarily appeared to be the nanoparticles. Backscatter electron imaging (chemical contrast imaging) was performed on the nanoparticle sample in HEPES buffered saline (**Figure 6.24** (**D**)). Electron dense materials, such as TiO_2, appear brighter when using backscatter electron imaging. The surface spots observed in **Figure 6.24** (**C**) did not correlate with the regions of high electron density in the backscatter electron image (**Figure 6.24** (**D**)), suggesting that the surface spots were an artefact of the dried buffer. However, the bright regions in **Figure 6.24** (**D**) suggest that the TiO_2NP.PAA (x/30) nanoparticles are embedded within the matrix of dried buffer.

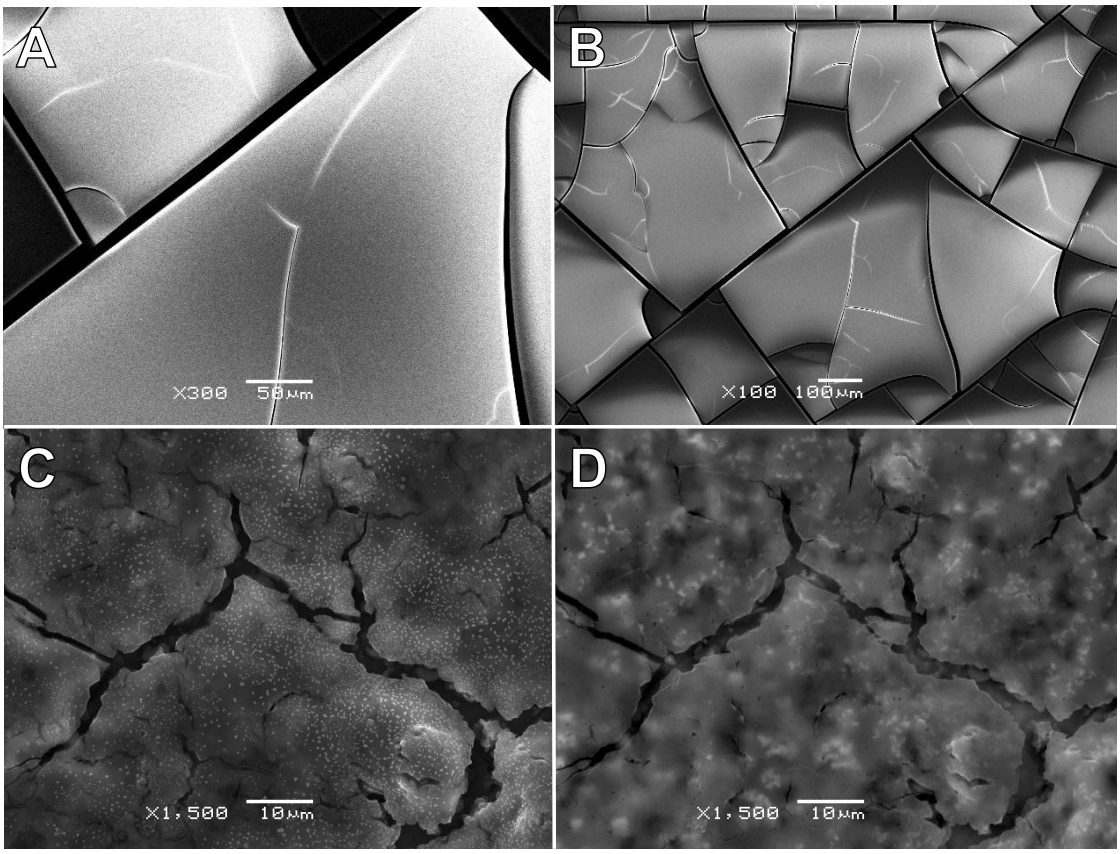

Figure 6.24 **SEM images of the purified TiO_2NP.PAA (x/30) nanoparticles. A and B) are secondary electron images (topical contrast images) of the purified TiO_2NP.PAA (x/30) nanoparticles in water. C) Secondary electron images (topical contrast images) of the purified TiO_2NP.PAA (x/30) nanoparticles in HEPES buffered saline (10 mM, 150 mM NaCl, pH 7.4). D) Backscatter electron images (chemical contrast images) of the nanoparticle sample shown in (C).**

To confirm the presence of TiO_2 within the purified nanoparticle sample, elemental analysis of the purified TiO_2NP.PAA (x/30) nanoparticle sample in water was performed using the Energy Dispersive X-ray Analysis (EDXA) function of the SEM (**Figure 6.25**). The analysis confirmed the strong presence of Ti and C originating from the TiO_2 nanoparticles and the organic PAA capping polymer, respectively. The presence of Au in the EDXA analysis is attributed to the gold coating used in the preparation of the samples prior to SEM imaging.

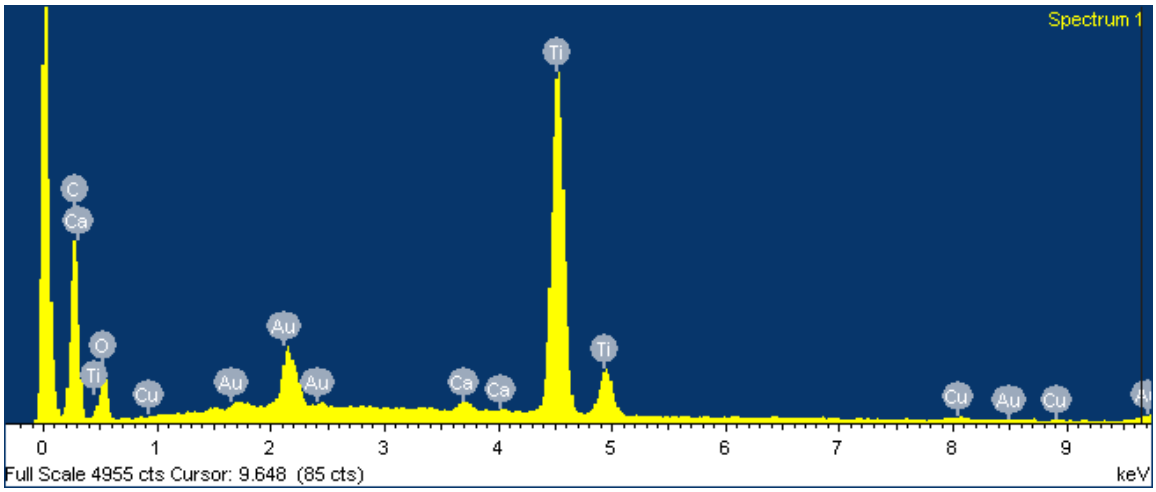

Figure 6.25 **Elemental analysis of a purified sample of TiO_2NP.PAA (x/30) nanoparticles performed using the EDXA function of the SEM microscope.**

The resolution of the TEM images of the unpurified TiO_2NP.PAA (x/30) nanoparticles was low (**Figure 6.18**), as the presence of the excess PAA was likely to impair the focus of the nanoparticles within the TEM imaging grid. TEM imaging was therefore performed on the purified TiO_2NP.PAA (x/30) nanoparticles, as described in **section 2.4.14**. The TEM image in **Figure 6.26** revealed that the nanoparticles remain largely non-aggregated following purification and had a mean diameter of 57.43 ± 11.29 nm (diameter ± 95% confidence interval; n = 20). The nanoparticles were not colloidal, but appeared irregular in morphology with a mixture of cubed, cuboidal and prismal structures. The resolution of the TEM images was vastly improved following purification and removal of the unbound PAA. Nanoparticle deterioration is also shown in **Figure 6.26**, which was observed following prolonged exposure to the electron beam.

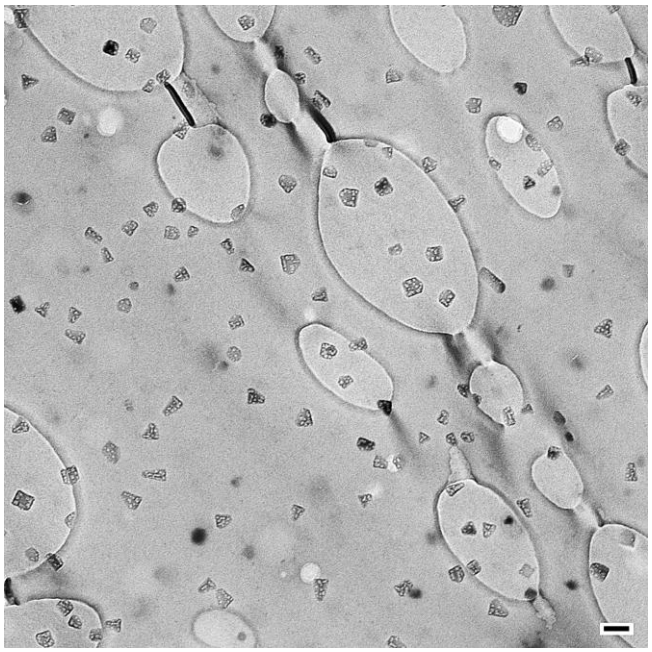

Figure 6.26 **TEM image of a purified sample of TiO_2NP.PAA (x/30) in HEPES buffered saline (10 mM, 150 mM NaCl, pH 7.4). (Scale bar is 100 nm).**

6.2.6 *In vitro* SDT of HT-29 cells using TiO_2 nanoparticles

Prior to exploring the *in vitro* sonodynamic efficacy of the TiO_2 nanoparticles, the tolerance of HT-29 cells to an ultrasonic field was evaluated by exposing the cells to 0, 15, 30 or 60 s of ultrasound irradiation (1 MHz, 0.5 $W.cm^{-2}$). HT-29 cell viability was assessed using the MTT assay following ultrasound irradiation, as described in **section 2.4.15** (**Figure 6.27**). Exposure of the HT-29 cells to 15 s or 30 s of ultrasound irradiation reduced cell viability by *ca.* 8.1%. However, when exposed to 60 s of ultrasound irradiation, a *ca.* 18.4% reduction in viability was observed. It was therefore decided that 30 s of ultrasound exposure would be sufficient, as a previous study observed a significant sonodynamic reduction in C32 melanoma cell viability when incubated with TiO_2 nanoparticles and exposed to 1 MHz ultrasound at 0.5 $W.cm^{-2}$ for 10 s.[25]

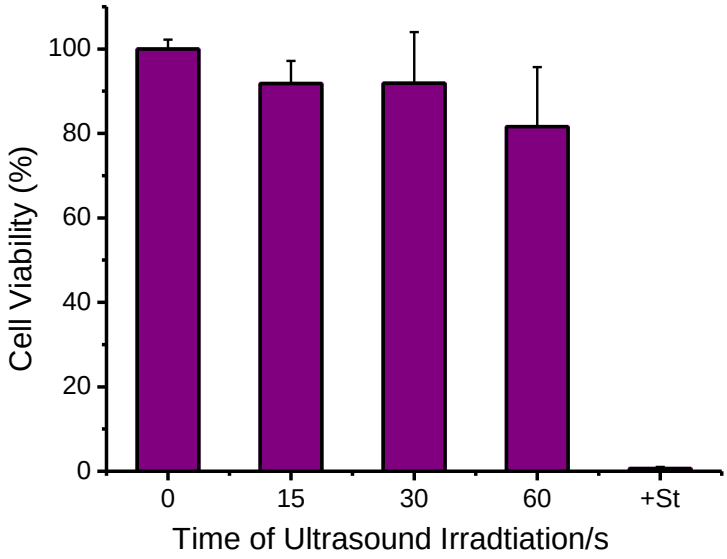

Figure 6.27 **MTT viability assay following the ultrasound irradiation (1 MHz, 0.5 W.cm^{-2}) of HT-29 cells in 6 well multidishes for a duration of 15, 30 and 60 s. The cells were kept in RPMI 1640 medium supplemented with 1.5 mM L-glutamine (L-Gln) and 10% foetal bovine serum (FBS). +St refers to incubation with 2 µM Staurosporine, which was used as a positive control for cytotoxicity. (Error bars are ± 95% confidence intervals).**

The attenuation of ultrasound frequency by different sizes of multidishes was examined using solutions of ADPA in RPMI 1640 medium, supplemented with 1.5 mM L-Gln and 10% FBS, as described in **section 2.4.16**. **Figure 6.28** shows that ADPA photobleaching following 15 min ultrasound irradiation was significantly enhanced when a 48 well multidish was used rather than a 6 well multidish. Therefore, the 48 well multidishes were used for the subsequent *in vitro* SDT treatment of the HT-29 cells. This difference in ADPA photobleaching could be due to the difference in depth of the medium within the wells exposed to the ultrasound, which is significantly greater when using the 48 well multidishes. A greater depth of the irradiated RPMI medium resulted in the exposure of a greater proportion of the medium to the ultrasonic field, which lead to an observable increase in microbubble formation and consequent ADPA photobleaching.

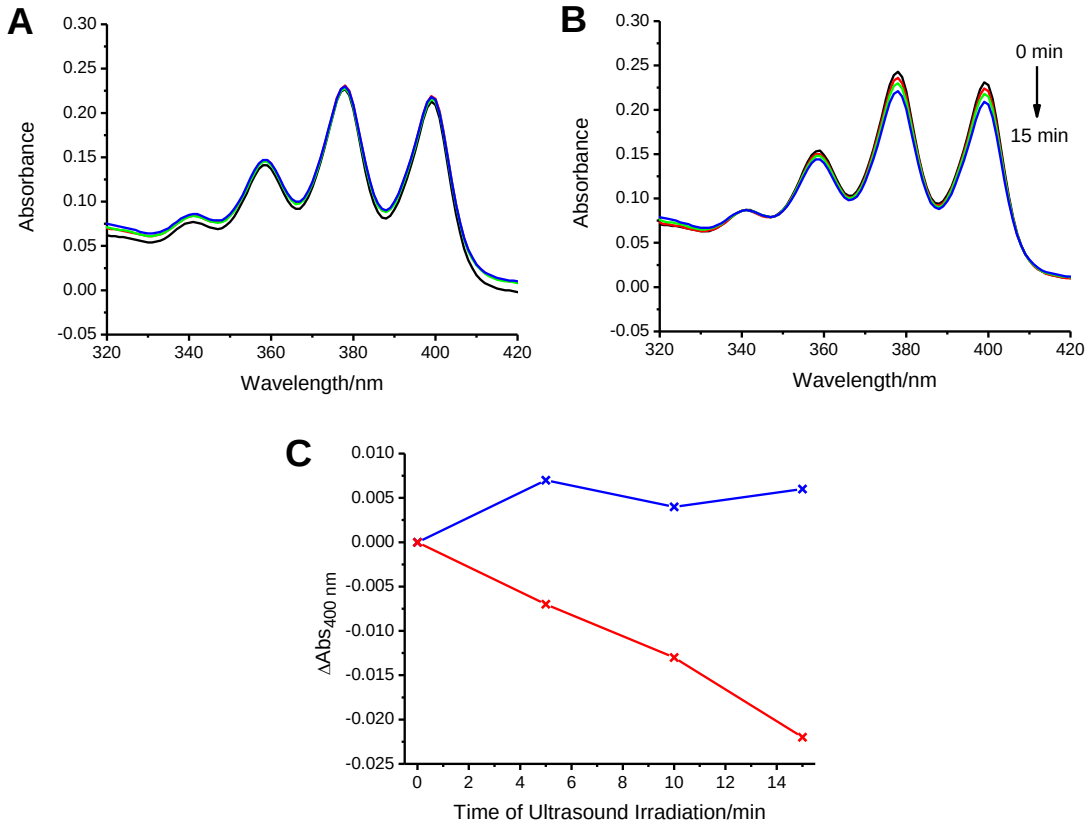

Figure 6.28 **Comparison of the attenuation of ultrasound frequency through A) 6 well and B) 48 well multidishes following 15 min ultrasound irradiation (1 MHz, 0.5 W.cm^{-2}) of ADPA (100 µM) in RPMI 1640 medium supplemented with 1.5 mM L-Gln and 10% FBS. C) The photobleaching of ADPA in 6 well (blue) or 48 well (red) multidishes is shown as a decay in absorbance intensity at 400 nm.**

HT-29 cells seeded onto 48 well multidishes were incubated with 0.29, 0.74 and 1.47 mM TiO_2 equivalent of purified TiO_2NP.PAA (x/30) nanoparticles and exposed to 30 s of ultrasound irradiation (1 MHz, 0.5 W.cm^{-2}), as described in **section 2.4.17**. The approximate concentrations of TiO_2 equivalent were calculated based on the assumption that all the titanium (IV) butoxide reacted during the synthesis. This assumption was made based on the fact that the water (5.56 moles) was present in a substantial molar excess of the titanium (IV) butoxide (3.53×10^{-5} moles) during the hydrolysis stage. Typically, the concentration of TiO_2 nanoparticles could be determined using the extinction coefficient of the particles. However, the extinction coefficient of TiO_2 nanoparticles is dependent on the particle diameter and the dispersity of the particles is critical. As the TiO_2NP.PAA (x/30) nanoparticle samples prepared in this chapter contain a

small proportion of aggregates, the determination of nanoparticle concentration using UV-visible absorption spectrophotometry would be unreliable. To accurately evaluate the concentration of TiO_2 present within the nanoparticle preparations elemental analysis of the titanium in the nanoparticle solutions can be quantified using ICP-OES analysis.

The results of the MTT viability assay in **Figure 6.29** show that in the absence of nanoparticles, cell viability is reduced to *ca.* 74% following ultrasound irradiation. The decrease in cell viability can be attributed to a combination of sonodynamic ROS generation and shear mechanical stresses. A dose-dependent cytotoxicity of the HT-29 cells was observed with increasing concentrations of the TiO_2NP.PAA (x/30) nanoparticles, both with and without ultrasound irradiation. When incubated with 0.29, 0.74 and 1.47 mM TiO_2 equivalent of nanoparticles without ultrasound irradiation, viability is reduced to *ca.* 91%, 73% and 58%, respectively. Following ultrasound exposure, cell viability of HT-29 cells incubated with 0.29, 0.74 and 1.47 mM TiO_2 equivalent of nanoparticles was at *ca.* 94%, 76% and 63%, respectively. Therefore, it was suggested that the reduction in viability was the direct result of nanoparticle toxicity. These findings suggest that the incubation of the TiO_2NP.PAA (x/30) nanoparticles with the HT-29 cancer cells followed by the removal of unbound or non-internalised particles is ineffective at inducing sonodynamic cytotoxicity. The degree of association or internalisation of the nanoparticles by the HT-29 cells is unknown; therefore conclusions regarding the efficiency of intracellular SDT cannot be made. Findings of a previously reported study suggest that the extracellular localisation of a porphyrin photo/sonosensitiser (ATX-70) is critical for sonodynamic cell death.[37] This dependence on extracellular sonosensitisation is likely to be due to the lack of evidence for intracellular acoustic cavitation required for intracellular sonodynamic activation of sonosensitisers.[12] Therefore, it is possible that an enhancement in the ultrasound induced cytotoxicity could be observed if the cells were exposed to ultrasound irradiation without the removal of the TiO_2 nanoparticles present extracellularly.[37]

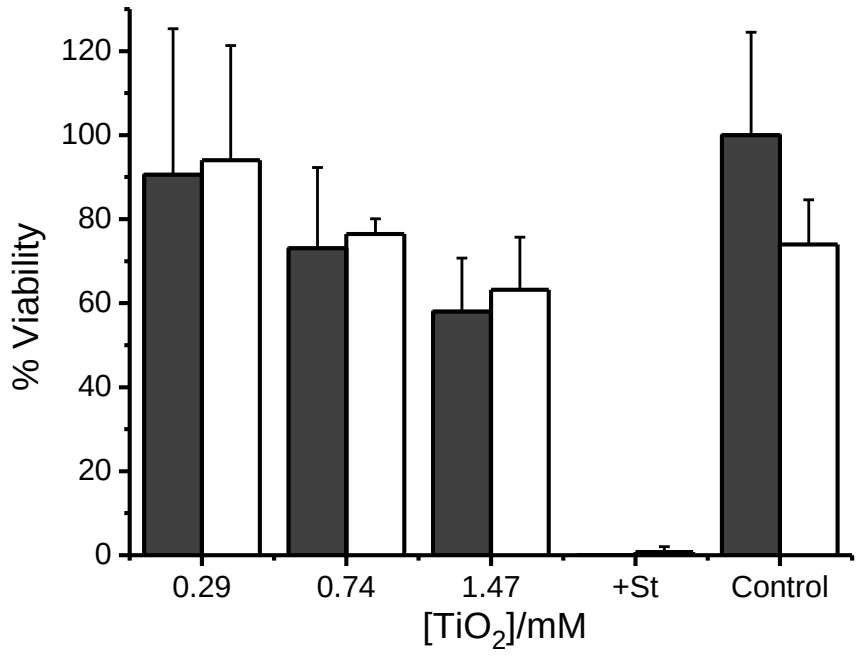

Figure 6.29 **MTT viability assay of HT-29 cells following SDT treatment using 0.29, 0.74 and 1.47 mM TiO_2 equivalent of TiO_2NP.PAA (x/30) nanoparticles. The cells were either irradiated with 30 s of ultrasound (1 MHz, 0.5 W.cm^{-2}; white) or non-irradiated (black). +St refers to incubation with 2 µM Staurosporine, which was used as a positive control for cytotoxicity. Cells not incubated with nanoparticles irradiated with 30 s of ultrasound (1 MHz, 0.5 W.cm^{-2}) were used as a control. (Error bars are ± 95% confidence intervals).**

6.3 Conclusions

In this chapter, the successful synthesis of colloidally stable TiO_2 nanoparticles capped with PAA was described. Initially the TiO_2 nanoparticles capped with TMAOH were synthesised and the thermal surface annealing of PAA in DMF was performed. Removal of the DMF and the unbound PAA was attempted, but recovery of dispersed nanoparticles was unsuccessful. Using an adapted version of a previously reported protocol,[34] PAA capped TiO_2 nanoparticles were synthesised *in situ* through the controlled hydrolysis of titanium (IV) butoxide in the presence of the capping polymer. The resultant nanoparticles appeared largely monodisperse and had a mean diameter of *ca.* 57 nm, as determined by TEM imaging and DLS size analysis. Elemental analysis using the EDXA function of the SEM microscope also confirmed the presence of titanium within the purified nanoparticle preparations.

The effect of ultrasound irradiation (1 MHz) on water was investigated using the singlet oxygen molecular probe ADPA and the dye methylene blue. Methylene blue has been previously shown to degrade in aqueous solutions exposed to ultrasound irradiation through sonochemically generated ·OH species.[33] It was shown that the sonochemical degradation of methylene blue is completely inhibited by the presence of 5.88% v/v methanol, a known scavenger for ·OH. The presence of the TiO_2 nanoparticles strongly inhibited the degradation of methylene blue, possibly due to ·OH quenching by the PAA coating. The predominant ROS species produced by the photoexcitation of TiO_2 nanoparticles are H_2O_2, $\cdot O_2^-$ and ·OH.[19] To maximise the therapeutic outcome of sonodynamic TiO_2 activation, the use of an alternative capping agent that doesn't quench ·OH species, yet retains the capacity for biofunctionalisation, could be explored.

ADPA was used to detect sonochemically generated singlet oxygen, which has been observed in air saturated solutions exposed to ultrasound.[5] The degradation of ADPA by sonochemically generated ·OH was not likely as the sonochemical decay of the ADPA absorbance intensity occurred even in the presence of the ·OH scavenger, methanol. The presence of the TiO_2 nanoparticles enhanced the photobleaching of ADPA during ultrasound irradiation, both in the absence and presence of 5.88% v/v methanol. The findings described herein suggest that the TiO_2 nanoparticles stabilised with PAA can effectively enhance the generation of singlet oxygen upon ultrasound irradiation, as confirmed by the photobleaching of the singlet oxygen molecular probe ADPA. Conversely, the presence of the nanoparticles prevents ultrasound induced ·OH degradation of methylene blue, possibly through quenching of the radical by the PAA coating. Methylene blue has been reported to electrostatically adsorb onto PAA coated nanoparticles, suggesting that the capping polymer plays a protective role against radical degradation of the dye.[38]

HT-29 colon adenocarcinoma cells exhibited a *ca.* 26% reduction in viability following 30 s of ultrasound irradiation (1 MHz, 0.5W.cm^{-2}). The ultrasound irradiation of the cells incubated with *ca.* 0.29, 0.74 and 1.47 mM TiO_2 equivalent of TiO_2NP.PAA (x/30) nanoparticles showed no significant enhancement in sonodynamic cytotoxicity, as compared to the cells not exposed to ultrasound irradiation. Incubation of the HT-29 cells with the nanoparticles, without exposure to ultrasound, resulted in a noticeable dose-dependent decrease in cell viability (*ca.* 9-42% reduction). Although no *in vitro* sonodynamic effect on the HT-29 cells was observed with the TiO_2 nanoparticles, further investigations into the association or internalisation of the nanoparticles within the 3 h

incubation period should be performed. Furthermore, the cells were washed to remove unbound nanoparticles prior to ultrasound irradiation and therefore no extracellular particles were present during the exposure of the cells to ultrasound. Reports on SDT suggest that acoustic cavitation occurs extracellularly, and that the extracellular presence of the sonosensitiser is critical for effective sonodynamic toxicity.[12,37]

In conclusion, the synthesis and characterisation of monodisperse TiO_2 nanoparticles coated with a biocompatible polymer, PAA, is described. Multiple carboxylic acid groups provide the nanoparticles with electrostatic stability, in addition to the potential of further biofunctionalisation. Ultrasound exposure of aqueous solutions of the nanoparticles appears to enhance the sonochemical generation of singlet oxygen, whilst inhibiting sonochemically produced $^{\bullet}OH$ species. The *in vitro* SDT treatment of HT-29 cells incubated with the TiO_2 nanoparticles showed no sonodynamic effect at the conditions of the experiment described. Further investigations of extracellular SDT could provide results that are consistent with those reported. Sonodynamic therapy using TiO_2 nanoparticles and ultrasound waves with optimal tissue penetration could prove to be invaluable for the treatment of solid tumours where visible or near-infrared light cannot typically reach during PDT treatment. Furthermore, bioconjugated TiO_2 nanoparticles could provide enhanced tumour selectivity for the sonodynamic destruction of cancerous tissue.

6.4 References

1. Mason, T. J.; Lorimer, J. P. *Sonochemistry: theory, applications and uses of ultrasound in chemistry*; Ellis Horwood, **1988**.
2. Ortiz, S. H. C.; Chiu, T.; Fox, M. D. *Biomed. Signal Proces.* **2012**, *7*, 419-428.
3. Duck, F. A.; Baker, A. C.; Francis A. Duck, A. C. B. H. C. S. *Ultrasound in Medicine*; CRC Press, **1998**.
4. Kennedy, J. E.; Ter Haar, G. R.; Cranston, D. *Br. J. Radiol.* **2003**, *76*, 590-599.
5. Davidson, R. S.; Safdar, A.; Spencer, J. D.; Robinson, B. *Ultrasonics* **1987**, *25*, 35-39.
6. Riesz, P.; Berdahl, D.; Christman, C. L. *Environ. Health Perspect.* **1985**, *64*, 233-252.
7. Sehgal, C.; Sutherland, R. G.; Verrall, R. E. *J. Phys. Chem.* **1980**, *84*, 388-395.
8. Suslick, K. S. *MRS Bull.* **1995**, *20*, 29-34.
9. Harvey, E. N. *J. Am. Chem. Soc.* **1939**, *61*, 2392-2398.
10. Suslick, K. S. *Proc. - IEEE Ultrason. Symp.* **1997**, 523-532.
11. Weissler, A. *J. Am. Chem. Soc.* **1959**, *81*, 1077-1081.
12. Rosenthal, I.; Sostaric, J. Z.; Riesz, P. *Ultrason. Sonochem.* **2004**, *11*, 349-363.
13. Liu, Q. H.; Wang, X. B.; Wang, P.; Xiao, L. N.; Hao, Q. *Cancer Chemother. Pharmacol.* **2007**, *60*, 671-680.
14. Liu, Q. H.; Li, X. Y.; Xiao, L. N.; Wang, P.; Wang, X. B.; Tang, W. *Ultrason. Sonochem.* **2008**, *15*, 943-948.
15. Dai, S. C.; Hu, S. S.; Wu, C. J. *Acta Neurochir.* **2009**, *151*, 1655-1661.
16. Tomankova, K.; Kolarova, H.; Kolar, P.; Kejlova, K.; Jirova, D. *Toxicol. In Vitro* **2009**, *23*, 1465-1471.
17. Chen, B.; Zheng, R.; Liu, D.; Li, B.; Lin, J.; Zhang, W. *Ultrason. Sonochem.* **2012**, *20*, 667–673.
18. Nomikou, N.; Sterrett, C.; Arthur, C.; McCaughan, B.; Callan, J. F.; McHale, A. P. *ChemMedChem* **2012**, *7*, 1465-1471.
19. Chen, X.; Mao, S. S. *Chem. Rev.* **2007**, *107*, 2891-2959.
20. Janczyk, A.; Krakowska, E.; Stochel, G.; Macyk, W. *J. Am. Chem. Soc.* **2006**, *128*, 15574-15575.
21. Crum, L. A. *Nature* **1979**, *278*, 148-149.
22. Borkent, B. M.; Arora, M.; Ohl, C. D. *J. Acoust. Soc. Am.* **2007**, *121*, 1406-1412.
23. Stride, E. P.; Coussios, C. C. *Proc. Inst. Mech. Eng., Part H* **2010**, *224*, 171-191.
24. Ogino, C.; Shibata, N.; Sasai, R.; Takaki, K.; Miyachi, Y.; Kuroda, S.; Ninomiya, K.; Shimizu, N. *Bioorg. Med. Chem. Lett.* **2010**, *20*, 5320-5325.

25. Harada, Y.; Ogawa, K.; Irie, Y.; Endo, H.; Feril, L. B.; Uemura, T.; Tachibana, K. *J. Controlled Release* **2011**, *149*, 190-195.
26. Yamaguchi, S.; Kobayashi, H.; Narita, T.; Kanehira, K.; Sonezaki, S.; Kudo, N.; Kubota, Y.; Terasaka, S.; Houkin, K. *Ultrason. Sonochem.* **2011**, *18*, 1197-1204.
27. Chemseddine, A.; Moritz, T. *Eur. J. Inorg. Chem.* **1999**, *1999*, 235-245.
28. Kanehira, K.; Banzai, T.; Ogino, C.; Shimizu, N.; Kubota, Y.; Sonezaki, S. *Colloids Surf., B* **2008**, *64*, 10-15.
29. Reddy, K. M.; Reddy, C. V. G.; Manorama, S. V. *J. Solid State Chem.* **2001**, *158*, 180-186.
30. King, M.; Kopelman, R. *Sens. Actuators, B* **2003**, *90*, 76-81.
31. Matthews, R. W. *Water Res.* **1991**, *25*, 1169-1176.
32. Satoh, A. Y.; Trosko, J. E.; Masten, S. J. *Environ. Sci. Technol.* **2007**, *41*, 2881-2887.
33. Shimizu, N.; Ogino, C.; Dadjour, M. F.; Murata, T. *Ultrason. Sonochem.* **2007**, *14*, 184-190.
34. Chen, H. J.; Jian, P. C.; Chen, J. H.; Wang, L.; Chiu, W. Y. *Ceram. Int.* **2007**, *33*, 643-653.
35. Monod, A.; Chebbi, A.; Durand-Jolibois, R.; Carlier, P. *Atmos. Environ.* **2000**, *34*, 5283-5294.
36. Iwai, Y.; Li, S. C. *Wear* **2003**, *254*, 1-9.
37. Miyoshi, N.; Misik, V.; Riesz, P. *Radiat. Res.* **1997**, *148*, 43-47.
38. Mak, S. Y.; Chen, D. H. *Dyes Pigm.* **2004**, *61*, 93-98.

Chapter 7

Conclusions and Future Work

This thesis describes the use of biofunctionalised nanoparticles for the targeted photodynamic therapy of cancer. The conclusions of the investigations into the efficacy of lectins as cancer-specific targeting agents for PDT using phthalocyanine-PEG gold nanoparticles are summarised in this chapter. Additionally, the findings of the comparative study using lectins and antibodies as targeting ligands are outlined. Furthermore, the potential use of titanium dioxide nanoparticles for sonodynamic cancer therapy is discussed. Suggestions for future work are highlighted.

7.1 Con A targeted PDT – proof-of-concept

In **Chapter 3** citrate capped gold nanoparticles, *ca.* 16 nm in diameter, were functionalised with the lectin Concanavalin A (Con A) and its dimeric derivative succinyl-Concanavalin A (S-Con A) for the colorimetric labelling of breast cancer cells. Conjugation of the lectins to the nanoparticles was initially achieved using the heterobifunctional linker 3-(2-pyridyldithio)propionic acid *N*-hydroxysuccinimide ester (SPDP). The stability of the nanoparticle conjugates during a 1 h incubation period with the MCF-7 and SK-BR-3 human breast adenocarcinoma cells at 37 °C was found to be dependent on the type of lectin. Using a nanoparticle concentration of 8.46 nM, the Con A functionalised nanoparticles were shown to be significantly less stable than the S-Con A functionalised particles, which showed no signs of aggregation. Additionally, the concentration of the nanoparticle conjugates used also had a direct impact on the stability of the particles. At lower nanoparticle concentrations of 0.25, 0.50 or 1.00 nM, 1 h incubation of the Con A functionalised nanoparticles with the MCF-7 cells at 37 °C did not result in particle aggregation. Overall, the nanoparticles conjugated to Con A or S-Con A through the SPDP linker were unable to successfully label the MCF-7 or SK-BR-3 cells.

To prevent nanoparticle aggregation, citrate capped gold nanoparticles were modified using a heterobifunctional polyethylene glycol linker (PEG). Conjugation of the lectins to the PEG modified gold nanoparticles was then achieved using covalent amide coupling. During a 24 h incubation period with the MCF-7 cells at 37 °C the Con A functionalised PEG

modified nanoparticles (0.25, 0.50 or 1.00 nM) were remarkably stable. The exceptional colloidal stability of the lectin-PEG gold nanoparticle conjugates demonstrated the importance of the PEG modification of gold nanoparticles for use in cell-based assays at physiological conditions. However, the Con A functionalised PEG gold nanoparticles were not able to colorimetrically label the MCF-7 breast cancer cells, possibly due to the lack of sensitivity of the inverted optical microscopy technique.

By using a formazan-based colorimetric cytoadhesion assay, the binding efficiency of MCF-7 cells to Con A adsorbed onto the wells of a 96 well multidish was found to be approximately 2-fold higher than to the S-Con A derivatised wells. MCF-7 cell binding to the sheep serum albumin (SSA) control wells was significantly lower than that to the Con A or S-Con A derivatised wells, thus suggesting that cell binding to the lectins was due to specific cell glycan recognition. Since the MCF-7 cells bound to the Con A with a significantly higher binding efficiency, Con A was selected as a cancer targeting ligand to deliver gold nanoparticles carrying the zinc phthalocyanine photosensitiser, C11Pc, for the targeted PDT treatment of breast cancer cells.

Gold nanoparticles, *ca.* 4 nm in diameter, were functionalised with the hydrophobic C11Pc photosensitiser and amphiphilic PEG derivative molecules as previously reported.[1] The method was further adapted to covalently conjugate Con A to the C11Pc-PEG gold nanoparticles. By using the singlet oxygen molecular probe, anthracene-9,10-dipropionic acid disodium salt (ADPA), the nanoparticles were shown to effectively produce singlet oxygen both with and without Con A conjugation upon irradiation at 633 nm. MCF-7 and SK-BR-3 human breast cancer cells were used to investigate the targeted PDT efficacy of Con A conjugated C11Pc-PEG gold nanoparticles. Following a 24 h incubation period of the MCF-7 cells with the nanoparticle conjugates (0.00-1.44 μM C11Pc equivalent) and 10 min irradiation at 633 nm, the colorimetric MTT viability assay revealed that Con A conjugation provided no enhancement in the phototoxicity of the MCF-7 cells, as compared to the non-conjugated nanoparticles. The fluorometric CellTiter-Blue™ viability assay was utilised to assess the viability of SK-BR-3 cells following Con A targeted PDT treatment, as the solublisation step required during the MTT assay resulted in a noticeable variation in the results. However, no significant enhancement in phototoxicity of the SK-BR-3 cells was observed, as compared to the non-conjugated particles. Con A was found to be unsuitable as a targeting ligand to selectively deliver C11Pc-PEG gold nanoparticles to the MCF-7 or SK-BR-3 breast cancer cells. However, an effective methodology was established through which potentially any lectin could be covalently conjugated to

nanoparticles carrying C11Pc and PEG molecules to generate singlet oxygen, and hence potentially induce cytotoxicity, upon irradiation at 633 nm. The revised nanoparticle synthetic method described in **Chapter 4** yielded C11Pc-PEG gold nanoparticles with a higher C11Pc loading efficiency. It is possible that Con A conjugation to the C11Pc-PEG gold nanoparticles with a higher C11Pc loading efficiency may enable positive cell kill results.

7.2 Targeting the T antigen for selective PDT treatment

In **Chapter 4** the lectin jacalin was covalent conjugated to C11Pc-PEG gold nanoparticles using EDC/NHS chemistry. Jacalin was used to target the cancer-associated Thomsen-Friedenreich (T) antigen at the surface of HT-29 human colon adenocarcinoma cells. Incubation with the jacalin conjugated C11Pc-PEG gold nanoparticles caused no significant difference in the viability of the irradiated or non-irradiated HT-29 cells. However, a dose-dependent inhibition in proliferation was observed. This observation was in agreement with findings that reported similar effects on HT-29 cell proliferation following incubation with jacalin.[2] The lack of morphological changes in the HT-29 cells following jacalin targeted PDT suggested that the reduction in viability was as a direct result of the anti-proliferative effects of jacalin binding, as oppose to cytotoxicity.

C11Pc-PEG gold nanoparticles synthesised in tetrahydrofuran were previously reported to carry *ca.* 10 molecules of C11Pc per gold nanoparticle, as determined by inductively coupled-plasma mass spectrometry analysis.[1] An alternative synthetic protocol using *N,N*-dimethylformamide (DMF) was therefore established, which produced nanoparticles with a higher photosensitiser loading efficiency of *ca.* 155 molecules of C11Pc per gold nanoparticle and a *ca.* 3-fold higher yield of C11Pc-PEG gold nanoparticles. The C11Pc-PEG gold nanoparticles synthesised using the DMF synthetic protocol were conjugated to jacalin and were shown to effectively produce singlet oxygen following irradiation at 633 nm. HT-29 cells incubated with these nanoparticle conjugates and irradiated at 633 nm exhibited drastic morphological changes upon examination with an inverted optical microscope, whereas cells incubated with the non-conjugated particles remained largely unaltered.

Laser scanning confocal microscopy, in combination with differential interference contrast (DIC) imaging, showed that jacalin conjugation significantly improved the intracellular

accumulation of the C11Pc-PEG gold nanoparticles, as compared to the non-conjugated particles. The fluorescence of the C11Pc-PEG gold nanoparticle conjugates following excitation with a 633 nm HeNe laser, revealed the localised intracellular accumulation of the nanoparticles, suggesting that their internalisation was through a receptor mediated endocytic pathway. Following irradiation for 6 min, the cells incubated with jacalin conjugated particles exhibited drastic morphological changes that were typically associated with cytotoxicity. Positive staining of the nuclei of those cells with propidium iodide confirmed that the cells had lost their membrane integrity, and jacalin targeted PDT was likely to have induced cytotoxicity through necrosis.

The MTT viability assay performed on the HT-29 cells following PDT treatment found that the jacalin conjugated C11Pc-PEG gold nanoparticles induced a significant reduction in viability (*ca.* 40% viability at 1.15 μM C11Pc equivalent concentration). The viability of the HT-29 cells following targeted PDT treatment was further reduced to *ca.* 4% following a 3 mm increase in the beam diameter of the 633 nm HeNe laser. A statistically significant sigmoidal dose-dependent relationship in phototoxicity was observed with the jacalin conjugated C11Pc-PEG gold nanoparticles, whereas the non-conjugated particles resulted in minimal phototoxicity. Thus, jacalin was shown to significantly enhance the endocytosis of the nanoparticle conjugates. Competitive inhibition of jacalin binding to the T antigen on the HT-29 cells was achieved using methyl-α-galactopyranoside and asialofetuin, confirming that the enhanced phototoxicity of the conjugates was dependent on the carbohydrate binding capacity of the lectin.[2,3] The ApoTox-Glo™ triplex assay was performed 6 h following PDT treatment to establish the primary mechanism of cytotoxicity following irradiation of the HT-29 cells incubated with the jacalin conjugated nanoparticles. It was found that the HT-29 cells exhibited a significant decrease in viability, an increase in cytotoxicity, and no indications of apoptosis following jacalin targeted PDT treatment. The findings suggest that necrosis was the predominant mechanism of cell death following jacalin targeted PDT treatment at the conditions of the experiment. The results described in **Chapter 4** show for the first time that lectins can be used to selectively deliver nanoparticles to cancer cells for targeted PDT. The methodology established in this thesis could be utilised to potentially conjugate any lectin to the C11Pc-PEG gold nanoparticles and assess the PDT efficacy of the nanoparticle conjugates. However, as demonstrated in **Chapter 3**, a variety of factors must be considered when selecting a lectin, as carbohydrate binding affinities, receptor densities and cell penetrating characteristics are all likely to contribute to the outcome of the targeted PDT treatment.

7.3 Comparative study of lectin *versus* antibody targeting

Chapter 5 outlined investigations comparing the efficiency of using the lectin, jacalin, and monoclonal anti-HER-2 antibodies as targeting ligands to deliver C11Pc-PEG gold nanoparticles. Jacalin was conjugated to the C11Pc-PEG gold nanoparticles to target the T antigen (*ca.* 4.4×10^7 antigens per HT-29 colon cancer cell).[2] The anti-HER-2 antibody was also conjugated to C11Pc-PEG gold nanoparticles to target the HER-2 receptor (*ca.* $1\text{-}2 \times 10^6$ receptors per SK-BR-3 breast cancer cell).[4]

Importantly, it was found that there was no significant difference in singlet oxygen production following the irradiation of either type of nanoparticle conjugate. As determined by the MTT assay, the viability of the HT-29 cells following PDT treatment with nanoparticles conjugated to either jacalin or anti-HER-2 antibodies was significantly reduced, as compared to the non-conjugated particles. HT-29 cell viability was reduced to *ca.* 10% and 19% following jacalin or anti-HER-2 antibody targeted PDT treatment, respectively, at the highest nanoparticle concentration of 1.15 μM C11Pc equivalent. However, at the same concentration, the non-conjugated particles reduced viability by only *ca.* 6%. Jacalin conjugated C11Pc-PEG gold nanoparticles were shown to be more effective than anti-HER-2 antibody conjugated nanoparticles at reducing HT-29 cell viability at 1.15 μM C11Pc equivalent ($p<0.05$). However, the enhanced reduction in HT-29 cell viability following jacalin targeted PDT was accompanied by a *ca.* 15% greater level of dark toxicity, as compared to the antibody conjugates at the same nanoparticle concentration of 1.15 μM C11Pc equivalent. Although jacalin appears to be effective at targeting the HT-29 cells, the use of antibody conjugated nanoparticles is favourable due to the lower levels of dark toxicity that are induced.

Using the CellTiter-Blue™ assay, the viability of the SK-BR-3 cells was reduced to *ca.* 3% and 5% following targeted PDT treatment with the nanoparticles conjugated to jacalin or anti-HER-2 antibodies, respectively (1.15 μM C11Pc equivalent). Once again, the same concentration of non-conjugated particles induced a minimal reduction in viability (*ca.* 5%) following irradiation.

The difference in PDT efficacy between the HT-29 cells and the SK-BR-3 cells could be due to a higher susceptibility of the SK-BR-3 cells to photodynamic damage, but could also be attributed to a number of other factors. For example, the assays used to measure cell viability following PDT treatment are different; therefore the differences in viability

between the two cell lines could be a result of variations when using either the MTT assay or the CellTiter-Blue™ assay.

To establish whether there was a difference between the jacalin or anti-HER-2 targeted PDT cell death pathways, the ApoTox-Glo™ triplex assay was performed on both the HT-29 cells and the SK-BR-3 cells. Nanoparticles conjugated to sheep serum albumin (SSA) were used as a control to explore the significance of non-specific protein-cell interactions in enhancing the PDT effect of the C11Pc-PEG gold nanoparticles. Furthermore, the use of either 0.1 μM or 1 μM C11Pc equivalent of conjugated nanoparticles was compared to investigate the impact of nanoparticle concentration on the cell death pathways. It was found that at a concentration of 0.1 μM C11Pc equivalent, no significant difference in the reduction of HT-29 cell viability was observed between the jacalin or anti-HER-2 antibody conjugated nanoparticles, and the SSA conjugated particles. However, at a concentration of 1 μM C11Pc equivalent, the jacalin and anti-HER-2 antibody conjugated nanoparticles reduced the viability of irradiated HT-29 cells significantly more than the SSA conjugated particles ($P<0.05$). The cytotoxicity of irradiated HT-29 cells was only detected when the cells were incubated with jacalin or anti-HER-2 antibody conjugated nanoparticles at 1 μM C11Pc equivalent. The SSA conjugated particles failed to increase HT-29 cell cytotoxicity at either concentration, suggesting that the HT-29 cell cytotoxicity was a result of active targeting by the lectin or antibody conjugated nanoparticles. Apoptosis was not observed with the HT-29 cells following PDT treatment using any type of the C11Pc-PEG gold nanoparticle conjugates.

At a nanoparticle concentration of 0.1 μM C11Pc equivalent, the jacalin and anti-HER-2 antibody conjugated nanoparticles reduced SK-BR-3 cell viability significantly more than the SSA conjugated particles ($P<0.0005$). At a nanoparticle concentration of 1 μM C11Pc equivalent, a dramatic reduction in SK-BR-3 cell viability was observed with all three types of nanoparticles (*ca.* 95-99%), suggesting that above certain nanoparticle concentrations SK-BR-3 cells non-specifically internalise the SSA conjugated C11Pc-PEG gold nanoparticles. The cytotoxicity of SK-BR-3 cells was observed at both concentrations of jacalin or anti-HER-2 antibody conjugated C11Pc-PEG gold nanoparticles (*ca.* 5.6-7.5-fold increase in cytotoxicity). SSA conjugated nanoparticles also elicited a *ca.* 7.8-fold increase in SK-BR-3 cell cytotoxicity at 1 μM C11Pc equivalent. However, at 0.1 μM C11Pc equivalent of SSA nanoparticle conjugates only a *ca.* 1.6-fold increase in cytotoxicity was observed, further demonstrating the effectiveness of specific targeting ligand-cell

interactions. No apoptosis was observed with the SK-BR-3 cells following PDT treatment with any of the nanoparticle conjugates at either concentration used.

Laser scanning confocal microscopy was used to assess the intracellular localisation of the jacalin and anti-HER-2 antibody conjugated C11Pc-PEG gold nanoparticles in the HT-29 cells and the SK-BR-3 cells. LysoSensor™ Green DND-189 was used as a fluorescent marker for acidic organelles. Colocalisation of the red C11Pc fluorescence from the conjugated nanoparticles with the green LysoSensor™ Green DND-189 fluorescence suggested that the nanoparticle conjugates accumulated within the acidic organelles. The degree of colocalisation was analysed using the BioImageXD software. It was found that both jacalin and anti-HER-2 antibody conjugated nanoparticles partially colocalised with the LysoSensor™ Green DND-189 and remained in the acidic organelles within the HT-29 cells (*ca.* 27% and 31% colocalisation, respectively) and within the SK-BR-3 cells (*ca.* 43% and 22% colocalisation, respectively). These findings suggested that both types of nanoparticle conjugates were internalised through receptor mediated endocytosis.

Despite the differences in the binding affinities of jacalin (K_d of *ca.* 500 nM)[2] and anti-HER-2 antibodies (K_d of *ca.* 14-36 nM)[5] to their respective antigens, it is apparent that cell surface receptor density could play a large role in the outcome of targeted PDT treatment. Antibodies are already in use for cancer therapy and the findings described in **Chapter 5** suggest the huge potential that lectins, such as jacalin, could have for the targeted PDT treatment of tumours using biofunctionalised nanoparticles.

7.4 Sonodynamic therapy

Chapter 7 describes the synthesis of titanium dioxide (TiO_2) nanoparticles coated with polyacrylic acid (PAA) for applications in the sonodynamic therapy of cancer. TiO_2 nanoparticles with diameters ranging from 5-10 nm capped with the organic base, tetramethylammonium hydroxide (TMAOH), were successfully synthesised. Thermal annealing of the biocompatible polymer PAA onto the nanoparticle surface was then performed. However, recovery of the modified nanoparticles was unsuccessful. The controlled *in situ* hydrolysis of titanium (IV) butoxide in the presence of PAA, followed by hydrothermal treatment yielded dispersed, water soluble TiO_2 nanoparticles with a mean diameter of *ca.* 57-66 nm, as determined by TEM imaging and dynamic light scattering.

The presence of titanium within the purified nanoparticle preparations was also confirmed by elemental analysis using Energy Dispersive X-ray Analysis.

The PAA capped TiO_2 nanoparticles were explored as potential sonocatalysts using ultrasound irradiation with a frequency of 1 MHz and an intensity of 0.5 $W.cm^{-2}$. Sonochemical generation of singlet oxygen was monitored by the photobleaching of ADPA and the sonochemical production of $^{\bullet}OH$ was monitored by the degradation of methylene blue.[6] Methanol is a known scavenger of $^{\bullet}OH$, and it was found that the sonochemical degradation of aqueous methylene blue was completely inhibited by the presence of 5.88% v/v methanol.[7] The presence of TiO_2 nanoparticles in an aqueous solution of methylene blue was found to prevent the sonochemical degradation of the dye, possibly through PAA protection from $^{\bullet}OH$ attack. However, the presence of the TiO_2 nanoparticles enhanced the photobleaching of ADPA upon exposure to ultrasound irradiation. This enhancement in ADPA photobleaching was also observed in the presence of 5.88% v/v methanol, thus suggesting that $^{\bullet}OH$ attack of ADPA was not responsible for its photobleaching, but was rather a result of sonocatalytic singlet oxygen production.[8,9]

The exposure of the HT-29 colon cancer cells to 30 s of ultrasound irradiation (1 MHz and 0.5 $W.cm^{-2}$) following a 3 h incubation with 0.29, 0.74 or 1.47 mM TiO_2 equivalent of PAA capped TiO_2 nanoparticles resulted in no significant enhancement in sonodynamic toxicity. Incubation of the HT-29 cells with nanoparticles without exposure to ultrasound resulted in a dose-dependent reduction in viability, which was not enhanced by ultrasound irradiation. The findings of the *in vitro* sonodynamic therapy study show that the incubation of the cells with the nanoparticles is insufficient for effective sonodynamic toxicity and that the extracellular presence of the particles may be required.

The studies described in this thesis exemplify how nanoparticles can act as multifunctional systems enhancing PDT therapies for cancer, by providing aqueous solubility of hydrophobic photosensitisers and by providing a platform for conjugation to cancer-specific targeting ligands. Specifically, this thesis highlights the first use of tumour-specific lectins to functionalise nanoparticles for the targeted PDT of cancer cells.[10] The targeted PDT efficacy of the T antigen-specific lectin jacalin was found to be similar to the targeting efficiency of the anti-HER-2 antibody. With consideration of the dissociation constants (K_d) that define the binding efficiencies of jacalin *versus* the anti-HER-2 antibody to their respective target antigen (*ca.* 500 nM *vs. ca.* 14-36 nM, respectively), this is somewhat a surprising result.[2,5] However, the similarity in targeting efficiency could

indicate the importance of receptor density on targeted treatments. Overall, nanoparticles have proven to be powerful mediators in photodynamic therapy that promise to maximise the clinical outcome of the treatment. Through the multifunctionality provided by nanoparticles, targeted cancer treatment using lectin conjugates hold great potential for selective cancer therapy.

7.5 Future Work

The *in vivo* biodistribution, tumour selectivity and targeting efficacy of the jacalin conjugated C11Pc-PEG nanoparticles could be investigated in tumour mouse models to further assess the clinical potential of lectin targeted PDT treatment. The targeting efficiency of alternative T antigen binding lectins, such as the *Agaricus bisporus* lectin and *Helix pomatia* agglutinin, could also be explored to selectively deliver the nanoparticles to cancer cells overexpressing the T antigen.[11-13] Additionally, lectins that target alternative cancer-associated carbohydrate antigens, such as the Tn antigen-specific *Vicia villosa* lectin, could be conjugated to the C11Pc-PEG gold nanoparticles for targeted PDT treatment of different cell lines.[14] However, the use of lectins that increase cell proliferation, such as the peanut agglutinin, must be avoided as these lectins are likely to have a negative impact on the therapeutic outcome of the treatment by promoting cancer cell growth.[15] The biomodulatory effects that some lectins exert on cancer cells upon binding could also be exploited for multimodal cancer therapy in a similar manner to treatment using functional blocking antibodies, such as anti-vascular endothelial growth factor (VEGF) antibodies.[16] Lectins, such as the *Maackia amurensis* lectin which is specific for α2,3-sialylated *O*-linked glycans, could be conjugated to photosensitising nanoparticle constructs to selectively deliver sensitisers to cancer cells whilst inhibiting cell growth and metastasis.[17] Alternatively, two or more lectins could be conjugated onto one nanoparticle carrying a PDT agent: a lectin to target the cancer-associated glycan, and a second lectin with potent anti-metastatic and anti-proliferative characteristics.

Further investigations into 'necroptosis' (programmed necrosis), cell cycle arrest and autophagic induction could be performed in order to elucidate the exact cellular processes that occur following jacalin targeted PDT treatment. Additionally, it would be informative to establish the nanoparticle concentration range at which jacalin targeted PDT occurs as a result of specific T antigen recognition.

The sonodynamic cytotoxic effect of TiO_2 nanoparticles could be further investigated by exposing the cancer cells to ultrasound irradiation during the extracellular presence of the particles. Furthermore, the bioconjugation of cancer-targeting ligands to the TiO_2 nanoparticles could be explored to establish whether an increase in the specific particle adhesion with the cancer cell membranes would promote their sonodynamic toxicity.

7.6 References

1. Stuchinskaya, T.; Moreno, M.; Cook, M. J.; Edwards, D. R.; Russell, D. A. *Photochem. Photobiol. Sci.* **2011**, *10*, 822-831.
2. Yu, L.-G.; Milton, J. D.; Fernig, D. G.; Rhodes, J. M. *J. Cell. Physiol.* **2001**, *186*, 282-287.
3. Hortin, G. L.; Trimpe, B. L. *Anal. Biochem.* **1990**, *188*, 271-277.
4. Orlova, A.; Bruskin, A.; Sivaev, I.; Sjöberg, S.; Lundqvist, H.; Tolmachev, V. *Anticancer Res.* **2006**, *26*, 1217-1223.
5. Tang, Y.; Wang, J.; Scollard, D. A.; Mondal, H.; Holloway, C.; Kahn, H. J.; Reilly, R. M. *Nucl. Med. Biol.* **2005**, *32*, 51-58.
6. Shimizu, N.; Ogino, C.; Dadjour, M. F.; Murata, T. *Ultrason. Sonochem.* **2007**, *14*, 184-190.
7. Monod, A.; Chebbi, A.; Durand-Jolibois, R.; Carlier, P. *Atmos. Environ.* **2000**, *34*, 5283-5294.
8. Davidson, R. S.; Safdar, A.; Spencer, J. D.; Robinson, B. *Ultrasonics* **1987**, *25*, 35-39.
9. Janczyk, A.; Krakowska, E.; Stochel, G.; Macyk, W. *J. Am. Chem. Soc.* **2006**, *128*, 15574-15575.
10. Obaid, G.; Chambrier, I.; Cook, M. J.; Russell, D. A. *Angew. Chem. Int. Ed.* **2012**, *51*, 6158-6162.
11. Yu, L.-G.; Fernig, D. G.; Smith, J. A.; Milton, J. D.; Rhodes, J. M. *Cancer Res.* **1993**, *53*, 4627-4632.
12. Sanchez, J. F.; Lescar, J.; Chazalet, V.; Audfray, A.; Gagnon, J.; Alvarez, R.; Breton, C.; Imberty, A.; Mitchell, E. P. *J. Biol. Chem.* **2006**, *281*, 20171-20180.
13. Sellei, J. *J. Immunogenet.* **1981**, *8*, 263-269.
14. Tollefsen, S. E.; Kornfeld, R. *J. Biol. Chem.* **1983**, *258*, 5172-5176.
15. Singh, R.; Subramanian, S.; Rhodes, J. M.; Campbell, B. J. *Glycobiology* **2006**, *16*, 594-601.
16. Ellis, L. M.; Hicklin, D. J. *Nat. Rev. Cancer* **2008**, *8*, 579-591.
17. Ochoa-Alvarez, J. A.; Krishnan, H.; Shen, Y.; Acharya, N. K.; Han, M.; McNulty, D. E.; Hasegawa, H.; Hyodo, T.; Senga, T.; Geng, J.-G.; Kosciuk, M.; Shin, S. S.; Goydos, J. S.; Temiakov, D.; Nagele, R. G.; Goldberg, G. S. *PLoS ONE* **2012**, *7*, e41845.

Publications and Presentations

Publications

Obaid, G., Chambrier, I., Cook, M.J. and Russell, D.A. Targeting the Oncofetal Thomsen–Friedenreich Disaccharide Using Jacalin-PEG Phthalocyanine Gold Nanoparticles for Photodynamic Cancer Therapy, *Angewandte Chemie International Edition* **2012**,51 (25), 6158-6162.

Girgis Obaid and David A. Russell, Nanoparticles for Photodynamic Therapy, Handbook of Photomedicine, Editors Michael R. Hamblin and Sulbha K. Sharma, *Taylor & Francis (June 15* 2013)**,** ISBN-13: 978-1439884690

Oral Presentations

Going for gold – new developments in cancer therapy. *Girgis Obaid* and *David A. Russell*. Showcase of Postgraduate Research, Norwich Forum, 17th June 2010. (First for best oral presentation)

T antigen disaccharide targeting for selective photodynamic therapy of colon cancer cells using lectin-phthalocyanine gold nanoparticles. *Girgis Obaid* and *David A. Russell*. School of Chemistry Colloquium, University of East Anglia, 12th July 2011. (First for best oral presentation)

Jacalin-phthalocyanine gold nanoparticles: carbohydrate targeting for photodynamic therapy of colon cancer cells. *Girgis Obaid* and *David A. Russell*. 9th International Symposium on Photodynamic Therapy and Photodiagnosis in Clinical Practice, Brixen/Bressanone, Italy, 17th October 2012.

Poster Presentations

Lectin-coated gold nanoparticles for the detection and destruction of cancer cells. *Girgis Obaid* and *David A. Russell*. Showcase of Postgraduate Research, Norwich Forum, 17th June 2010. (Runner-up prize for most informative poster)

Lectin-gold nanoparticle platforms for the molecular recognition and destruction of cancer cells. *Girgis Obaid* and *David A. Russell*. RSC Analytical Research Forum, Loughborough University, 26-28th July 2010.

Lectin-gold nanoparticle platforms for the molecular recognition and destruction of cancer cells. *Girgis Obaid* and *David A. Russell*. School of Chemistry Colloquium, University of East Anglia, July 2010.

Jacalin-phthalocyanine gold nanoparticles: carbohydrate targeting for photodynamic therapy of colon cancer cells. *Girgis Obaid* and *David A. Russell*. School of Chemistry Colloquium, University of East Anglia, 5th July 2012.